APPLICATIONS AND MECHANISTIC STUDIES OF POLYMORPH SELECTION BY POLYMER HETERONUCLEI

by

Vilmalí López-Mejías

A dissertation submitted in partial fulfillment
of the requirements for the degree of
Doctor of Philosophy
(Chemistry)
in The University of Michigan
2011

Doctoral Committee:

Professor Adam J. Matzger, Chair
Professor Zhan Chen
Professor Michael D. Morris
Associate Professor Naír Rodríguez-Hornedo

DEDICATION

To Love, and all the expressions of it in my life. I love you.

Acknowledgements

I would not be sitting here, writing this acknowledgement page without the support and motivation of so many people with whom I have had the opportunity to cross paths throughout my life. As I do not intend this to be a comprehensive list, I offer my sincere apologies to anyone who I might have forgotten in my attempt to make this section as brief as it can be.

First, I would like to thank my thesis adviser Professor Adam J. Matzger for providing me with the opportunity to do research in his laboratory. You have allowed me to develop as an individual researcher, motivating me to do chemistry outside my comfort zone, providing me with onsite state of the art instrumentation whenever I need it and ultimately supporting me unconditionally in all my decisions. I also thank Professor Zhan Chen for his collaboration in the research discussed in Chapter 6 and for this participation in my thesis committee. I would also like to thank the other members of my thesis committee Associate Professor Naír Rodríguez-Hornedo, and Professor Michael D. Morris for their participation in my professional development through serving in this committee.

My most heartfelt thanks the collaborators of the research presented in this thesis. Dr. Charles L. Brooks III and Dr. Jennifer Lynn Knight for their participation in the research presented in Chapter 3 and 6. Dr. Arthur A. McClelland who worked closely with me during the SFG studies discussed in Chapter 5. Dr. Jeff W. Kampf which at times I am sure felt like my personal crystallographer, I thank you for solving the structures of my most naughty crystals presented Chapters 2, 3, and 4.

I would like to thank current and former members of the Matzger research group for their friendship, support and collaboration throughout my years in the group. Also, I would like extend my gratitude to the Chemistry Department, Rackham Graduate School and The University of Michigan for support through the different resources that made my life as a graduate student easier in so many ways it would be hard to point individually.

I would like to thank my earlier mentors Dr. Katherine Barnhard, Dr. Ingrid Montes, Dr. Joseph Bloom and Dr. Daryl L. Bush for their support and motivation during my years as an undergraduate researcher.

Ultimately, I would like to thank my family and closest friends for being my support system through the hard and the good times of my graduate life. Thanks mom and dad for supporting this journey and for teaching me the value of hard work and perseverance, but above that for loving me unconditionally. Dad, I will always remember what you said to us when you were about to send us to military school “I can’t offer you much, but this I can…and no one can take that (education) from you.” I will always be grateful for the sacrifices you made for us. I love you. Mom, every time something when wrong in lab, and there were many instances, I would always remember what you used to say to us when we were down “eso son pajitas que le caen a la leche” those and many others words of wisdom brought me to this point. I love you. José, I hope you are as proud of me as I am of you. You have grown to be a wonderful brother and dad, I would like to take some credit for that but I can’t, it is all you. I love you. To those who I proudly call my friends, your presence in my life makes me really appreciate each moment of it. I love you all.

Table of Contents

CHAPTER 1. INTRODUCTION TO CRYSTAL POLYMORPHISM

CHAPTER 2. POLYMER-INDUCED HETERONUCLEATION OF TOLFENAMIC ACID: STRUCTURAL INVESTIGATION OF A PENTAMORPH

CHAPTER 3. CRYSTAL POLYMORPHISM OF NIFLUMIC AND FLUFENAMIC ACID

CHAPTER 4. THE POLYMORPHOPHORE: ANOTHER FABLE IN CRYSTAL ENGINEERING?

CHAPTER 5. PEERING AT A BURIED POLYMER-CRYSTAL INTERFACE: PROBING HETEROGENEOUS NUCLEATION BY SUM FREQUENCY GENERATION VIBRATIONAL SPECTROSCOPY

CHAPTER 6. ON THE MECHANISM OF POLYMORPH SELECTION BY POLYMER HETERONUCLEI

List of Figures

List of Tables

CHAPTER 1

INTRODUCTION TO CRYSTAL POLYMORPHSISM

1.1 Introduction

Polymorphism arises when a given compound packs in multiple arrangements and/or conformations due to a fine interplay between attractive and repulsive interactions among and within molecules in a crystal.[1] Crystal polymorphism occurs across a broad range of materials from small molecules to macromolecules.[1] Understanding the balance between attractive and repulsive interactions as well as controlling and predicting their supramolecular motif has become an area of extensive research in solid-state chemistry due to the profound impact of polymorphism on the solid-state properties of these materials.

Polymorphism in pharmaceutical compounds has gathered a lot of attention, as a result of regulatory concerns on polymorphic purity[2] and the effect of solid form on the solubility and bioavailability among other solid-state properties. Accounts of polymorphic transformations occurring during manufacturing of pharmaceuticals are not uncommon.[3] Therefore, a comprehensive identification of all the energetically viable polymorphs of a pharmaceutical compound early in the drug development is highly desirable in order to select the suitable solid form and avoid the cost of unexpected transformations.

Even though fewer than 5% of the compounds in the Cambridge Structural Database (CSD) are polymorphic,[4] its occurrence is very common in pharmaceutical compounds with at least one third of these displaying polymorphism.[5] A recent search of the CSD, which contains close to 400,000 crystal structures, for highly polymorphic compounds revealed that there are only a few pharmaceutical compounds which possess more than five structurally characterized crystal forms. To date, only four pharmaceutical compounds in the CSD are pentamorphic: sulfathiazole,[6-9] chlorpropamide,[10-13] aripiprazole,[14-16] and tolfenamic acid (TA)[17, 18] (Figure 1.1). Additionally, if the definition of polymorph is expanded to include tautomers, sulfapyridine (Figure 1.1), a pharmaceutical compound which can assume two tautomeric forms, can also be considered pentamorphic.[19, 20] Currently, a pharmaceutical precursor, 5-methyl-2-[(2-nitrophenyl)amino]-3-thiophenecarbonitrile (ROY, Figure 1.1), possesses the largest number of structurally characterized polymorphs in the CSD, with seven forms.[21-25] The occurrence of only a few examples of highly polymorphic pharmaceutical compounds in the CSD serves to illustrate the need for alternative approaches for polymorph discovery, specifically in the pharmaceutical industry, where appropriate solid form selection and control is crucial for drug performance.

Traditional methods of screening for polymorphism rely mostly in altering crystallization variables such as temperature, solvent and degree of supersaturation. However, such methods do not explicitly target nucleation, a critical step in the formation of different polymorphs.[26] More recent efforts have been focused on controlling the formation of nuclei to produce different crystal phases. These approaches include the use of monolayers,[27-33] tailored-made soluble additives[34-36] and epitaxy.[21, 37-41] For these techniques, previous knowledge of the crystal structure is desirable in order to select the conditions that will control the formation of given nuclei. More general approaches that target nucleation are critical if the intent is to access all kinetically trapped polymorphs.

The application of polymers as heteronucleants has been demonstrated to be a powerful technique in the control and discovery of solid-state forms throughout a broad spectrum of materials.[17, 42-48] Polymer-induced heteronucleation (PIHn) utilizes diverse libraries of insoluble polymers differing in surface chemistry as heteronuclei to promote interactions that favor polymorph formation, therefore, offering a general method to attain selective control over nucleation. The application of polymer heteronucleants to investigate polymorphism in potent nonsteroidal anti-inflammatory drugs (NSAIDs) of the fenamic acid family and analogues thereof demonstrates the capability of PIHn to access novel crystalline forms.

Pentamorphism in tolfenamic acid (TA),[17] a NSAID previously thought to be dimorphic,[18] has been established through the use of non-polar aromatic polymers as heteronuclei. These findings are discussed in Chapter 2. The occurrence of conformational changes among the forms, whole molecule disorder in form V, space group diversity, as well as varying numbers of molecules in the asymmetric unit all occurring within a very narrow energy window make the solid-state chemistry of TA exceptionally intricate among the few pharmaceuticals that display this high number of polymorphic structures. Consequently, TA serves as a paradigm for the notion that when certain structural motifs are incorporated into a structure, they favor the formation of polymorphic crystals: the polymorphophore.[49, 50]

Previous accounts have implied a relationship between molecular structure and the polymorphic propensity of a given compound.[17, 49-54] Multiple investigations exist in which analogues of highly polymorphic compounds like ROY[21-25] and carbamezepine (CBZ)[55] are studied in order to explore their polymorphic behavior. From the investigations concerning ROY derivatives (Figure 1.2),[50, 56-59] it can be concluded that the addition or subtraction of a methyl group to the molecular structure of ROY or the ethynyl linkage of two ROY molecules does not eliminate the ability of these compounds to arrange differently in the solid state. With the exception of Br-ROY all of these analogues display polymorphism. CBZ is a pharmaceutical compound presenting four structurally characterized forms,[55, 60-64] and numerous solvates[65-68] and co-crystals[46, 69-73] which in some cases present polymorphism[46] as well. In the case of investigations concerning CBZ analogues (Figure 1.3),[74-76] it can be observed that the removal of the double bond or its transformation into a ketone does not affect the ability of the analogues to display polymorphism but disturbing the hydrogen bonding provided by the amide functionality seems to hinder the ability to form other crystalline phases. Collectively, these investigations present the first evidence that a polymorphophore might be responsible for the appearance of multiple crystalline phases in these analogues and highlight the need for a systematic approach in order to gain understanding of the structural factors that influence polymorphism in molecular compounds.

Computationally, the notion that an ensemble of steric and electronic features in a molecule provide a fine interplay of the interactions ultimately responsible for the appearance of multiple crystal forms has been explored in an effort to predict the number of energetically viable crystal forms that can be accessed for a given molecular structure.[77-83] The strength of these computational methods can only be validated once all the predicted forms are experimentally determined.[84] Therefore, it would be desirable if a relationship between molecular structure and polymorphism could be derived experimentally. Chapters 3 and 4 explore the application of insoluble polymers as heteronucleants in the control and discovery of crystal forms of the commercially available NSAIDs niflumic (NA), flufenamic (FFA), and mefanamic acid (MA), pharmaceutical precursor fenamic acid (FA) as well as four synthesized analogues of TA (Figure 1.4), with aim of understanding if a common molecular theme in these compounds favors the display of polymorphism in this set of analogues.

The use of polymers as heteronuclei has allowed access to and structural determination of two novel forms of NA and four of the previously proposed forms of FFA,[85-87] providing evidence for polymorphism in NA[88] for the first time and expanding on the number of structurally characterized forms for the highly studied FFA. Although structures for at least two other forms of FFA remain unsolved, the occurrence of most of these forms under one crystallization condition through PIHn illustrates that a fine interplay of kinetic factors lead to form selection in FFA. Additionally, the transformation at low temperature of FFA form IV has allowed access to and structural elucidation of form VI, making FFA the only pharmaceutical compound currently reaching the level of heptamorphism. Polymorphism in NA and FFA is also discussed in the broader context of the concept of the polymorphophore,[49, 50] in Chapter 3.

The strength of PIHn as a polymorph discovery tool was tested against solvent-based crystallization in the absence of polymers in Chapter 4. Using a small scale conventional polymorph screening based on crystallization from fourteen commonly used solvents, only a few of the solvents were able to access multiple crystalline phases for each analogue of TA, this finding contrasts with the large number of polymorphs accessed when PIHn was employed. Additionally, crystal growth from the vapor phase in the absence of polymer only provided accesses to one crystal form for each of the analogues explored. All four synthesized analogues and MA display polymorphism. For each molecular structure presenting polymorphism, several crystal structures were elucidated. In the case of FA, although many efforts were employed in order to access new forms, they remain unfruitful and no polymorphs of this analogue were found.

The ability to access and structurally solve multiple crystal phases of TA and all its analogues allowed the exploration of possible energy landscapes through molecular mechanics simulations. Proposed virtual structures of each analogue and TA were computed from the experimentally determined crystal structures, in order to evaluate if isostructural forms remained inaccessible after the employment of PIHn. These results are discussed in Chapter 4. The appearance of polymorphism in all analogues studied, except FA, supports the notion that certain structural motifs within a molecular class promote the adoption of multiple packing modes, and that this polymorphophore provides a fine interplay of the interactions ultimately responsible for the appearance of these kinetically driven solid forms. The systematic study of the structure-polymorphism relationship will help predict the polymorphic propensity of a given molecular motif and provide a pathway to engineer molecular compounds less prone to polymorphism.

The utility of the PIHn approach to control polymorphism in other pharmaceutical compounds such as acetaminophen (ACM),[47, 48] ROY,[21-25] and CBZ[55, 60-64] has been previously demonstrated. In addition, this methodology has been utilized to access novel solid forms of compounds such as cabamazepine cocrystals[46] with saccharin and nicotinamide, oxcarbezepine,[49] ethynyl linked bis-ROY,[50] TA[17] and many of its structurally related analogues. In these studies, a possible relation between the polymorph produced and the specific polymer surface from which it is grown has been implied.[48] Also, it has been observed that the orientation of crystals grown from a polymer surface varies depending on the polymer utilized which suggests that the polymer functionality might be a primary driving force in stabilizing the crystal nucleus leading to the controlled production of a particular polymorph.

The phase-selective crystallization of ACM (Figure 1.5) using insoluble polymers as heteronuclei was investigated in a combined experimental and computational effort to elucidate the mechanism of PIHn in Chapters 5 and 6. ACM crystals were deposited on polymer coated substrates from aqueous supersaturated solutions as well as, from vapor deposition and analyzed using sum frequency generation vibrational spectroscopy (SFG-VS)[89] and powder X-ray diffraction (PXRD).[90] As was previously reported,[47, 48] ACM heteronucleates from supersaturated aqueous solution in the metastable orthorhombic crystal form, on poly(methyl methacrylate) (PMMA, Figure 1.5) surfaces, whereas the thermodynamically stable monoclinic crystal form is observed to form on poly(*n*-butyl methacrylate) (PBMA, Figure 1.5) surfaces. When the ACM crystals were grown by sublimation, only the monoclinic form was observed on both PMMA and PBMA. SFG-VS results indicate that hydrogen bonds are formed between PMMA C=O groups and the orthorhombic ACM crystals at the PMMA-ACM interface. At the PBMA-monoclinic ACM interfaces, no hydrogen bond formation was observed. These results are discussed in Chapter 5. Furthermore, each crystallization condition employed led to a unique

PXRD pattern with the major preferred orientation corresponding to the crystallographic faces in which these crystal phases nucleate from surfaces of the polymers. The molecular recognition events leading to these outcomes are elucidated with the aid of computed polymer-crystal binding energies using docking simulations. These results are discussed in Chapter 6. These investigations illuminate the mechanism by which phase-selection occurs during the crystallization of ACM using polymers as heteronuclei paving the way for the improvement of methods for polymorph selection and discovery based on heterogeneous nucleation promoters.

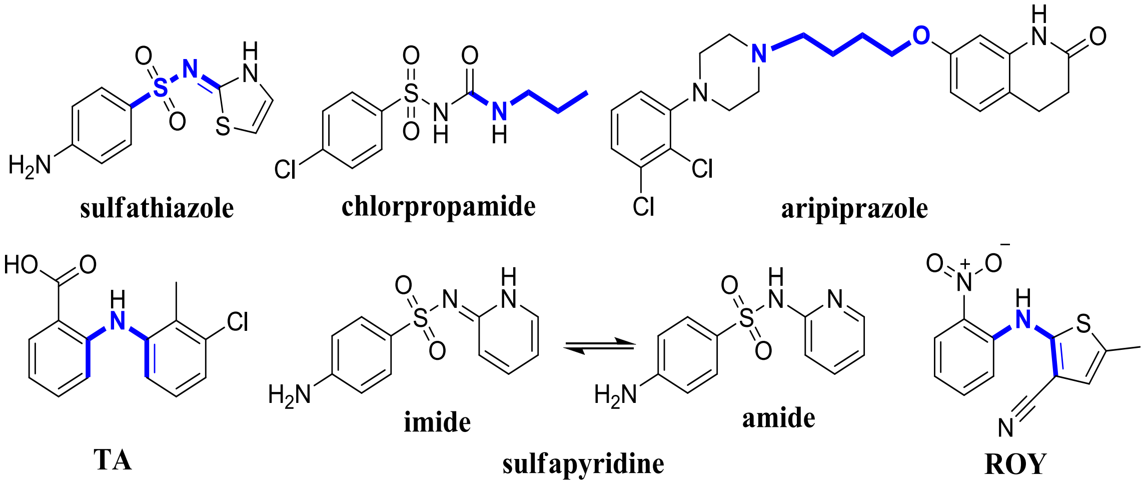

Figure 1.1. Chemical structures of sulfathiazole, chlorpropamide, aripiprazole, tolfenamic acid (TA), both tautomers of sulfapyridine, and 5-methyl-2-[(2-nitrophenyl)amino]-3-thiophenecarbonitrile (ROY) illustrating the torsion angles (τ, bonds in blue) differing among the conformers.

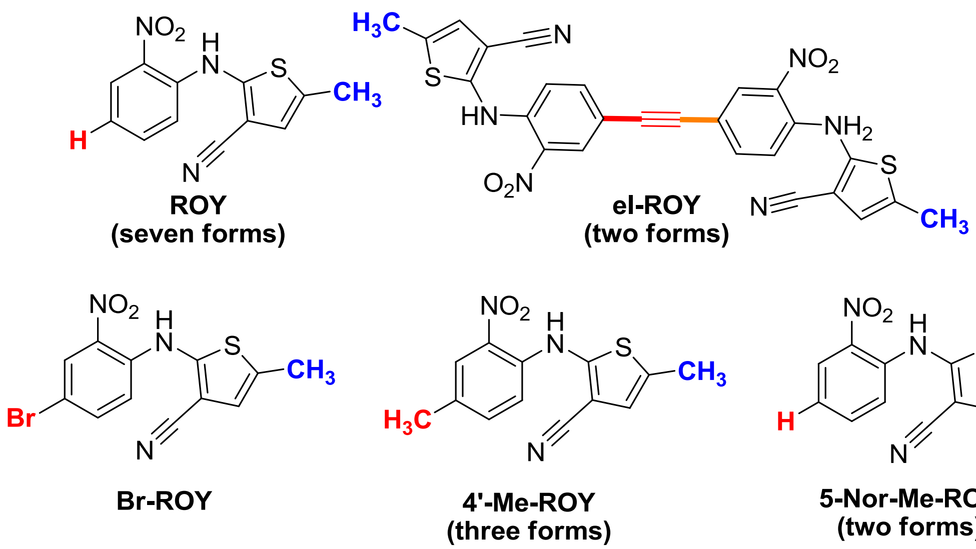

Figure 1.2. Chemical structures of 5-methyl-2-[(2-nitrophenyl)amino]-3-thiophenecarbonitrile (ROY) and structural analogues; ethynyl linked bis-ROY (el-ROY), Br-ROY, 4'-Me-ROY, and 5-Nor-Me-ROY with the number of structurally characterized forms in parenthesis. To date, Br-ROY possesses only one known crystal form. Substitutions in the phenyl group are indicated in red, whereas substitutions in the thiophene ring are indicated in blue.

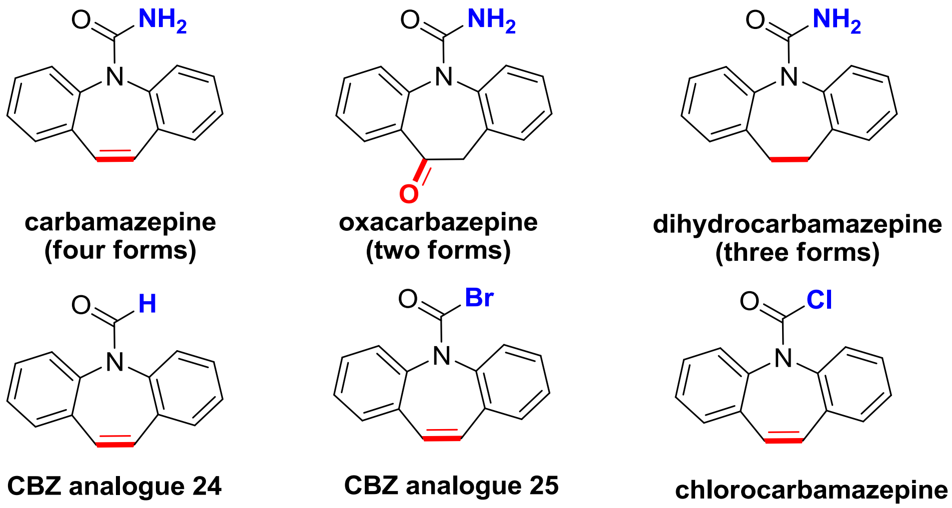

Figure 1.3. Chemical structures of carbamazepine, and structural analogues; oxacarbazepine, dihydrocarbamazepine, CBZ analogue 24, CBZ analogue 25, and chlorozarbamazepine with the number of structurally characterized forms in parenthesis. Substitutions in the seven member ring heterocycle are indicated in red, whereas substitutions in the nitrogen are indicated in blue.

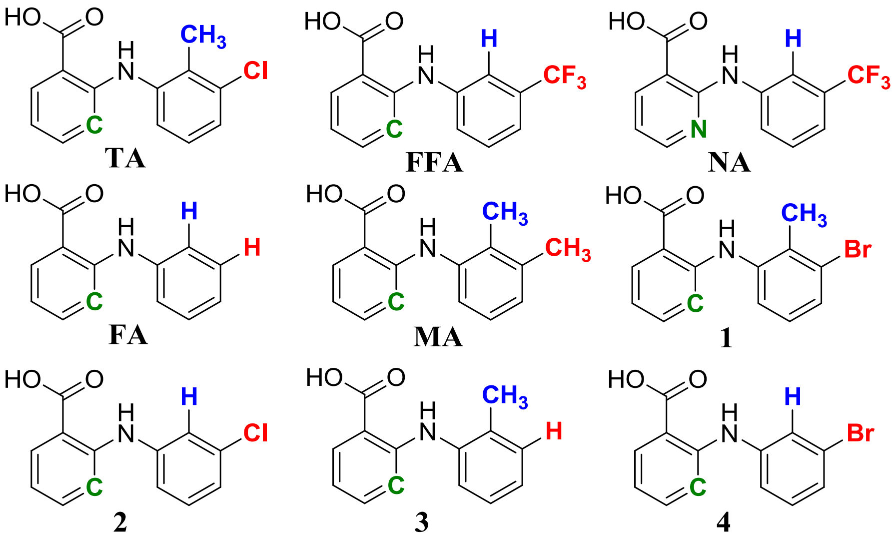

Figure 1.4. Molecular structure of tolfenamic acid (TA), flufenamic acid (FFA), niflumic acid (NA), mefenamic acid (MA), fenamic acid (FA), and synthesized analogues **1-4** investigated by PIHn. Substitutions in the non-carboxylated phenyl ring are indicated in blue for the ortho position and red for the para position, substitutions in the carboxylated phenyl ring are indicated in green.

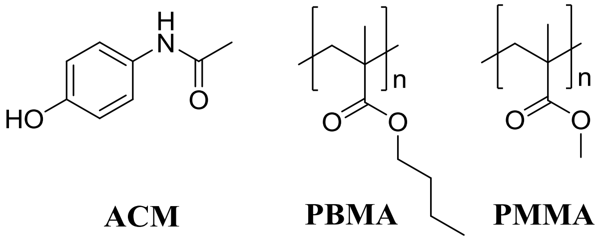

Figure 1.5. Chemical structures of acetaminophen (ACM), poly(*n*-butyl methacrylate) (PBMA), and poly(methyl methacrylate) (PMMA).

1.2 References

1. Bernstein, J.; *Polymorphism in Molecular Crystals;* Oxford University Press: Oxford Clarendon Press, New York, **2002.**

2. Byrn, S.; Pfeiffer, R.; Ganey, M.; Hoiberg, C.; Poochikian, G., Pharmaceutical Solids - a Strategic Approach to Regulatory Considerations. *Pharmaceutical Research* **1995,** 12, (7), 945-954.

3. Matsunaga, H.; Eguchi, T.; Nishijima, K.; Enomoto, T.; Sasaoki, K.; Nakamura, N., Solid-state characterization of candesartan cilexetil (TCV-116): Crystal structure and molecular mobility. *Chemical & Pharmaceutical Bulletin* **1999,** 47, (2), 182-186.

4. Brittain, H. G.; *Polymorphism in Pharmaceutical Solids*; M. Dekker: New York, **1999**.

5. Dunitz, J. D.; Bernstein, J., Disappearing Polymorphs. *Accounts of Chemical Research* **1995,** 28, (4), 193-200.

6. Blagden, N.; Davey, R. J.; Lieberman, H. F.; Williams, L.; Payne, R.; Roberts, R.; Rowe, R.; Docherty, R., Crystal chemistry and solvent effects in polymorphic systems -

Sulfathiazole. *Journal of the Chemical Society-Faraday Transactions* **1998,** 94, (8), 1035-1044.

7. Hughes, D. S.; Hursthouse, M. B.; Threlfall, T.; Tavener, S., A new polymorph of sulfathiazole. *Acta Crystallographica Section C-Crystal Structure Communications* **1999,** 55, 1831-1833.
8. Kruger, G. J.; Gafner, G., Crystal Structure of Sulphathiazole .2. *Acta Crystallographica Section B-Structural Crystallography and Crystal Chemistry* **1971,** B 27, 326.
9. Kruger, G. J.; Gafner, G., Crystal-Structures of Polymorphs-I and III of Sulfathiazole. *Acta Crystallographica Section B-Structural Crystallography and Crystal Chemistry* **1972,** B 28, 272.
10. Drebushchak, T. N.; Chukanov, N. V.; Boldyreva, E. V., A new gamma-polymorph of chlorpropamide: 4-chloro-N-(propylamino-carbonyl)benzenesulfonamide. *Acta Crystallographica Section C-Crystal Structure Communications* **2007,** 63, O355-O357.
11. Drebushchak, T. N.; Chukanov, N. V.; Boldyreva, E. V., A new polymorph of chlorpropamide: 4-chloro-N-(propylaminocarbonyl)benzenesulfonamide. *Acta Crystallographica Section E-Structure Reports Online* **2006,** 62, O4393-O4395.
12. Drebushchak, T. N.; Chukanov, N. V.; Boldyreva, E. V., Two polymorphs of chlorpropamide: the delta-form and the high-temperature epsilon-form. *Acta Crystallographica Section C-Crystal Structure Communications* **2008,** 64, O623-O625.
13. Koo, C. H.; Cho, S. I.; Yeon, Y. H., Crystal and Molecular Structure of Chlorpropamide. *Archives of Pharmacal Research (Seoul)* **1980,** 3, (1), 37-50.
14. Tessler, L.; Goldberg, I., Crystal structures of aripiprazole, a new anti-psychotic drug, and of its inclusion compounds with methanol, ethanol and water. *Journal of Inclusion Phenomena and Macrocyclic Chemistry* **2006,** 55, (3-4), 255-261.
15. Braun, D. E.; Gelbrich, T.; Kahlenberg, V.; Tessadri, R.; Wieser, J.; Griesser, U. J., Stability of Solvates and Packing Systematics of Nine Crystal Forms of the Antipsychotic Drug Aripiprazole. *Crystal Growth & Design* **2009,** 9, (2), 1054-1065.
16. Braun, D. E.; Gelbrich, T.; Kahlenberg, V.; Tessadri, R.; Wieser, J.; Griesser, U. J., Conformational Polymorphism in Aripiprazole: Preparation, Stability and Structure of Five Modifications. *Journal of Pharmaceutical Sciences* **2009,** 98, (6), 2010-2026.
17. López-Mejías, V.; Kampf, J. W.; Matzger, A. J., Polymer-Induced Heteronucleation of Tolfenamic Acid: Structural Investigation of a Pentamorph. *Journal of the American Chemical Society* **2009,** 131, (13), 4554.
18. Andersen, K. V.; Larsen, S.; Alhede, B.; Gelting, N.; Buchardt, O., Characterization of 2 Polymorphic Forms of Tolfenamic Acid, N-(2-Methyl-3-Chlorophenyl)Anthranilic Acid - Their Crystal-Structures and Relative Stabilities. *Journal of the Chemical Society-Perkin Transactions 2* **1989**, (10), 1443-1447.
19. Gelbrich, T.; Bingham, A. L.; Threlfall, T. L.; Hursthouse, M. B., delta-Sulfanilamide. *Acta Crystallographica Section C-Crystal Structure Communications* **2008,** 64, O205-O207.
20. Gelbrich, T.; Threlfall, T. L.; Bingham, A. L.; Hursthouse, M. B., Polymorph VI of sulfapyridine: interpenetrating two- and three-dimensional hydrogen-bonded nets formed from two tautomeric forms. *Acta Crystallographica Section C-Crystal Structure Communications* **2007,** 63, O323-O326.

21. Mitchell, C. A.; Yu, L.; Ward, M. D., Selective nucleation and discovery of organic polymorphs through epitaxy with single crystal substrates. *Journal of the American Chemical Society* **2001,** 123, (44), 10830-10839.
22. Stephenson, G. A.; Borchardt, T. B.; Byrn, S. R.; Bowyer, J.; Bunnell, C. A.; Snorek, S. V.; Yu, L., Conformational and Color Polymorphism of 5-Methyl-2-[(2-Nitrophenyl)Amino]-3-Thiophenecarbonitrile. *Journal of Pharmaceutical Sciences* **1995,** 84, (11), 1385-1386.
23. Yu, L.; Stephenson, G. A.; Mitchell, C. A.; Bunnell, C. A.; Snorek, S. V.; Bowyer, J. J.; Borchardt, T. B.; Stowell, J. G.; Byrn, S. R., Thermochemistry and conformational polymorphism of a hexamorphic crystal system. *Journal of the American Chemical Society* **2000,** 122, (4), 585-591.
24. Chen, S.; Guzei, I. A.; Yu, L., New polymorphs of ROY and new record for coexisting polymorphs of solved structures. *Journal of the American Chemical Society* **2005,** 127, (27), 9881-9885.
25. Chen, S. A.; Xi, H. M.; Yu, L., Cross-nucleation between ROY polymorphs. *Journal of the American Chemical Society* **2005,** 127, (49), 17439-17444.
26. Rodríguez-Hornedo, N.; Murphy, D., Significance of controlling crystallization mechanisms and kinetics in pharmaceutical systems. *Journal of Pharmaceutical Sciences* **1999,** 88, (7), 651-660.
27. Frostman, L. M.; Bader, M. M.; Ward, M. D., Nucleation and Growth of Molecular-Crystals on Self-Assembled Monolayers. *Langmuir* **1994,** 10, (2), 576-582.
28. Frostman, L. M.; Ward, M. D., Nucleation of molecular crystals beneath guanidinium alkanesulfonate monolayers. *Langmuir* **1997,** 13, (2), 330-337.
29. Landau, E. M.; Wolf, S. G.; Levanon, M.; Leiserowitz, L.; Lahav, M.; Sagiv, J., Stereochemical Studies in Crystal Nucleation - Oriented Crystal-Growth of Glycine at Interfaces Covered with Langmuir and Langmuir-Blodgett Films of Resolved Alpha-Amino-Acids. *Journal of the American Chemical Society* **1989,** 111, (4), 1436-1445.
30. Weissbuch, I.; Majewski, J.; Kjaer, K.; Alsnielsen, J.; Lahav, M.; Leiserowitz, L., Mixed Monolayers for the Design of Structured Surfaces to Induce Oriented 3-D Crystallization. *Journal of Physical Chemistry* **1993,** 97, (49), 12848-12857.
31. Weissbuch, I.; Berfeld, M.; Bouwman, W.; Kjaer, K.; AlsNielsen, J.; Lahav, M.; Leiserowitz, L., Separation of enantiomers and racemate formation in two-dimensional crystals at the water surface from racemic alpha-amino acid amphiphiles: Design and structure. *Journal of the American Chemical Society* **1997,** 119, (5), 933-942.
32. Kang, J. F.; Zaccaro, J.; Ulman, A.; Myerson, A., Nucleation and growth of glycine crystals on self-assembled monolayers on gold. *Langmuir* **2000,** 16, (8), 3791-3796.
33. Aizenberg, J.; Black, A. J.; Whitesides, G. M., Control of crystal nucleation by patterned self-assembled monolayers. *Nature* **1999,** 398, (6727), 495-498.
34. Davey, R. J.; Blagden, N.; Potts, G. D.; Docherty, R., Polymorphism in molecular crystals: Stabilization of a metastable form by conformational mimicry. *Journal of the American Chemical Society* **1997,** 119, (7), 1767-1772.
35. Weissbuch, I.; Popovitzbiro, R.; Lahav, M.; Leiserowitz, L., Understanding and Control of Nucleation, Growth, Habit, Dissolution and Structure of 2-Dimensional and 3-Dimensional Crystals Using Tailor-Made Auxiliaries. *Acta Crystallographica Section B-Structural Science* **1995,** 51, 115-148.

36. Weissbuch, I.; Lahav, M.; Leiserowitz, L., Toward stereochentical control, monitoring, and understanding of crystal nucleation. *Crystal Growth & Design* **2003,** 3, (2), 125-150.
37. Carter, P. W.; Ward, M. D., Directing Polymorph Selectivity During Nucleation of Anthranilic Acid on Molecular Substrates. *Journal of the American Chemical Society* **1994,** 116, (2), 769-770.
38. Damman, P.; Dosiere, M.; Smith, P.; Wittmann, J. C., Orientation of P-Nitrophenol Molecules Induced by Epitaxial Crystallization on Friction-Transferred Poly(Tetrafluoroethylene) Substrates. *Journal of the American Chemical Society* **1995,** 117, (3), 1117-1120.
39. Damman, P.; Coppee, S.; Geskin, V. M.; Lazzaroni, R., What is the mechanism of oriented crystal growth on rubbed polymer substrates? Topography vs epitaxy. *Journal of the American Chemical Society* **2002,** 124, (51), 15166-15167.
40. Bonafede, S. J.; Ward, M. D., Selective Nucleation and Growth of an Organic Polymorph by Ledge-Directed Epitaxy on a Molecular-Crystal Substrate. *Journal of the American Chemical Society* **1995,** 117, (30), 7853-7861.
41. Hooks, D. E.; Fritz, T.; Ward, M. D., Epitaxy and molecular organization on solid substrates. *Advanced Materials* **2001,** 13, (4), 227.
42. Grzesiak, A. L.; Uribe, F. J.; Ockwig, N. W.; Yaghi, O. M.; Matzger, A. J., Polymer-induced heteronucleation for the discovery of new extended solids. *Angewandte Chemie-International Edition* **2006,** 45, (16), 2553-2556.
43. Grzesiak, A. L.; Matzger, A. J., Selection and discovery of polymorphs of platinum complexes facilitated by polymer-induced heteronucleation. *Inorganic Chemistry* **2007,** 46, (2), 453-457.
44. Grzesiak, A. L.; Matzger, A. J., New form discovery for the analgesics flurbiprofen and sulindac facilitated by polymer-induced heteronucleation. *Journal of Pharmaceutical Sciences* **2007,** 96, 2978-2986.
45. Grzesiak, A. L.; Matzger, A. J., Selection of protein crystal forms facilitated by polymer-induced heteronucleation. *Crystal Growth & Design* **2008,** 8, (1), 347-350.
46. Porter, W. W.; Elie, S. C.; Matzger, A. J., Polymorphism in carbamazepine cocrystals. *Crystal Growth & Design* **2008,** 8, (1), 14-16.
47. Lang, M. D.; Grzesiak, A. L.; Matzger, A. J., The use of polymer heteronuclei for crystalline polymorph selection. *Journal of the American Chemical Society* **2002,** 124, (50), 14834-14835.
48. Price, C. P.; Grzesiak, A. L.; Matzger, A. J., Crystalline polymorph selection and discovery with polymer heteronuclei. *Journal of the American Chemical Society* **2005,** 127, (15), 5512-5517.
49. Lutker, K. M.; Matzger, A. J., Crystal Polymorphism in a Carbamazepine Derivative: Oxcarbazepine. *Journal of Pharmaceutical Sciences* 99, (2), 794-803.
50. Lutker, K. M.; Tolstyka, Z. P.; Matzger, A. J., Investigation of a privileged polymorphic motif: A dimeric ROY derivative. *Crystal Growth & Design* **2008,** 8, (1), 136-139.
51. Bacchi, A.; Mori, G.; Pelizzi, G.; Pelosi, G.; Nebuloni, M.; Panzone, G. B., Polymorphism-Structure Relationships of Rifamexil, An Antibiotic Rifamycil Derivative. *Molecular Pharmacology* **1995,** 47, (3), 611-623.

52. Gelbrich, T.; Hursthouse, M. B., Systematic investigation of the relationships between 25 crystal structures containing the carbamazepine molecule or a close analogue: a case study of the XPac method. *Crystengcomm* **2006,** 8, (6), 448-460.
53. Kitamura, M.; Hara, T., Dependence of polymorphism on molecular structure of BPT esters. *Crystal Growth & Design* **2007,** 7, (9), 1575-1579.
54. Mesley, R. J.; Houghton, E. E., Infrared Identification of Pharmaceutically Important Sulphonamides with Particular Reference to the Occurrence of Polymorphism. *Journal of Pharmacy and Pharmacology* **1967,** 19, (5), 295-&.
55. Grzesiak, A. L.; Lang, M. D.; Kim, K.; Matzger, A. J., Comparison of the four anhydrous polymorphs of carbamazepine and the crystal structure of form I. *Journal of Pharmaceutical Sciences* **2003,** 92, (11), 2260-2271.
56. He, X. R.; Griesser, U. J.; Stowell, J. G.; Borchardt, T. B.; Byrn, S. R., Conformational color polymorphism and control of crystallization of 5-methyl-2-[(4-methy1-2-nitrophenyl)amino]-3-thiophenecarbonitrile. *Journal of Pharmaceutical Sciences* **2001,** 90, (3), 371-388.
57. Li, H.; Stowell, J. G.; Borchardt, T. B.; Byrn, S. R., Synthesis, conformational polymorphism, and construction of a G-T diagram of 2-[(2-nitrophenyl)amino]-3-thiophenecarbonitrile. *Crystal Growth & Design* **2006,** 6, (11), 2469-2474.
58. Li, H.; Stowell, J. G.; He, X. R.; Morris, K. R.; Byrn, S. R., Investigations on solid-solid phase transformation of 5-methyl-2-[(4-methyl-2-nitrophenyl)amino]-3-thiophenecarbonitrile. *Journal of Pharmaceutical Sciences* **2007,** 96, (5), 1079-1089.
59. Borchardt, T. B.; Stowell, J. G.; Byrn, S. R., The Crystallization of 5-Methyl-2-[(2-nitrophenyl)amino]-3-thiophenecarbonitrile in the Presence of Structurally Similar Compounds. *Molecular Crystals and Liquid Crystals Science and Technology Section a-Molecular Crystals and Liquid Crystals* **1998,** 313, 271-276.
60. Himes, V. L.; Mighell, A. D.; Decamp, W. H., Structure of Carbamazepine - "5h-Dibenz[B.F]Azepine-5-Carboxamide. *Acta Crystallographica Section B-Structural Science* **1981,** 37, 2242-2245.
61. Reboul, J. P.; Cristau, B.; Soyfer, J. C.; Astier, J. P., 5h-5-Dibenzyl[B,F]Azepinecarboxamide (Carbamazepine). *Acta Crystallographica Section B-Structural Science* **1981,** 37, 1844-1848.
62. Lowes, M. M. J.; Caira, M. R.; Lotter, A. P.; Vanderwatt, J. G., Physicochemical Properties and X-Ray Structural Studies of the Trigonal Polymorph of Carbamazepine. *Journal of Pharmaceutical Sciences* **1987,** 76, (9), 744-752.
63. Lisgarten, J. N.; Palmer, R. A.; Saldanha, J. W., Crystal and Molecular-Structure of 5-Carbamyl-5h-Dibenzo[B, F] Azepine. *Journal of Crystallographic and Spectroscopic Research* **1989,** 19, (4), 641-649.
64. Lang, M. D.; Kampf, J. W.; Matzger, A. J., Form IV of carbamazepine. *Journal of Pharmaceutical Sciences* **2002,** 91, (4), 1186-1190.
65. Hickey, M. B.; Peterson, M. L.; Scoppettuolo, L. A.; Morrisette, S. L.; Vetter, A.; Guzman, H.; Remenar, J. F.; Zhang, Z.; Tawa, M. D.; Haley, S.; Zaworotko, M. J.; Almarsson, O., Performance comparison of a co-crystal of carbamazepine with marketed product. *European Journal of Pharmaceutics and Biopharmaceutics* **2007,** 67, (1), 112-119.
66. Harris, R. K.; Ghi, P. Y.; Puschmann, H.; Apperley, D. C.; Griesser, U. J.; Hammond, R. B.; Ma, C. Y.; Roberts, K. J.; Pearce, G. J.; Yates, J. R.; Pickard, C. J.,

Structural studies of the polymorphs of carbamazepine, its dihydrate, and two solvates (vol 9, pg 902, 2005). *Organic Process Research & Development* **2006,** 10, (1), 165-165.

67. Harris, R. K.; Ghi, P. Y.; Puschmann, H.; Apperley, D. C.; Griesser, U. J.; Hammond, R. B.; Ma, C. Y.; Roberts, K. J.; Pearce, G. J.; Yates, J. R.; Pickard, C. J., Structural studies of the polymorphs of carbamazepine, its dihydrate, and two solvates. *Organic Process Research & Development* **2005,** 9, (6), 902-910.

68. Rodríguez-Hornedo, N.; Murphy, D., Surfactant-facilitated crystallization of dihydrate carbamazepine during dissolution of anhydrous polymorph. *Journal of Pharmaceutical Sciences* **2004,** 93, (2), 449-460.

69. Jayasankar, A.; Roy, L.; Rodríguez-Hornedo, N., Transformation Pathways of Cocrystal Hydrates When Coformer Modulates Water Activity. *Journal of Pharmaceutical Sciences* 99, (9), 3977-3985.

70. Good, D. J.; Rodríguez-Hornedo, N., Solubility Advantage of Pharmaceutical Cocrystals. *Crystal Growth & Design* **2009,** 9, (5), 2252-2264.

71. Bethune, S. J.; Huang, N.; Jayasankar, A.; Rodríguez-Hornedo, N., Understanding and Predicting the Effect of Cocrystal Components and pH on Cocrystal Solubility. *Crystal Growth & Design* **2009,** 9, (9), 3976-3988.

72. Seefeldt, K.; Miller, J.; Alvarez-Nunez, F.; Rodríguez-Hornedo, N., Crystallization pathways and kinetics of carbamazepine-nicotinamide cocrystals from the amorphous state by in situ thermomicroscopy, spectroscopy and calorimetry studies. *Journal of Pharmaceutical Sciences* **2007,** 96, (5), 1147-1158.

73. Nehm, S. J.; Rodríguez-Spong, B.; Rodríguez-Hornedo, N., Phase solubility diagrams of cocrystals are explained by solubility product and solution complexation. *Crystal Growth & Design* **2006,** 6, (2), 592-600.

74. Hempel, A.; Camerman, N.; Camerman, A.; Mastropaolo, D., Oxcarbazepine: structure and anticonvulsant activity. *Acta Crystallographica Section E-Structure Reports Online* **2005,** 61, O1313-O1315.

75. Harrison, W. T. A.; Yathirajan, H. S.; Anilkumar, H. G., An orthorhombic polymorph of 10,11-dihydrocarbamazepine. *Acta Crystallographica Section C-Crystal Structure Communications* **2006,** 62, O240-O242.

76. Leech, C. K.; Florence, A. J.; Shankland, K.; Shankland, N.; Johnston, A., 10,11-dihydrocarbamazepine (form III). *Acta Crystallographica Section E-Structure Reports Online* **2007,** 63, O675-O677.

77. Gavezzotti, A., Generation of Possible Crystal-Structures from the Molecular-Structure for Low-Polarity Organic-Compounds. *Journal of the American Chemical Society* **1991,** 113, (12), 4622-4629.

78. Holden, J. R.; Du, Z. Y.; Ammon, H. L., Prediction of Possible Crystal-Structures for C-Containing, H-Containing, N-Containing, O-Containing and F-Containing Organic-Compounds. *Journal of Computational Chemistry* **1993,** 14, (4), 422-437.

79. Lommerse, J. P. M.; Motherwell, W. D. S.; Ammon, H. L.; Dunitz, J. D.; Gavezzotti, A.; Hofmann, D. W. M.; Leusen, F. J. J.; Mooij, W. T. M.; Price, S. L.; Schweizer, B.; Schmidt, M. U.; van Eijck, B. P.; Verwer, P.; Williams, D. E., A test of crystal structure prediction of small organic molecules. *Acta Crystallographica Section B-Structural Science* **2000,** 56, 697-714.

80. Mitchell-Koch, K. R.; Matzger, A. J., Evaluating computational predictions of the relative stabilities of polymorphic pharmaceuticals. *Journal of Pharmaceutical Sciences* **2008,** 97, (6), 2121-2129.

81. Neumann, M. A.; Leusen, F. J. J.; Kendrick, J., A major advance in crystal structure prediction. *Angewandte Chemie-International Edition* **2008,** 47, (13), 2427-2430.

82. Williams, D. E., Computer Calculation of Molecular Crystal Structures. *Science* **1968,** 159, (3815), 645-&.

83. Williams, D. E.; Starr, T. L., Calculation of Crystal-Structures of Hydrocarbons by Molecular Packing Analysis. *Computers & Chemistry* **1977,** 1, (3), 173-177.

84. Roy, S.; Matzger, A. J., Unmasking a Third Polymorph of a Benchmark Crystal-Structure-Prediction Compound. *Angewandte Chemie-International Edition* **2009,** 48, (45), 8505-8508.

85. Krc, J., Crystallographic Properties of Flufenamic Acid. *Microscope* **1977,** 25, (1), 31-45.

86. Lee, E. H.; Boerrigter, S. X. M.; Rumondor, A. C. F.; Chamarthy, S. P.; Byrn, S. R., Formation and solid-state characterization of a salt-induced metastable polymorph of flufenamic acid. *Crystal Growth & Design* **2008,** 8, (1), 91-97.

87. Burger, A.; Ramberger, R., Thermodynamic Relationships between Polymorphic Modifications - Flufenamic Acid and Mefenamic-Acid. *Mikrochimica Acta* **1980,** 1, (1-2), 17-28.

88. Krishna Murthy, H. M.; Vijayan, M., 2-3 Tri Fluoromethylphenylamino-3 Pyridinecarboxylic-Acid Niflumic-Acid. *Acta Crystallographica Section B Structural Crystallography and Crystal Chemistry* **1979,** 35, (1), 262-263.

89. McClelland, A. A.; López-Mejías, V.; Matzger, A. J.; Chen, Z., Peering at a Buried Polymer-Crystal Interface: Probing Heterogeneous Nucleation by Sum Frequency Generation Vibrational Spectroscopy, *Langmuir,* (ASAP), **2011**.

90. López-Mejías,V.; Knight, J. L.; Brooks, C. L. III; Matzger, A. J, On the Mechanism of Crystalline Polymorph Selection by Polymer Heteronuclei, submitted to *Langmuir,* **2011**.

CHAPTER 2

POLYMER-INDUCED HETERONUCLEATION OF TOLFENAMIC ACID: STRUCTURAL INVESTIGATION OF A PENTAMORPH

PUBLISHED IN *JACS* 2009, *131*, 4554.

2.1 Introduction

Molecules exhibiting multiple crystalline forms differing solely in the arrangement or conformation of the building units, polymorphic compounds, have long represented an active area of research in solid-state chemistry. In addition to important implications for properties including drug bioavailability and pigment color, such systems offer a challenging test for crystal structure prediction and, in cases where thermodynamic relationships have been derived, an invaluable opportunity to refine computational approaches.

Definitive evidence for polymorphism is offered by single crystal X-ray diffraction. The number of compounds in the Cambridge Structural Database (CSD) with two structurally characterized polymorphs figures in the tens of thousands, whereas structures with three or four structurally characterized forms are considerably more rare. There are four pharmaceuticals in the CSD reaching the level of five structurally characterized polymorphs: sulfathiazole,[1-4] chlorpropamide,[5-8] aripiprazole,[9-11] and tolfenamic acid[12, 13] (Figure 2.1). Crystals structures of sulfathiazole were obtained over a period of nearly 30 years using solvent-based methods; remarkably all forms are in the same space group.[1-4] Similarly, the five crystal structures of chlorpropamide were also obtained over a period of about 30 years using solvent-based methods.[5-8] All the chlorpropamide polymorphs can be obtained by crystallization from a heptanes-ethyl acetate solution under slightly different conditions, and are often present as mixtures in the same batch.[7] All five forms of chlorpropamide contain one molecule in the asymmetric unit, differing in the conformation of the ethyl tail and the propyl tail.[5-8] In the case of the pharmaceutical compound aripiprazole, the first crystal structure was reported in 2006 along with that of many solvates.[9] In June 2009, four additional modifications were elucidated, all the aripiprazole polymorphs can be accessed from solvents, or alternatively by solid-solid transformation and melt crystallization.[10] Aripiprazole polymorphs crystallized in three different space groups, and present conformational changes varying among all five forms.[9-11] Additionally, if the definition of polymorph is expanded to include tautomers, sulfapyridine, a pharmaceutical compound which can assume two tautomeric forms can also be considered as a pentamorphic.[14] Four of the structures determined adopt the imide form (II-V), whereas the fifth form (VI) presents a combination of the imide and amide forms.[14] Currently, a pharmaceutical precursor, 5-methyl-2-[(2-nitrophenyl)amino]-3-thiophenecarbonitrile (ROY, Figure 2.1), has the largest number of structurally characterized polymorphs in the CSD, and three different space groups are represented among its crystal phases.[15-17] Six of the seven structurally characterized forms were obtained by solvent-based screening methods between 1995 and 2000, whereas the last form was first accessed by melt crystallization and solid-state transformation in 2005.[15-17] These examples serve to illustrate that there is a need for alternative approaches for polymorph discovery, especially in the pharmaceutical industry. Screening approaches that accelerate the pace of solid form discovery, thus preventing the unexpected appearance of undesirable forms at late stages of evaluation or during manufacturing, would be of considerable value.

This investigation reports on the structural and conformational polymorphism of a nonsteroidal anti-inflammatory drug (NSAID) tolfenamic acid (TA) and demonstrates unambiguously that this pharmaceutical possesses at least five polymorphs.[12] TA (Figure 2.1) is a member of a large class of NSAIDs that contain a monocarboxylated diphenyl amine nucleus; several of these analogues display polymorphism.[18-20] As such, TA offers a good test case for the notion that certain molecular motifs, when incorporated into a structure, render the compound polymorphic: the polymorphophore.[21, 22] As a well-studied pharmaceutical, it also offers a challenge for polymorph discovery techniques, such as polymer-induced heteronucleation (PIHn).[23, 24] This is a screening technique in which a single solvent/temperature condition leads to novel form discovery enabled by a diverse array of insoluble polymers acting as heterogeneous growth sites.[23-29]

2.2 Experimental Section

2.2.1 Materials

Commercial TA was obtained from Sigma-Aldrich (St. Louis, MO, USA) and stored at room temperature.

2.2.2 Cross-linked Polymer Synthesis

The components used to build the non-polar aromatic polymer library are the following. Six non-polar aromatic monomers: 4-acetoxystyrene (AOS), *n*-butyl methacrylate (*n*-BuMA), *tert*-butyl methacrylate (*t*-BuMA), benzyl methacrylate (BzMA), methyl methacrylate (MMA), and styrene (STY) were crosslinked with divinylbenzene (DVB). The library was synthesized in a 96-well plate using a previously described procedure.[24] Briefly, six 1:1 (v/v) monomer solutions in ethanol were dispensed as 90 pair wise combinations of varied ratios (86:14, 71:29, 57:43, 43:57, 29:71, and 14:86) and six pure monomer solutions by a Gilson 215 liquid handler to a volume of 113 µL. To each of these 96 solutions was added 57 µL of a 1:1 solution of DVB in ethanol containing 2 mol % 2,2'-azobisisobutyronitrile (AIBN) with respect to DVB. The solutions were divided into four round bottom 96-well plates using a HYDRA-96 liquid dispenser (40 µL to each plate) and then the mixtures were photopolymerized in a nitrogen atmosphere. Finally, the polymers are annealed at 85 °C under vacuum to produce the cross-linked polymer library.

2.2.3 Crystallizations of TA in Non-polar Aromatic Polymer Library

A saturated solution (7.2 mg/mL) of TA was prepared by equilibrating the commercial powder with absolute ethanol. The solution was filtered using a 0.45 µm pore size PTFE filter and heated. Following that, the solution was dispensed into a 96-well plate containing cross-linked polymers. Supersaturation was achieved by allowing the solvent to evaporate uncovered at room temperature.

The crystal used for structure determination of TA form III grew on a DVB:*n*-BuMA:MMA (26:29:60) derived polymer, while the crystal of form IV TA used for structural determination grew on a DVB:*t*-BuMA:MMA (26:37:52) containing polymer. Other crystals of form IV that were screened initially grew on DVB:*t*-BuMA (26:73), DVB:AOS:*t*-BuMA (26:12:77), DVB:AOS:*t*-BuMA (26:25:64). Finally, the crystal used for structure determination of TA form V grew on a DVB:*n*-BuMA:STY (26:60:29) derived polymer, while other crystals used for screening grew on DVB:*n*-BuMA:STY (26:37:52).

2.2.4 Optical Microscopy

Images of TA forms I–V were collected using a Spot Flex Mosaic 15.2 camera coupled to a Leica DMLP microscope. Images were processed using Spot Advanced software (version 4.6).

2.2.5 Raman Spectroscopy

Raman spectra were collected using a Renishaw inVia Raman microscope equipped with a Leica microscope, RenCam CCD detector, 633 nm He-Ne laser, 1200 lines/nm grating, and 50 μm slit. Spectra were collected in extended scan mode in the range of 3500-100 cm^{-1} and then analyzed using Wire 2.0 software package. Calibration was performed using a silicon standard.

2.2.6 Powder X-ray Diffraction

Powder X-ray diffraction (PXRD) patterns were collected at ambient temperature using a Rigaku R-Axis Spider diffractometer with an image plate detector and graphite monochromated Cu-Kα radiation (1.5406 Å). Samples were mounted on a cryoloop and images were collected for five minutes while rotating the sample about the φ-axis at 10°/sec, oscillating ω between 120° and 180° at 1°/sec with χ fixed at 45°. Images were integrated from 5° to 50° with a 0.05° step size using AreaMax2 software. PXRD patterns were processed in Jade Plus3 to calculate peak positions and intensities.

2.2.7 Single Crystal X-ray Diffraction

2.2.7.1 Single Crystal X-ray Diffraction of TA Form III

A crystal of dimensions 0.27 × 0.23 × 0.19 mm^3 was mounted on a Bruker SMART APEX CCD based X-ray diffractometer equipped with a low temperature device and fine focus Mo-target X-ray tube (λ = 0.71073 Å) operated at 1500 W power (50 kV, 30 mA).

The X-ray intensities were measured at 85(2) K; the detector was placed at a distance 5.055 cm from the crystal. A total of 2695 frames were collected with a scan width of 0.5° in ω and 0.45° in ϕ with an exposure time of 20 s/frame. The frames were integrated with the Bruker SAINT software package with a narrow frame algorithm. The integration of the data yielded a total of 55895 reflections to a maximum 2θ value of 56.72° of which 6036 were independent and 5446 were greater than $2\sigma(I)$. The final cell constants were based on the xyz centroids of 9917 reflections above $10\sigma(I)$. Analysis of the data showed negligible decay during data collection; the data were processed with SADABS and corrected for absorption. The structure was solved and refined with the Bruker SHELXTL (version 6.12) software package, using the space group $P2_1/c$ with $Z = 8$ for the formula $C_{14}H_{12}NO_2Cl$. All non-hydrogen atoms were refined anisotropically with the hydrogen atoms placed in idealized positions with the exception of those involved in hydrogen bonding which were allowed to refine isotropically. Full matrix least-squares refinement based on F2 converged at R1 = 0.0448 and wR2 = 0.1169 [based on $I > 2\sigma(I)$], R1 = 0.0488 and wR2 = 0.1208 for all data.

2.2.7.2 Single Crystal X-ray Diffraction of TA Form IV

A crystal of dimensions $0.28 \times 0.13 \times 0.09$ mm^3 was mounted on a Bruker SMART APEX CCD based X-ray diffractometer equipped with a low temperature device and fine focus Mo-target X-ray tube (λ = 0.71073 Å) operated at 1500 W power (50 kV, 30 mA). The X-ray intensities were measured at 85(2) K; the detector was placed at a distance 5.055 cm from the crystal. A total of 2640 frames were collected with a scan width of 0.5° in ω and 0.45° in ϕ with an exposure time of 30 s/frame. Indexing was performed by use of CELL_NOW which indicated that the crystal was a two-component nonmerohedral twin. The frames were integrated with the Bruker SAINT software package with a narrow frame algorithm. The integration of the data yielded a total of 61047 reflections to a maximum 2θ value of 52.96° of which 7521 were independent and 6236 were greater than 2σ(I). The final cell constants were based on the xyz centroids of 9878 reflections above 10σ(I). Analysis of the data showed negligible decay during data collection; the data were processed with TWINABS and corrected for absorption. The structure was solved and refined with the Bruker SHELXTL (version 6.12) software package, using the space group P with $Z = 6$ for the formula $C_{14}H_{12}NO_2Cl$. All non-hydrogen atoms were refined anisotropically with the hydrogen atoms placed in idealized positions with the exception of those involved in hydrogen bonding which were allowed to refine isotropically. The twin components were related by a rotation of 179.9 ° about the (1 0 –1) direct axis. The twin fractional volume refined to 0.220(2). Full matrix least-squares refinement based on F2 converged at R1 = 0.0723 and wR2 = 0.1658 [based on I > 2σ (I)], R1 = 0.0888 and wR2 = 0.1752 for all data.

2.2.7.3 Single Crystal X-ray Diffraction of TA Form V

A crystal of dimensions 0.16 × 0.13 × 0.09 mm^3 was mounted on a Bruker SMART APEX CCD based X-ray diffractometer equipped with a low temperature device and fine focus Mo-target X-ray tube (λ = 0.71073 Å) operated at 1500 W power (50 kV, 30 mA). The X-ray intensities were measured at 85(2) K; S10 the detector was placed at a distance 5.055 cm from the crystal. A total of 2413 frames were collected with a scan width of 0.5° in ω and 0.45° in ϕ with an exposure time of 30 s/frame. The frames were integrated with the Bruker SAINT software package with a narrow frame algorithm. The integration of the data yielded a total of 11316 reflections to a maximum 2θ value of

56.88° of which 2479 were independent and 1869 were greater than 2σ(I). The final cell constants were based on the xyz centroids of 2118 reflections above 10σ(I). Analysis of the data showed negligible decay during data collection; the data were processed with SADABS and corrected for absorption. The structure was solved and refined with the Bruker SHELXTL (version 6.12) software package, using the space group *P* with *Z* = 2 for the formula $C_{14}H_{12}NO_2Cl$. All non-hydrogen atoms were refined anisotropically with the hydrogen atoms placed in idealized positions with the exception of those involved in hydrogen bonding which were allowed to refine isotropically. The structure exhibits ‘whole molecule disorder’ with the disorder present at a 50/50 occupancy ratio. Full matrix least-squares refinement based on F2 converged at R1 = 0.0658 and wR2 = 0.1257 [based on I > 2σ(I)], R1 = 0.0933 and wR2 = 0.1374 for all data.

2.2.8 Hirshfeld Surface Analysis

Hirshfeld surfaces (HSs) of each of the molecules in the asymmetric unit of the ordered polymorphs of TA were constructed using the program Crystal Explorer v2.0.10. Crystallographic information files were uploaded to the program after the normalization of N-H, O-H and C-H bond lengths (1.008, 0.983, and 1.083 Å, respectively) to average neutron values was performed.[30-32] The molecular HSs is defined as the partitioning of space in the crystal where the electron distribution of the sum of spherical atoms for the molecule (promolecule) contributes more than twice the electron distribution of the corresponding sum of the whole crystal (procrystal).[30-32] These surfaces are derived from Hirshfeld’s stockholders partitioning which are described in detail elsewhere.[30-32] Each point on the surfaces is colored according to the fraction of the total surface area contained in the bin. The 2D fingerprint plots and their decompositions into different intermolecular contacts are extracted from three dimensional HSs. These fingerprints are constructed by plotting d_e values, the distances between the nearest atoms in the exterior, as a function of d_i values, the distances between the nearest atoms in the interior of the surface. During the breakdown of the surfaces and the fingerprint plots into specific intermolecular contacts; in the case of O···H contacts for example, only portions where the hydrogen is the closest atom inside of the surface, and oxygen is the closest atom outside the surface (and *vice versa*) are colored. Consequently, if the area of the colored surface is summed and then divided by the total HSs area the relative contribution of the O···H type contacts to the whole surface area of the molecule can be determined.[33]

2.2.9 Relative Stability Studies

Qualitative determination of the stability relationship between the TA polymorphs was performed through polymorphic conversion experiments while melting endotherms were used to quantitatively describe differences in the enthalpies of the five forms. At room temperature in the absence of solvent, well-formed crystals of forms I-V do not undergo conversion for at least a year as determined by X-ray diffraction and Raman spectroscopy. Heating forms III and V at 80 °C caused transformation to form I within minutes to hours.

2.2.10 Differential Scanning Calorimetry

At 10 °C/min heating rate, the thermograms of forms I, II, and IV suggest that these forms melt without discernable solid-solid transformations within a 10 degree range. In the thermogram of form III, a transformation happens at 92.3 °C followed by melting at 214.1 °C. Crystals of form IV melt as a pure phase without solid-solid transformations around 206.8 °C as shown in the thermogram of Figure 2.14. In form V, the thermogram shows an endothermic transition with onset at 146.4 °C which is followed by melting at 215.2 °C. Thermograms of the samples were recorded in a TA instruments DSC Q10. Data were analyzed with TA Universal Analysis software Version 4.3A. Samples (0.6-1.5 mg weighed to a precision of 0.0001mg) were placed in hermetically sealed pans crimped using a TA instrument crimper. Thermal behavior of the samples was studied under a nitrogen purge at 10 °C/min heating rate, starting at room temperature and cycling between 230 °C and −20 °C. The instrument was calibrated with an indium standard.

2.2.11 Free Energy Relationships Among Forms

The optical absorbance of TA polymorphs in isooctane was monitored *in situ* over time using a Cary 300 Bio UV-vis double beam spectrometer in the range of 500-200 nm at 300 ± 1 K. Spectrosil® Quartz semimicro cells, with black walls fitted with PTFE stoppers were used for this experiment. The wavelength of maximum absorbance (λ_{max}) of TA in isooctane was located at 283 nm. A time-dependent absorbance curve was used to determine the absorbance at equilibrium and these values were employed in relative free energy (ΔG) determination (Equation 1) for each of these forms as well as to monitor conversions in solution over a longer period of time. The solute remaining was identified using powder X-ray diffraction and Raman spectroscopy. In the case of form I and form II, no transformation was observed within the time frame of the experiment, whereas in the cases of forms III, IV and V transformation occurred to form I and/or mixture of form I and II.

$$\Delta G = RT\ln(S_2/S_1) \qquad (1)$$

2.2.12 Lattice Energy Calculation

The lattice energy, U_{latt}, of the ordered polymorphs of TA was calculated using the Free-Cell method previously described by Mitchell-Koch *et al.*[34] According to this calculation for the ordered polymorphs of TA, form I has the greatest enthalpy followed by form II, form III, form IV.

2.3 Results and Discussion

Three novel phases of TA were grown from an ethanol solution using non-polar aromatic polymers as heteronuclei.[23, 24] Optical examination revealed noticeable differences in the morphology of the crystals (Figure 2.2). The previously reported colorless and yellow needles (forms I and II)[13] were observed as well as prisms (form III) and colorless plates (forms IV and V). When the samples were examined by Raman spectroscopy, four main spectral regions (3375-3300, 1645-1565, 1180-1040, and 815-760 cm^{-1}) aided in the identification of the five polymorphs (Figure 2.3 and Table 2.1).

PXRD confirms that unique crystalline phases (Figures 2.4-2.8 and Table 2.2) were obtained for TA. Structure determination revealed that, as in the case of sulfathiazole and ROY, each form contains different conformers (Figure 2.1). In contrast to ROY, several structures of TA vary in the number of inequivalent molecules in the asymmetric unit. TA is known to crystallize in two monoclinic forms,[13] both containing one molecule in the asymmetric unit. The now accessible form III crystallizes in the space group $P2_1/c$ with $Z' = 2$, whereas forms IV and V crystallize in the space group P with $Z' = 3$ and $Z' = 1$, respectively (Figures 2.9-2.11 and Table 2.3).

TA displays conformational polymorphism. Form II possesses the smallest torsion angle[13] τ[C-N-C-C] of 42.2°, whereas form I has the largest torsion angle measuring

107.7° (Figure 2.1). The small dihedral angle in form II causes extended conjugation not present in the other TA forms, thus giving this form its characteristic yellow color. Modifications I, II, IV, and V form hydrogen bonded anti dimers that connect the carboxylic acids through an inversion center. Form III displays a similar motif but between crystallographically inequivalent molecules. Intramolecular hydrogen bonding occurs between the amino group and the carbonyl oxygen in all modifications. In TA form I, each dimer interacts with eight adjacent molecules through close C–H···π contacts between the chlorinated aromatic ring and the carboxylated aromatic ring. The contacts alternate between four donors and four acceptors to form a 2D sheet in the *ac*-plane. Close contacts between the chlorine and the methyl group along the *b*-axis join these sheets into a 3D structure.[13] In form II, the hydrogen bonded dimers pack in columns along the *a*-axis; additional donation from a neighboring methyl group to the carbonyl above and below it connects the columnar packing along the same direction. Adjacent pairs of dimers pack through C–Cl···π (3.41 Å) interactions.[13] Crystallographic information files were normalized to average neutron values (C–H = 1.083 Å, N–H = 1.08 Å, and O–H = 0.983 Å) prior to distance determination. All reported C–H···π, π···π and C–Cl···π distances were measured from hydrogen to carbon (C–H···C), from carbon to carbon (C···C) and from chlorine to carbon (C–Cl···C) in each of the cases.

The newly accessed crystal phases pack in columnar arrangements (Figures 2.12). In form III, heterodimers pack tilted along the columnar axis at an angle of 63°, where a supramolecular ring is formed by two short contacts between the carbon atom of the carboxylic acid and the π system located above and below each heterodimer. Other aromatic C–H···π (2.86 Å and 2.85 Å) and methyl C–H···π (2.89 Å) short contacts reinforce the columns along the same direction. Adjacent columns of heterodimers are connected by Cl···Cl (3.38 Å) interactions as well as C–Cl···π (3.44 Å) donor-acceptor interactions between the inequivalent molecules. In form IV, the shortest contacts observed are methyl C–H···π (2.65 Å) donation from the chlorinated aromatic ring of the homodimers to the chlorinated aromatic ring of the heterodimer as well as aromatic C–H···π interactions (2.75 and 2.79 Å) from the chlorinated aromatic ring of the heterodimer to the carboxylated aromatic ring of the homodimer. These interactions expand the packing of the tilted dimers within the *bc*-plane. Other important contacts present include Cl···Cl (3.41 Å) interactions, which are only observed between heterodimers, and aromatic C–H···O=C (2.68 Å) contacts between the carboxylated aromatic ring and the carboxylic acid in adjacent heterodimers. In polymorph V, dimers pack through Cl···Cl interactions aligned with the *c*-axis in one of the disordered models and C–Cl···H interactions along the *b*-axis in the other disordered model; however, additional assignments regarding molecular packing are hampered by the complexity of the whole molecule disorder in the crystal structure.

Hirshfeld surface (HSs)[30-33] analysis was performed to determine the relative contribution of the important intermolecular contacts present in each of the molecules in the asymmetric unit of the ordered TA polymorphs. The C···H contacts compose 42.6% of the HSs in conformer c of TA form IV and only 10.0% in form II (Figure 2.13). In addition, examination of the HSs demonstrates the great contribution (11.9%) of π···π contacts to the planar conformation present in form II as well as the low contribution of the C···H contacts resulting from extensive π···π interactions in this form. A higher contribution (1.8-1.3% vs 0.5-0.2%) of the Cl···Cl contacts is also observed in all of the newly accessed polymorphs of TA. Remarkably, although the crystal phases differ significantly in packing arrangements and conformations, the strong hydrogen bonding contacts (O···H and N···H) remain fairly constant among all of the five forms of TA. To assess the effect of these structural differences on the energies of TA polymorphs, relative free energies were established experimentally (Table 2.4) through determination of the equilibrium solubility, all five polymorphs exist within a ~0.3 kcal/mol free energy window. This free energy difference may represent a slight underestimation due to a slow conversion of form IV to form I under the experimental conditions employed to determine their equilibrium solubility ratio. Additionally, the enthalpies were determined by experiment (Figure 2.14 and Table 2.5) as well as by theory (Table 2.6). Polymorphs I, II and IV do not undergo transformation upon heating, therefore the heat of fusion rule can be applied to establish their thermodynamic relationship. This rule suggests that an enantiotropic relationship exists only between the polymorphic pairs of form I and form II; whereas polymorphic pairs between forms I and IV, and forms II and IV present a monotropic relationship. According to the lattice energy calculations, form I has the greatest enthalpy among the five polymorphs of TA which concords with the experimentally determined enthalpies for polymorphs that do not undergo transformation.

2.4 Conclusions

PIHn has allowed access to three new metastable phases of TA, making this compound one of the few highly polymorphic pharmaceutical compounds structurally characterized. The range of different conformations, space groups, packing motifs, varying number of inequivalent molecules, and very narrow range of free energy differences make TA a particularly challenging model compound for polymorph prediction methods, in addition to a valuable test case to assess the robustness of other solid form discovery methods.

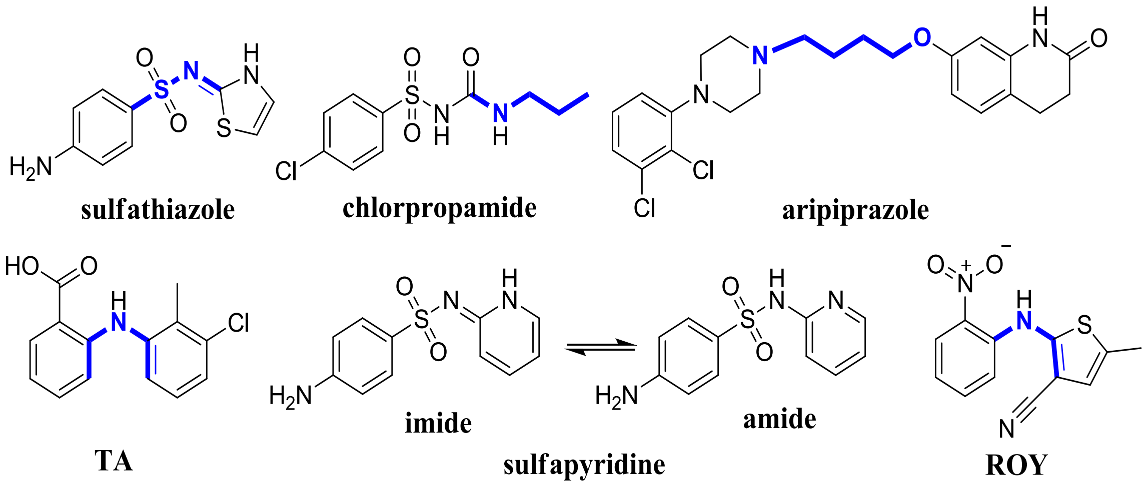

Figure 2.1. Chemical structures of sulfathiazole, chlorpropamide, aripiprazole, tolfenamic acid (TA), both tautomers of sulfapyridine, and 5-methyl-2-[(2-nitrophenyl)amino]-3-thiophenecarbonitrile (ROY) illustrating the torsion angles (τ, bonds in blue) differing among the conformers.

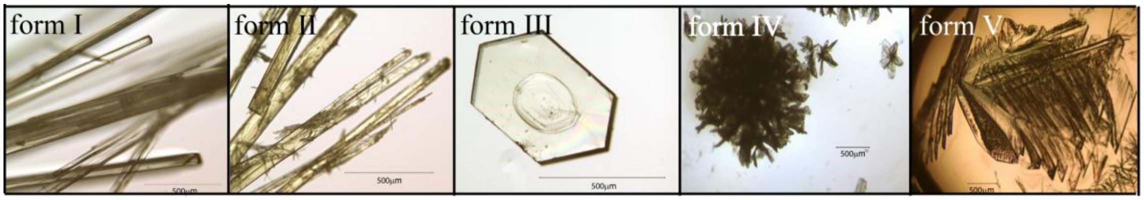

Figure 2.2. Optical microscopy of TA forms I-V (left to right).

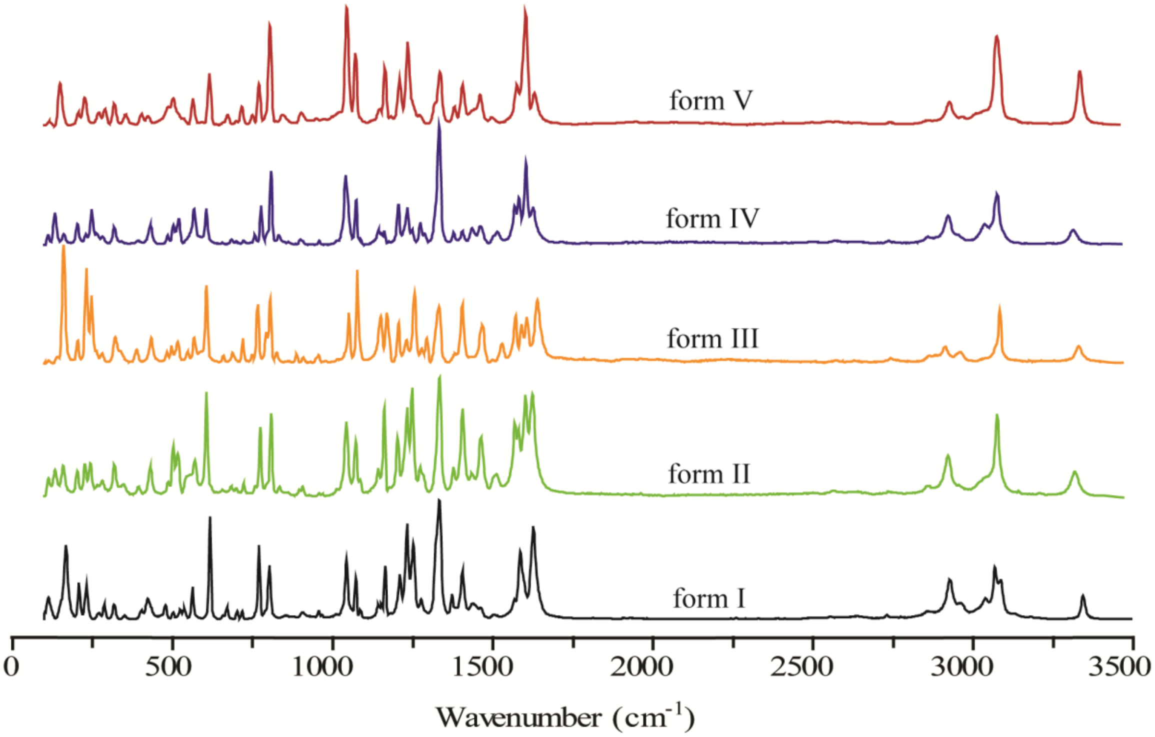

Figure 2.3. Raman spectra of TA polymorphs I-V.

Table 2.1. Frequency of Raman vibrational modes (cm^{-1}) of TA forms I-V.

form I		**form II**		**form III**		**form IV**		**form V**	
3344	967	3328	1052	3313	1145	3319	1074	3334	805
3086	957	3085	958	3077	1075	3143	1044	3074	772
3069	905	2959	950	2923	1041	3076	959	2927	751
2929	857	2914	888	2858	959	2923	908	2738	717
2774	804	2863	827	2739	900	2859	897	1605	673
2731	772	2743	807	2568	832	2735	809	1578	617
2640	718	2568	794	2127	809	2566	775	1461	566
1628	703	1906	768	2053	778	1965	724	1407	505
1587	672	1856	721	1627	759	1626	700	1382	406
1508	619	1640	689	1605	686	1604	683	1337	321
1465	564	1607	660	1583	607	1582	607	1236	291
1407	538	1591	607	1570	569	1570	571	1211	270
1374	527	1572	569	1515	521	1510	519	1166	226
1335	503	1531	549	1465	503	1465	503	1084	208
1278	480	1470	518	1435	486	1435	488	1072	151
1254	424	1407	498	1407	433	1408	432	1045	902
1234	405	1334	484	1379	319	1378	319		
1211	319	1295	435	1334	249	1335	282		
1166	288	1280	391	1276	231	1285	244		
1154	232	1258	323	1250	204	1274	227		
1144	209	1232	264	1236	134	1250	204		
1088	168	1207	248	1206		1234	160		
1074	115	1169	232	1163		1204	134		
1044		1153	205	1153		1163	115		
		1079	161			1144			
						1086			

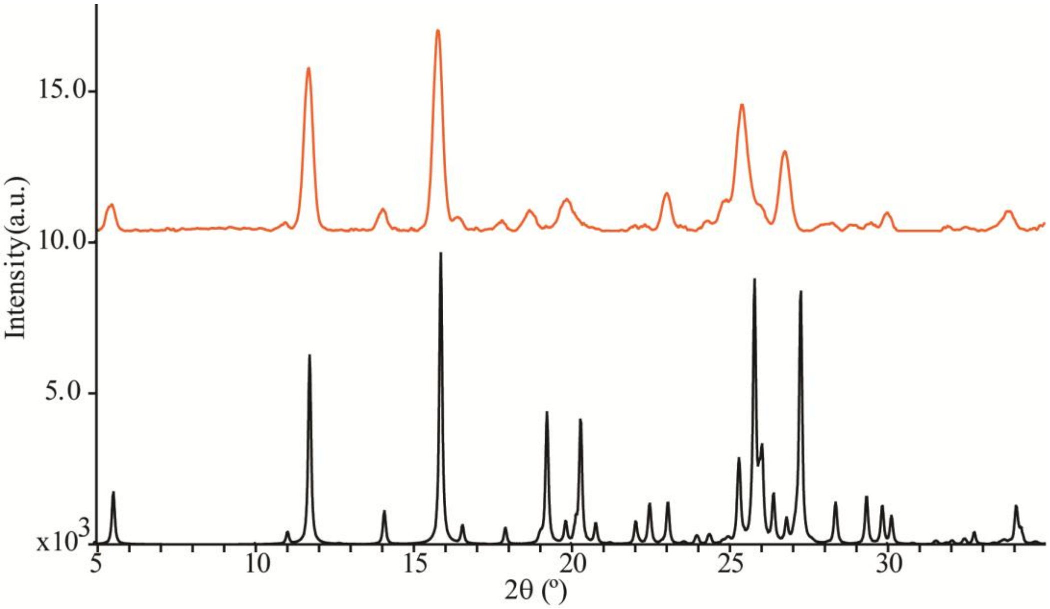

Figure 2.4. Simulated (bottom) and experimental (top) PXRD of TA form I.

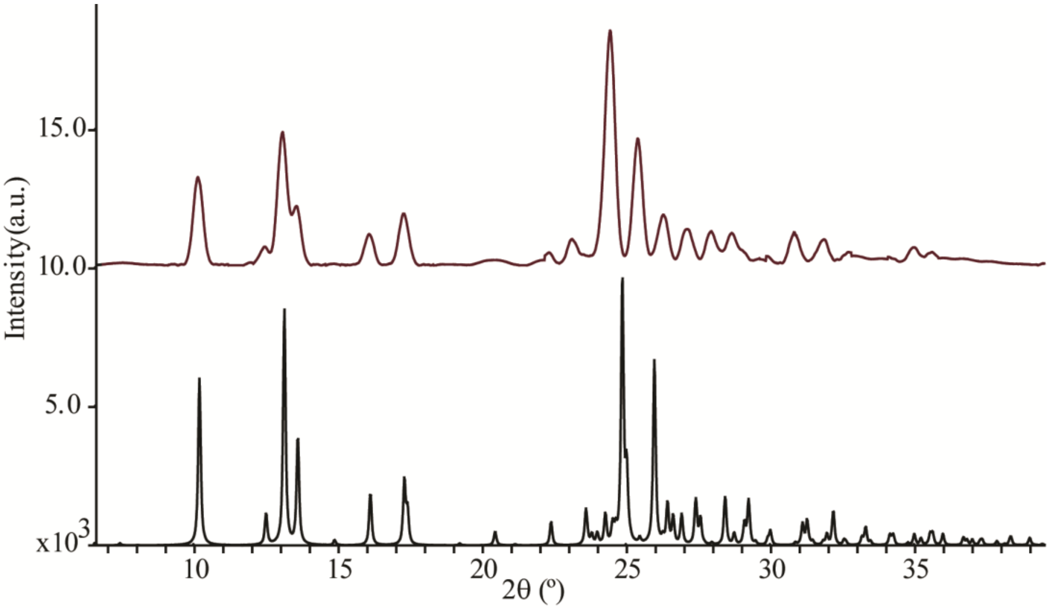

Figure 2.5. Simulated (bottom) and experimental (top) PXRD of TA form II.

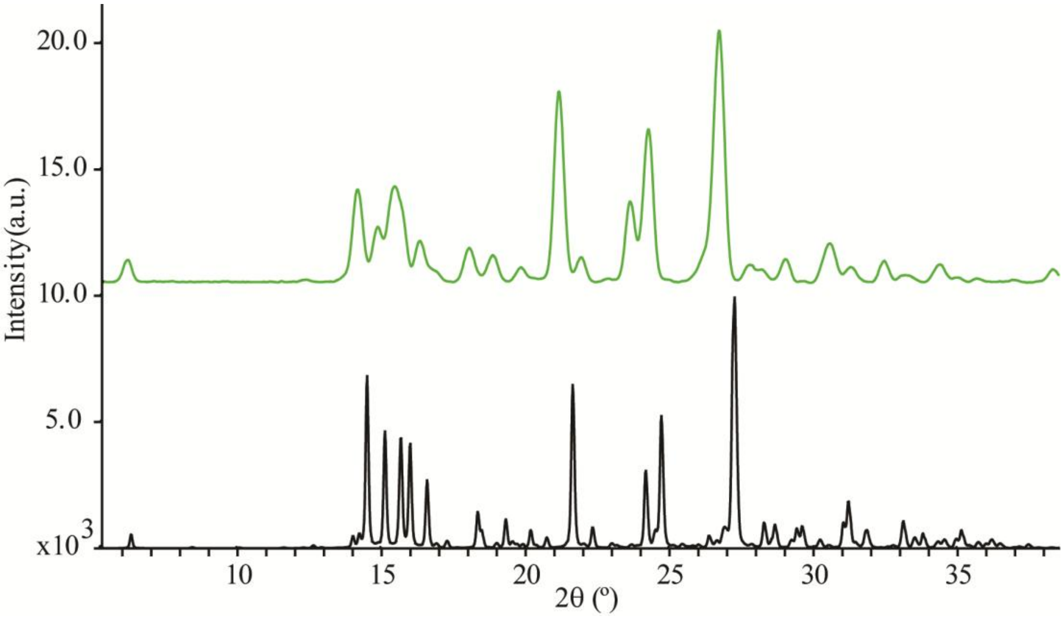

Figure 2.6. Simulated (bottom) and experimental (top) PXRD of TA form III.

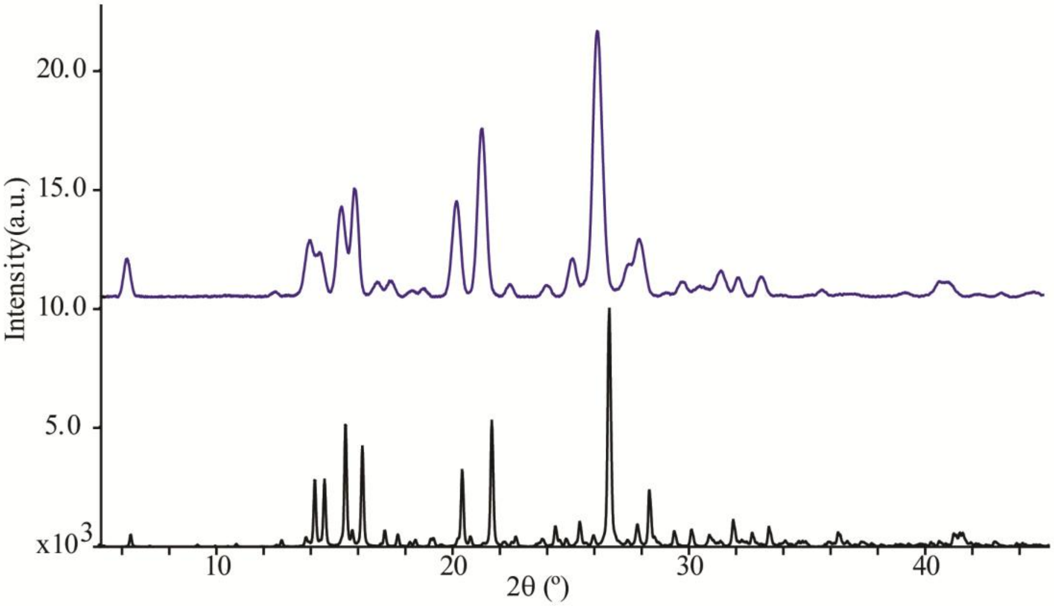

Figure 2.7. Simulated (bottom) and experimental (top) PXRD of TA form IV.

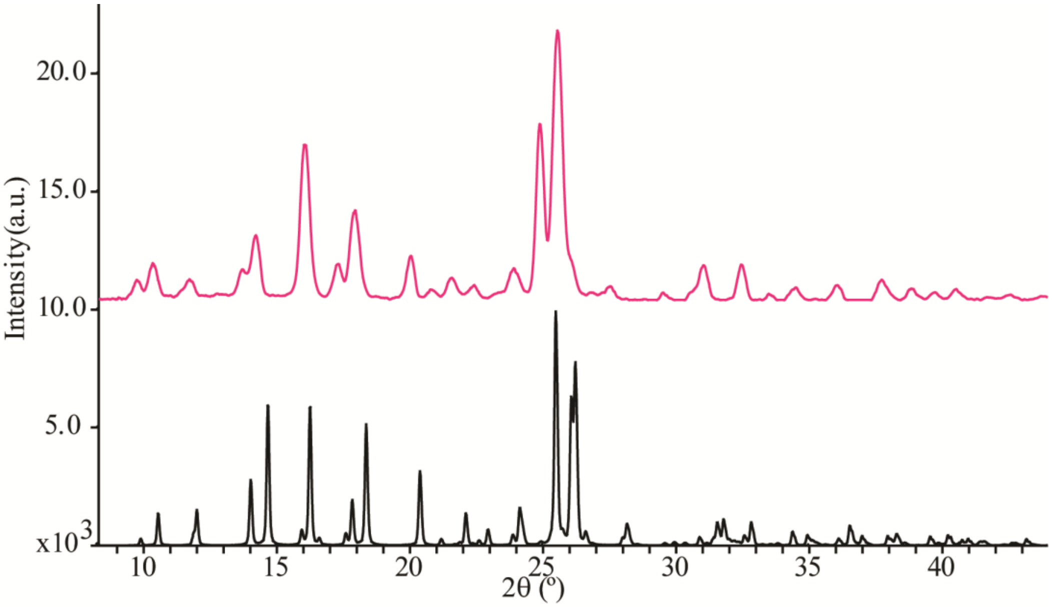

Figure 2.8. Simulated (bottom) and experimental (top) PXRD of TA form V.

Table 2.2. Experimental PXRD pattern peak positions (º) and the relative intensity (%) of TA forms I-V.

form I		**form II**		**form III**		**form IV**		**form V**	
2θ	**I/I_0**	**2θ**	**I/I_0**	**2θ**	**I/I_0**	**2θ**	**I/I_0**	**2θ**	**I/I_0**
5.4	13.2	10.1	37.4	6.2	8.8	6.2	14.2	9.8	7.1
10.9	3.9	12.4	7.8	14.2	31.2	12.5	1.9	10.4	13.4
11.7	81.0	13.1	56.7	14.9	11.2	14.0	20.8	11.7	7.3
14.0	10.7	13.5	25.1	15.5	29.7	14.3	16.4	13.8	11.0
15.8	100.0	16.1	13.2	18.0	11.9	15.3	33.5	14.2	23.6
16.4	6.8	17.3	21.9	18.9	7.8	15.8	40.3	16.1	57.8
17.8	5.1	22.3	5.3	19.8	5.1	16.8	5.4	17.3	13.0
18.7	10.2	23.1	11.0	21.2	74.9	17.3	5.9	17.9	33.1
19.8	15.8	24.4	100.0	21.9	5.6	18.3	2.2	20.0	16.0
22.0	2.4	25.4	53.9	23.6	30.0	18.7	3.1	20.8	3.5
22.3	3.0	26.3	21.4	24.3	60.2	20.2	35.9	21.6	7.8
23.0	18.9	27.1	15.3	26.7	100.0	21.2	63.2	22.4	5.1
24.3	4.9	27.9	14.3	27.8	5.9	22.4	4.6	23.9	11.4
24.9	15.1	28.6	13.6	28.1	4.0	24.0	4.3	24.9	64.7
25.4	63.4	30.0	3.8	29.0	8.4	25.1	14.4	25.6	100.0
26.1	12.9	30.8	13.9	30.6	14.9	26.1	100.0	26.9	2.5
26.7	39.8	31.8	10.9	31.3	3.7	27.5	12.2	27.5	5.0
28.2	4.0	32.7	5.5	32.4	7.8	27.9	21.6	29.5	2.7
28.9	3.2	34.1	3.4	34.4	6.9	29.0	1.5	31.0	12.7
29.5	4.0	35.0	7.5	38.3	4.9	29.7	5.6	32.5	12.9
30.0	9.0	35.6	5.5	40.6	2.2	30.5	4.1	34.5	4.4
31.9	2.3			41.4	2.8	31.4	9.7	36.1	5.4
32.5	1.9			43.1	3.5	32.1	7.2	37.7	7.4
33.8	9.8					33.1	7.5	38.9	4.2
35.1	4.6					35.6	2.6	39.7	2.8
35.7	4.1					39.1	1.4	40.5	3.9
36.0	3.4					40.6	5.5	42.5	1.9
37.2	1.4					43.2	1.5	43.8	1.4
37.9	4.7								
38.8	3.0								

Table 2.3. Crystallographic data for polymorphs of TA I-V.

form	**I**	**II**	**III**	**IV**	**V**
crystal system	monoclinic	monoclinic	monoclinic	triclinic	triclinic
space group	$P2_1$/c	$P2_1$/n	$P2_1$/c	P	P
temperature (K)	110	110	85(2)	85(2)	85(2)
a (Å)	4.826(2)	3.836(2)	7.6356(15)	7.5237(8)	7.6488(13)
b (Å)	32.128(1)	21.997(5)	11.305(2)	14.3308(16)	9.0160(15)
c (Å)	8.041(4)	14.205(7)	28.065(6)	17.592(2)	9.4184(15)
α (°)	90.0	90.0	90.0	103.680(2)	107.385(3)
β (°)	104.88(3)	94.11(4)	93.03(3)	98.253(2)	92.062(3)
γ (°)	90.0	90.0	90.0	93.038(2)	101.662(3)
cell volume ($Å^3$)	1205(2)	1196(2)	2419.1(8)	1816.41	603.81(17)
calc density (g/cm^3)	1.443	1.450	1.437	1.435	1.439
Z	4	4	8	6	2
Z'	1	1	2	3	1
unique reflections	2990	8471	6036	7521	2479
R	0.052	0.029	0.0448	0.0723	0.0658
R_w	0.071	0.041	0.1169	0.1658	0.1257

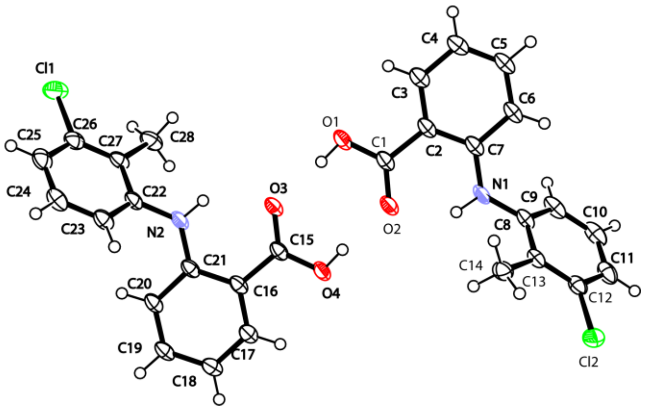

Figure 2.9. ORTEP diagram of TA form III.

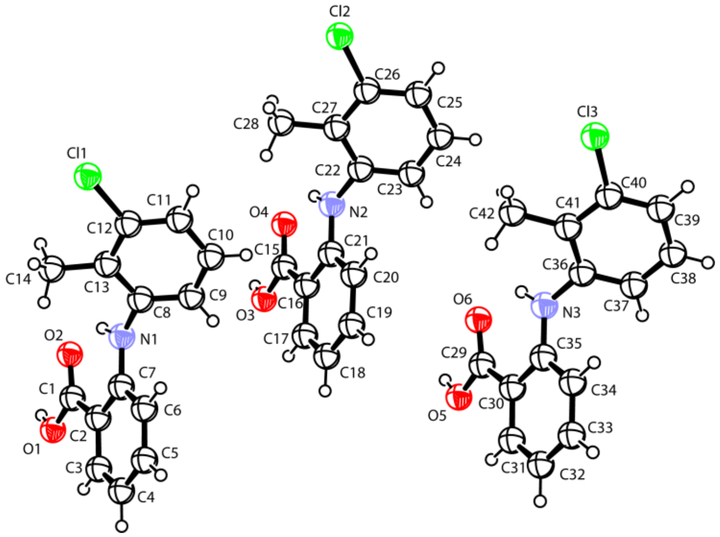

Figure 2.10. ORTEP diagram of TA form IV.

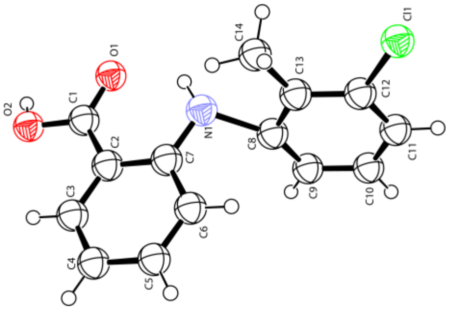

Figure 2.11. ORTEP diagram of TA form V. This represents 50% occupancy of the whole molecule disordered structure.

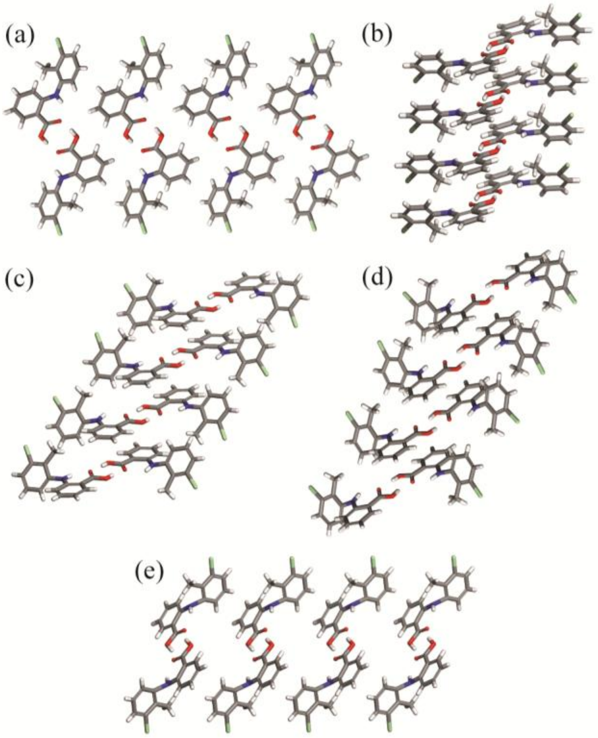

Figure 2.12. Molecular packing and hydrogen bonding motif of TA polymorphs (a) sheets of TA in form I, columns of TA in forms (b) II, (c) III, (d) IV, and (e) V. Form V represents 50% occupancy of the whole molecule disorder structure.

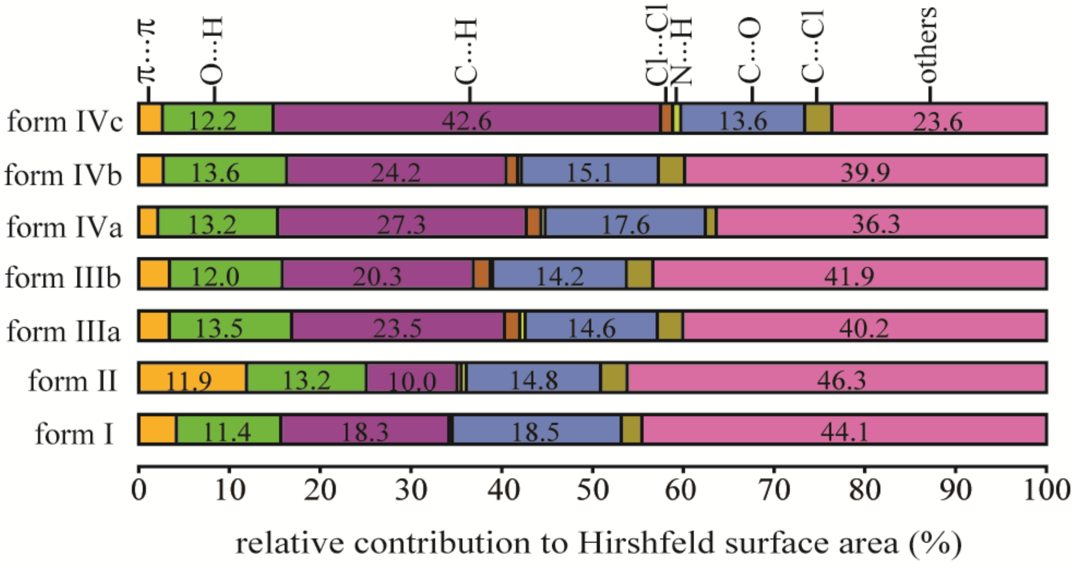

Figure 2.13. Percent relative contribution to the HSs of the important intermolecular interactions present in each of the molecule in the asymmetric unit of the ordered TA polymorphs. The letters *a*, *b*, and *c* represent different conformers in the structures with *Z*´ > 1.

Table 2.4. Difference in free energy (ΔG) of TA polymorphs calculated from mean absorbance at equilibrium ($\lambda_{max.}$= 283 nm, 300 ± 1 K).

form	ΔG (kcal/mol)
I	0.00
II	0.04
III	0.10
IV	0.27*
V	0.23

*This free energy difference may represent a slight underestimation due to a slow conversion of this form to form I under the experimental conditions.

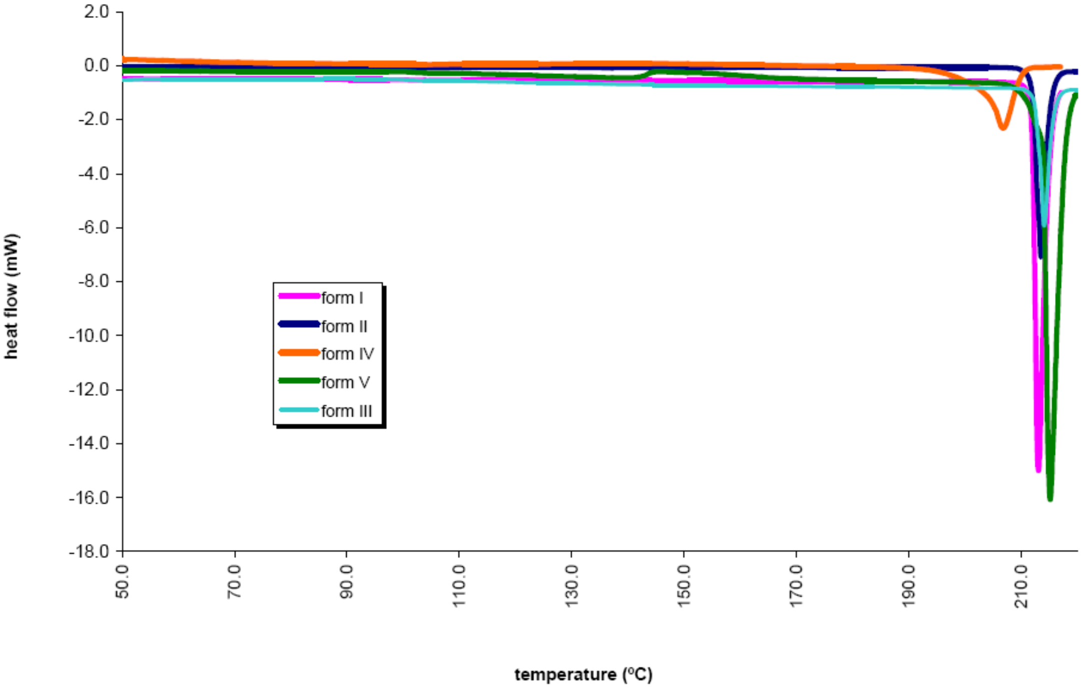

Figure 2.14. Thermograms of TA polymorphs: form I (pink), form II (dark blue), form III (light blue), form IV (orange), and form V (green).

Table 2.5. Summary of DSC data for TA polymorphs I-V.

initial form	T_m (°C)	ΔH_{fus} (kcal/mol)
I	213.10	9.41
II	213.52	9.25
III	214.09	9.99
IV	206.78	7.62
V	215.17	9.95

Table 2.6. Lattice energy from calculations in Ceruis[2] using Compass force field.

form	U_{latt} Free Cell (kcal/mol)	ΔU_{latt} Free Cell (kcal/mol)
I	-37.1715	0.0000
II	-36.1845	0.9870
III	-36.0370	1.1340
IV	-35.4193	1.7522

2.5 References

1. Blagden, N.; Davey, R. J.; Lieberman, H. F.; Williams, L.; Payne, R.; Roberts, R.; Rowe, R.; Docherty, R., Crystal chemistry and solvent effects in polymorphic systems - Sulfathiazole. *Journal of the Chemical Society-Faraday Transactions* **1998,** 94, (8), 1035-1044.
2. Hughes, D. S.; Hursthouse, M. B.; Threlfall, T.; Tavener, S., A new polymorph of sulfathiazole. *Acta Crystallographica Section C-Crystal Structure Communications* **1999,** 55, 1831-1833.
3. Kruger, G. J.; Gafner, G., Crystal Structure of Sulphathiazole .2. *Acta Crystallographica Section B-Structural Crystallography and Crystal Chemistry* **1971,** B 27, 326.
4. Kruger, G. J.; Gafner, G., Crystal-Structures of Polymorphs-I and Iii of Sulfathiazole. *Acta Crystallographica Section B-Structural Crystallography and Crystal Chemistry* **1972,** B 28, 272.
5. Drebushchak, T. N.; Chukanov, N. V.; Boldyreva, E. V., A new polymorph of chlorpropamide: 4-chloro-N-(propylaminocarbonyl)benzenesulfonamide. *Acta Crystallographica Section E-Structure Reports Online* **2006,** 62, O4393-O4395.
6. Drebushchak, T. N.; Chukanov, N. V.; Boldyreva, E. V., A new gamma-polymorph of chlorpropamide: 4-chloro-N-(propylamino-carbonyl)benzenesulfonamide. *Acta Crystallographica Section C-Crystal Structure Communications* **2007,** 63, O355-O357.
7. Drebushchak, T. N.; Chukanov, N. V.; Boldyreva, E. V., Two polymorphs of chlorpropamide: the delta-form and the high-temperature epsilon-form. *Acta Crystallographica Section C-Crystal Structure Communications* **2008,** 64, O623-O625.
8. Koo, C. H.; Cho, S. I.; Yeon, Y. H., Crystal and Molecular Structure of Chlorpropamide. *Archives of Pharmacal Research (Seoul)* **1980,** 3, (1), 37-50.
9. Tessler, L.; Goldberg, I., Crystal structures of aripiprazole, a new anti-psychotic drug, and of its inclusion compounds with methanol, ethanol and water. *Journal of Inclusion Phenomena and Macrocyclic Chemistry* **2006,** 55, (3-4), 255-261.
10. Braun, D. E.; Gelbrich, T.; Kahlenberg, V.; Tessadri, R.; Wieser, J.; Griesser, U. J., Conformational Polymorphism in Aripiprazole: Preparation, Stability and Structure of Five Modifications. *Journal of Pharmaceutical Sciences* **2009,** 98, (6), 2010-2026.
11. Braun, D. E.; Gelbrich, T.; Kahlenberg, V.; Tessadri, R.; Wieser, J.; Griesser, U. J., Stability of Solvates and Packing Systematics of Nine Crystal Forms of the Antipsychotic Drug Aripiprazole. *Crystal Growth & Design* **2009,** 9, (2), 1054-1065.
12. López-Mejías, V.; Kampf, J. W.; Matzger, A. J., Polymer-Induced Heteronucleation of Tolfenamic Acid: Structural Investigation of a Pentamorph. *Journal of the American Chemical Society* **2009,** 131, (13), 4554.

13. Andersen, K. V.; Larsen, S.; Alhede, B.; Gelting, N.; Buchardt, O., Characterization of 2 Polymorphic Forms of Tolfenamic Acid, N-(2-Methyl-3-Chlorophenyl)Anthranilic Acid - Their Crystal-Structures and Relative Stabilities. *Journal of the Chemical Society-Perkin Transactions 2* **1989**, (10), 1443-1447.

14. Gelbrich, T.; Threlfall, T. L.; Bingham, A. L.; Hursthouse, M. B., Polymorph VI of sulfapyridine: interpenetrating two- and three-dimensional hydrogen-bonded nets formed from two tautomeric forms. *Acta Crystallographica Section C-Crystal Structure Communications* **2007,** 63, O323-O326.

15. Stephenson, G. A.; Borchardt, T. B.; Byrn, S. R.; Bowyer, J.; Bunnell, C. A.; Snorek, S. V.; Yu, L., Conformational and Color Polymorphism of 5-Methyl-2-[(2-Nitrophenyl)Amino]-3-Thiophenecarbonitrile. *Journal of Pharmaceutical Sciences* **1995,** 84, (11), 1385-1386.

16. Chen, S.; Guzei, I. A.; Yu, L., New polymorphs of ROY and new record for coexisting polymorphs of solved structures. *Journal of the American Chemical Society* **2005,** 127, (27), 9881-9885.

17. Chen, S. A.; Xi, H. M.; Yu, L., Cross-nucleation between ROY polymorphs. *Journal of the American Chemical Society* **2005,** 127, (49), 17439-17444.

18. Burger, A.; Ramberger, R., Thermodynamic Relationships between Polymorphic Modifications - Flufenamic Acid and Mefenamic-Acid. *Mikrochimica Acta* **1980,** 1, (1-2), 17-28.

19. Krc, J., Crystallographic Properties of Flufenamic Acid. *Microscope* **1977,** 25, (1), 31-45.

20. Lee, E. H.; Boerrigter, S. X. M.; Rumondor, A. C. F.; Chamarthy, S. P.; Byrn, S. R., Formation and solid-state characterization of a salt-induced metastable polymorph of flufenamic acid. *Crystal Growth & Design* **2008,** 8, (1), 91-97.

21. Lutker, K. M.; Tolstyka, Z. P.; Matzger, A. J., Investigation of a privileged polymorphic motif: A dimeric ROY derivative. *Crystal Growth & Design* **2008,** 8, (1), 136-139.

22. Lutker, K. M.; Matzger, A. J., Crystal Polymorphism in a Carbamazepine Derivative: Oxcarbazepine. *Journal of Pharmaceutical Sciences* 99, (2), 794-803.

23. Lang, M. D.; Grzesiak, A. L.; Matzger, A. J., The use of polymer heteronuclei for crystalline polymorph selection. *Journal of the American Chemical Society* **2002,** 124, (50), 14834-14835.

24. Price, C. P.; Grzesiak, A. L.; Matzger, A. J., Crystalline polymorph selection and discovery with polymer heteronuclei. *Journal of the American Chemical Society* **2005,** 127, (15), 5512-5517.

25. Grzesiak, A. L.; Matzger, A. J., Selection and discovery of polymorphs of platinum complexes facilitated by polymer-induced heteronucleation. *Inorganic Chemistry* **2007,** 46, (2), 453-457.

26. Grzesiak, A. L.; Matzger, A. J., New form discovery for the analgesics flurbiprofen and sulindac facilitated by polymer-induced heteronucleation. *Journal of Pharmaceutical Sciences* **2007,** 96, 2978-2986.

27. Grzesiak, A. L.; Matzger, A. J., Selection of protein crystal forms facilitated by polymer-induced heteronucleation. *Crystal Growth & Design* **2008,** 8, (1), 347-350.

28. Grzesiak, A. L.; Uribe, F. J.; Ockwig, N. W.; Yaghi, O. M.; Matzger, A. J., Polymer-induced heteronucleation for the discovery of new extended solids. *Angewandte Chemie-International Edition* **2006,** 45, (16), 2553-2556.
29. Porter, W. W.; Elie, S. C.; Matzger, A. J., Polymorphism in carbamazepine cocrystals. *Crystal Growth & Design* **2008,** 8, (1), 14-16.
30. McKinnon, J. J.; Fabbiani, F. P. A.; Spackman, M. A., Comparison of polymorphic molecular crystal structures through Hirshfeld surface analysis. *Crystal Growth & Design* **2007,** 7, (4), 755-769.
31. McKinnon, J. J.; Jayatilaka, D.; Spackman, M. A., Towards quantitative analysis of intermolecular interactions with Hirshfeld surfaces. *Chemical Communications* **2007**, (37), 3814-3816.
32. Spackman, M. A.; McKinnon, J. J., Fingerprinting intermolecular interactions in molecular crystals. *Crystengcomm* **2002**, 378-392.
33. Spackman, M. A.; Jayatilaka, D., Hirshfeld surface analysis. *Cryst Eng Comm* **2009,** 11, (1), 19-32.
34. Mitchell-Koch, K. R.; Matzger, A. J., Evaluating computational predictions of the relative stabilities of polymorphic pharmaceuticals. *Journal of Pharmaceutical Sciences* **2008,** 97, (6), 2121-2129.

CHAPTER 3

CRYSTAL POLYMORPHISM OF NIFLUMIC AND FLUFENAMIC ACID

3.1 Introduction

Understanding the balance between attractive and repulsive interactions responsible for the appearance of multiple crystalline forms (polymorphs) in molecular compounds, has become an area of extensive research in solid-state chemistry due to the profound impact of solid-state packing on material propierties.[1,2] It has been suggested that all compounds present polymorphism and that the experimental observation of this phenomena in some compounds and not others, is merely a consequence of the time and money invested in their investigation.[3] Although the sentiment resonates with the experience of many researchers in the field, with the correct methodology polymorph discovery need not always be an expensive long term endeavor. Toward this goal, a general method for polymorph discovery has been developed: polymer-induced heteronucleation (PIHn).[4, 5] In this method, polymer heteronucleants direct novel form discovery and selection with demonstrations for a broad cross-section of compounds.[6-10]

This investigation on the polymorphism of the potent non-steroidal anti-inflammatory drugs (NSAIDs) niflumic (NA) and flufenamic (FFA) acid (Figure 3.1) demonstrates the capability of PIHn to access novel crystalline forms. These compounds are of particular interest to test within the fenamic acid series the concept of the polymorphophore, a structural element that when incorporated into a compound favors the formation of polymorphic crystals.[8, 10] Despite the numerous investigations concerning relative stability,[11-15] spectroscopic properties,[16-20] conformational,[21] and crystallization behavior,[22-25] to date only one crystal structure of NA has been reported.[26] Although the existence of several polymorphs have been proposed[11, 27,25] in the case of FFA, only two forms (forms I and III) have been structurally characterized.[26] Furthermore, outside of the potential significance of polymorphism for influencing the bioavailability of these drugs, their supramolecular chemistry is of considerable interest as analogs of tolfenamic acid (TA),[6] one of the most polymorphic drugs known, and other structurally related compounds (Figure 3.1).[28, 29] Here, we report on the trimorphism of NA and expand on the structural identification of FFA polymorphs by elucidating the crystal structure of FFA forms II, IV, V, VII and VI.

3.2 Experimental Section

3.2.1 Materials

Commercial NA (2-{[3-(trifluoromethyl)phenyl]aniline}nicotinic acid) and FFA (2-{[3-(trifluoromethyl)phenyl]amino}benzoic acid) were obtained from Sigma-Aldrich (St. Louis, MO, USA). The solvents methanol, 2-propanol, 1-pentanol, ethyl acetate, methylene chloride, acetonitrile, chloroform, 1-butanol, and acetone were purchased from Fisher Scientific (Pittsburgh, PA, USA). The solvents iso-butylalcohol and 1-propanol were purchased from Burdick and Jackson Laboratories, Inc. (Muskegon, MI, USA), whereas 1,4-butanediol and sec-butanol were purchased from Acros Organics (New

Jersey, USA). Ethanol was purchased from Decon Laboratories, Inc. (King of Prussia, PA, USA).

3.2.2 Preparation of the Polymer Libraries

The components used to build the polymer libraries were the following; for the non-polar aromatic library monomers 4-acetoxystyrene (AOS), *n*-butyl methacrylate (*n*-BuMA), *tert*-butyl methacrylate (*t*-BuMA), benzyl methacrylate (BzMA), methyl methacrylate (MMA), and styrene (STY) with divinylbenzene (DVB) where utilized, for the acidic polymer library, acrylic acid (AA), 2-ethoxyethylmethaacrylate (EEMA), ethylene glycol methacrylate phosphate (EGMAP), 2-hydroxyethylmetharylate (HEMA), methacrylic acid (MAA), and methyl methacrylate (MMA), with divinylbenzene (DVB) were utilized. Each library was synthesized in a round bottom 96-well plate using a previously described procedure.[6] In brief, six 1:1 (v/v) monomer solutions in ethanol were dispensed as 90 pairwise combinations of varied ratios (86:14, 71:29, 57:43, 43:57, 29:71, and 14:86) and six pure monomer solutions by a Gilson 215 liquid handler to a volume of 113 μL. To each of these 96 solutions was added 57 μL of a 1:1 solution of DVB in ethanol containing 2 mol% 2,2'-azobisisobutyronitrile (AIBN) with respect to DVB. The solutions were divided into four round bottom 96-well plates using a HYDRA-96 liquid dispenser (40 μL to each plate), then the mixtures were photopolymerized in a N_2 atmosphere for 2 hrs. Finally, the polymers were annealed at 85 °C under vacuum for 4 hrs to produce the cross-linked polymer library.

3.2.3 Crystallization of NA in the Presence of Polymers

NA form I is the commercially available form. In addition, form I can be obtained through slow evaporation of an ethanol solution. Form II was accessed through evaporation of a 2-propanol solution (~0.2 mL of a ~12.0 mg/mL solution were equally dispensed among the 96-wells) in the presence of cross-linked acidic polymers at room temperature. Form II was also produced by dissolving 5.2 mg of NA in 1 mL of methanol and heating the solution to 85 °C until homogeneous in a 4 mL vial. Once homogeneous, the cap was removed and the solvent was allowed to rapidly evaporate by heating at 65 °C until crystals formed. Form III was obtained through the evaporation of an ethanol solution (~0.2 mL of a ~23.3 mg/mL solution were equally dispensed among the 96-wells) in the presence of cross-linked acidic polymers at room temperature. In addition to methanol, thirteen other solvents were employed in attempts to obtain forms II and III through solvent-based screening in the absence of polymer. This method was unable to access these forms.

Single crystals of NA form II grew selectively in AA:EEMMA (86:14), AA:MMA 14:86 and EGMAP:MAA 71:29, while powders grew concomitantly with form I in other combinations of these same monomers. Single crystals of NA form III were obtained in 100% AA. After its initial discovery and characterization, later attempts to produce polymorph III were unsuccessful.

3.2.4 Crystallization of FFA in the Presence of Polymers

FFA form I is the commercially available form, which can also be obtained by slow evaporation of an ethanol solution. Form III was produced by dissolving 50 mg of FFA in 1 mL of ethanol and heating the solution to 85 °C until homogeneous. The solution was then allowed to cool to room temperature or placed in a −18 °C freezer until crystals formed. Crystals of form I-V, VII, VIII and IX grew selectively through the evaporation of an ethanol solution (~0.2 mL of a ~30.0 mg/mL solution were equally dispensed among the 96-wells) in the presence of cross-linked non-polar aromatic polymers at room temperature.

Fourteen different solvents were utilized in an attempt to produce these polymorphs through conventional solvent based methods. Form IV could be obtained by dissolving 5.8 mg of FFA in 0.3 mL of methanol or 0.5 mL chloroform followed by slow evaporation of the solvent. Under the latter crystallization condition forms II and V were also observed concomitantly with form IV and in less frequency as pure forms. To obtain form VII, 5.0 mg of FFA was weighed into a 4 mL vial, and 1 mL of acetonitrile or chlorobenzene was added. The solution was heated to 100 °C until homogeneous, then after cooling the solution, the vial was uncapped and left for solvent evaporation. The solvent was allowed to slowly evaporate at room temperature until crystals formed. Thermal analysis of form IV, revealed a solid-solid transformation at low temperature (~ −130 °C) to form VI. Bulk form VI was accessed by submerging a 4 mL vial containing crystals (~5.0 mg) of form IV into a dewar flask containing N_2 *(l)* for 10-15 minutes. The crystallization vial was warmed to room temperature prior to PXRD analysis which confirmed form IV transformation to form VI had occurred. Forms VIII and IX could not be accessed in the absence of polymer; attempts to produce either one of these forms through conventional solvent based methods were unsuccessful.

In the case of FFA polymorphs, single crystals of form I-III were found in multiple wells of a non-polar polymer library while single crystals of form IV and V grew selectively in AOS:*t*-BuMA (57:43) and AOS:BzMA (71:29), respectively. Form IV and V grew concomitantly with form III in combination of AOS with other monomers, for example, MMA and *n*-BuMA. Forms VII-IX grew in the presence of multiple cross-linked non-polar aromatic polymers (mainly in pure AOS, *n*-BuMA, and *t*-BuMA or multiple combinations thereof) as well, in most cases concomitantly with form III. The single crystal of form VII used for single crystal X-ray diffraction was selected from a MAA (100%) well in which it grew concomitantly with form III, whereas the single crystal of form VIII used for single crystal X-ray diffraction was selected from a *n*-BuMA (100%) well. Elucidation of this crystal structure is ongoing.

3.2.5 Raman Vibrational Spectroscopy

Raman spectra were recorded on a Renishaw inVia Raman Microscope equipped with a Leica Microscope, RenCam CCD detector, 633 nm He-Ne laser, 1800 lines/nm grating and 50 µm slit. Spectra were collected in extended scan mode utilizing a 20× objective. The scan range was 3800-100 cm^{-1} using 3 scans of length 20 s per spectrum with cosmic ray removal enabled. Calibration was performed using a silicon standard.

3.2.6 Powder X-ray Diffraction

Powder X-ray diffraction (PXRD) analysis was performed using a Rigaku R-Axis Spider diffractometer equipped with an image plate detector and graphite monochromated Cu-Kα radiation (1.5406 Å, 50 kV, 40 mA). Samples were mounted on a CryoLoop™ and images were collected for 5 min while rotating sample about the φ-axis at 10°/sec, oscillating ω between 120° and 180° at 1°/sec with χ fixed at 45°. All images were integrated from 5° to 50° with a 0.05° step size using AreaMax[2] software. Powder patterns were processed in Jade Plus[3] to calculate peak positions (°) and relative intensities (%).

3.2.7 Single Crystal X-ray Diffraction

Measurements for NA forms I-III, FFA form II and FFA form V were made on a Rigaku R-Axis Spider diffractometer with an image plate detector using graphite monochromated Cu-Kα radiation (1.5406 Å) operating at 50 kV and 40 mA. The data collection was carried out at 95 K with the sample mounted on a MiTeGen MicroMount™. The structures were solved by direct methods. All calculations were performed using the CrystalStructure crystallographic software package except for refinement, which was performed using SHELXL-97.

Measurements for FFA forms IV, VI, VII and VIII were made on a Rigaku AFC10K Saturn 944+ CCD-based X-ray diffractometer equipped with a low temperature device and Micromax-007HF Cu-target micro-focus rotating anode (1.54187 Å) operated at 1.2 kW power (20 kV, 10 mA). The X-ray intensities were measured at 85(1) K (forms VI VII, and VIII) or 273(1) K (form IV) with the crystal mounted on a CryoLoop™. The structure was solved and refined with the Bruker SHELXTL (version 2008/4) software package.

3.2.8 Hirshfeld Surface Analysis

Hirshfeld surface (HSs) analysis of each of the molecules in the asymmetric unit of the structurally characterized polymorphs of NA and FFA were constructed using the program Crystal Explorer v2.0.[30-32] Crystallographic information files were uploaded to the program after the normalization of N–H, O–H and C–H bond lengths (1.008, 0.983, and 1.083 Å, respectively) to average neutron values was performed.

3.2.9 Relaxed Potential Energy Surface Scans

Two-dimensional scans were performed for both NA and FFA molecules using Gaussian03. Optimized geometries and corresponding energies were obtained at the HF/6-31G* level of theory at 10° intervals. All calculations were performed on a dual 2.66 GHz Intel Xeon Quad Core CPU.

3.2.10 Differential Scanning Calorimetry

Thermograms of the samples were recorded in a TA instruments DSC Q10. Data was analyzed with TA Universal Analysis software Version 4.3A. Samples (0.3 - 2.0 mg) were weighed to a precision of 0.0001 mg and placed in pans, then sealed using a TA Instruments crimper. Thermal behavior of the samples was studied under a nitrogen purge at 10 ºC/min heating rate. The temperature range was 25 - 250 °C for NA and 25 - 180 °C for FFA. The instrument was calibrated with an indium standard.

3.2.11 Variable Temperature Powder X-ray Diffraction

Variable temperature powder X-ray diffraction (VTPXRD) analysis was performed using a Rigaku R-Axis Spider diffractometer equipped with an image plate detector and graphite monochromated Cu-Kα radiation (1.5406 Å, 50 kV and 40 mA). A 0.5 mm glass capillary was filled with sample and images were collected continuously for 3 min while rotating sample about the φ-axis at 10°/sec, oscillating ω between 0° and 360° at 1°/sec with χ fixed at 45°. All images were integrated from 5° to 50° with a 0.05° step size using AreaMax[2] software. PXRD patterns were processed in Jade Plus[3] to create the 3D overlay.

3.2.12 Free Energy Relationships Among Forms

The optical absorbance of NA and FFA polymorphs in hexanes and water, respectively and monitored *in situ* over time using an Agilent 8453 UV-visible spectrometer in the range of 100-1900 nm at 300 ± 1 K. The wavelength of maximum absorbance ($\lambda_{max.}$) of NA in hexanes was located at 357 nm, whereas the wavelength of maximum absorbance ($\lambda_{max.}$) of FFA in water was 288 nm. A time-dependent absorbance curve was used to determine the absorbance at equilibrium and these values were employed in relative free energy determination (Equation 1) for each of these forms as well as to monitor conversions in solution over a longer period of time. The solute remaining was identified using PXRD.

$$\Delta(\Delta G) = RT\ln(S_2/S_1) \qquad (1)$$

3.2.13. Lattice Energy Calculations

The lattice energy, U_{latt}, of the structurally elucidated polymorphs of NA and FFA were calculated using the Free-Cell method previously described by Mitchell-Koch *et al.*[33]

3.2.14. Cambridge Structural Database (CSD) Search for *Z´* ≥ 6 structures.

In the current CSD (Feb. 2011 release), a search for crystal structures with $Z' \geq 6$ was performed. To obtain these statistics, we retrieved all entries containing the qualifier "3D coordinates determined." Hits were sorted by hand to yield only structures that present six or more independent molecules in the asymmetric unit. Exactly 286 (0.07% occurrence in the CSD) hits resulted.

3.3 Results and Discussion

Several investigations concerning the thermodynamic,[8-15] spectroscopic,[13-17] conformational,[21] and structural[19-22] aspects of the only known form of NA and its polymorphic analogue FFA (Figure 3.1), have been published in the last two decades. Our recent discovery of a pentamorphic analogue, TA,[6] motivated us to reopen the investigation into the polymorphism of these two NSAIDs with the ultimate goal of establishing the common polymorphic motif among these and other close related analogues such as 2-(2-M3CA)[28] and 2-PNA,[29] (Figure 3.1). Here, two novel forms of NA were prepared using acidic cross-linked polymers as heteronuclei, yellow needles of form II grew selectively from 2-propanol, whereas colorless plates of form III grew selectively when ethanol was utilized as a solvent. All crystals formed in the 96-well plate where analyzed by Raman vibrational spectroscopy. Noticeable differences were observed among each of the polymorphs in four main spectral regions: 550-800, 1280-1405, 1600-1650, and 2900-3400 cm^{-1} (Figure 3.2 and Table 3.1).

PXRD establishes that unique packing arrangements are present in each of the polymorphs of NA (Figure 3.3-3.6 and Table 3.2). The crystal structure of NA form I was re-determined, this time at low temperature (95 K), and those of forms II and III were determined for the first time. A common feature in analogues of NA is the presence of hydrogen bonded dimers that propagate in sheets through slight different intermolecular interactions (Figure 3.7). In polymorphs I and II, dimers connect the carboxylic acid of the only molecule in the asymmetric unit through an inversion center, whereas in polymorph III heterodimers participate utilizing the same intermolecular contacts. Intramolecular hydrogen bonding with the amino group of the biphenyl amine is also present in all three forms of NA as well as in its other structural analogues. NA form I crystallizes in space group $P2_1/c$ with one molecule in the asymmetric unit, whereas the second polymorph of NA belongs to the triclinic space group $P\bar{1}$, and as in the case of form I, possesses one molecule in the asymmetric unit. NA form III belongs to the same triclinic space group as form II, $P\bar{1}$, but this modification possess two molecules in the asymmetric unit. A summary of the crystallographic data for NA polymorphs I–III can be found in Table 3.3.

HSs analysis[30-32] was performed on each molecule in the asymmetric unit of the NA polymorphs in order to determine the relative contribution of important intermolecular contacts (Figures 3.8 and 3.9) to the unique crystal packing observed in all forms. This analysis, revealed that the relative contribution of the O···H intermolecular contacts vary moderately (9.6 - 12.5 %) among all NA polymorphs, possibly owing to the robustness of the hydrogen bonded anti-dimer motif. In NA form I, F···H and $\pi\cdots\pi$ contacts comprise 33.5 % of the HSs, whereas the C···H contacts compose 20.1 %; these values present a significantly higher contribution relative to any of the other NA modifications. In form II, the $\pi\cdots\pi$ contacts contribute close to 10% to the HSs, a value double that of any of the other conformer surfaces. Dominance of the $\pi\cdots\pi$ contacts in form II, reiterates the importance of these contacts in the slipped packing motif of the chains in this particular modification. The relative contribution of F···C (6.9 %) contacts to the HSs in NA form III is almost double that of the other two forms (~3.0%), indicating that this contact contributes to the propagation of the hydrogen bonded dimers chains in form III more so than in form I and II.

All NA polymorphs exhibit differences in conformation as well as packing motifs. The torsion angle that defines the orientation of the carboxyl group with respect to the phenyl ring bearing it, τ_3, does not deviate from planarity by more than 6° in any of the structures examined so far. This may result from the intramolecular hydrogen bond and the resonance interaction between the phenyl and carboxylic acid moiety which provides stabilization to the nearly coplanar arrangement observed in each of the three forms. Table 3.4 lists the torsion angles (τ_1 and τ_2) between the planes defined by biphenyl amine functionality in NA as well as τ_3. A conformational search of the potential energy[21,30] in a single molecule of NA, revealed that in all three modifications, the molecules in the asymmetric unit present conformations that fall within a 0.4 kcal/mol energy window (Figure 3.10 and Table 3.4) when compared to that of the lowest energy conformation calculated in Gaussian03 and are located within a single conformational energy minima.

After its initial discovery, other attempts to make NA form III were unsuccessful and therefore relative stability of only form I and form II was determined *in situ* through equilibrium solubility experiments in hexanes. The solubility ratio between this polymorphic pair was utilized to determine the differences in free energy at 27 °C. The solute remaining was identified using PXRD, no polymorphic conversion occurred during the experimental time. Results indicate that NA form I is the most thermodynamically stable polymorph by about 0.5 kcal/mol of the two forms examined.

Thermal behavior of forms I-III was investigated utilizing DSC (Figure 3.11 and Table 3.5). No polymorphic transformations were observed in NA polymorphs I and III. Form I presents the highest melting point centered at 204.6 °C (ΔH_{fus} = 9.1 kcal/mol). In the thermogram of polymorph II an exothermic event is observed between 170.6 - 203.4

°C (0.4 kcal/mol) prior to the melting endotherm which centered at 204.2 °C (ΔH_{fus} = 8.1 kcal/mol). Form III melts at the lowest temperature occurring at 203.1 °C (ΔH_{fus} = 8.7 kcal/mol). NA polymorphs I and III do not undergo transformation upon heating, therefore the heat of fusion rule can be applied to establish their thermodynamic relationship. NA form I presents the highest melting point and enthalpy of fusion among the two, their thermodynamic relationship can be classified as monotropic based on the heat of fusion rule. According to the lattice energy calculations (Table 3.6), form I has the greatest enthalpy among the polymorphs of NA which is in accordance with the experimental enthalpies determined for NA polymorph.

For more than forty years, the existence of polymorphism in FFA has been known. During that time, numerous investigations addressing the spectroscopic,[13-17] conformational,[18] as well as the thermodynamic relationships[8-12] among each of the eight proposed forms of FFA have emerged. Elucidation of the first crystal structure of FFA (form III) occurred in 1973, and nearly ten years later the structure of form I was reported. The existence of extensive polymorphism in this compound has offered a challenge for research methodologies developed for polymorph discovery and control from the use of soluble additives,[25] to epitaxy,[24] and presently PIHn. Eight crystalline phases of FFA were grown from an ethanol solution using polymers as heteronuclei. Optical examination revealed noticeable differences in the morphology of the crystals. The previously reported colorless and yellow needles (forms I and III) were observed as well as colorless plates (forms II and VIII), colorless prisms (forms IV and V) and colorless needles (forms VII and IX). Furthermore, in the case of form IV, a low temperature transformation of this form to form VI (~ −130 °C) allowed access to this polymorph which is quite stable at room temperature. When the samples were examined by Raman vibrational spectroscopy, four main regions (700-810, 1000-1250, 1320-1630, and 3000-3400 cm^{-1}) aided the identification of each polymorph (Figure 3.12 and Table 3.7).

Powder X-ray diffraction (PXRD) establishes that a unique structural fingerprint exists for all nine polymorphs of FFA (Figures 3.13-3.22 and Tables 3.8 and 3.9). Comparing the PXRD patterns obtained in the present experiment with those found previously for forms I-III,[11] confirms that the undisclosed structure in this set corresponds to FFA form II,[27] whereas diffraction patterns for forms IV-IX are reported here for the first time. Structure determination revealed that (Figure 3.23 and Table 3.10), as in the case of the majority of the highly polymorphic compounds, each FFA form contains different conformers. In contrast to ROY, several structures of FFA vary in the number of inequivalent molecules in the asymmetric unit. FFA is known to crystallize in two monoclinic forms, both containing one molecule in the asymmetric unit. The now accessible forms II, V and VII crystallize in the space group $P2_1$/c with $Z' = 1$, $Z' = 4$ and $Z' = 2$, respectively (Table 3.10). Form IV crystallizes in the space group P with $Z' =$ 3, whereas modification form VI crystallizes in the same space group but possesses six molecules in the asymmetric unit, a rare occurrence in the CSD with less than 300 examples reported. Each FFA polymorph presents unique packing modes, as illustrated in Figure 3.23. Although the packing modes occurring in forms IV and VI are very similar, both forms present different conformations in each of the molecules of the asymmetric unit as well as have been demonstrated to coexist at room temperature which supports that form VI is not a superstructure or modulation of form IV occurring at low temperature (Figures 3.24 and 3.25) and provides additional evidence of the distinctiveness of each form. Structural elucidation of FFA form VIII will be the focus of future efforts and appears promising.

HSs analysis[30-32] was performed on each molecule in the asymmetric unit of the FFA polymorphs in order to determine the relative contribution of important intermolecular contacts (Figures 3.26-3.29) to the unique crystal packing observed in all forms. This analysis, a larger contribution of π···π contacts is observed in all the newly accessed polymorphs of FFA than in previously characterized forms I and III. Contrastingly, a larger contribution of C···H contacts is observed in form I and III, whereas C···H contacts do not contribute significantly to the HSs of all other forms of FFA that have been structurally characterized (Figures 3.26-3.29). Other intermolecular contacts, including intermolecular and intramolecular hydrogen bonding (O···H and N···H), fluctuate slightly in their relative contribution to the HSs. A larger contribution of π···π contacts (10.3 %) and F···H–C (32.0 %) contacts as well as a low contribution of F···F contacts (0.8 %) and C···H contacts (9.5 %) is observed in form II FFA; this stands in contrast to the approximately constant contribution of these intermolecular contacts to the HSs in forms I and III (Figures 3.26 and 3.28). In the case of all the newly accessed forms of FFA, ‘other’ intermolecular contacts such as the O···O, C···N, and N···H contacts generally weigh in more for conformers in forms I and III. Additionally, all conformers of form V and some conformers in form VI present a large contribution of F···C (5.2 -7.3 %) contacts when compared to all other conformers of the other forms. The distinctive appearance of the HSs and their constructed fingerprint plots highlights the unique role of different intermolecular contacts in the exclusive packing arrangements expressed in the newly accessed forms of FFA (Figures 3.26-3.29).

Polymorphs of FFA also present a nearly coplanar arrangement between the carboxyl group and the phenyl ring bearing it, τ_3. Table 3.11 lists the torsion angles (τ_1, and τ_2) between the planes defined by the biphenyl amine functionality in these seven FFA polymorphs as well as τ_3 (Figure 3.30). A conformational search of the potential energy[21,30] in a single molecule of FFA, revealed that most conformations that fall within a 1.8 kcal/mol energy window (Figure 3.30) when compared to that of the lowest energy conformation calculated in Gaussian03.

To assess the effect of these conformational and structural differences on the energies of FFA polymorphs, relative stabilities were determined experimentally. The optical absorbance of FFA in water for polymorphs I-IV and VII was monitored *in situ* over time to determine the absorbance at equilibrium at 27 °C. Polymorphs I and II slowly transformed during the experimental time frame to form III; therefore the relative free energies presented for forms I and II are a slight underestimations. This study established that form III is the thermodynamically most stable form by at least 0.3 kcal/mol among all forms examined (Table 3.12).

Enthalpies for FFA polymorphs were determined by experiment and theory. FFA forms I-III melt without transformation prior to melting whereas in forms IV-VII additional events are observed in each of the respective thermograms (Figure 3.31 and Table 3.13). According to the lattice energy calculations, form III has the greatest enthalpy among the eight polymorphs of FFA (Table 3.14) which is in accordance with the experimental enthalpies determined for polymorphs that do not undergo transformation.

3.4 Conclusions

PIHn has allowed access to and structural determination of two previously unexplored polymorphs of NA, establishing NA as a trimorphic NSAID, whereas in the case of FFA PIHn has allowed access to at least eight of its previously proposed forms, and an additional form discovered through solid-solid transformation at low temperature. While crystal structures of at least two other forms of FFA remain elusive, the presence of these forms has been confirmed through multiple characterization methods including Raman spectroscopy and PXRD for the first time. The appearance of polymorphic behavior in these TA analogues, specifically the polymorphic behavior of NA which is reported here for the first time, and the high degree of polymorphism present in FFA supports the notion that certain structural motifs are in fact privileged with regard to polymorphic propensity.

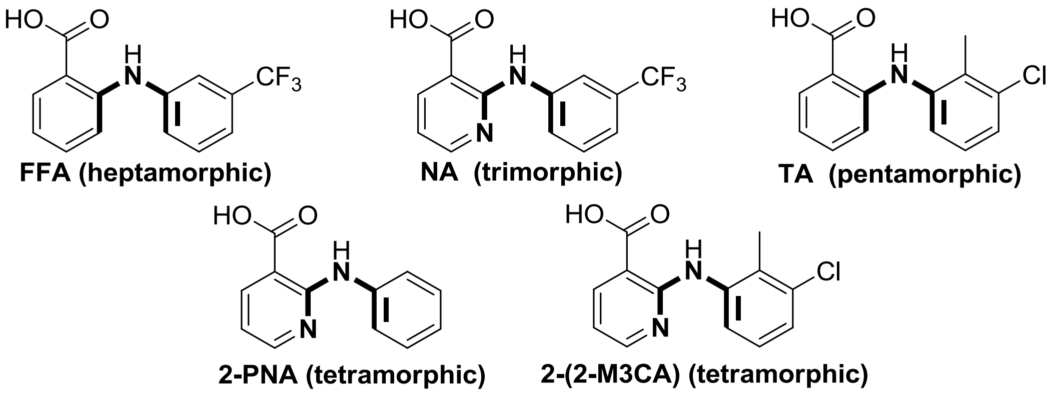

FFA (heptamorphic) **NA (trimorphic)** **TA (pentamorphic)**

2-PNA (tetramorphic) **2-(2-M3CA) (tetramorphic)**

Figure 3.1. Chemical structures of flufenamic acid (FFA), niflumic acid (NA), tolfenamic acid (TA), 2-(phenylamino)nicotinic acid (2-PNA), and 2-(2-methyl-3-chlroanilino)nicotinic acid (2-(2-M3CPA)) illustrating torsion angles (τ_1 and τ_2, in bold) differing among the forms. In parentheses, the number of structurally characterized polymorphs for each molecular structure.

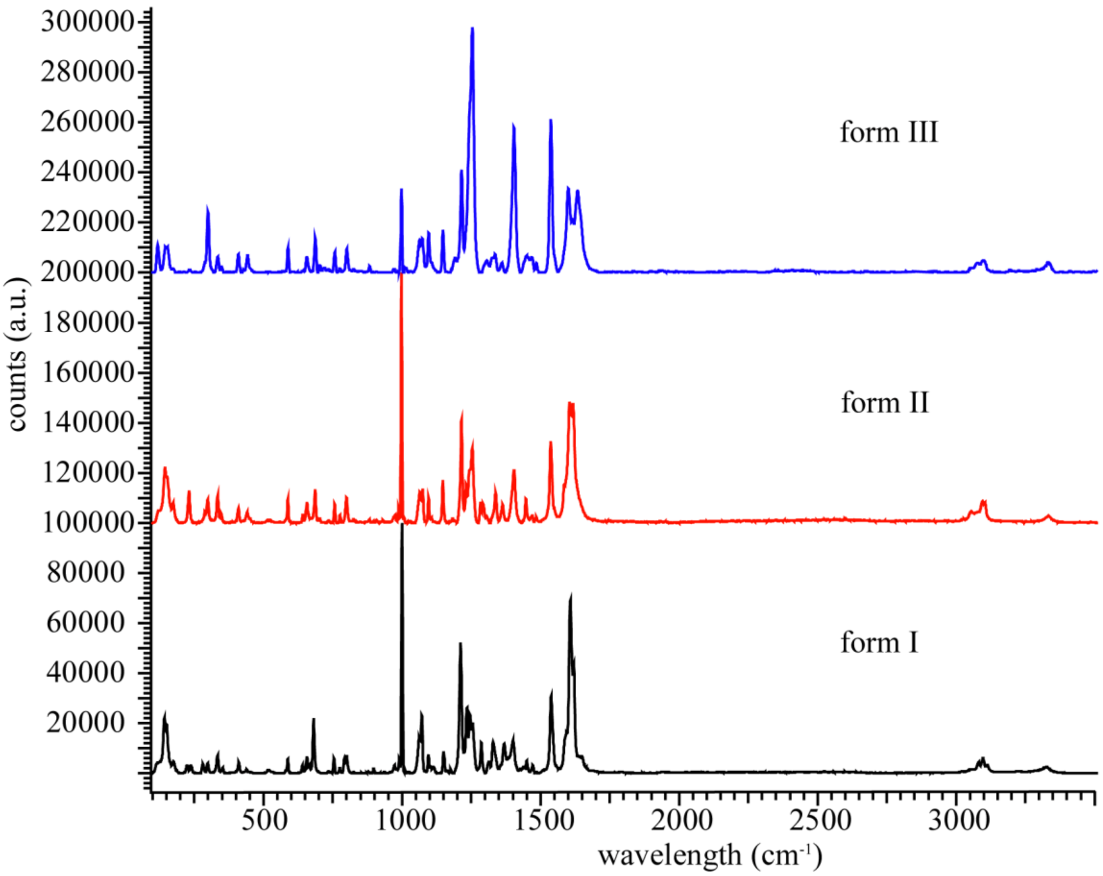

Figure 3.2. Raman spectra of NA polymorphs I-III.

Table 3.1. Frequencies of Raman vibrational modes (cm^{-1}) of NA forms I-III.

form I	form II	form III
3325	3333	3325
3113	3104	3105
3097	3095	3091
3081	3053	3037
1649	1617	1622
1620	1605	1605
1609	1587	1533
1594	1537	1473
1539	1470	1423
1473	1447	1350
1450	1404	1330
1427	1337	1322
1369	1294	1261
1329	1255	1215
1314	1215	1162
1256	1192	1152
1246	1149	1052
1235	1096	1001
1212	1075	987
1152	999	937
1096	988	863
1072	976	807
1063	970	800
1001	801	750
990	757	713
973	687	6801
801	657	617
793	589	585
755	443	523
681	410	455
657	335	442
589	300	409
412	290	347
335	233	338
283	154	253
239	145	200
177	119	145
152		121
143		
111		

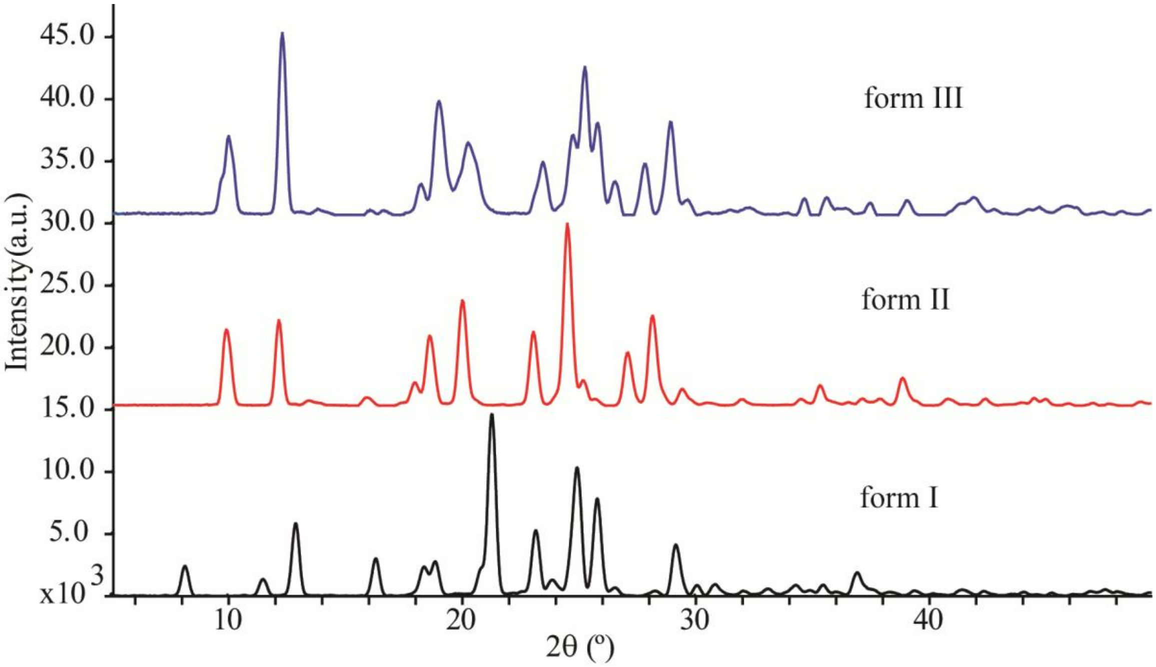

Figure 3.3. PXRD patterns of the three polymorphs of NA form I (bottom), form II (middle) and form III (top).

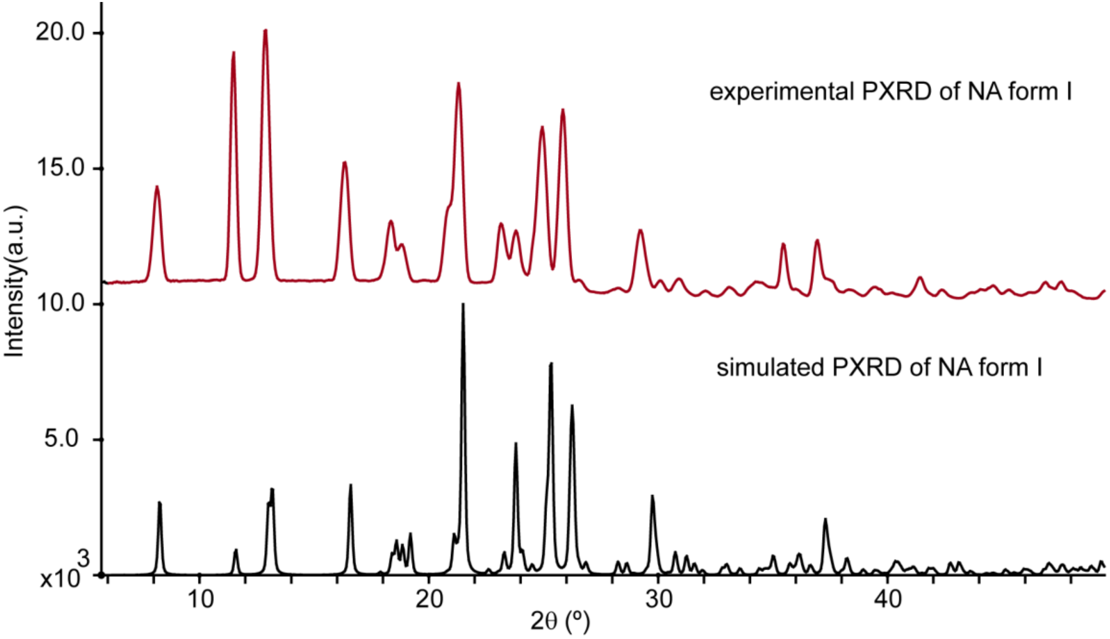

Figure 3.4. Experimental (top) and simulated (bottom) PXRD patterns for NA form I.

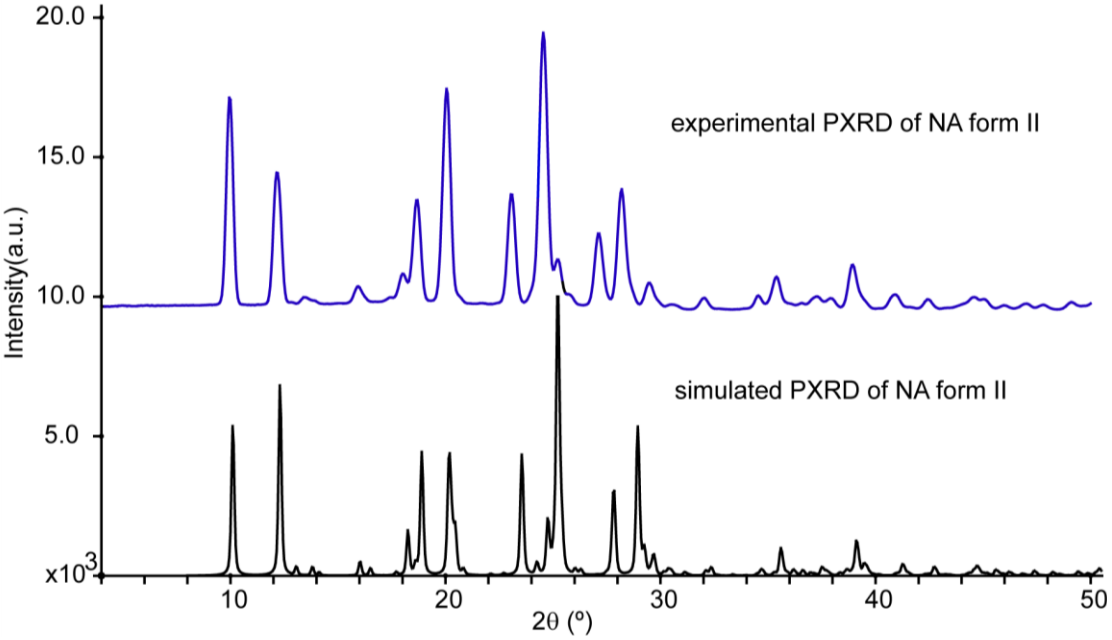

Figure 3.5. Experimental (top) and (bottom) simulated PXRD patterns for NA form II.

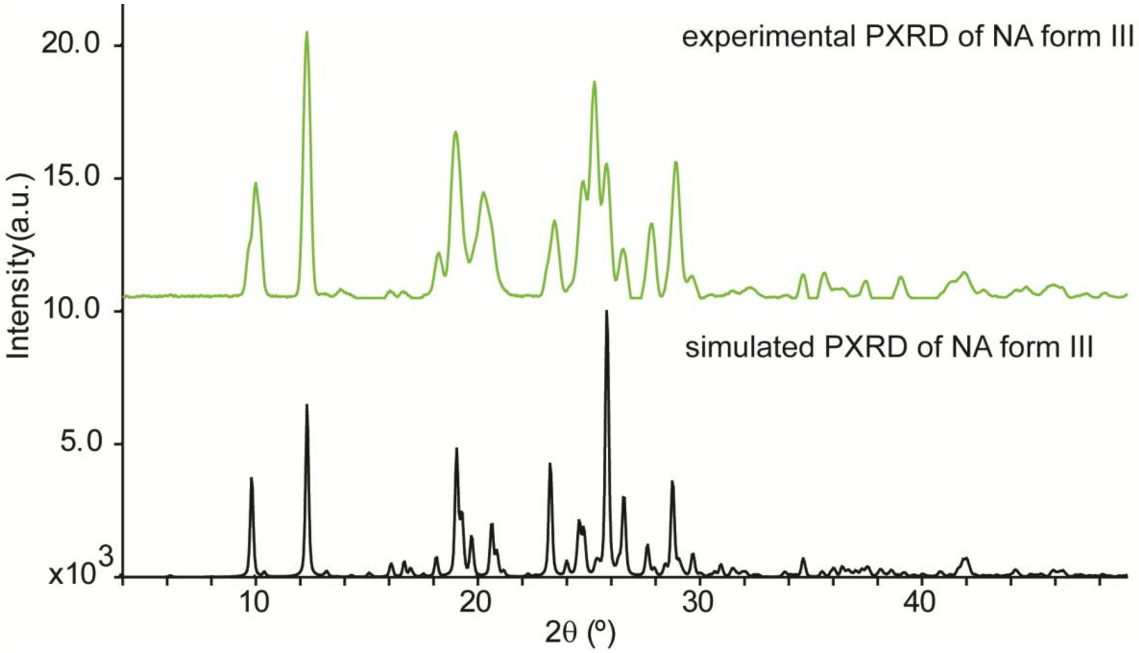

Figure 3.6. Experimental (top) and simulated (bottom) PXRD patterns for NA form III.

Table 3.2. Experimental PXRD pattern peak positions (°) and relative intensities (%) of NA forms I-III.

form I		**form II**		**form III**	
2θ	**I/I_0**	**2θ**	**I/I_0**	**2θ**	**I/I_0**
8.1	12.1	9.9	42.9	10.1	42.8
12.9	25.5	12.2	100.0	12.3	100.0
16.3	15.1	15.9	3.2	13.8	3.3
18.4	21.4	16.6	2.5	16.1	2.7
18.8	20.8	18.6	16.1	16.6	2.4
20.8	12.1	20.0	65.3	18.2	17.0
21.3	100.0	20.1	41.7	19.0	62.8
23.1	19.7	23.4	26.9	20.3	39.9
24.9	73.5	24.5	41.3	23.5	29.9
25.8	49.7	25.2	74.3	24.7	44.1
29.2	22.6	25.7	47.0	25.2	81.8
30.9	6.4	26.6	12.8	25.8	50.7
32.1	2.7	27.1	28.6	26.5	18.4
3.1	2.9	28.2	49.6	27.8	28.1
37.0	8.9	29.7	2.8	28.9	51.3
44.1	3.0	32.3	3.1	29.6	8.3
45.3	3.0	34.6	9.9	30.5	1.4
49.5	3.1	35.4	9.8	31.5	2.7
		36.3	2.2	32.3	4.0
		37.4	7.1	33.9	1.1
		38.9	11.6	34.6	8.9
		41.9	7.4	35.6	9.5
		42.4	1.2	36.4	3.7
		44.6	3.0	37.5	6.4
		45.9	4.2	39.0	7.9
		48.3	1.6	41.4	6.3
				41.9	9.6
				42.8	3.1
				44.7	4.3
				45.9	5.0
				47.4	1.7
				48.2	2.0

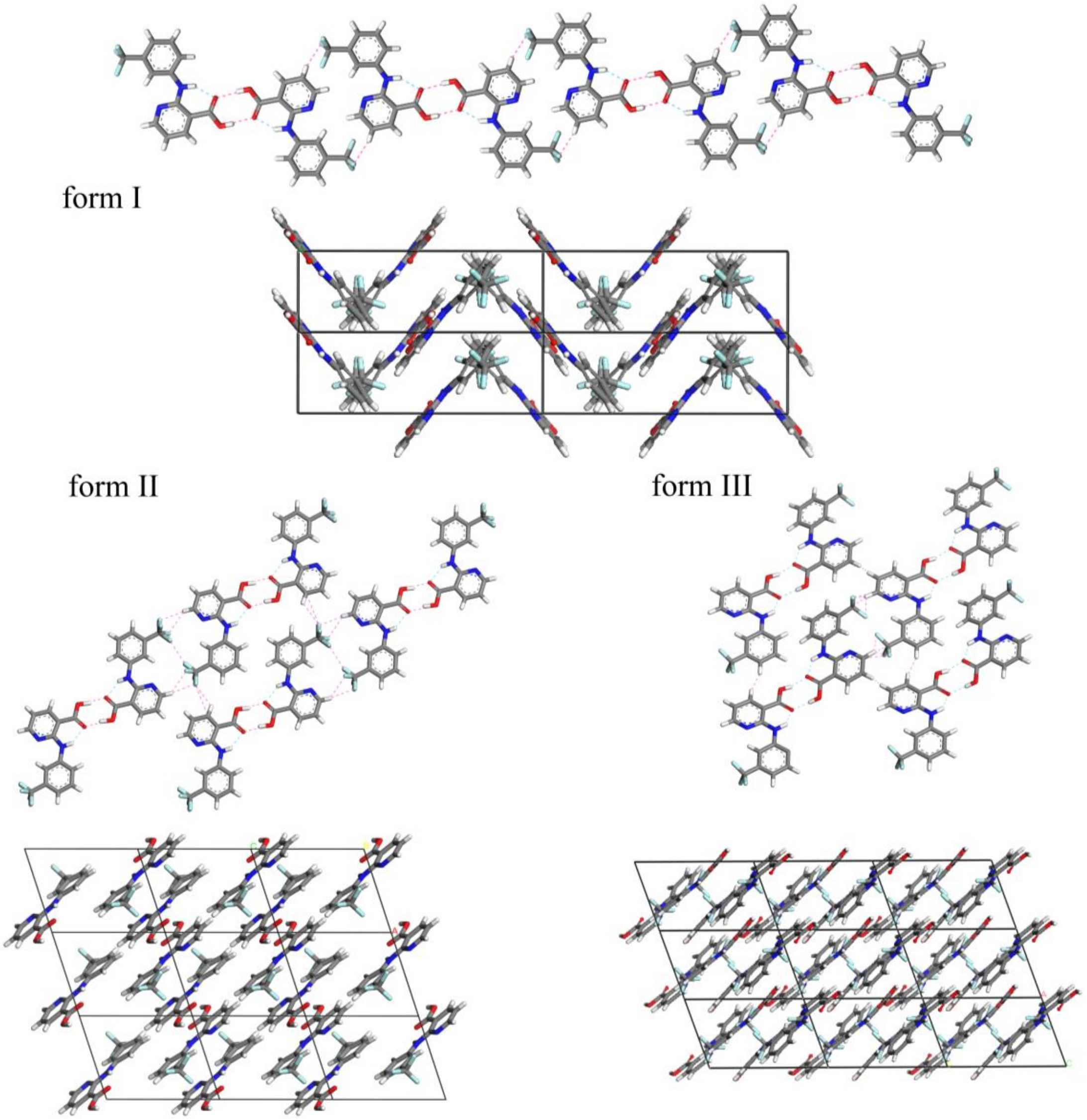

Figure 3.7. Molecular packing and hydrogen bonding motifs of NA polymorphs; (a) hydrogen bonded dimers form sheets viewed along the *a*-axis in form I, (b) form II, and (c) form III. Form II represents 50% occupancy of the disorder present in the –CF_3 group.

Table 3.3. Crystallographic data for polymorphs of NA forms I-III.

form	**I**	**II**	**III**
crystal system	monoclinic	triclinic	triclinic
space group	$P2_1/c$	$P\bar{1}$	$P\bar{1}$
temperature (K)	95	95	95
a (Å)	5.06965(9)	7.2820(8)	7.2979(5)
b (Å)	14.9555(3)	9.2997(11)	11.7962(7)
c (Å)	15.6229(3)	9.3603(10)	14.6142(9)
α (°)	90.00	100.807(7)	83.517(3)
β (°)	102.0620(10)	105.022(7)	80.234(4)
γ (°)	90.00	102.282(7)	69.533(3)
cell volume (Å^3)	1158.4	578.0	1159.6
calc. density (g/cm)	1.618	1.621	1.212
Z	4	2	4
Z'	1	1	2
M (Cu-Kα, Å)	1.54187	1.54187	1.54187
R$_f$ (%)	3.09	7.68	13.85

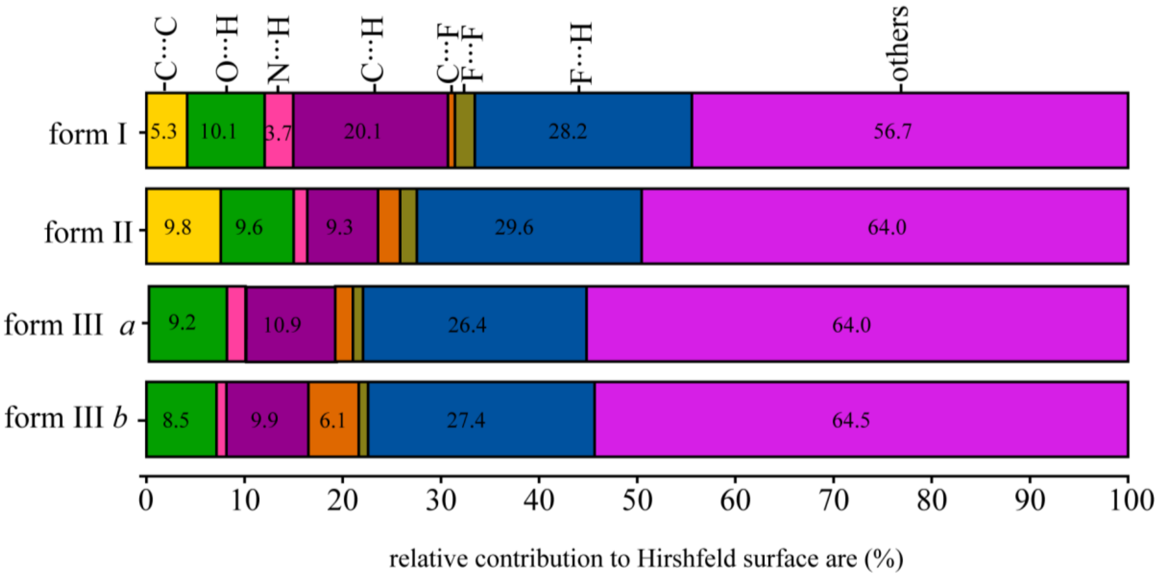

Figure 3.8. Percent relative contribution to the HSs of the important intermolecular interactions present in each molecule of the asymmetric unit of the NA polymorphs I-III. The letters *a* and *b* represent different conformers for structures where *Z*´ > 1.

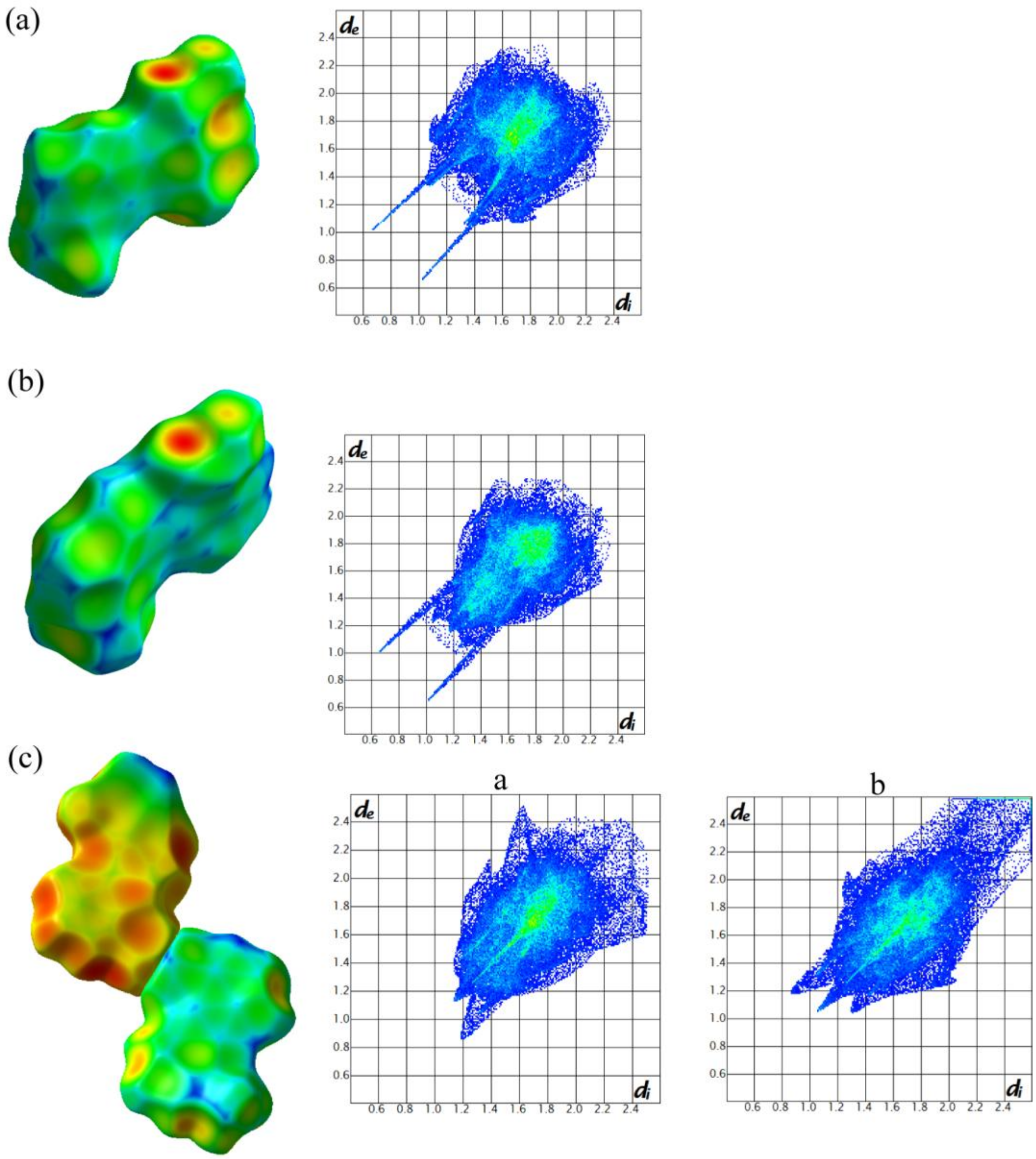

Figure 3.9. Hirshfeld surfaces (left) and fingerprint plots (right) of NA polymorphs (a) form I, (b) form II, and (c) form III. Letters *a* and *b* represent different conformers in the structures where $Z' > 1$.

Table 3.4. Measured torsion angles (τ_1, τ_2 , and τ_3) for molecules in the asymmetric unit of the different NA polymorphs along with the difference in the relaxed potential energy (ΔE_{conf}) among the experimentally determined conformations for each analogue and the lowest energy conformation calculated in Gaussian03. Letters *a* and *b* represent different conformers in the structure where *Z´* > 1.

polymorph	**τ_1(°)**	**τ_2(°)**	**τ_3(°)**	**ΔE_{conf} (kcal/mol)**
NA I	-6.46	-5.26	-0.08	0.4
NA II	-8.08	6.42	2.77	0.4
NA III *a*	9.02	-7.31	5.75	0.3
NA III *b*	-6.12	1.83	-5.52	0.3

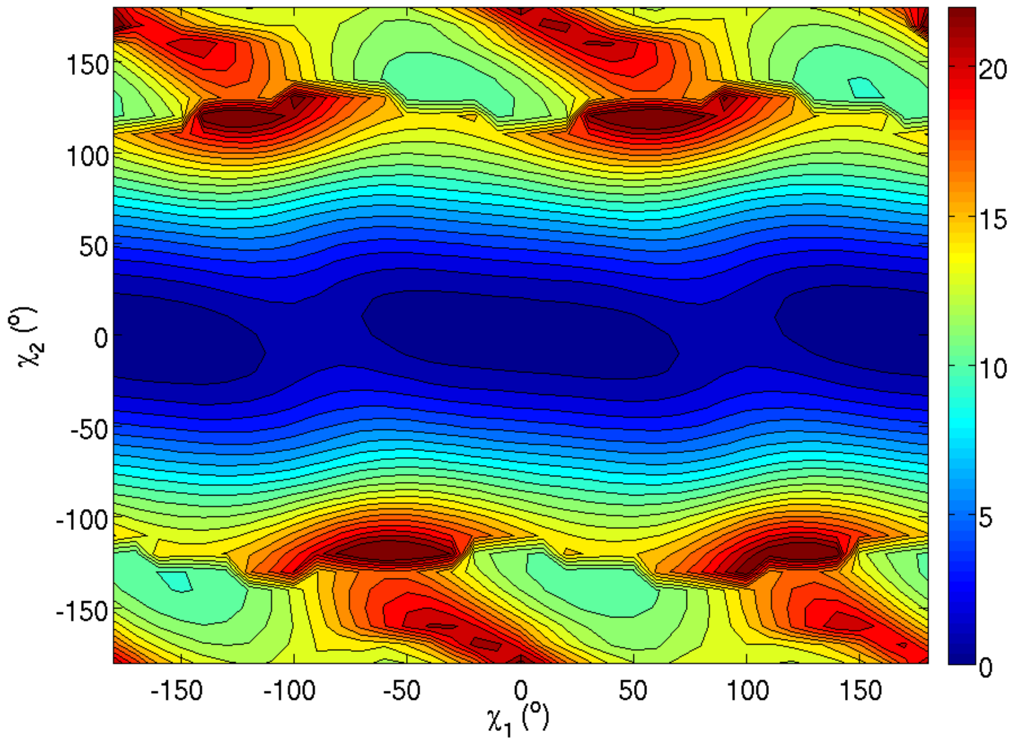

Figure 3.10. Conformational analysis of NA. Conformations present in structurally characterized polymorphs of NA are listed in Table 3.4.

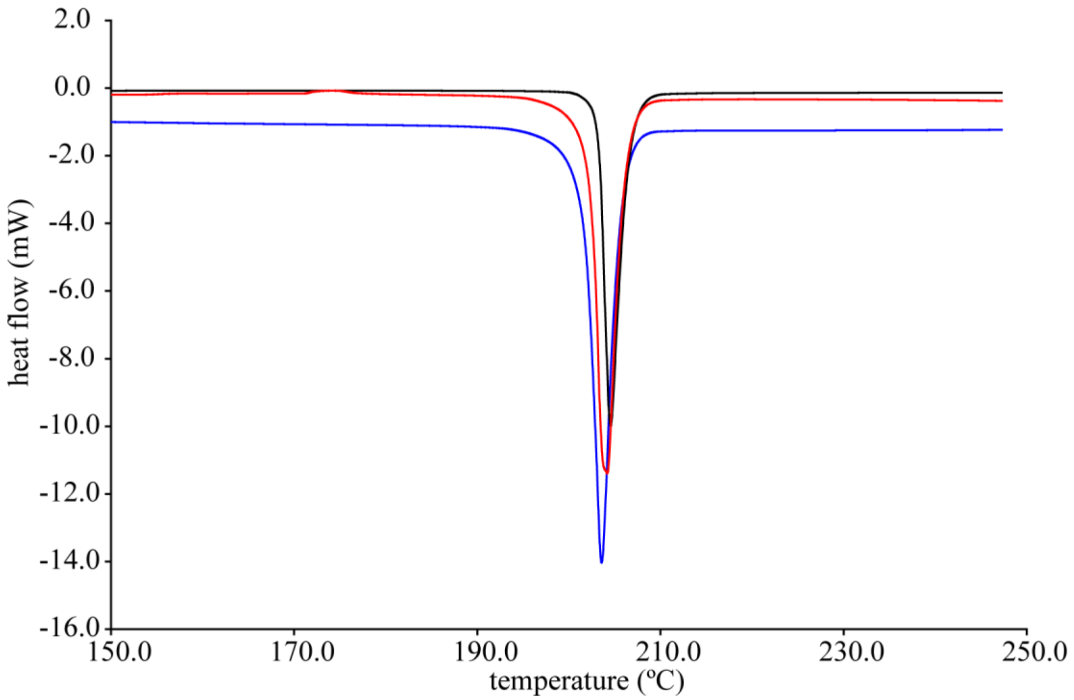

Figure 3.11. Thermograms of NA polymorphs: form I (black), form II (red), and form III (blue).

Table 3.5. Summary of DSC data for NA polymorphs I-III.

initial form	**T_m (°C)**	**ΔH_{fus} (kcal/mol)**
I	204.6	9.1
II	204.2*	8.1*
III	203.1	8.7

*In cases where transformation is observed the first melting endotherm and its respective enthalpy are listed.

Table 3.6. Lattice energy for structurally characterized polymorphs of NA from calculations in Material Studio using Compass force field.

form	**U_{latt} Free Cell (kcal/mol)**	**ΔU_{latt} Free Cell (kcal/mol)**
I	-66.8	0.0
II	-65.3	1.4
III	-65.2	1.6

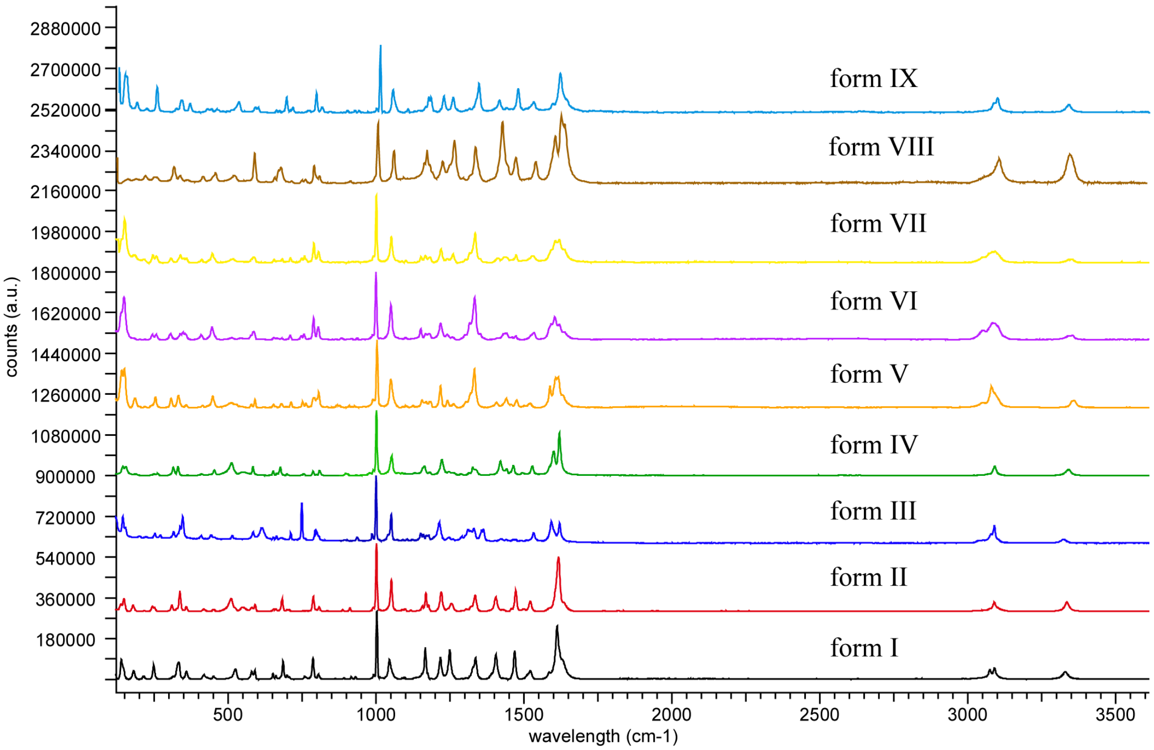

Figure 3.12. Raman spectra of FFA polymorphs I-IX.

Table 3.7. Frequencies of Raman vibrational modes (cm^{-1}) of FFA forms I-IX.

form I	form II	form III	form IV	form V	form VI	form VII	form VIII	form IX
3329	3335	3322	3334	3360	3353	3323	3338	3330
3326	3089	3103	3088	3080	3085	3104	3085	3328
3088	1635	3089	3081	1615	1655	3090	3052	3088
3074	1617	1621	1633	1587	1620	1621	1620	3080
3055	1586	1602	1616	1521	1604	1604	1604	3075
2985	1521	1599	1583	1475	1591	1533	1533	1610
1673	1472	1593	1521	1439	1532	1472	1439	1468
1664	1458	1331	1472	1407	1472	1349	1431	1404
1630	1405	1321	1404	1332	1441	1329	1352	1335
1612	1384	1212	1335	1217	1353	1323	1334	1174
1593	1335	1152	1254	1181	1334	1260	1219	1166
1583	1320	1051	1220	1155	1218	1214	1176	1145
1468	1292	1000	1168	1049	1181	1161	1151	1002
1438	1254	800	1051	1012	1150	1070	1050	786
1404	1221	794	1002	1003	1101	1051	999	685
1337	1168	712	911	993	1049	1000	805	590
1327	1157	442	806	908	999	986	788	578
1249	1099	252	787	868	937	800	757	525
1218	1051	200	682	805	881	748	584	145
1166	1001	144	591	751	789	615	445	115
1136	990	120	510	712	756	584	148	
1097	912		449	679	747	522		
1045	886		337	652	710	514		
1003	807		310	589	654	441		
992	787		178	511	588	347		
805	763		148	447	583	270		
787	682		115	413	543	252		
764	653			331	511	200		
686	591			306	445	144		
651	578			253	409	121		
590	509			184	347			
525	485			149	305			
359	449			139	257			
333	358				147			
330	336				138			
181	309							
145	243							
140	215							
115	178							
	147							
	114							

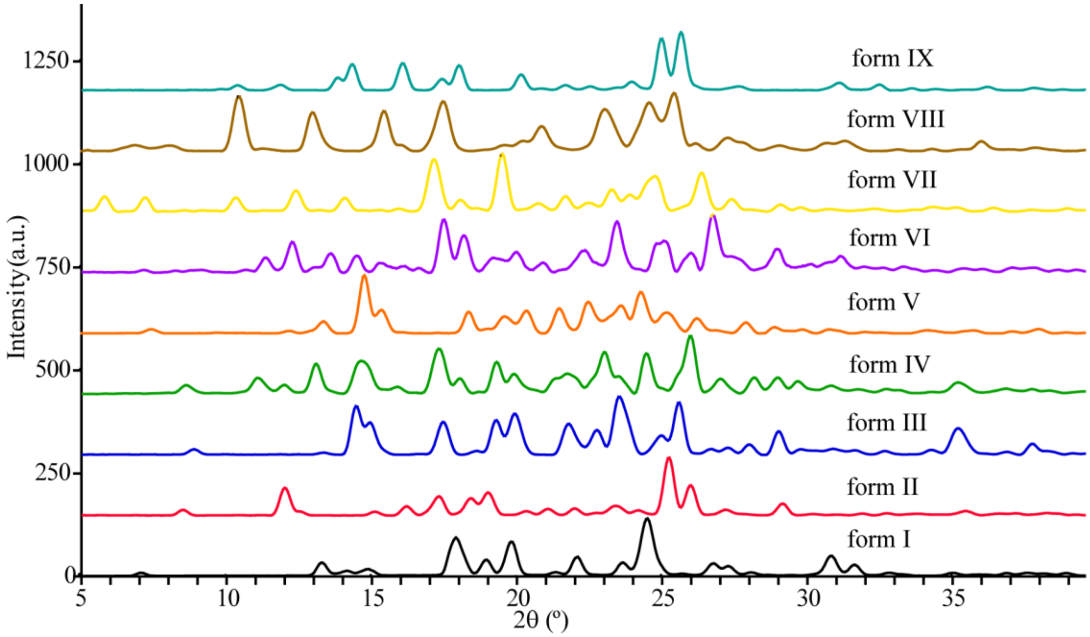

Figure 3.13. PXRD patterns of FFA polymorphs I-IX.

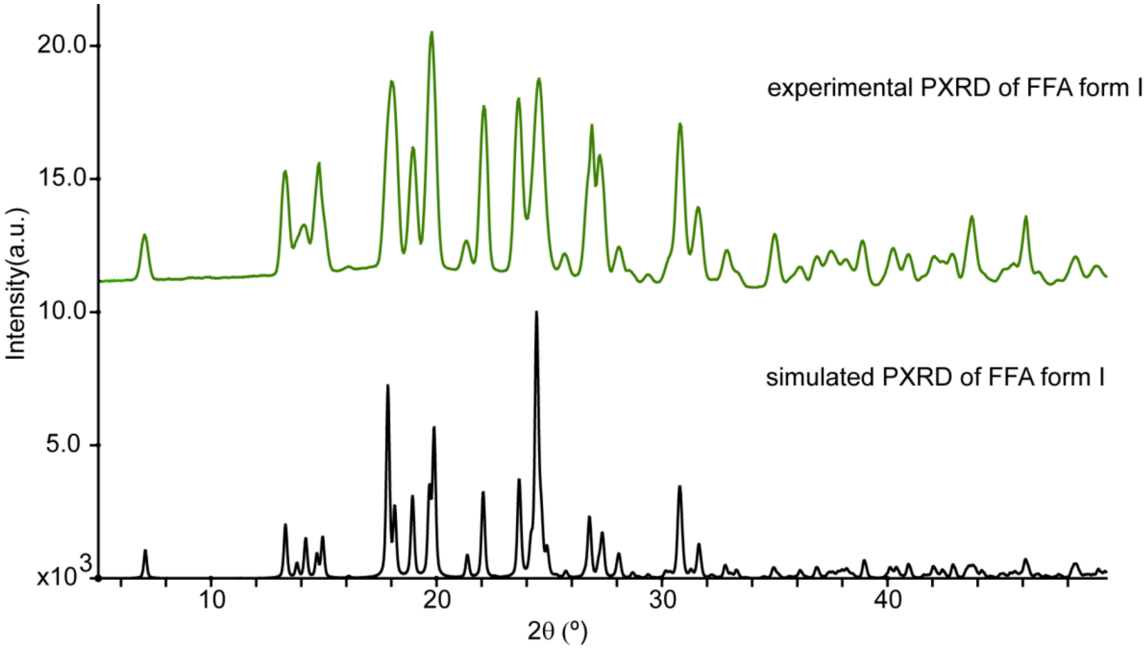

Figure 3.14. Experimental (top) and simulated (bottom) PXRD patterns for FFA form I.

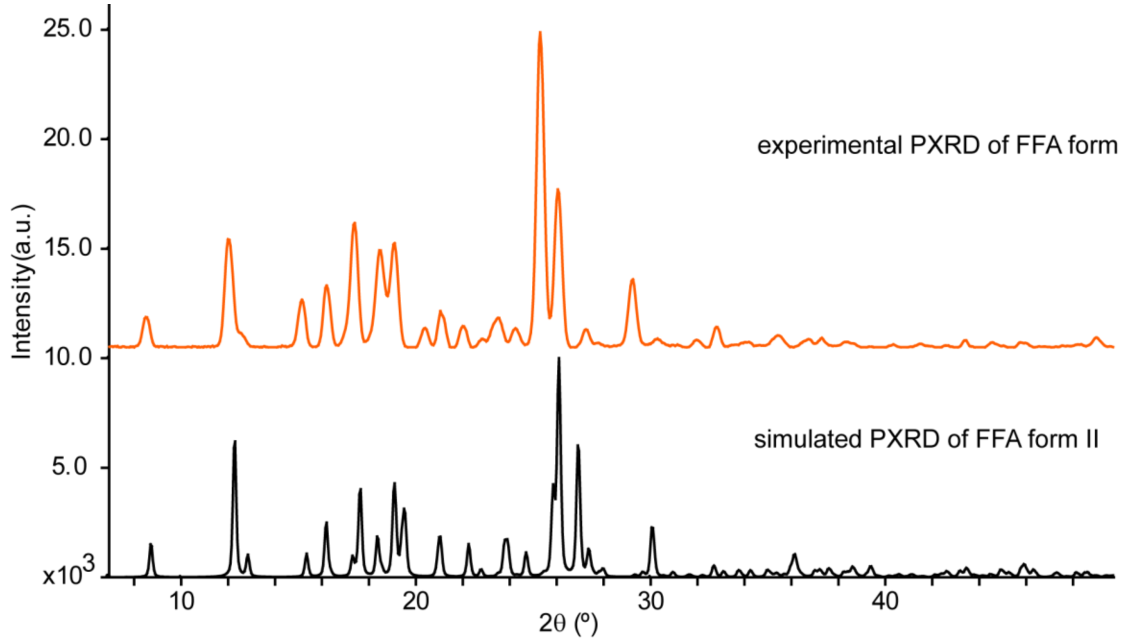

Figure 3.15. Experimental (top) and simulated (bottom) PXRD patterns for FFA form II.

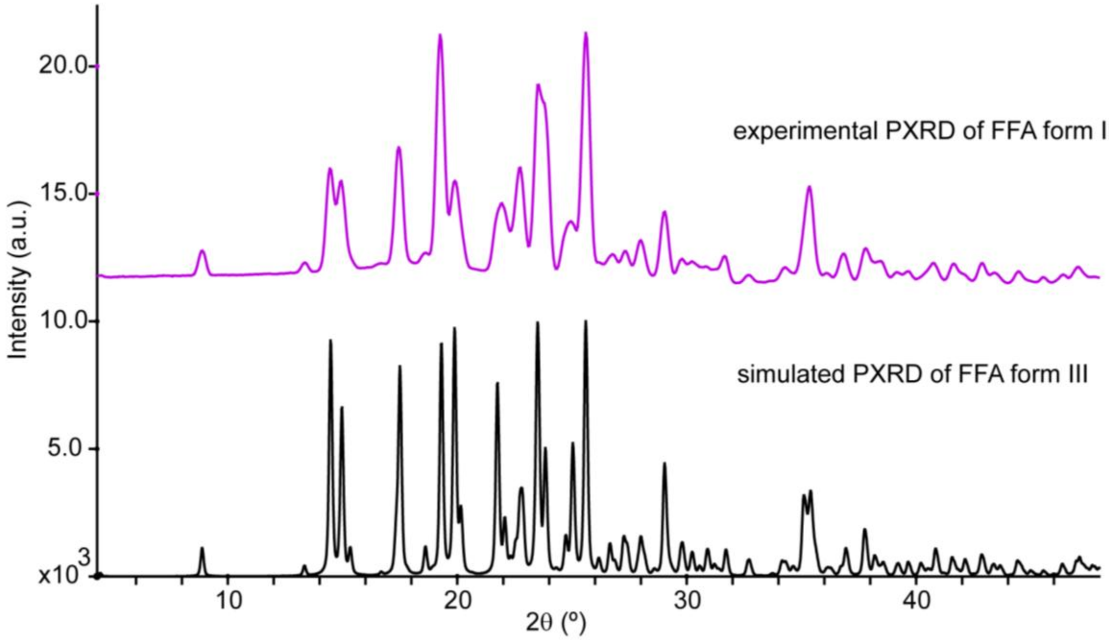

Figure 3.16. Experimental (top) and simulated (bottom) PXRD patterns for FFA form III.

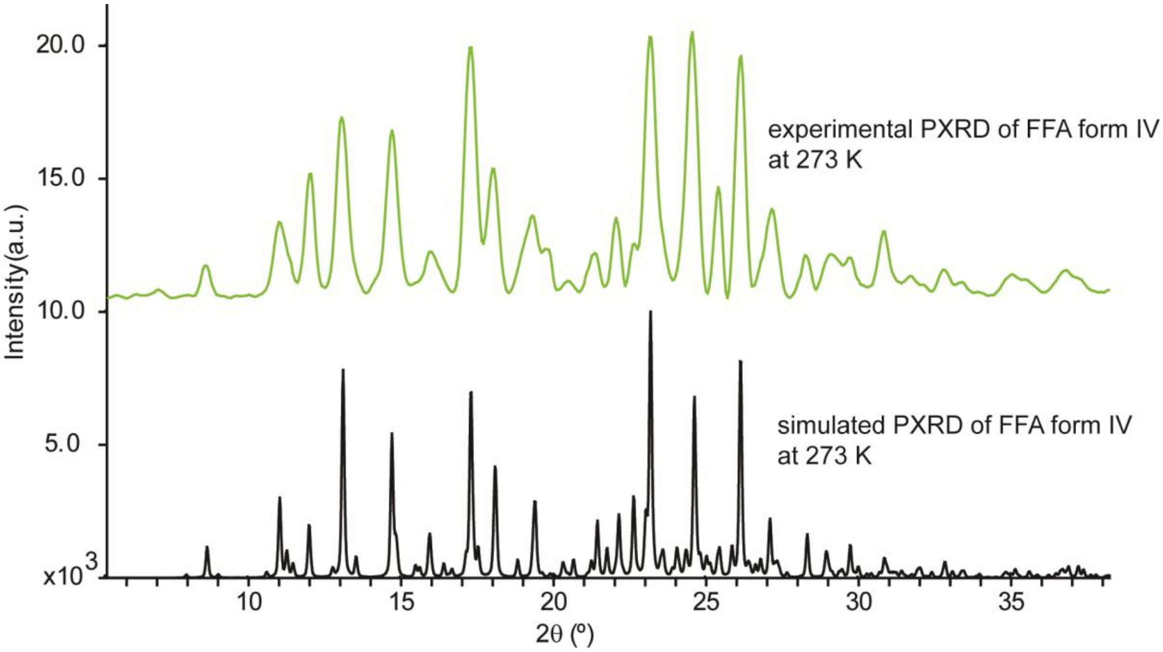

Figure 3.17. Experimental (top) and simulated (bottom) PXRD patterns for FFA form IV.

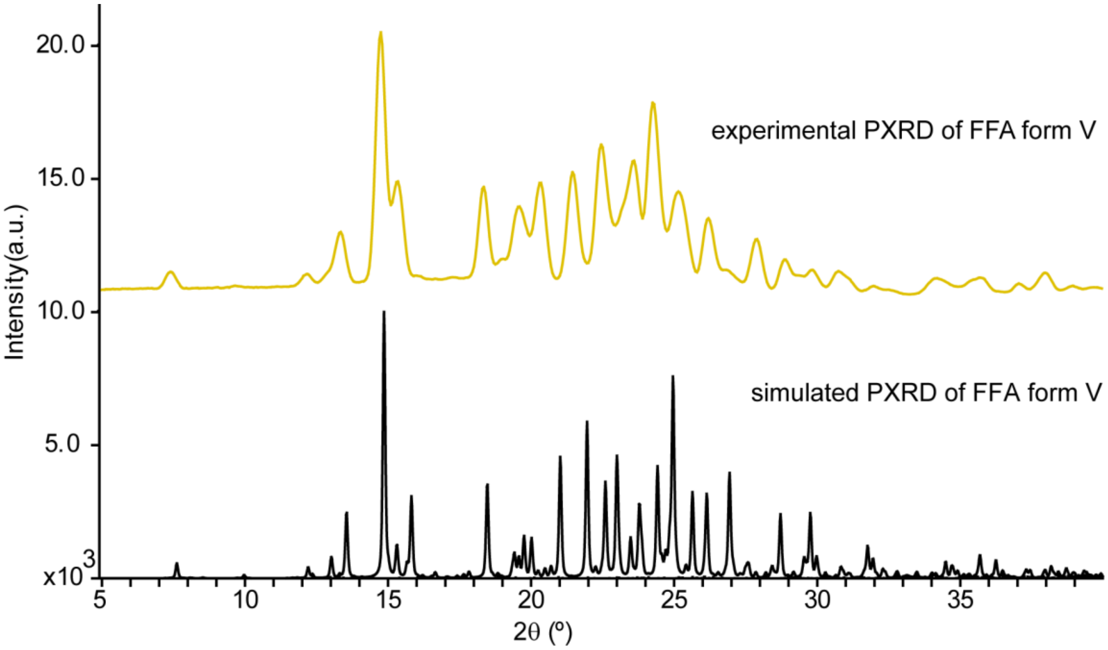

Figure 3.18. Experimental (top) and simulated (bottom) PXRD patterns for FFA form V.

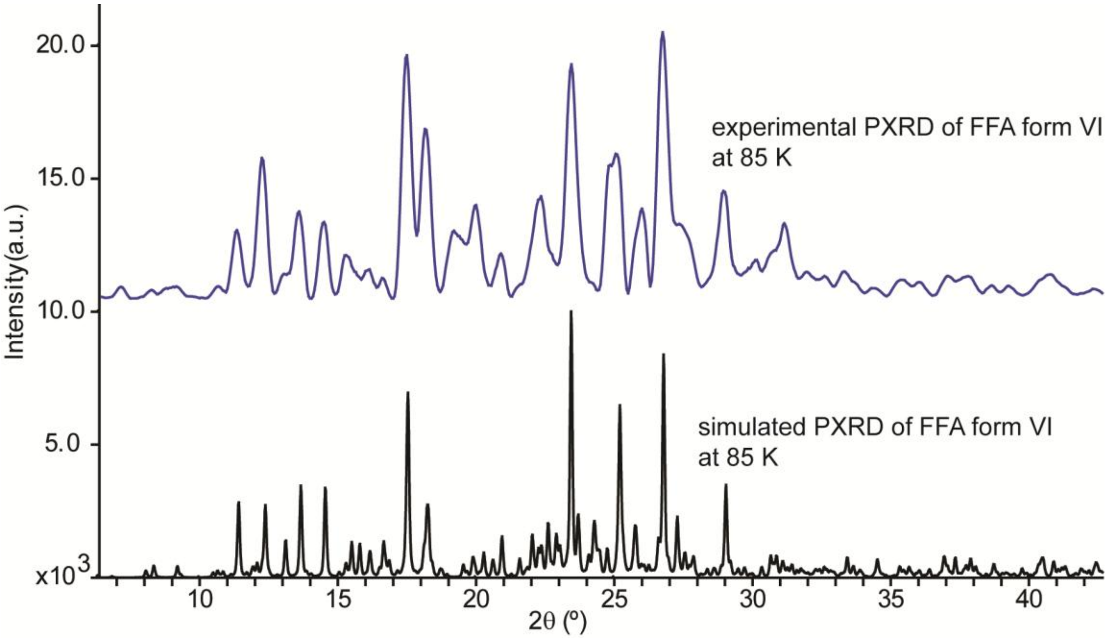

Figure 3.19. Experimental (top) and simulated (bottom) PXRD patterns for FFA form VI.

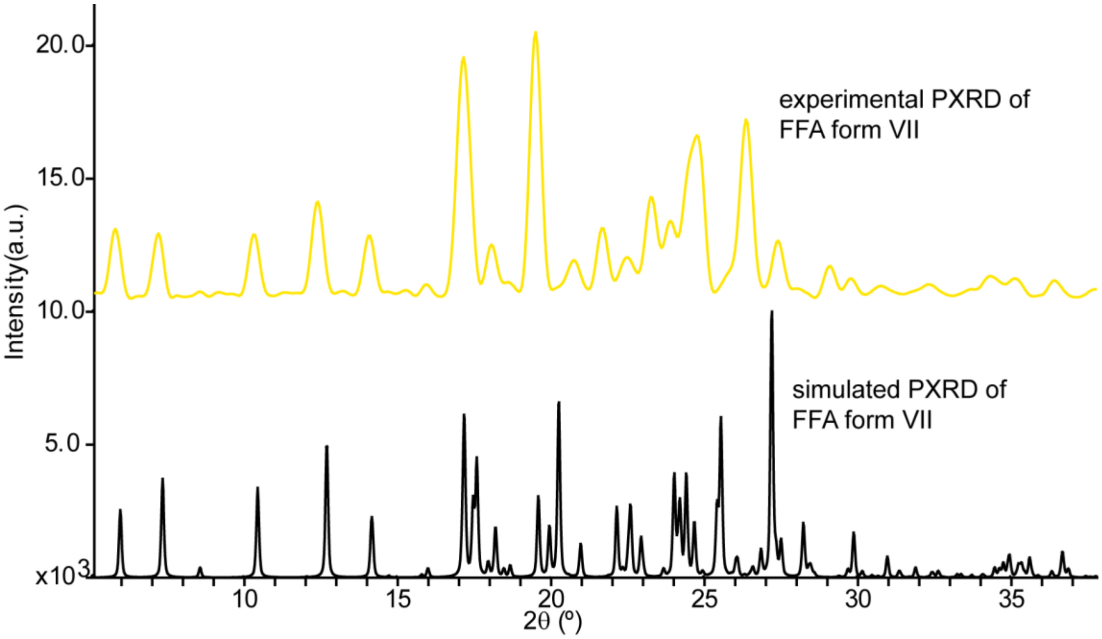

Figure 3.20. Experimental (top) and simulated (bottom) PXRD pattern for FFA form VII.

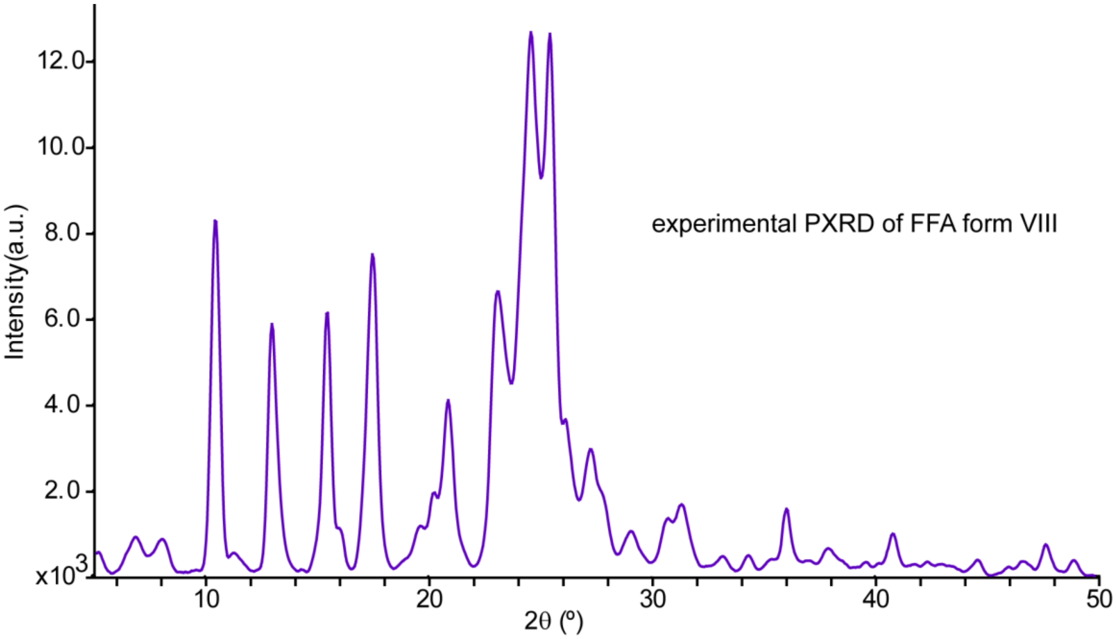

Figure 3.21. Experimental PXRD pattern for FFA form VIII.

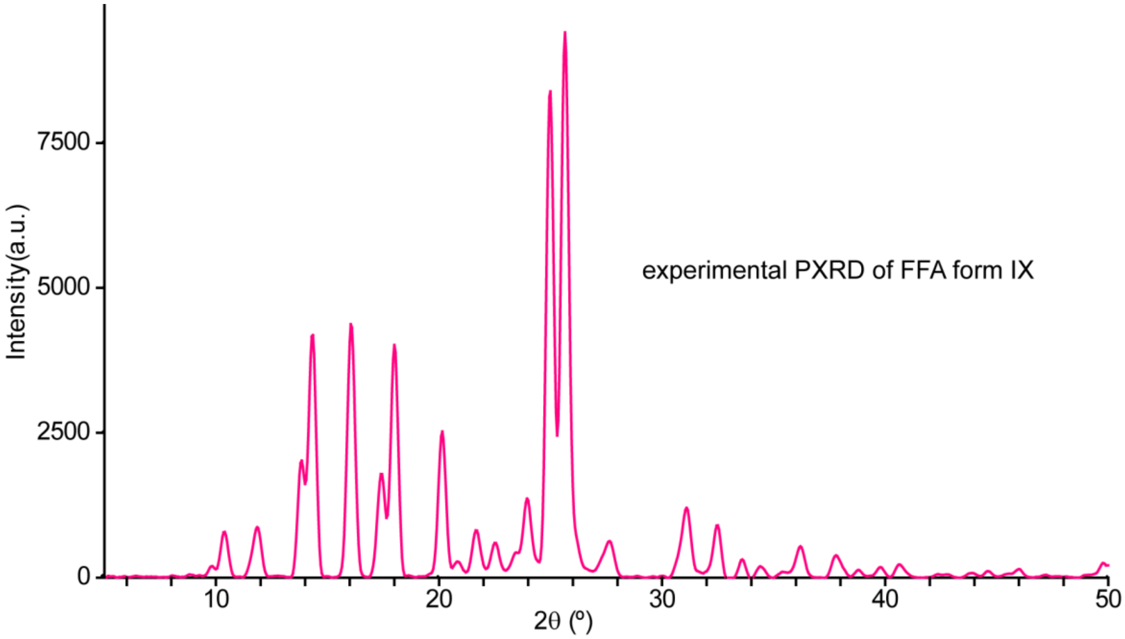

Figure 3.22. Experimental PXRD pattern for FFA form IX.

Table 3.8. Experimental PXRD pattern peak positions (°) and relative intensities (%) of FFA structurally characterized forms I-V.

form I		**form II**		**form III**		**form IV**		**form V**	
2θ	**I/I_0**	**2θ**	**I/I_0**	**2θ**	**I/I_0**	**2θ**	**I/I_0**	**2θ**	**I/I_0**
7.0	17.0	8.5	9.4	8.9	9.0	8.6	12.3	7.4	6.8
13.3	41.2	12.0	33.8	13.3	3.7	11.1	25.4	12.2	3.7
17.9	77.9	15.1	14.9	14.5	39.5	12.0	11.6	13.3	20.3
18.9	50.7	16.2	19.5	17.4	48.1	13.1	58.1	14.7	100.0
19.8	100.0	20.4	6.7	19.3	96.1	14.7	48.0	15.3	37.3
22.1	69.2	21.1	12.1	19.9	36.4	15.9	13.9	18.3	33.1
23.6	73.1	22.0	7.5	21.9	28.3	17.2	63.1	19.6	21.8
24.5	81.1	23.5	10.3	22.7	43.5	18.0	30.5	20.3	24.1
25.7	7.9	24.3	7.2	23.6	78.7	19.3	32.5	21.5	39.7
26.9	66.1	25.3	100.0	25.0	22.2	20.4	2.4	22.5	47.9
29.4	3.0	26.1	50.8	25.8	100.0	21.3	17.6	23.6	41.4
30.8	69.6	27.2	6.3	26.8	9.6	22.1	9.9	24.3	65.0
31.6	33.3	29.2	20.3	27.3	11.1	23.1	92.2	25.2	32.2
32.9	15.4	30.3	2.0	28.0	15.8	24.5	82.0	26.2	22.4
35.0	21.7	32.0	2.0	29.0	28.2	26.0	100.0	27.9	18.5
37.5	8.1	33.0	6.2	29.9	9.1	27.0	19.4	28.9	9.5
38.0	5.2	34.1	1.5	31.5	10.6	28.2	18.0	29.8	3.8
38.9	14.9	35.4	3.4	35.3	39.6	28.9	10.3	30.8	6.7
43.7	27.6	36.7	2.1	36.8	11.9	29.6	14.0	32.0	2.2
46.1	30.7	37.3	2.6	37.8	14.3	30.8	11.2	34.2	4.7
48.3	11.7	38.4	1.7	38.3	8.8	31.9	3.7	35.7	4.7
49.2	6.3	40.3	0.9	40.7	8.1	32.8	5.1	37.0	2.6
		41.5	1.1	41.7	7.9	33.1	4.3	38.0	6.7
		43.4	2.2	42.9	8.2	35.0	4.6	38.9	1.4
		44.6	1.6	43.3	4.1	36.7	6.2	41.3	2.3
		45.9	1.6	44.5	4.7	37.2	5.0	42.6	3.0
		49.0	3.0	45.5	2.3	39.4	2.3	43.9	4.4
				46.3	3.1	40.6	2.4		
				47.0	6.2	41.9	1.6		
				48.7	6.4	43.4	2.0		

Table 3.9. Continuation of the experimental PXRD pattern peak positions (°) and relative intensities (%) of FFA structurally characterized forms VI-VIII and the structurally elusive form IX.

form VI		**form VII**		**form VIII**		**form IX**	
2θ	**I/I_0**	**2θ**	**I/I_0**	**2θ**	**I/I_0**	**2θ**	**I/I_0**
10.7	4.2	5.8	33.8	6.7	5.7	9.9	1.9
11.3	25.5	7.2	28.9	8.0	5.3	10.4	8.2
12.3	52.7	8.5	3.2	10.4	74.0	11.8	9.1
13.6	32.6	9.2	2.5	13.0	51.1	13.9	22.1
14.5	28.6	10.3	26.9	15.4	52.4	14.3	44.7
15.3	16.1	12.4	38.1	17.5	62.3	16.1	46.0
16.1	10.8	14.1	24.8	20.9	28.3	17.4	18.7
17.5	91.4	15.3	2.1	23.1	52.2	18.0	42.9
18.2	63.6	16.0	4.7	24.6	100.0	20.1	26.5
19.2	25.3	17.2	88.3	25.4	98.3	20.8	3.0
20.0	35.0	18.1	16.0	27.2	23.0	21.8	8.7
20.9	16.7	19.5	100.0	29.1	4.3	22.5	6.3
22.4	38.3	20.7	10.4	30.7	6.5	23.5	4.7
23.5	88.0	21.7	21.8	31.3	10.4	24.0	14.3
25.1	54.3	22.5	6.5	33.1	2.4	25.0	89.2
26.0	33.6	23.3	30.4	34.3	2.8	25.6	100.0
26.8	100.0	23.9	19.4	36.0	10.6	27.6	6.5
27.4	27.1	24.8	58.4	38.0	3.0	31.1	12.4
29.0	40.3	26.4	63.3	40.8	6.3	32.5	9.5
30.1	14.3	27.4	18.0	44.6	2.6	33.6	3.2
31.2	28.1	29.1	11.7	46.6	1.8	34.4	1.9
32.0	9.8	29.8	6.4	47.7	4.6	36.2	5.6
32.6	8.2	30.8	2.8	48.9	2.5	37.8	4.0
33.3	10.0	32.3	3.5			38.8	1.4
34.4	3.7	34.3	7.4			39.8	1.8
35.4	6.9	35.1	7.0			40.7	2.4
36.0	6.0	36.4	6.0			43.9	0.9
37.1	8.3	37.8	2.5			44.6	1.2
37.8	8.2	39.0	3.9			45.9	1.5
38.7	4.7	40.3	2.1				
39.3	4.6	41.5	6.7				
40.8	8.9	43.8	1.0				
42.4	3.4	44.8	2.8				
43.2	3.6	45.9	1.4				
44.2	2.2	48.5	2.2				

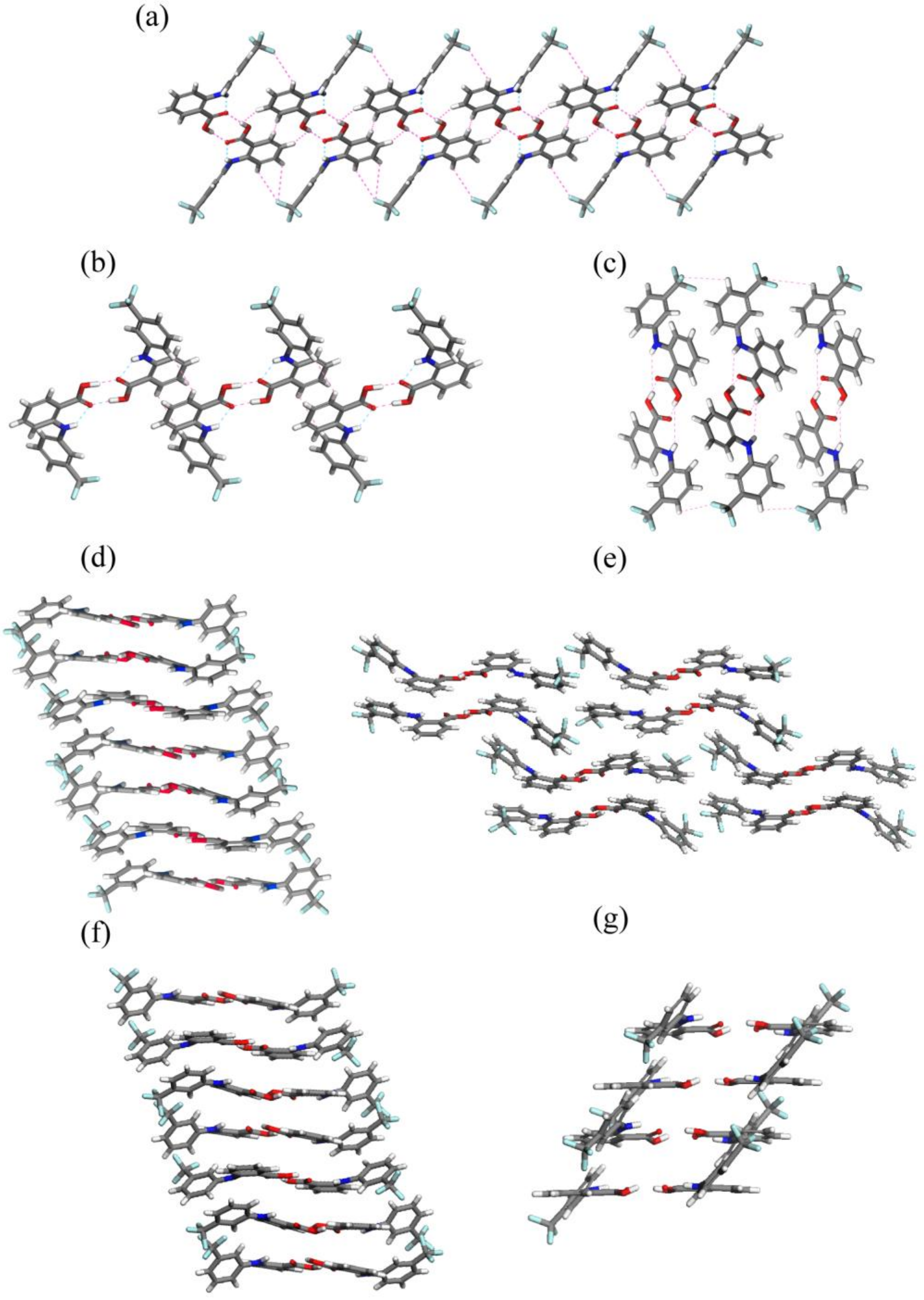

Figure 3.23. Molecular packing and hydrogen bonding motifs of FFA polymorphs; (a) form I viewed along the *a*-axis, (b) form II viewed along the *a*-axis, (c) form III viewed along the *a*-axis, (d) form IV viewed along the *a*-axis, (e) form V viewed along the *b*-axis, (f) form VI viewed along the *a*-axis, and (g) form VII viewed along the *b*-axis.

Table 3.10. Crystallographic data for polymorphs of FFA forms I-VII.

form	**I**	**II**	**III**	**IV**	**V**	**VI**	**VII**
crystal system	monoclinic	monoclinic	monoclinic	triclinic	monoclinic	triclinic	monoclinic
space group	$P2_1$/c	$P2_1$/c	$C2$/c	$P\bar{1}$	$P2_1$/c	$P\bar{1}$	$P2_1$/c
temperature (K)	300	95	300	273	95	85	85
***a* (Å)**	12.523(4)	10.8816(6)	39.84	8.7589(2)	26.6592(18)	8.6485(2)	14.9687(14)
***b* (Å)**	7.868(6)	10.2483(5)	5.10	11.6629(3)	7.9007(2)	11.5115(2)	20.641(2)
***c* (Å)**	12.874(3)	11.7535(6)	12.24	20.0229(14)	23.2430(5)	38.895(3)	7.9486(8)
***α* (°)**	90	90	90	80.632(6)	90	87.914(6)	90
***β* (°)**	95.2(2)	111.270(3)	92.47	81.041(6)	94.084(7)	85.910(6)	98.316(7)
***γ* (°)**	90	90	90	73.534(5)	90	72.260(5)	90
cell volume (Å^3)	1263.27	1221.44	2488.57	1922.3	4883.2	3678.32	2430.1
calc. density (g/cm^3)	1.470	1.529	-	1.458	1.530	1.523	1.537
Z	4	4	8	6	16	12	8
Z´	1	1	1	3	4	2	2
M (Cu-Kα, Å)	1.54187	1.54187	1.54187	1.54187	1.54187	1.54187	1.54187
R$_f$ (%)	7.40	10.04	4.90	5.42	7.27	16.13	10.11

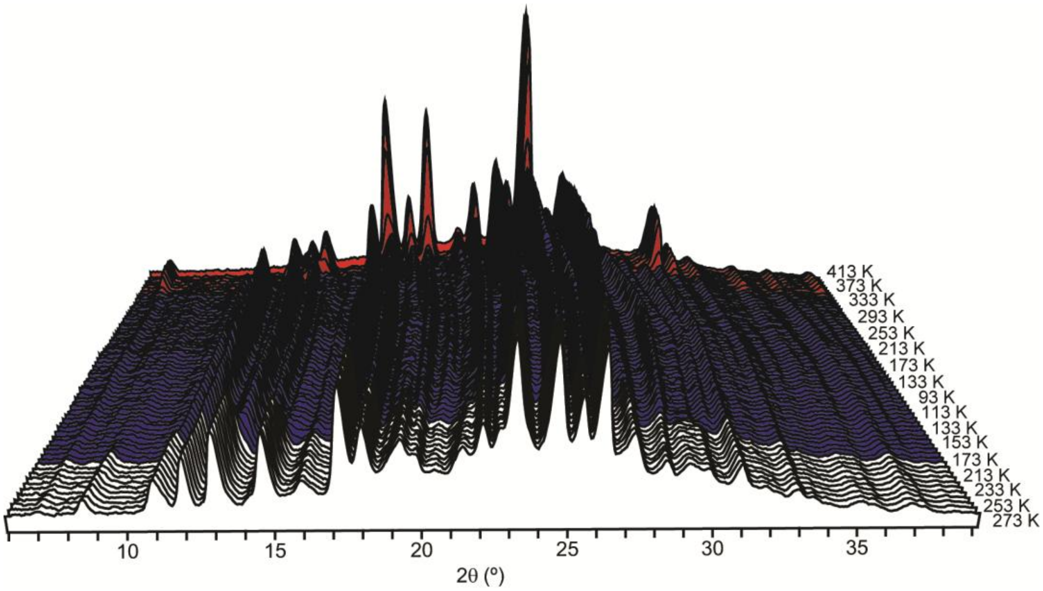

Figure 3.24. VTPXRD overlay of FFA form IV cooled 273-95 K and then heated from 95-413 K, showing transformation to form VI around 140 K (~ -130 °C, in blue) prior to transformation to form I (in red) and then melting.

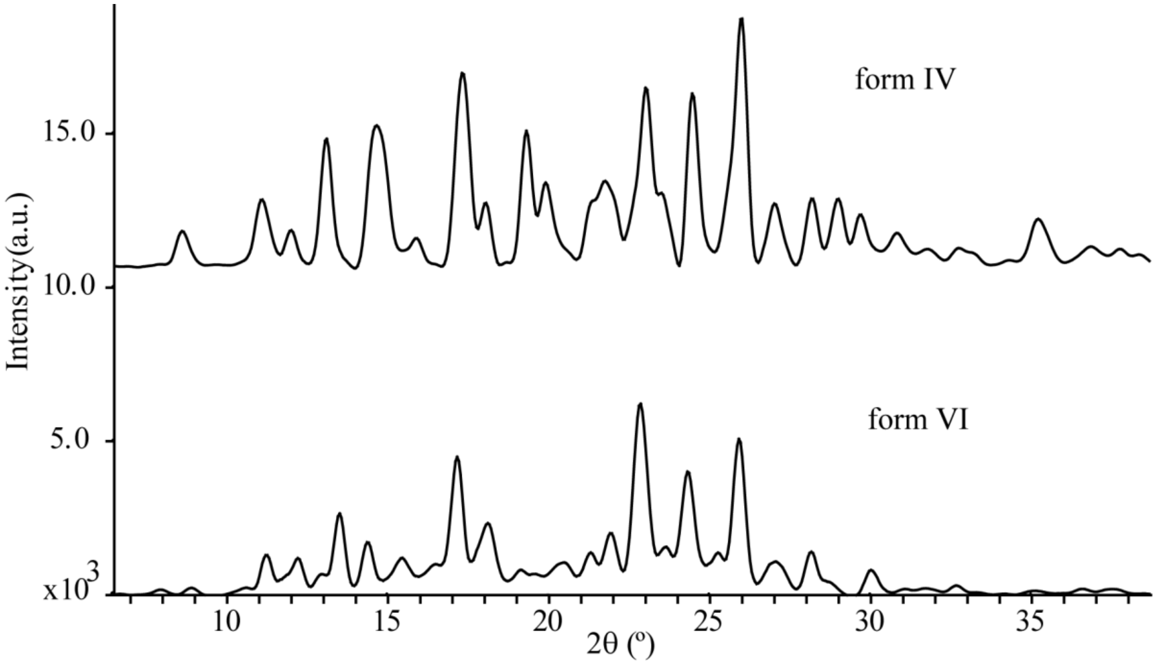

Figure 3.25. Experimental PXRD patterns of FFA form VI (bottom) and form IV (top) at room temperature.

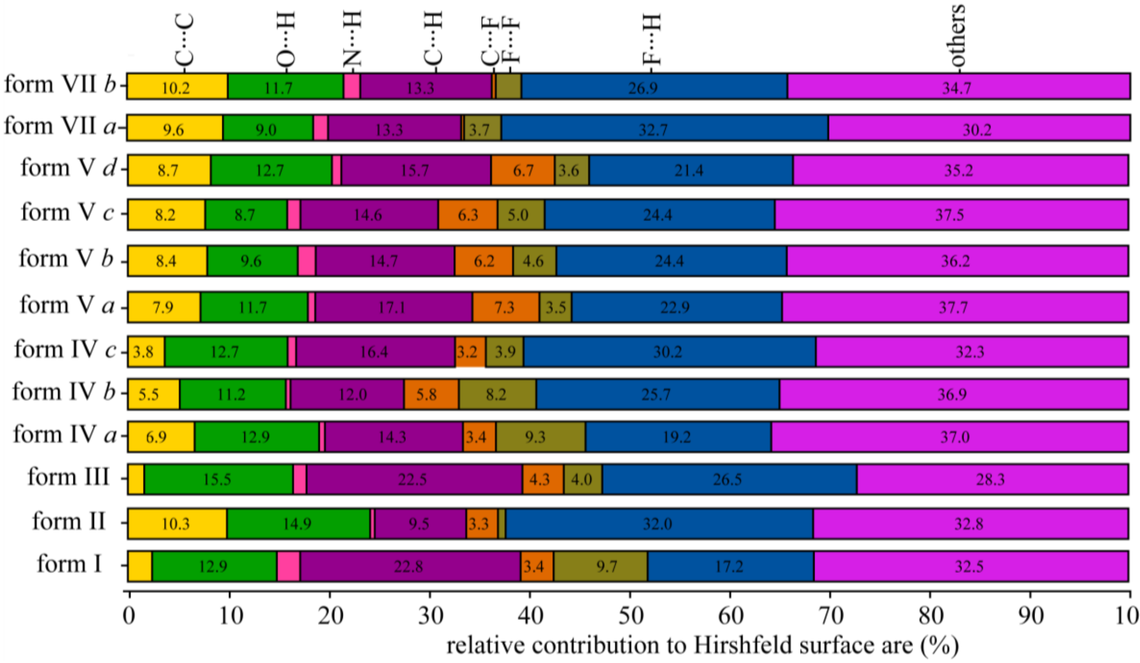

Figure 3.26. Percent relative contribution to the HSs of the important intermolecular interactions present in each molecule of the asymmetric unit of the FFA polymorphs I-V and VII. The letters *a*, *b*, c, and *d* represent different conformers in the structures where $Z' > 1$.

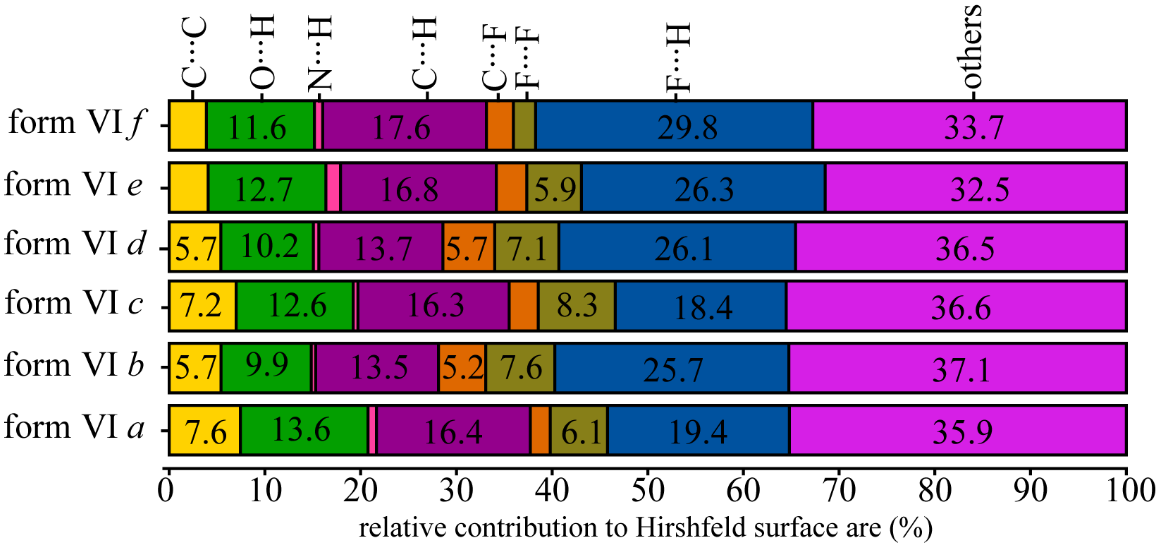

Figure 3.27. Percent relative contribution to the HSs of the important intermolecular interactions present in each molecule of the asymmetric unit of FFA polymorph VI. The letters *a*, *b*, c, *d*, *e* and *f* represent different conformers in this structure.

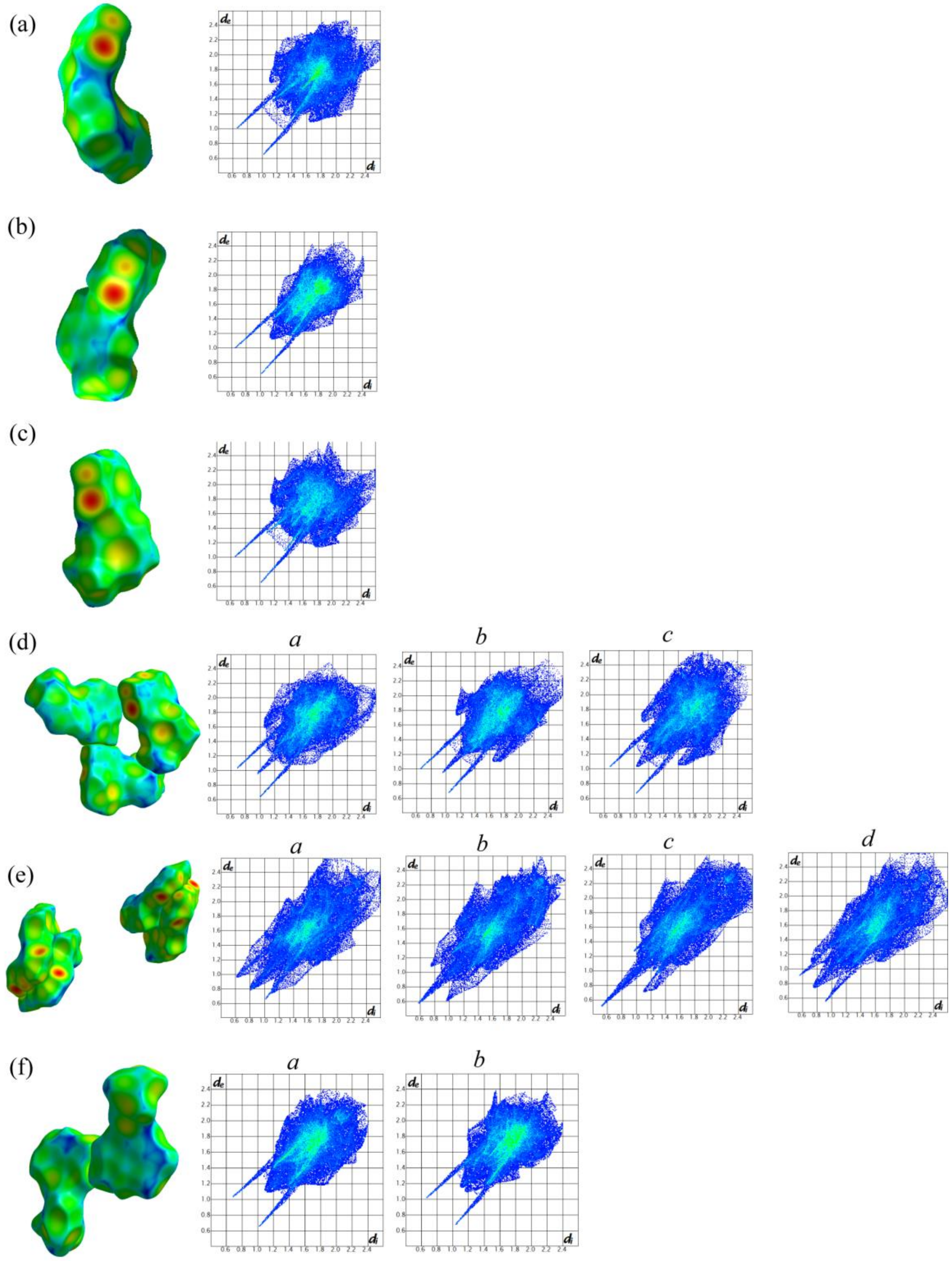

Figure 3.28. Hirshfeld surfaces (left) and fingerprint plots (right) of FFA polymorphs (a) form I, (b) form II, (c) form III, (d) form IV, and (e) form V. Letters *a*, *b*, *c*, and *d* represent different conformers in the structures where $Z' > 1$.

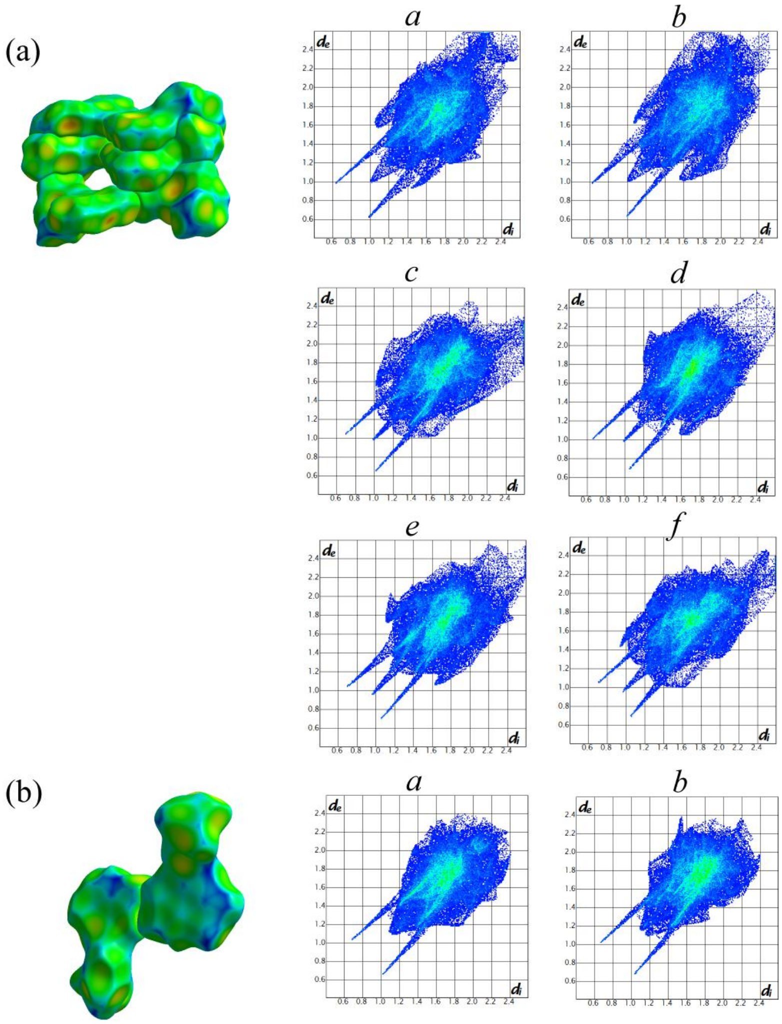

Figure 3.29. Hirshfeld surfaces (left) and fingerprint plots (right) of FFA polymorphs; (a) form VI and (b) form VII. The letters *a*, *b*, c, *d*, *e* and *f* represent different conformers in the structures where *Z´* > 1.

Table 3.11. Measured torsion angles (τ_1, τ_2 , and τ_3) for molecules in the asymmetric unit of the different FFA polymorphs along with the difference in the relaxed potential energy (ΔE_{conf}) among the experimentally determined conformations for each analogue and the lowest energy conformation calculated in Gaussian03. Letters *a, b, c, d, e,* and *f* represent different conformers in the structures where $Z' > 1$.

polymorph	**τ_1(°)**	**τ_2(°)**	**τ_3(°)**	**ΔE_{conf} (kcal/mol)**
FFA I	1.76	53.94	0.51	1.8
FFA II	-13.75	-42.69	-0.13	1.1
FFA III	37.09	8.72	0.60	0.4
FFA IV *a*	-22.53	-35.91	4.59	0.7
FFA IV *b*	16.77	28.83	-0.28	0.8
FFA IV *c*	12.84	41.82	-2.28	1.1
FFA V *a*	-26.54	-28.95	-1.71	0.4
FFA V *b*	-9.99	-37.67	5.58	1.1
FFA V *c*	-30.87	-27.77	-2.11	0.4
FFA V *d*	-13.17	-40.14	-3.60	1.1
FFA VI *a*	-12.39	-40.70	10.04	1.1
FFA VI *b*	15.44	37.53	-3.37	0.9
FFA VI *c*	-16.04	-27.56	4.17	1.1
FFA VI *d*	24.70	33.59	-4.20	0.8
FFA VI *e*	-22.95	-35.59	-12.09	0.7
FFA VI *f*	19.87	24.50	-0.46	1.3
FFA VII *a*	-14.81	-42.85	-2.10	1.1
FFA VII *b*	10.97	42.11	-2.81	1.1

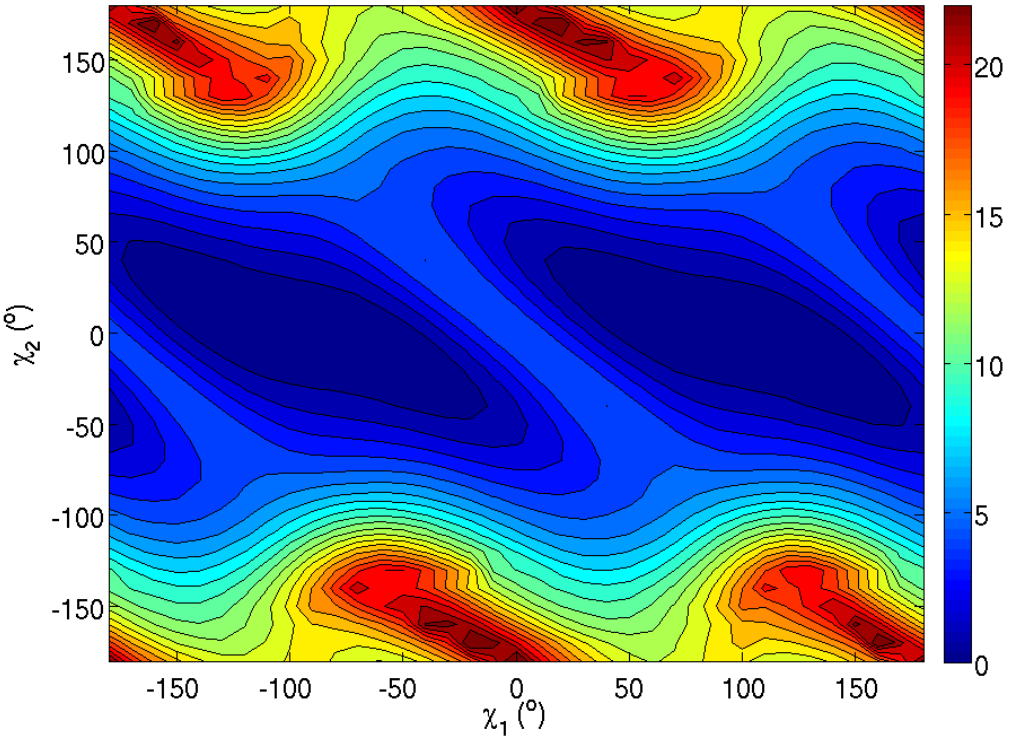

Figure 3.30. Conformational analysis in FFA. Conformations present in structurally characterized polymorphs of FFA are listed in Table 3.11.

Table 3.12. Difference in free energy, Δ(ΔG), of FFA polymorphs I-VI, VI, and VII calculated from mean absorbance at equilibrium ($\lambda_{max.}$= 288 nm, 300 ± 1 K).

form	**Δ(ΔG) (kcal/mol)**
I	0.04*
II	0.11*
III	0.00
IV	0.17
V	–
VI	0.18
VII	0.25

*Polymorphs I and II slowly transformed during the experimental time frame to form III, therefore the free energies presented in this table are a slight underestimation of the free energies due to polymorphic transformation.

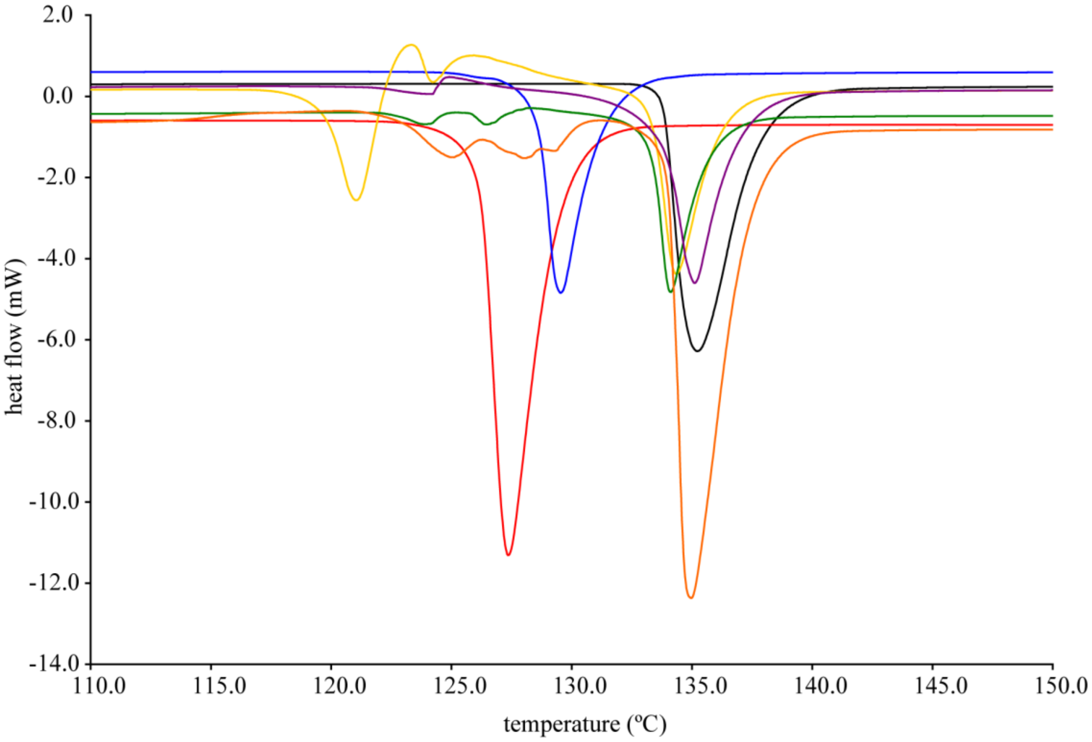

Figure 3.31. Thermograms of FFA polymorphs: form I (black), form II (red), form III (blue), form IV (green), form V (orange), form VI (purple), and form VII (yellow).

Table 3.13. Summary of DSC data for FFA polymorphs I-VII.

initial form	T_m (°C)	ΔH_{fus} (kcal/mol)
I	134.5	6.6
II	129.6	5.9
III	127.4	7.1
IV	123.9	5.4
V	124.9	5.8
VI	124.2	5.9
VII	120.7	5.2

Table 3.14. Lattice energy for structurally characterized polymorphs of FFA from calculations in Material Studio using Compass force field.

form	U_{latt} Free Cell (kcal/mol)	ΔU_{latt} Free Cell (kcal/mol)
I	-41.4	0.3

II	-41.5	0.2
III	-41.6	0.0
IV	-40.5	1.1
V	-40.1	1.5
VI	-40.5	1.2
VII	-41.1	0.5

3.5 References

1. Brittain, H. G.; *Polymorphism in Pharmaceutical Solids*; M. Dekker: New York, **1999**.
2. Bernstein, J.; *Polymorphism in Molecular Crystals*; Oxford University Press: Oxford Clarendon Press, New York, **2002**.
3. McCrone, W. C.; *Physics and Chemistry of the Organic Solid State*; Interscience Publishers, London, **1965**.
4. Lang, M. D.; Grzesiak, A. L.; Matzger, A. J., The use of polymer heteronuclei for crystalline polymorph selection. *Journal of the American Chemical Society* **2002,** 124, (50), 14834-14835.
5. Price, C. P.; Grzesiak, A. L.; Matzger, A. J., Crystalline polymorph selection and discovery with polymer heteronuclei. *Journal of the American Chemical Society* **2005,** 127, (15), 5512-5517.
6. López-Mejías, V.; Kampf, J. W.; Matzger, A. J., Polymer-Induced Heteronucleation of Tolfenamic Acid: Structural Investigation of a Pentamorph. *Journal of the American Chemical Society* **2009,** 131, (13), 4554.
7. Porter, W. W.; Elie, S. C.; Matzger, A. J., Polymorphism in carbamazepine cocrystals. *Crystal Growth & Design* **2008,** 8, (1), 14-16.
8. Lutker, K. M.; Matzger, A. J., Crystal Polymorphism in a Carbamazepine Derivative: Oxcarbazepine. *Journal of Pharmaceutical Sciences* 99, (2), 794-803.
9. Grzesiak, A. L.; Matzger, A. J., Selection and discovery of polymorphs of platinum complexes facilitated by polymer-induced heteronucleation. *Inorganic Chemistry* **2007,** 46, (2), 453-457.
10. Lutker, K. M.; Tolstyka, Z. P.; Matzger, A. J., Investigation of a privileged polymorphic motif: A dimeric ROY derivative. *Crystal Growth & Design* **2008,** 8, (1), 136-139.
11. Burger, A.; Ramberger, R., Thermodynamic Relationships between Polymorphic Modicafications- Flufenamic acid and Mefenamic acid. *Mikrochimica Acta* **1980,** 1, (1-2), 17-28.
12. Hu, Y. R.; Wikstrom, H.; Byrn, S. R.; Taylor, L. S., Estimation of the transition temperature for an enantiotropic polymorphic system from the transformation kinetics monitored using Raman spectroscopy. *Journal of Pharmaceutical and Biomedical Analysis* **2007,** 45, (4), 546-551.
13. Perlovich, G. L.; Surov, A. O.; Bauer-Brandl, A., Thermodynamic properties of flufenamic and niflumic acids - Specific and non-specific interactions in solution and in crystal lattices, mechanism of solvation, partitioning and distribution. *Journal of Pharmaceutical and Biomedical Analysis* **2007,** 45, (4), 679-687.
14. Surov, A. O.; Surov, O. V., Thermochemistry of Fenamates Vaporization. *Russian Journal of General Chemistry* **2008,** 78, (8), 1481-1487.

15. Surov, A. O.; Terekhova, I. V.; Bauer-Brandl, A.; Perlovich, G. L., Thermodynamic and Structural Aspects of Some Fenamate Molecular Crystals. *Crystal Growth & Design* **2009,** 9, (7), 3265-3272.

16. Al-Dulaimi, S.; Aina, A.; Burley, J., Rapid polymorph screening on milligram quantities of pharmaceutical material using phonon-mode Raman spectroscopy. *Crystengcomm* 12, (4), 1038-1040.

17. Alvarez, A. J.; Singh, A.; Myerson, A. S., Polymorph Screening: Comparing a Semi-Automated Approach with a High Throughput Method. *Crystal Growth & Design* **2009,** 9, (9), 4181-4188.

18. Gilpin, R. K.; Zhou, W., Infrared studies of the polymorphic states of the fenamates. *Journal of Pharmaceutical and Biomedical Analysis* **2005,** 37, (3), 509-515.

19. Hu, Y. R.; Liang, J. K.; Myerson, A. S.; Taylor, L. S., Crystallization monitoring by Raman spectroscopy: Simultaneous measurement of desupersaturation profile and polymorphic form in flufenamic acid systems. *Industrial & Engineering Chemistry Research* **2005,** 44, (5), 1233-1240.

20. Munro, S. L. A.; Craik, D. J., NMR Conformational Studies of Fenamate Non-Steroidal Anti-inflammatory Drugs. *Magnetic Resonance in Chemistry* **1994,** 32, (6), 335-342.

21. Lozano, J. J.; Pouplana, R.; Lopez, M.; Ruiz, J., Conformational Analysis of the Anti-Inflammatory Fenamates: A Molecular Mechanics and Semi Empirical Molecular Orbital Study. *Theochem-Journal of Molecular Structure* **1995,** 335, 215-227.

22. Chen, X. M.; Li, T. L.; Morris, K. R.; Byrn, S. R., Crystal packing and chemical reactivity of two polymorphs of flufenamic acid with ammonia. *Molecular Crystals and Liquid Crystals* **2002,** 381, 121-131.

23. Dhanaraj, V.; Vijayan, M., Structural Studies of Analgesics and their Interactions 12. Structure and Interactions of Anti-Inflammatory Fenamates: A Concerted Crystallographic and Theoretical Conformational Study. *Acta Crystallographica Section B-Structural Science* **1988,** 44, 406-412.

24. Lee, E. H.; Boerrigter, S. X. M.; Byrn, S. R., Epitaxy of a Structurally Related Compound on the (100) Faces of Flufenamic Acid Form I and III Single Crystals. *Crystal Growth & Design* 10, (2), 518-527.

25. Lee, E. H.; Boerrigter, S. X. M.; Rumondor, A. C. F.; Chamarthy, S. P.; Byrn, S. R., Formation and solid-state characterization of a salt-induced metastable polymorph of flufenamic acid. *Crystal Growth & Design* **2008,** 8, (1), 91-97.

26. Krishna Murthy, H. M.; Vijayan, M., 2-{[3-(trifluoromethyl)phenyl]amino}nicotinic acid: Niflumic Acid. *Acta Crystallographica Section B Structural Crystallography and Crystal Chemistry* **1979,** 35, (1), 262-263.

27. Krc, J., Crystallographic Properties of Flufenamic Acid. *Microscope* **1977,** 25, (1), 31-45.

28. Takasuka, M.; Nakai, H.; Shiro, M., Infrared Spectral and X-ray Studies of Polymorphic Forms of 2-(2-methyl-3-chloroanilino)nicotinic acid. *Journal of the Chemical Society-Perkin Transactions 2* **1982**, (9), 1061-1067.

29. Long, S. H.; Parkin, S.; Siegler, M. A.; Cammers, A.; Li, T. L., Polymorphism and Phase Behaviors of 2-(Phenylamino)nicotinic Acid. *Crystal Growth & Design* **2008,** 8, (11), 4006-4013.

30. McKinnon, J. J.; Mitchell, A. S.; Spackman, M. A., Hirshfeld surfaces: A new tool for visualising and exploring molecular crystals. *Chemistry-a European Journal* **1998,** 4, (11), 2136-2141.

31. McKinnon, J. J.; Jayatilaka, D.; Spackman, M. A., Towards quantitative analysis of intermolecular interactions with Hirshfeld surfaces. *Chemical Communications* **2007**, (37), 3814-3816.

32. Spackman, M. A.; McKinnon, J. J., Fingerprinting intermolecular interactions in molecular crystals. *Cryst. Eng. Comm.* **2002**, 378-392.

33. Mitchell-Koch, K. R.; Matzger, A. J., Evaluating computational predictions of the relative stabilities of polymorphic pharmaceuticals. *Journal of Pharmaceutical Sciences* **2008,** 97, (6), 2121-2129.

CHAPTER 4

THE POLYMORPHOPHORE: ANOTHER FABLE IN CRYSTAL ENGINEERING?

4.1 Introduction

An important issue in drug development is solid-state form; in fact, the majority of pharmaceutical compounds are dosed in some sort of solid formulation. The existence of molecules exhibiting multiple crystalline phases differing in the arrangement or conformations of the molecules within a crystal lattice,[1] poses a challenge for formulation of solid dosages because, in addition to regulatory issues,[2] polymorphism has important implications for the solubility and stability of pharmaceutical compounds.[3] Therefore it is not only important to understand the molecular structure of a drug substance, but also how this structure influences behavior in the solid-state in order to control drug performance.

To date, there is no experimental method capable of determining if a given molecular structure is prone to display polymorphism nor is there a method to establish the number of crystals phases that are energetically accessible. Computational methods have shown promising results in polymorph prediction,[4-9] but their efficacy can only be evaluated once every structure is experimentally determined.[10] Hence, it would be beneficial if a relationship between a molecular structure and its propensity to give rise to polymorphic behavior could be experimentally derived.

Previous accounts have implied a relationship between molecular structure and polymorphism for specific compounds.[11-17] Analogues of the highly polymorphic compounds 5-methyl-2-[(2-nitrophenyl)amino]-3-thiophenecarbonitrile (ROY)[16, 18-22] and carbamezepine (CBZ)[15, 23-25] have been studied in order to explore their polymorphic behavior. Collectively, these investigations support the idea that an ensemble of steric and electronic features in a molecule provides a fine interplay of interactions ultimately responsible for the appearance of multiple crystal phases and highlight the need for a systematic approach in order to gain understanding of the structural factors that influence the appearance of polymorphism in molecular compounds.

In analogy to how pharmacophores are identified, this investigation undertakes a systematic study of the proposed structure-polymorphism relationship connecting molecular analogues of tolfenamic acid (TA). The polymorphic behavior of six analogues of TA, a highly polymorphic non-steroidal anti-inflammatory drug (NSAID), is explored (Figure 4.1). TA possesses complex solid-state chemistry including whole molecule disorder (form V), varying numbers of molecules in the asymmetric unit, as well as a diverse array of conformations and packing arrangements, all of which occur within a very narrow free energy window.[14] As such, this pentamorphic compound makes an excellent test case for examining the notion that a structure containing certain structural motifs will favor the formation of polymorphic crystals: the polymorphophore.[15, 16] The polymorphophore, as in the case of the pharmacophore, does not represent a real molecule or discrete association of functional groups; it is an abstract concept that accounts for the common structural motif, in a group of structurally related compounds associated with their propensity to display multiple crystalline phases. The systematic study of the structure-polymorphism relationship will help predict polymorphism of a given molecular motif and perhaps ultimately provide a pathway to engineer molecular compounds less prone to polymorphism.

4.2 Experimental Section

4.2.1 Materials

Mefenamic acid (MA) and fenamic acid (FA) were obtained from Sigma-Aldrich (St. Louis, MO, USA). Analogues **2** and **4** were synthesized according to literature procedure,[26, 27] whereas the literature procedures was modified accordingly for the synthesis of analogues **1** and **2.** The solvents methanol, 2-propanol, 1-pentanol, ethyl acetate, methylene chloride, acetonitrile, chloroform, 1-butanol, and acetone were purchased from Fisher Scientific (Pittsburgh, PA, USA). Iso-butylalcohol and 1-propanol were purchased from Burdick and Jackson Laboratories, Inc. (Muskegon, MI, USA), whereas 1,4-butanediol, sec-butanol and 3-bromoaniline were purchased from Acros Organics (New Jersey, USA). Ethanol was purchased from Decon Laboratories, Inc. (King of Prussia, PA, USA). The reagents 2-bromobenzoic acid, 2-chlorobenzoic acid, 3-chloroaniline, and *o*-toluidine were purchased from Aldrich (St. Louis, MO, USA). The reagent 2-methyl-3-bromoaniline was purchased from Alfa Aesar (Ward Hill, MA, USA). All commercially available reagents, compounds, and solvents were used without further purification.

4.2.2 General Procedure of the Cu-catalyzed Amination of Aryl Halides

A mixture of aniline (9.3 mmol, 5.0 g), 2-bromobenzoic acid or 2-chlorobenzoic acid (8.8 mmol, 7.0 g), K_2CO_3 (8.8 mmol, 6.0 g), Cu powder (powder, 1 μm, 0.8 mmol, 0.2 g), Cu_2O (powder, < 5 μm, 0.4 mmol, 0.3 g), and 10 mL of 2-ethoxyethanol were heated to reflux for 24 hrs under a N_2 atmosphere. The cooled reaction mixture was passed through a glass fritted filter and the solvent removed using rotary evaporation. The resulting solid was dissolved in 5% Na_2CO_3 and precipitated with 0.5 M HCl. The precipitate was collected on a glass fritted filter and dissolved in 5% Na_2CO_3 and precipitated again with 0.5 M HCl. The final product was obtained by sublimation (~15 mTorr) between 120-140 °C.

4.2.2.1 *N*-(3-bromo-2-methylphenyl)anthranilic acid (1)

Amination of 2-bromobenzoic acid with 2-methyl-3-bromoaniline gave anthranilic acid **1**, as a light yellow solid in 50.1 % yield (Figure 4.2). m.p. 212.5 – 213.8 °C. ^{1}H NMR (500 MHz, $CDCl_3$, δ): 2.37 (s, 3H), 6.75 (m, 2H), 7.08 (t, *J* = 16.1, 8.3 Hz, 1H), 7.28 (d, *J* = 8.3 Hz, 1H), 7.30-7.35 (m, 1H), 7.44 (dd, *J* = 8.3, 1.0 Hz, 1H), 8.0 (dd, *J* = 8.3, 1.5 Hz 1H), 9.19 (bs, 1H). ^{13}C NMR (125 MHz, $CDCl_3$, δ): 18.2, 109.9, 113.8, 117.0, 124.5, 126.2, 127.4, 129.6, 132.5, 134.0, 135.3, 139.9, 149.4, 173.0. Anal. Calcd for $C_{14}H_{12}NO_2Br$: C, 54.92; H, 3.95; N, 4.58. Found; C, 55.08; H, 3.82; N, 4.58.

4.2.2.2 *N*-(3-chlorophenyl)anthranilic acid (2)

Amination of 2-chlorobenzoic acid with 3-chloroaniline gave anthranilic acid **2**, as a light yellow solid in 53.0 % yield (Figure 4.3). m.p. 168.9 – 169.9 °C. ^{1}H NMR (500 MHz, $CDCl_3$, δ): 6.83 (m, 1H), 7.08 (d, 1H), 7.14 (d, 1H), 7.25-7.30 (m, 3H), 7.41 (m, 1H), 8.07 (dd, *J* = 8.1, 1.7 Hz, 1H), 9.32 (bs, 1H). ^{13}C NMR (125 MHz, $CDCl_3$, δ): 111.1, 114.4, 118.1, 120.4, 122.2, 123.7, 130.4, 132.7, 135.0, 153.3, 141.8, 147.8, 173.0. Anal. Calcd for $C_{13}H_{10}NO_2Cl$: C, 63.04; H, 4.07; N, 5.66. Found: C, 63.15; H, 3.94; N, 5.63.

4.2.2.3 *N*-(2-methylphenyl)anthranilic acid (3)

Amination of 2-chlorobenzoic acid with *o*-toluidine gave anthranilic acid **3**, as a colorless solid in 50.0 % yield (Figure 4.4). m.p. 192.1 – 193.0 °C. ^{1}H NMR (500 MHz, $CDCl_3$, δ): 2.29 (s, 3H) 6.72 (m, 1H), 6.85 (d, *J* = 8.31 Hz, 1H), 7.13 (m, 1H), 7.22 (m, 1H), 7.28-7.35 (m, 3H), 8.05 (dd, *J* = 8.1, 1.7 Hz, 1H) 9.14 (bs, 1H). ^{13}C NMR (125 MHz, $CDCl_3$, δ): 18.0, 109.7, 113.7, 116.5, 124.9, 125.2, 126.7, 131.3, 132.5, 133.5, 135.2, 138.6, 149.7, 173.4. Anal. Calcd for $C_{14}H_{13}NO_2$**:** C, 73.99; H, 5.77; N, 6.16. Found: C, 73.74; H, 5.88; N, 6.10.

4.2.2.4 *N*-(3-bromophenyl)anthranilic acid (4)

Amination of 2-bromobenzoic acid with 3-bromoaniline gave anthranilic acid **4**, as a light yellow solid in 69.9 % yield (Figure 4.5). m.p. 171.1 – 172.4 °C. ^{1}H NMR (500 MHz, $CDCl_3$, δ): 6.82 (t, *J* = 7.8, 1.0 Hz, 1H), 7.27-7.18 (m, 4H), 7.41 (m, 2H), 8.07 (dd, *J* = 7.8, 1.5 Hz, 1H), 9.32 (s, 1H). ^{13}C NMR (125 MHz, $CDCl_3$, δ): 111.2, 114.4, 118.1, 120.9, 123.0, 125.2, 126.7, 130.6, 132.7, 135.3, 142.1, 147.9, 173.1. Anal. Calcd for $C_{13}H_{10}NO_2Br$: C, 54.03; H, 3.45; N, 4.85. Found: C, 53.45; H, 3.45; N, 4.79.

4.2.3 Crystallization in the Presence of Polymers

Polymer-induced-heteronucleation (PIHn) was used as the primary method for polymorph discovery.[28, 29] Solutions (~12.5 mg/mL) of each analogue were prepared in ethanol, methanol or acetonitrile. Solutions were dispensed equally (~0.2 mL) into each well in the 96-well plate containing non-polar aromatic or acidic polymers. Crystals grew during evaporation of the solvent in the presence of polymers.

4.2.4 Crystallization in the Absence of Polymers

Solutions (~12.5 mg/mL) of each analogue were prepared in ethanol, methanol, 2-propanol, 1-pentanol, ethyl acetate, methylene chloride, acetonitrile, chloroform, isobutylalcohol, 1-butanol, 1-propanol, 1,4-butanediol, sec-butanol, and acetone. Solutions were dispensed equally (~0.2 mL) into an uncapped 4 mL vial after dissolving the solute. Crystal grew through evaporation of the solvent in the absence of polymer.

Additionally, analogues were sublimed by placing the powdered sample (~100 mg) inside a sublimation chamber and evacuating (~15 mTorr) the chamber while it was submerged in an oil bath 120-140 °C. After ~35 minutes, most of the sample had sublimed onto the cold finger.

4.2.5 Polymorph Characterization

Polymorphic crystals obtained in the 96-wells plates were first identified optically by differences in morphology and/or color. Powder X-ray diffraction (PXRD) was utilized to confirm structural dissimilarity among the suspected polymorphs of each analogue.

PXRD analysis was performed using a Rigaku R-Axis Spider diffractometer equipped with an image plate detector and graphite monochromated Cu-Kα radiation (1.54178 Å, 50 kV, 40 mA). Samples were mounted on a CryoLoop™ and images were collected for 5 min while rotating the sample about the φ-axis at 10°/sec, oscillating ω between 120° and 180º at 1°/sec with χ fixed at 45°. All images were integrated from 5° to 50° with a 0.05° step size using AreaMax[2] software. PXRD patterns were processed in Jade Plus[3] (v. 8.2) to calculate peak positions (º) and relative intensities (%). Ultimately, if crystal quality permitted it, structures were determined through single crystal X-ray diffraction.

4.2.6 Single Crystal X-ray Diffraction

Measurements for analogue **1** forms I and III, and analogue **3** forms I and II were made on a Rigaku R-Axis Spider diffractometer with an image plate detector using graphite monochromated Cu-Kα radiation (1.5406 Å) operating at 50 kV and 40 mA. The data collection was carried out at 95(1) K with the sample mounted on a MiTeGen MicroMount™. The structures were solved by direct methods. All calculations were performed using the CrystalStructure crystallographic software package except for refinement, which was performed using SHELXL-97.

Measurements for analogue **1** form II, analogue **2** forms I, II and IV and analogue **4** form I were made on a Rigaku AFC10K Saturn 944+ CCD-based X-ray diffractometer equipped with a low temperature device and Micromax-007HF Cu-target micro-focus rotating anode (1.54187 Å) operated at 1.2 kW power (40 kV, 20 mA). The X-ray intensities were measured at 85(1) K (analogue **1** form II, analogue **2** form I, and analogue **4** form I), 253(1) K (analogue **2** form II), or 187(1) K (analogue **2** form IV) with the crystal mounted on a CryoLoop™. The structures were solved and refined with the Bruker SHELXTL (version 2008/4) software package.

4.2.7 Variable Temperature Powder X-ray Diffraction

Variable temperature powder X-ray diffraction (VTPXRD) analysis was performed using a Rigaku R-Axis Spider diffractometer equipped with an image plate detector and graphite monochromated Cu-Kα radiation (1.5406 Å, 50 kV and 40 mA). A 0.5 mm glass capillary was filled with the sample and images were collected continuously for 3 min while rotating the sample about the φ-axis at 10°/sec, oscillating ω between 0° and 360° at 1°/sec with χ fixed at 45°. All images were integrated from 5° to 50° with a 0.05°

step size using AreaMax[2] software. PXRD patterns were processed in Jade Plus[3] to create the 3D overlay. The data collection was carried out between 290-190 K.

4.2.8 Relaxed Potential Energy Surface Scans

Two-dimensional scans were performed for each of the analogues using Gaussian03. Optimized geometries and corresponding energies were obtained at the HF/6-31G* level of theory at 10° intervals. All calculations were performed on a dual 2.66 GHz Intel Xeon Quad Core CPU.

4.2.9 Lattice Energy Calculation

The ability to access and structurally characterize multiple crystal phases of TA, and its six structural analogues allowed the exploration of possible isostructural relationships. The lattice energies were calculated based on the Free-Cell method previously described by Mitchell-Koch *et al.*[30] All calculations were performed in Material Studio version 4.3 in the Forcite module using Compass force field. Once the lattice energy of every crystal structure elucidated was determined, the molecular structure of each analogue was substituted into each of the four ordered experimental lattices of TA polymorphs. The virtual crystal structure was then optimized (including cell parameters) and its lattice energy, $U_{\text{latt (virtual analogue)}}$, was compared to that of the lowest lattice energy calculated, $U_{\text{latt (analogue)}}$, for different polymorphs of each analogue. Structurally similar or isostructural analogues will present small lattice energy differences, ΔU_{latt}, indicating that the experimental observation of these ‘virtual’ analogues is energetically viable (Equation 1 and Figure 4.6).

$$\Delta U_{\text{latt}} = U_{\text{latt (virtual analogue)}} - U_{\text{latt (analogue)}} \qquad (1)$$

In a complementary experiment, the molecular structure of TA was substituted into each of the experimentally determined structures of the analogues in order to determine if additional polymorphs of TA were likely to be favorable. The magnitude of the lattice energy difference, ΔU_{latt}, between the lattice energy of the virtual TA structure, $U_{latt\ (virtual\ TA)}$, and the lowest lattice energy calculated, $U_{latt\ (TA)}$, for the TA polymorphs, suggests the viability of obtaining additional polymorphs of TA that are isostructural to the analogues (Equation 2 and Figure 4.6).

$$\Delta U_{latt} = U_{latt\ (virtual\ TA)} - U_{latt\ (TA)} \qquad (2)$$

4.3 Results and Discussion

The structural factors that lead to polymorphism in some molecules and not in others are not well understood. Here a systematic investigation of the structure-polymorphism relationships connecting molecular analogues of the highly polymorphic pharmaceutical compound TA aims to delineate the origin of polymorphism in this molecule, in other words to identify, if one exists for this compound, the polymorphophore. Towards this goal, an extensive experimental and computational investigation into the solid-form diversity in TA and structurally related analogues was carried out. A series of molecular analogues, **1-4**, consisting of the TA skeleton with different substitutions in the non-carboxylated phenyl ring at the 2,3-positions were synthesized through Ullman-Golberg condensations.[26, 27] These four analogues and commercially available MA and FA yielded six structurally related compounds to explore (Figure 4.1).

At the outset of this investigation it was hypothesized that subtle structural changes in the non-carboxylated phenyl ring at the 2,3-positions have the potential to give rise to isostructural analogues of TA, whereas disturbing the carboxylic acid dimerization would prevent the appearance of the previously observed packing motifs, all of which involve hydrogen bonded dimers. In the molecular structure of analogue **1** and MA, the chlorine present in TA is exchanged by bromine and methyl, respectively. Exchange of chlorine by bromine will allow similar intermolecular interactions to occur possibility permitting previously observed TA packing motifs to be present in the solid-state for this analogue.[31] For the chloro-methyl exchanged analogue MA, it was hypothesized that since chlorine (19 Å^3) and methyl (24 Å^3) groups have similar volumes,[32, 33] their substitution would also lead to isostructural crystal forms if halogen interactions do not play a critical role in controlling the packing. The molecular structures of analogues **2** and **3** display the absence of methyl or chlorine groups compared to TA and the appearance of isostructural forms of these analogues would provide insights into the role that each of these functional groups plays in the emergence of the multiple crystalline phases observed in TA. Analogue **4** exhibits both the absence of the methyl and halogen substitution; the combination of these structural changes would together reinforce observations made on the role of the methyl and the chlorine as key functional groups in the display of polymorphic crystalline phases by these analogues. The absence of both methyl and chlorine is displayed in the molecular structure of FA; to date, no polymorphs of this analogue have been reported.[34] The discovery of novel forms of FA would provide insights into the contribution of the *N*-phenylanthranilic acid functionality to isostructural packing modes within the polymorphophore.

The efficiency of PIHn as a polymorph discovery tool was tested against solvent-based crystallizations in the absence of polymers. In a conventional polymorph screen based on crystallization from fourteen commonly used solvents, only a few of the solvents were able to access multiple crystalline phases of each analogue; this finding contrasts with the large number of polymorphs accessed when PIHn was employed. Additionally, crystal growth from the vapor phase in the absence of polymer only provided access to one crystal form for each of the analogues explored. These results are summarized in Table 4.1.

The use of polymer heteronuclei allowed access to two previously reported forms of MA, and one previously reported form of FA (Figures 4.7 and 4.8). No further polymorphs of these commercial analogues were identified. Both FA and MA form I present unique PXRD patterns, while the comparison of PXRD patterns of MA form II and TA form V indicates that these forms are isostructural (Figure 4.9).

Three polymorphs of analogue **1** were grown from non-polar aromatic and acidic polymers. PXRD patterns of the white needles (form I), the yellow needles (form II), and the white plates (form III) obtained through PIHn present distinctive reflections demonstrating that each form is structurally distinct (Figure 4.10). Furthermore, the comparison of their PXRD patterns suggests that forms I and II of this analogue are isostructural with forms I and II of TA (Figures 4.11 and 4.12).

In the case of analogue **2**, three polymorphs were accessed through the use of acidic polymers as heteronuclei. Form I crystallizes in a plate-like habit, and crystals are colorless, whereas in forms II and III crystals are light yellow needles. Examination of the PXRD patterns reveals that analogue **2** presents unique PXRD patterns, and therefore suggests the possibility that their packing arrangements are distinct from those previously observed for TA and any of its analogues (Figure 4.13).

PXRD patterns of the two polymorphs of analogue **3** accessed by PIHn, suggest structural dissimilarity when compared to all other analogues and TA (Figure 4.14). Three crystals form of analogue **4**, presenting the absence of methyl and halogen substitution, were discovered using PIHn. PXRD patterns confirm the presence of unique packing arrangements among analogue **4** polymorphs (Figure 4.15).

Evaluation of the previously reported and newly determined crystal structures of the TA analogues will aid in the classification of these solid forms as isostructural or structurally similar to one another. Isostructural forms will have similar cell constants, the same space groups, and almost identical packing motifs, whereas structurally similar forms may present deviations in cell constants and space groups but still preserve some similarities in the packing arrangements. A unifying theme among all analogues and TA is the presence of the hydrogen bonded dimers. Also commonly observed is the presence of an intramolecular hydrogen bond between the carbonyl oxygen and the nitrogen in all structures elucidated thus far.

MA represents the chloro-methyl exchanged analogue of TA; it was hypothesized that this substitution would lead to isostructural crystal forms. Experimentally, this was only observed in the case of MA form II and TA form V. When compared, both structures present similar packing arrangements although complete evaluation of the resemblance present in each crystal form is difficult due to the presence of disorder in both structures. TA form V exhibits whole molecule disorder, whereas in the case of this chloro-methyl exchanged analogue only half of the molecule exhibits disorder. Prior to distance determination, all the crystallographic information files were normalized to average neutron values (C–H = 1.083 Å, N–H = 1.08 Å, and O–H = 0.983 Å). All the reported C–H···π, π···π and C–X···π distances were measured from hydrogen to carbon (C–H···C), from carbon to carbon (C···C) and from halogen to carbon (C–X···C) in each of the cases. Dimers in TA form V pack through Cl···Cl interactions in one of the disordered models, whereas in MA form II dimers pack through C–H···O=C contacts; in both cases the dimers are aligned along the *c*-axis. Additional assignments for intermolecular contacts are hampered by the disorder present in these structures.

The crystal structures for the three polymorphs of analogue **1** were elucidated (Table 4.2). Examination of the cell parameters, hydrogen bonding, conformations and packing motifs establishes that **1** forms I and II are isostructural to TA forms I and II, whereas **1**-form III shares only some structural similarities with TA form III. Table 4.3 lists the torsion angles that define the planes between the diphenyl amine functionality, τ_1 and τ_2, and the orientation of the carboxyl group with respect to the phenyl ring bearing it, τ_3, in forms I-III of analogue **1** as well as in TA form I-III. Molecular conformations of forms I and II in both TA and **1** are equivalent, whereas the conformations present in form III are not shared by any of the experimentally observed TA polymorphs. As in the case of TA form II, **1**-form II presents the most coplanar conformation among all forms; this planarity causes the display of a light yellow color in the crystals of both forms.

As in the cases of TA forms I and II, analogue **1** forms I and II crystallize in the same space group ($P2_1/c$). In analogy to TA forms I-II, dimers in **1**-forms I and II are joined by an inversion center, whereas in **1**-form III heterodimers are formed. In TA form I, each dimer interacts with eight adjacent molecules through close C–H···π contacts between the chlorinated aromatic ring and the carboxylated aromatic ring, while in **1**-form I each dimer interacts with four adjacent molecules through close C–H···π (2.83 Å) contacts between the brominated aromatic ring and the carboxylated aromatic ring forming 2D sheets along the *c*-axis. Along the *a*-axis, C–H···π (2.78, 2.83, and 2.84 Å) contacts connect these sheets into a 3D packing motif (Figure 4.16a and b). A structural overlay of **1**-form I and TA form I yielded an RMSD of 0.06 Å, indicating a close structural match exists between these polymorphs.

In the case of **1**-form II, hydrogen bonded anti-dimers pack in columns along the *a*-axis. Like in the case of TA form II, donation from a neighboring methyl group to the carbonyl above and below it (2.73 Å) connects the columnar packing of this form along the *a*-axis. Adjacent pairs of dimers in this polymorph, pack through two C–Br···π (3.44 and 3.45 Å) contacts, whereas in TA form II the dimers pack through two C–Cl···π (3.41 Å) contacts. A C–H···Br (3.01 Å) contact expands four adjacent dimers along the *b*-axis (Figure 4.16c and d). The structural overlay of **1**-form II and TA form II yielded an RMSD of 0.04 Å, demonstrating isostructurality exists among these crystalline phases.

In a similar fashion to TA form III, in **1**-form III, heterodimers propagate in a columnar arrangement. Slipped columns in **1**-form III expand through C=O···π contacts (3.36 and 3.39 Å) from carboxylated aromatic ring of one conformer to the carboxylated aromatic ring of the other as well as C–H···π contacts (2.78, 2.88 and 2.89 Å) between the carboxylated aromatic ring and the brominated aromatic ring which expand tilted along the *a*-axis at an angle of ~60°. Adjacent columns are connected by C–Br···π contacts (3.34 and 3.37 Å) between inequivalent molecules in **1**-form III, whereas in TA form III C–Cl···π (3.44 Å) donor-acceptor interactions connect the columnar arrangement (Figure 4.16e and f). Structural overlay of **1**-form III and TA form III yielded an RMSD of 0.09 Å, indicative of structural similarity between these forms.

Crystal structures for analogue **2** polymorphs I-II were determined (Figure 17 and Table 4.4), whereas that of form III remains elusive. Both forms crystallize in the triclinic space group, $P\bar{1}$ with one molecule in the asymmetric unit. A solid-solid transformation at low temperature (~ −90 °C) of **2-**form II yielded **2-**form IV (Figure 4.18). The crystal structure of **2-**form IV was determined at 187 K, and it is shown to crystallized in the space group, $P\bar{1}$. Notably, **2**-form IV contains six unique molecules in the asymmetric unit, a rare occurrence in the Cambridge Structural Database (CSD) (0.07%).[35, 36] Table 4.5 presents a summary of the torsion angles for each of the crystallographically independent molecules in the structures of analogue **2** forms I, II and IV. All conformations present in analogue **2** polymorphs present an *anti* conformation between the carboxylated phenyl ring and the chlorinated phenyl ring.

In **2**-form I, homodimers pack in columns through three close π···π (3.39 Å, 3.42 Å, and 3.43 Å) interactions among the carboxylated aromatic rings along the *a*-axis. Along the *b*-axis, dimers connect through C–H···O=C (2.73 Å) contacts between the chlorinated aromatic ring and the carboxylated aromatic ring forming sheets, these sheets expand tilted at ~35° along the same axis (Figure 4.17a). In polymorph II, dimers extend in chains through C–H···Cl (2.95 Å) contacts between the carboxylated aromatic ring and the chlorinated aromatic ring along the *c*-axis. Neighboring chains are connected through additional C–H···Cl (2.97 Å) contacts between the carboxylated aromatic ring and the chlorinated aromatic ring along the *a*-axis (Figure 4.17b). These chains stack in columns along the *b*-axis. Form IV possesses the same chain packing motif as its precursor form, form II. Three chains of heterodimers are formed, which propagate tilted along the *b*-axis through C–H···Cl (2.87 Å and 2.92 Å for conformer *d* and *f*, 2.86 Å for conformer *e* and *c*, 2.91 Å for conformer *e* and *b*, and 2.91 Å for conformer *a* and *b*) contacts between the carboxylated aromatic ring and the chlorinated aromatic ring. Adjacent chains connect through C–H···π contacts among the chlorinated aromatic rings for all three conformers (2.87 Å for conformer *a* and *b,* 2.89 Å for conformer *c* and *e*, and 3.30 Å for conformer *d* and *f*) forming columns along the *a*-axis (Figure 4.17c). Polymorphs II and IV of analogue **2** present very similar columnar packing arrangements to TA form IV (Figure 19).

The two polymorphs of analogue **3** were structurally characterized (Figure 20 and Table 4.6). Colorless needles of **3**-form I crystallize in the monoclinic space group *C*2/c whereas colorless plates of **3**-form II crystallize in $P2_1$/n; both structures contain one molecule in the asymmetric unit, each presenting a unique conformation (Table 4.7). In **3**-form I, slipped columns expand in a columnar arrangement along the *a*-axis at an angle of ~65°, where a supramolecular ring is formed by two short contacts between the carbon atom of the carboxylic acid and the carboxylated aromatic ring located above and below each (3.38 Å) dimer. Other aromatic C–H···π (2.88 Å, 2.89 Å, and 2.92 Å) contacts between the methylated aromatic ring and the carboxylated aromatic ring propagate within adjacent columns along the same direction (Figure 4.20a). The absence of Cl···Cl and C–Cl···π contacts in this form plays an important role in the packing arrangement observed here versus TA form III and analogue **1**-form III which present similar packing arrangements to this form (Figure 4.21). The comparison of the crystal structures of analogue **3**-form II with that of TA polymorphs I-V revealed that no pronounced similarities exist among these crystalline forms.

Although three polymorphs of analogue **4** were accessed through the use of polymers as heteronuclei, only one form has been structurally characterized. Form I crystallizes in the triclinic space group $P\overline{1}$ with a single molecule in the asymmetric unit. Dimers are joined in a chain motif through C–H···Br (2.98 Å) contacts between the brominated aromatic ring and the carboxylated aromatic ring along the *c*-axis; neighboring chains connect through C–H···Br (3.14 Å) contacts between the carboxylated aromatic ring and the chlorinated aromatic ring along the *b*-axis (Figure 4.22a and Table 4.8). The packing modes of **4**-form I resemble that of **2**-form II demonstrating structural similarity exists between these polymorphs (Figure 4.22).

To probe the effect of conformational changes on the polymorphic-structure relationships presented among these analogues and TA, a conformational search of the potential energy for each of the analogue molecules was performed along the diphenyl amine functionality. Conformational plots can be divided into two groups, those that present similar contours to TA (Figures 4.23-4.26) and those that present dissimilar contours (Figures 4.27-4.29). These conformational plots provide a possible explanation for the presence of isostructural forms among TA and MA, and TA and analogue **1** as well as explain the unexpected isostructuralism present among analogue **2** and analogue **4** based on the contribution of the conformational energy to the total lattice energy. The potential energy associated with the experimentally determined conformation of each analogue was calculated and compared to that of the lowest energy conformation calculated in Gaussian03. These results are summarized in Table 4.9. Analogues presenting isostructural or structurally similar packing arrangements also present similar conformations and therefore their conformational energy differences, ΔE_{conf}, are also of comparable magnitude.

To further explore the structural relationships that emerged in these TA analogs, lattice energy calculations were carried out in which the six analogues were substituted in turn into each of the four distinct experimental lattices observed for ordered polymorphs of TA. Four simulated, or "virtual", structures were obtained for each analogue. These structures were then optimized and their lattice energy, $U_{latt\ (virtual\ analogue)}$, was compared to that of the lowest lattice energy calculated, $U_{latt\ (analogue)}$, for different polymorphs of each analogue (Figure 4.6). Among these structures, those corresponding to analogue **1**-forms I-IV are low on the lattice energy plot and comparable in stability with the forms I-IV of TA (Figure 4.30 and Table 4.10). As suggested by this calculations, isostructural forms to TA in the case of analogue **1** (forms I and II) where experimentally accessed with the aid of polymers as heteronuclei.

In order to determine if all energetically accessible forms of TA have been accessed, lattice energy calculations were carried out in which TA was substituted in turn into each of the experimental lattices determined for all six analogues and their polymorphs. The lattice energy difference, ΔU_{latt}, for several virtual structures fall within 2 kcal/mol (Figure 4.31 and Table 4.11). Although experimentally some of these crystal structures have not been observed for TA, most of the virtual structures that fall within this minima present isostructural or structurally similar packing arrangements to TA. The approach of combining experimental screening and lattice energy substitution calculations provides a strategy to maximize the probability that all energetically viable crystalline phases are accessed.

4.4 Conclusions

The appearance of polymorphism in analogues of TA supports the notion that certain structural motifs within this molecular class promote the adoption of multiple packing modes. Several structural factors are common in structures that display multiple crystalline phases within this set analogues, among them, the most pronounced are conformational changes of the diphenyl amine functionality, and the ability to stack the hydrogen bonded dimer motif in different packing arrangements from chains, to sheets and columns through a diversity of π···π, halogen···π, and halogen···halogen interactions. Crystal growth using PIHn yielded structurally similar and isostructural phases for the majority of compounds examined, all presenting hydrogen bonded dimers as the dominant intermolecular hydrogen bonding motif. The occurrence of isostructural forms only in the cases of MA and analogue **1** indicates that collectively the ensemble of steric and electronic features common to MA, analogue **1**, and TA provides a pathway for the emergence of polymorphism in this NSAID.

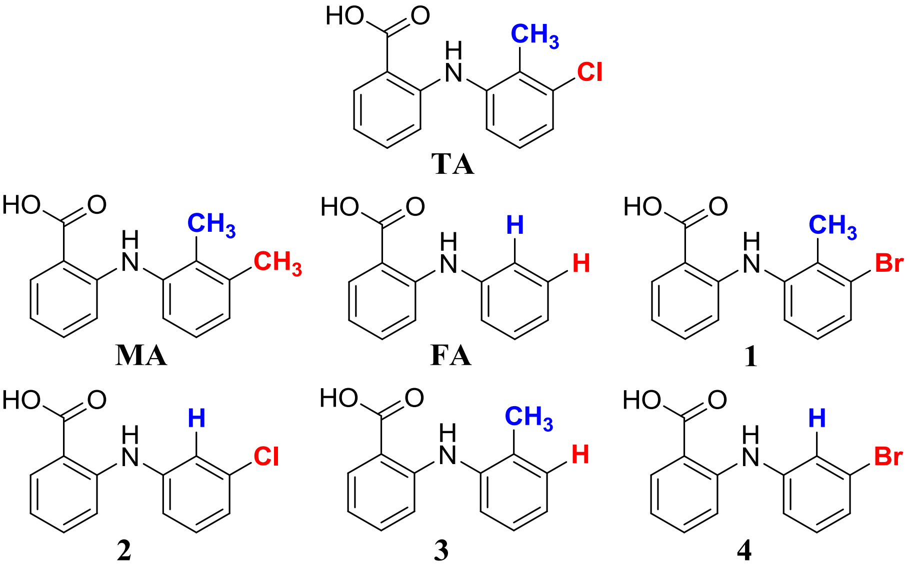

Figure 4.1. Chemical structure of tolfenamic acid (TA), mefenamic acid (MA), fenamic acid (FA), and synthesized analogues **1-4**. Structural changes in the non-carboxylated phenyl ring are indicated in blue for the ortho position and red for the para substituent.

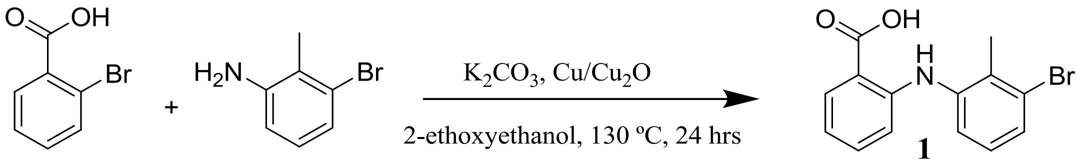

Figure 4.2. Schematic diagram of the synthesis of analogue *N*-(3-bromo-2-methylphenyl)anthranilic acid (**1**).

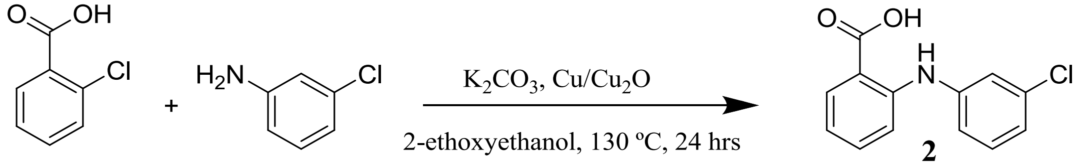

Figure 4.3. Schematic diagram of the synthesis of analogue *N*-(3-chlorophenyl)anthranilic acid (**2**).

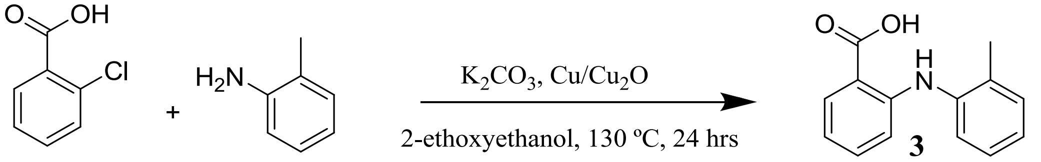

Figure 4.4. Schematic diagram of the synthesis of analogue *N*-(2-methylphenyl)anthranilic acid (**3**).

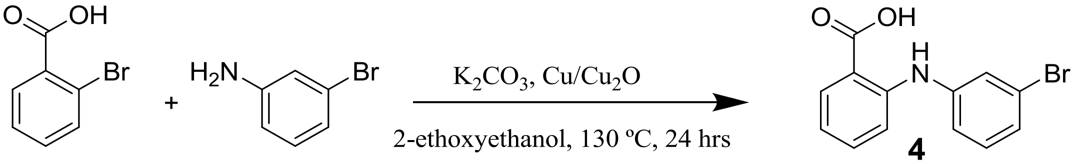

Figure 4.5. Schematic diagram of the synthesis of analogue *N*-(3-bromophenyl)anthranilic acid (**4**).

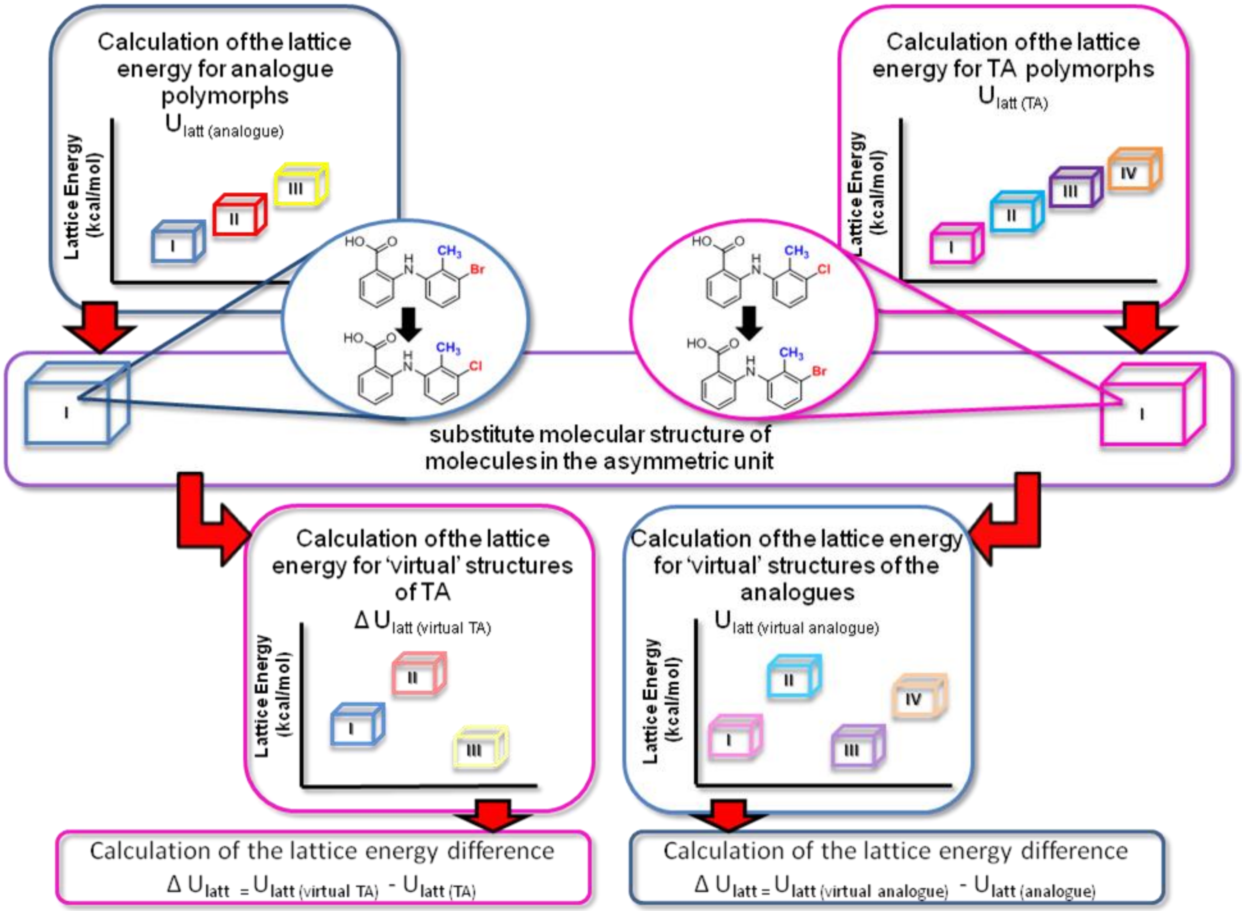

Figure 4.6. Determination of lattice energy difference (ΔU_{latt}) between simulated/'virtual' structures and real/experimentally determined structures for TA and its analogues.

Table 4.1. Summary of results of crystallization of TA analogues in different solvents and absence of solvent versus crystallization using polymer as heteronuclei.

crystallization	**MA**	**FA**	**1**	**2**	**3**	**4**
ethanol	I	I	I/III$_{\text{pure}}$	I	I	I
methanol	I	I	I	I	I	I
2-propanol	I	I	I	I	I	I
1-pentanol	I	I	I	I	I	I
ethyl acetate	I	I	I	I	I	I
methylene chloride	I	I	I	I	I	I
acetonitrile	ND	ND	I	I	I	I
chloroform	I	I	I	I	I	I/III$_{\text{mix}}$
isobutylalcohol	I	I	I	I	I	I
1-butanol	I	I	I	I	I	I
1-propanol	I	I	I	I	I	I
1,4-butanediol	I	I	I	I	I	I
sec-butanol	I	I	I	I	I/II$_{\text{mix}}$	I
Acetone	I	I	I	I	I	I
sublimation	I	I	I	I	I	I
acidic polymers (ethanol, acetonitrile)	I/II	I	I/II/III	I/II/III	I/II	I/II
non-polar aromatic polymers (ethanol)	I/II	I	I/III	I/II	I/II	I/II/III

Subscript "pure" indicates that each form was isolated in different trials, whereas subscript "mix" indicates a mixture of forms was found during different trials, "ND" indicates at ~12.5 mg/mL solute did not dissolve.

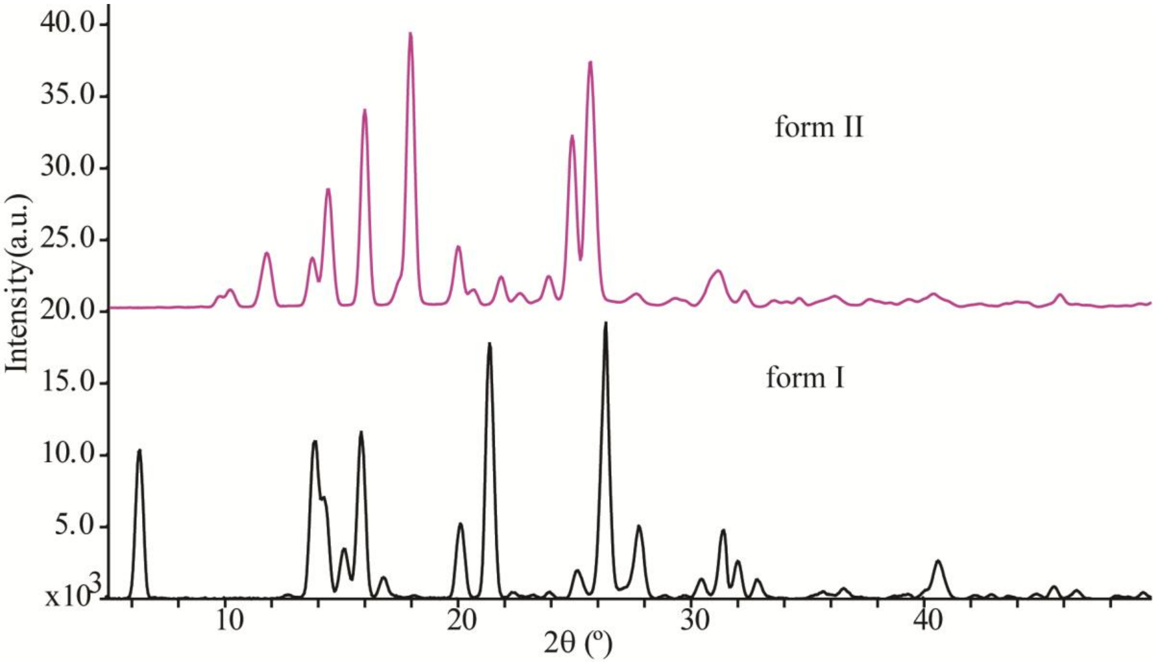

Figure 4.7. Experimental PXRD patterns of the polymorphs of MA obtained through PIHn.

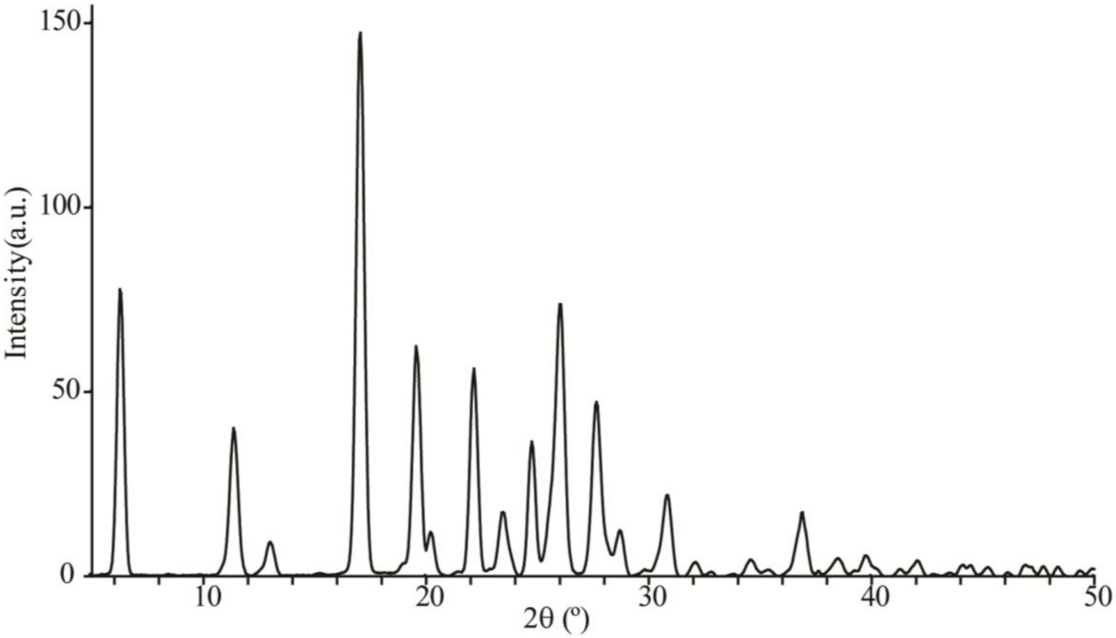

Figure 4.8. Experimental PXRD pattern of FA obtained through PIHn.

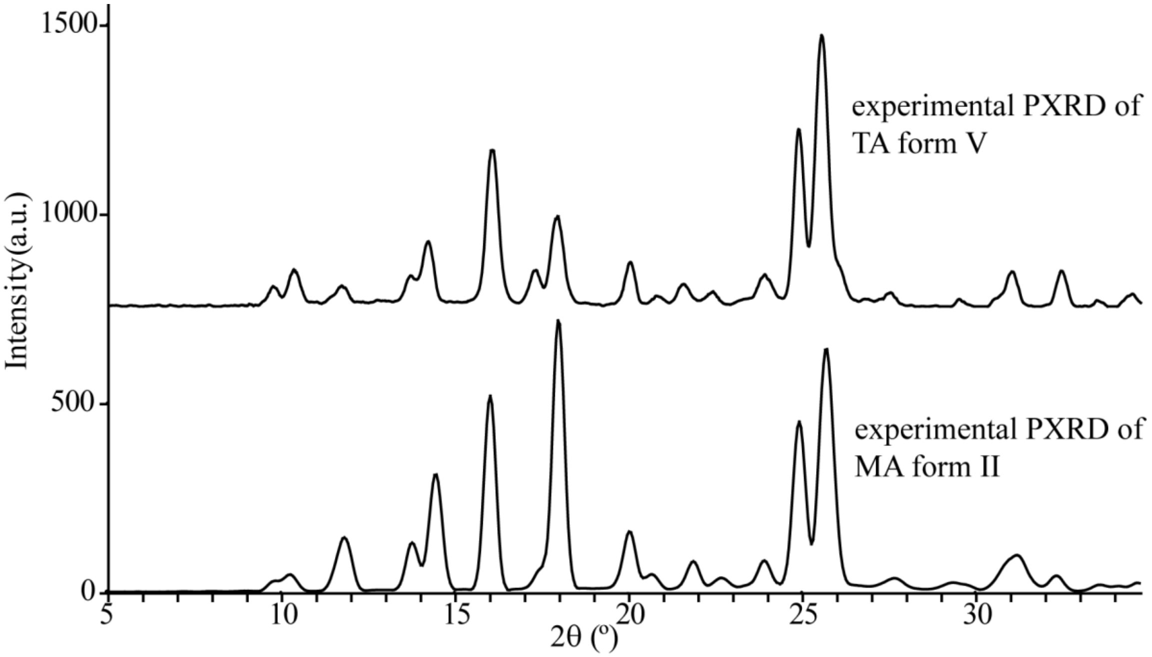

Figure 4.9. Experimental PXRD patterns of the MA form II (bottom) and TA form V (top) obtained through PIHn.

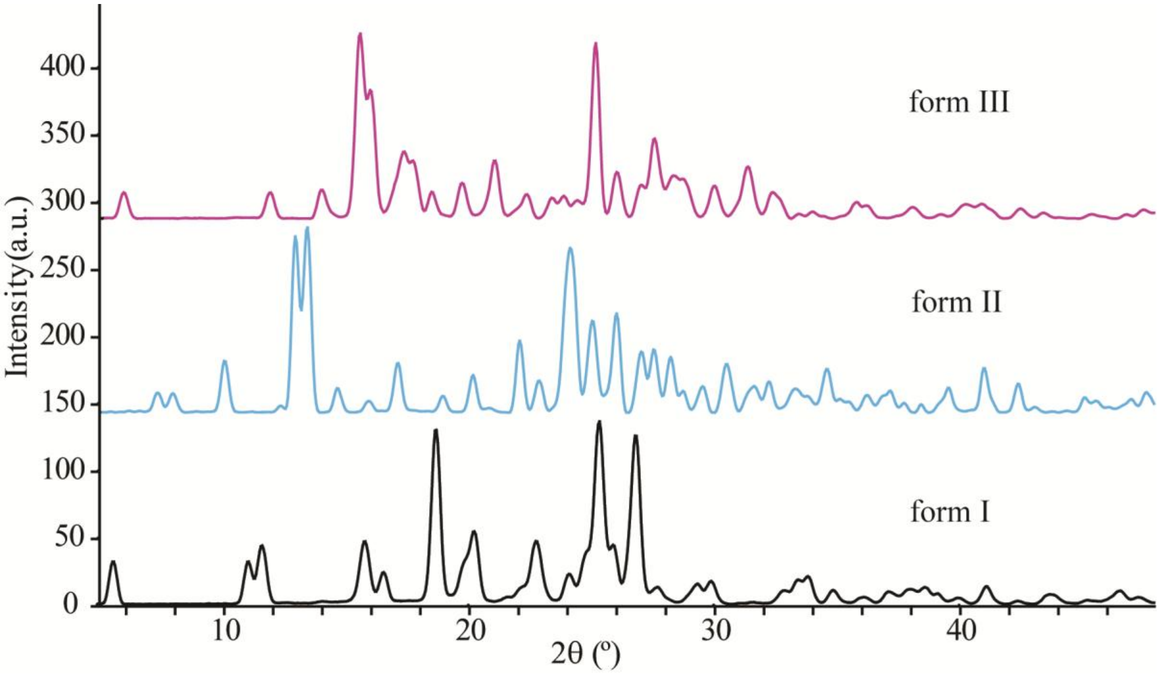

Figure 4.10. Experimental PXRD patterns of the polymorphs of analogue **1** obtained through PIHn.

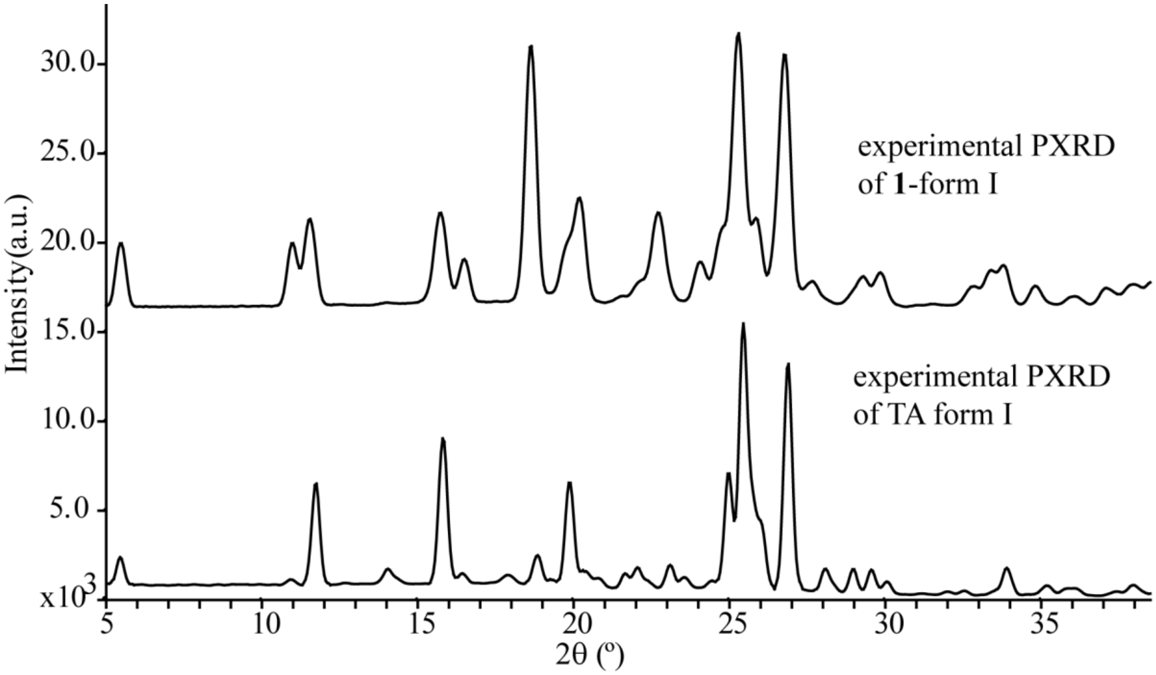

Figure 4.11. Experimental PXRD patterns of TA form I (bottom) and analogue **1**-form I (top) obtained through PIHn.

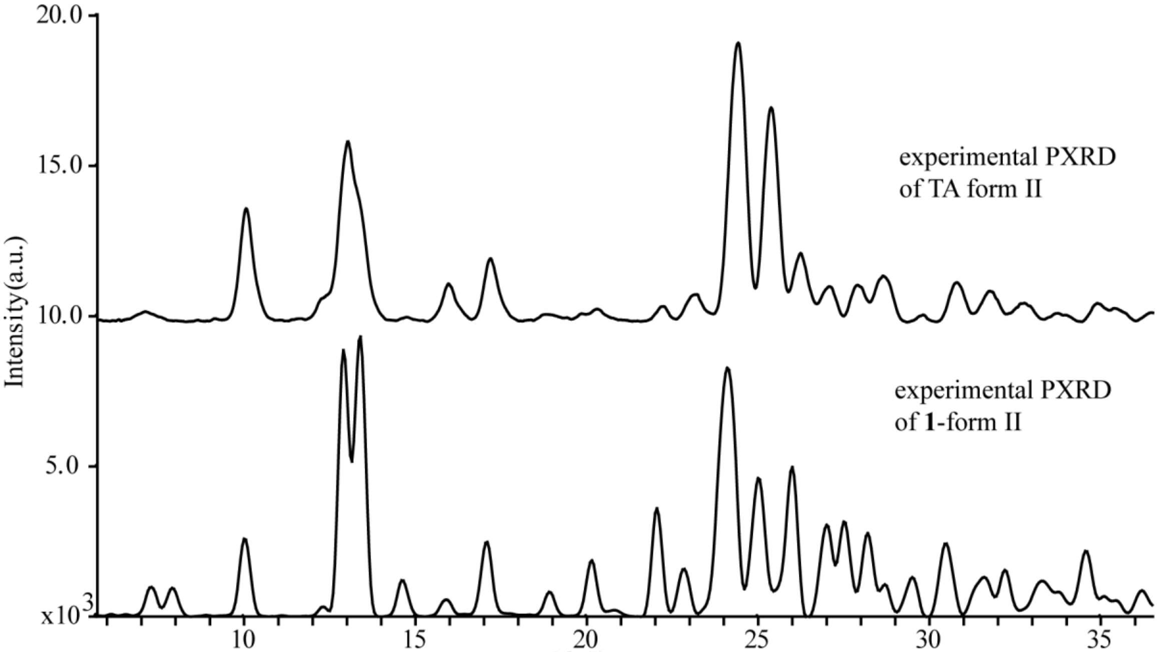

Figure 4.12. Experimental PXRD patterns of analogue **1**-form II (bottom) and TA form II (top) obtained through PIHn.

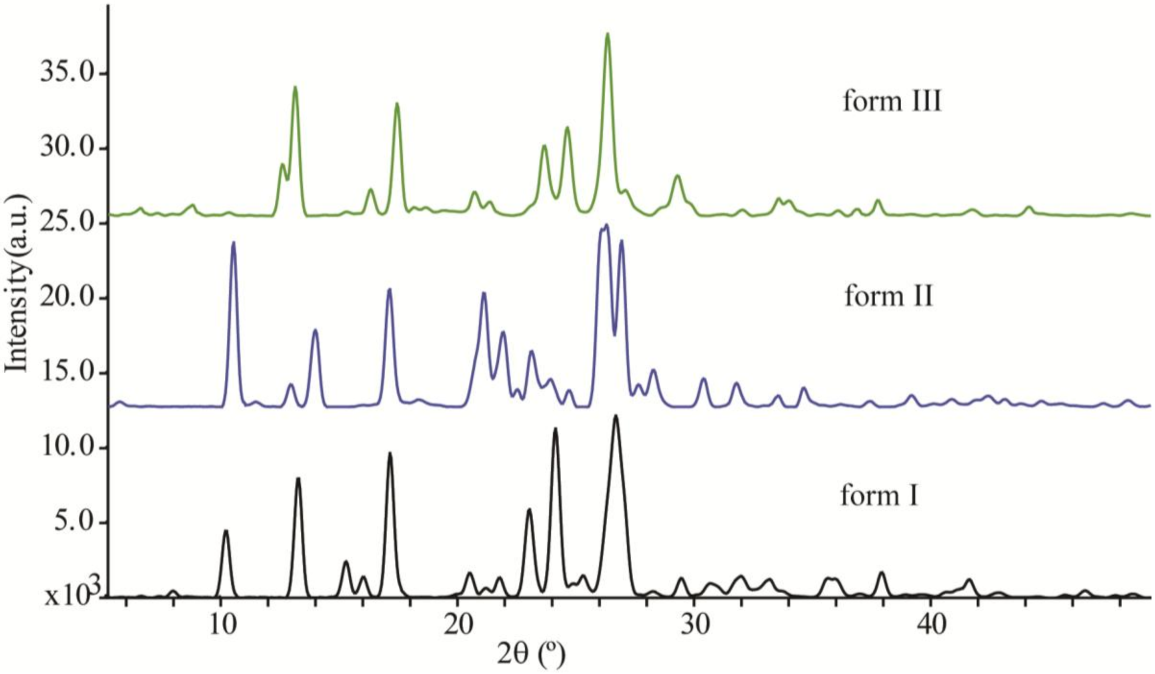

Figure 4.13. Experimental PXRD patterns of the polymorphs of analogue **2** obtained through PIHn.

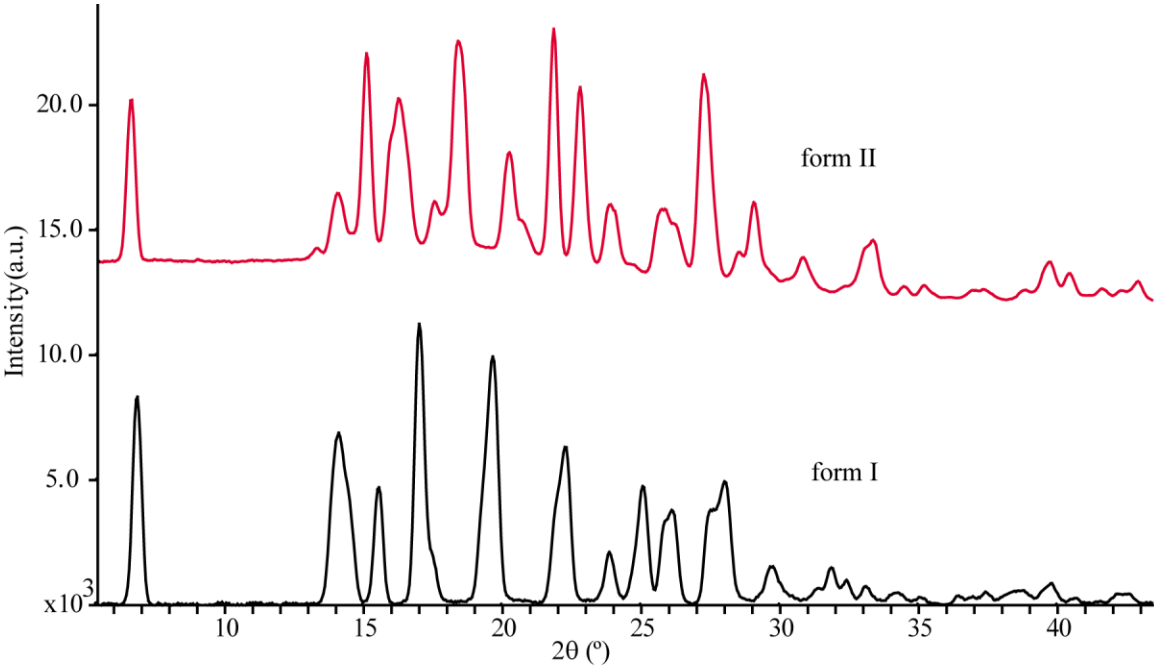

Figure 4.14. Experimental PXRD patterns of the polymorphs of analogue **3** obtained through PIHn.

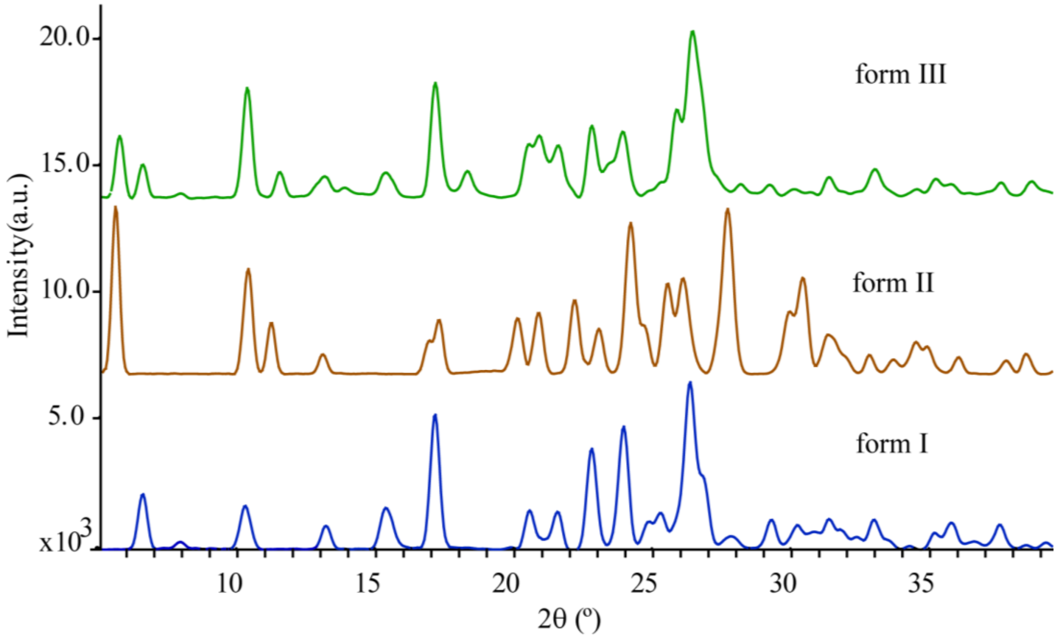

Figure 4.15. Experimental PXRD patterns of the polymorphs of analogue **4** obtained through PIHn.

Table 4.2. Summary of crystallographic data for analogue **1** polymorphs I-III.

form	**I**	**II**	**III**
crystal system	monoclinic	monoclinic	triclinic
space group	$P2_1/n$	$P2_1/n$	$P\bar{1}$
temperature (K)	95	85	95
***a* (Å)**	4.88	3.89	6.83
***b* (Å)**	31.85	22.20	6.83
***c* (Å)**	8.12	14.33	29.53
α (°)	90	90	85.56
β (°)	104.10	94.99	85.53
γ (°)	90	90	67.60
cell volume (Å^3)	1225.2	1234.7	1270.0
calc. density (g/cm^3)	1.665	1.650	1.601
Z	4	4	4
Z′	1	1	2
unique reflections	1967	2261	1693
R	5.67	3.39	8.39
R_w	14.85	8.58	28.42

Table 4.3. Torsion angles (τ_1, τ_2, and τ_3) for molecules in the asymmetric unit of analogue **1** and TA polymorphs. Letters *a* and *b* represent different conformers in structures where $Z' > 1$.

analogue 1	**τ_1(°)**	**τ_2(°)**	**τ_3(°)**	**TA**	**τ_1(°)**	**τ_2(°)**	**τ_3(°)**
I	-0.61	107.93	1.01	**I**	0.45	107.74	1.11
II	10.93	41.04	-4.14	**II**	7.99	42.23	-3.48
III *a*	46.99	8.02	-3.52	**III *a***	1.72	-57.64	3.45
III *b*	10.45	45.18	-0.34	**III *b***	17.67	44.19	-1.97

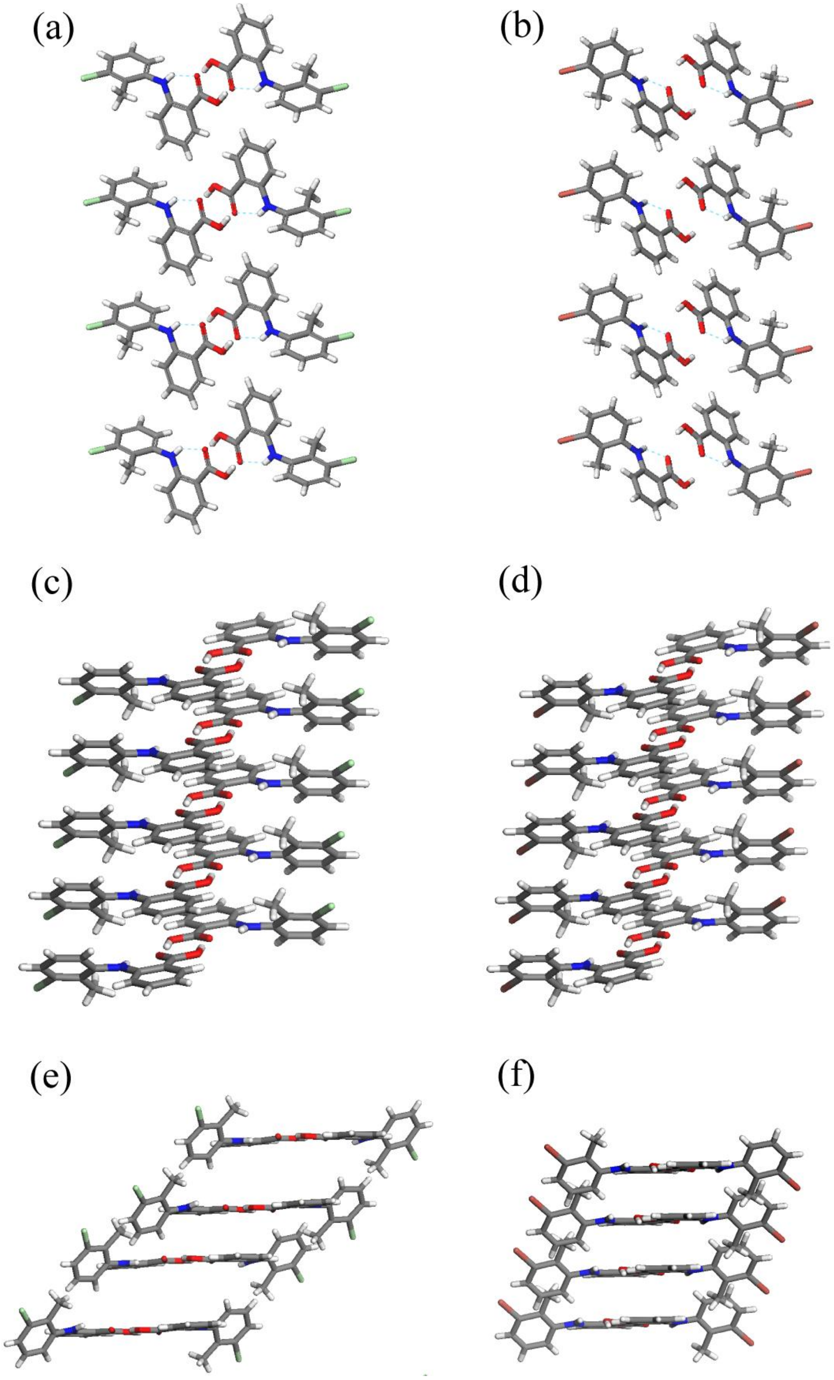

Figure 4.16. Comparison of the molecular packing and hydrogen bonding motif in (a) **1**-form I along the *a*-axis, (b) TA form I along the *a*-axis, (c) **1**-form II along the *c*-axis, (d) TA form II along the *c*-axis, (e) **1**-form III along the *b*-axis, and (f) TA form III along the *a*-axis.

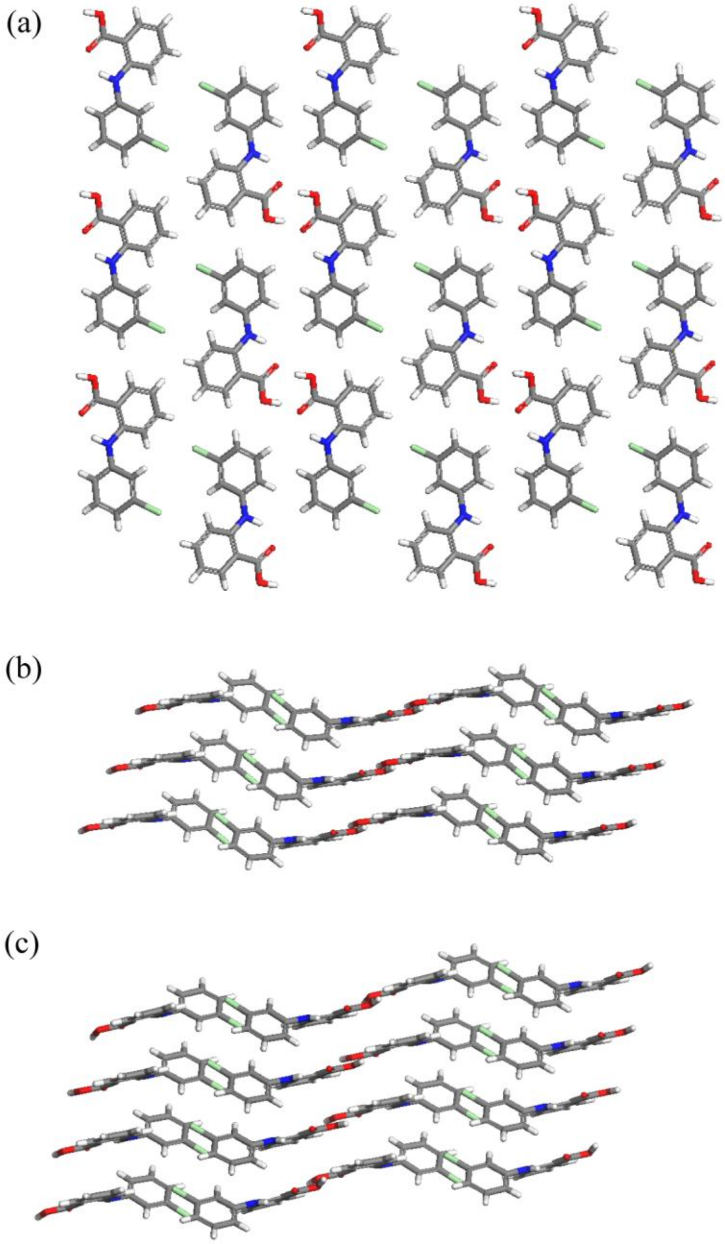

Figure 4.17. Molecular packing and hydrogen bonding motif of (a) **2**-form I along the *a*-axis, (b) **2**-form II along the *a*-axis, and (c) **2**-form IV along the *b*-axis.

Table 4.4. Summary of crystallographic data for analogue **2** polymorphs I, II, and IV.

form	**I**	**II**	**IV**
crystal system	triclinic	triclinic	triclinic
space group	$P\bar{1}$	$P\bar{1}$	$P\bar{1}$
temperature (K)	85	253	187
a **(Å)**	3.81	4.29	8.70
b **(Å)**	11.13	8.70	17.80
c **(Å)**	13.25	15.79	23.37
α **(°)**	91.31	101.46	105.72
β **(°)**	90.82	90.97	91.76
γ **(°)**	97.69	99.14	103.66
cell volume (Å^3)	555.9	570.2	3369.1
calc. density (g/cm^3)	1.480	1.443	1.465
Z	2	2	12
Z′	1	1	6
unique reflections	1962	2002	11707
R	6.4	4.1	4.6
R$_w$	18.3	11.8	10.7

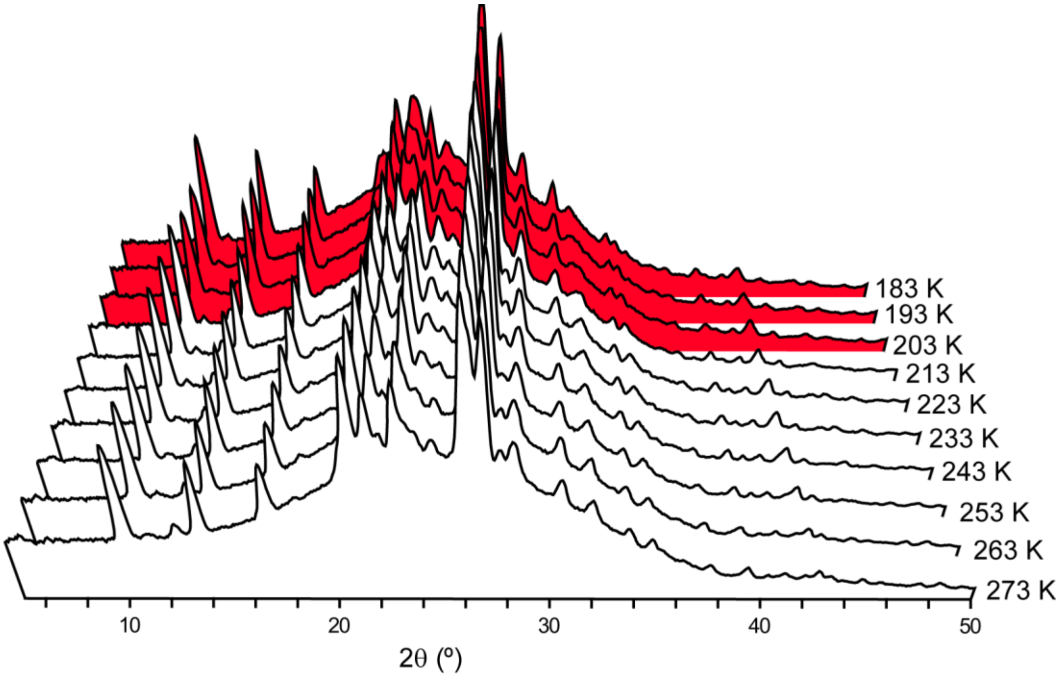

Figure 4.18. VTPXRD starting with **2**-form II and cooling to 183 K allowed access to **2**-form IV.

Table 4.5. Torsion angles (τ_1, τ_2, and τ_3) for molecules in the asymmetric unit of analogue **2** polymorphs I-II and IV. Letters *a*, *b, c, d, e,* and *f* represent different conformers in the structure where $Z' > 1$.

analogue 2	τ_1(°)	τ_2(°)	τ_3(°)
I	-6.71	140.50	3.41
II	-1.88	129.78	1.10
IV *a*	0.95	-129.39	-2.87
IV *b*	-4.13	131.90	-0.86
IV *c*	-1.11	132.33	-0.40
IV *d*	-0.12	132.70	0.54
IV *e*	-0.64	-130.28	-4.55
IV *f*	1.06	-132.75	0.25

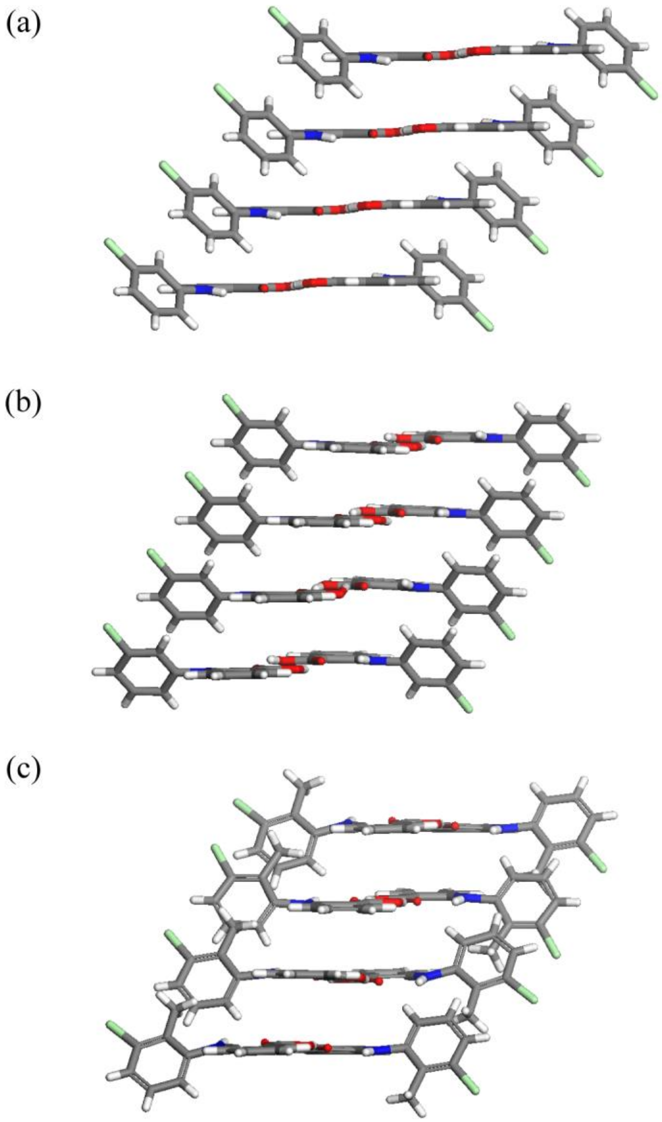

Figure 4.19. Comparison of the molecular packing and hydrogen bonding motif in (a) **2**-form II along the *b*-axis, (b) **2**-form IV along the *a*-axis and (c) TA form IV along the *a*-axis.

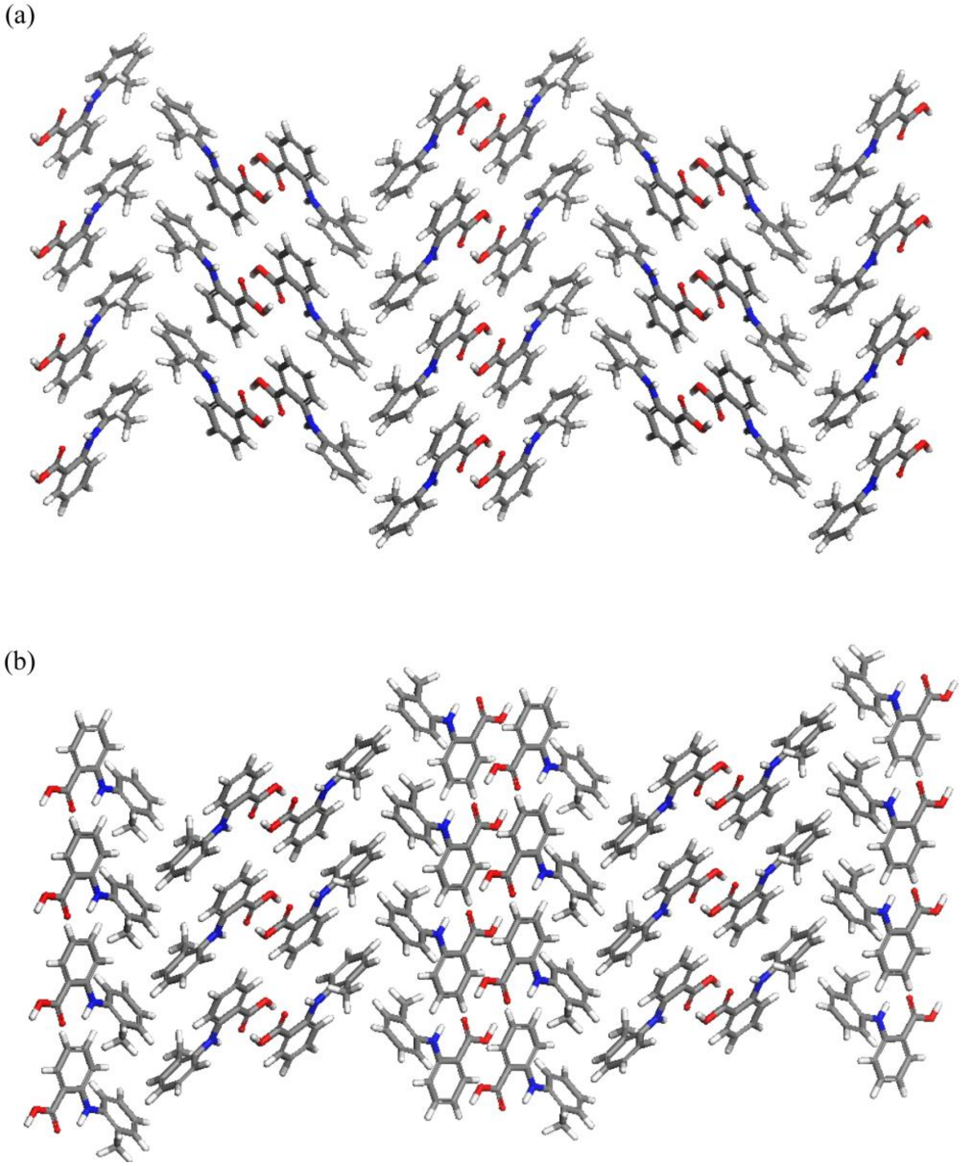

Figure 4.20. Molecular packing and hydrogen bonding motif of (a) **3**-form I and (b) **3**-form II along the *a*-axis.

Table 4.6. Summary of crystallographic data for analogue **3** polymorphs I-II.

form	**I**	**II**
crystal system	monoclinic	monoclinic
space group	*C*2/c	$P2_1$/c
temperature (K)	95	95
a **(Å)**	11.75	7.15
b **(Å)**	7.42	25.06
c **(Å)**	26.52	7.37
α **(°)**	89.99	90
β **(°)**	100.32	118.38
γ **(°)**	89.99	90
cell volume (Å^3)	2271.0	1164.7
calc density (g/cm^3)	1.329	1.298
Z	8	4
Z’	1	1
unique reflections	1909	2050
R	3.68	7.17
R$_w$	10.18	19.97

Table 4.7. Torsion angles (τ_1, τ_2, and τ_3) for molecules in the asymmetric unit of analogue **3** polymorphs I-II.

analogue 3	**τ_1(°)**	**τ_2(°)**	**τ_3(°)**
I	-10.54	-47.51	2.77
II	-4.71	-48.90	3.32

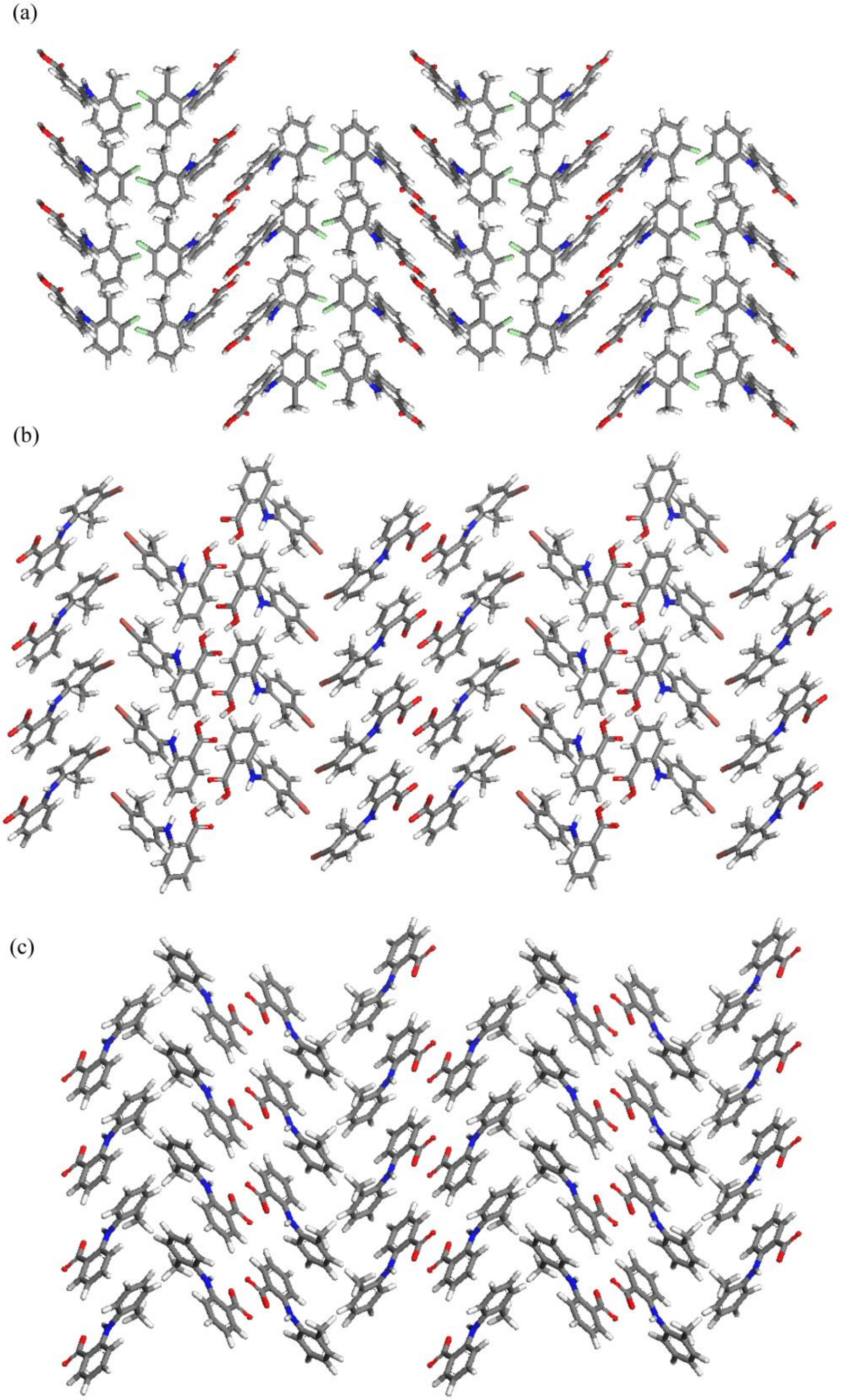

Figure 4.21. Comparison of the molecular packing and hydrogen bonding motif in (a) TA form III, (b) **1**-form III and (c) **3**-form I along the *a*-axis.

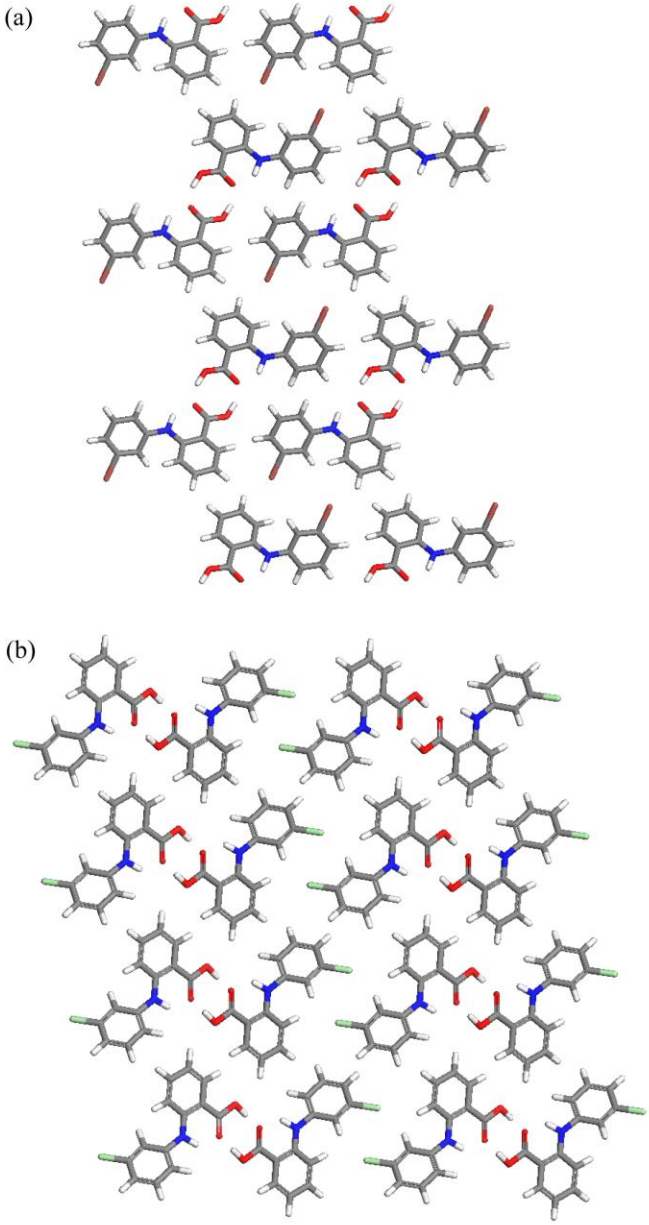

Figure 4.22. Comparison of the molecular packing and hydrogen bonding motif in (a) **4**-form I and (b) **2**-form II along the *a*-axis.

Table 4.8. Summary of crystallographic data for analogue **4**.

	I
crystal system	triclinic
space group	$P\bar{1}$
temperature (K)	85
a **(Å)**	3.87
b **(Å)**	11.19
c **(Å)**	13.29
α **(°)**	90.58
β **(°)**	91.09
γ **(°)**	98.17
cell volume (Å^3)	569.35
calc. density (g/cm^3)	1.704
Z	2
Z'	1
unique reflections	2016
R	11.77
R$_w$	27.44

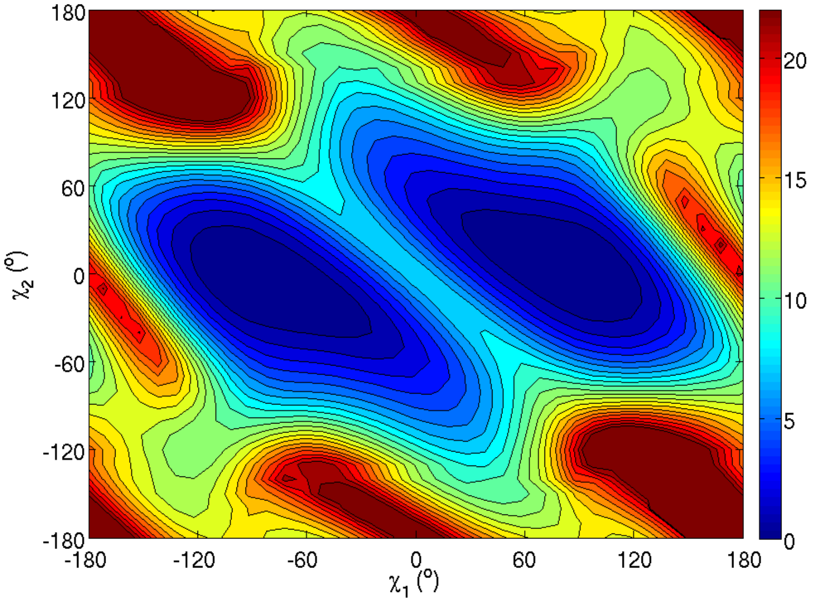

Figure 4.23. Relaxed potential energy 2D surface scans for TA.

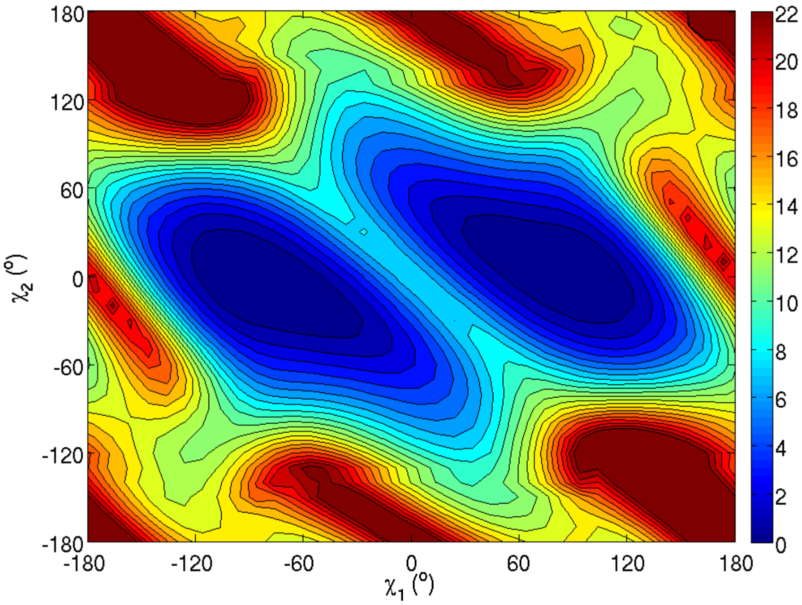

Figure 4.24. Relaxed potential energy 2D surface scans for MA.

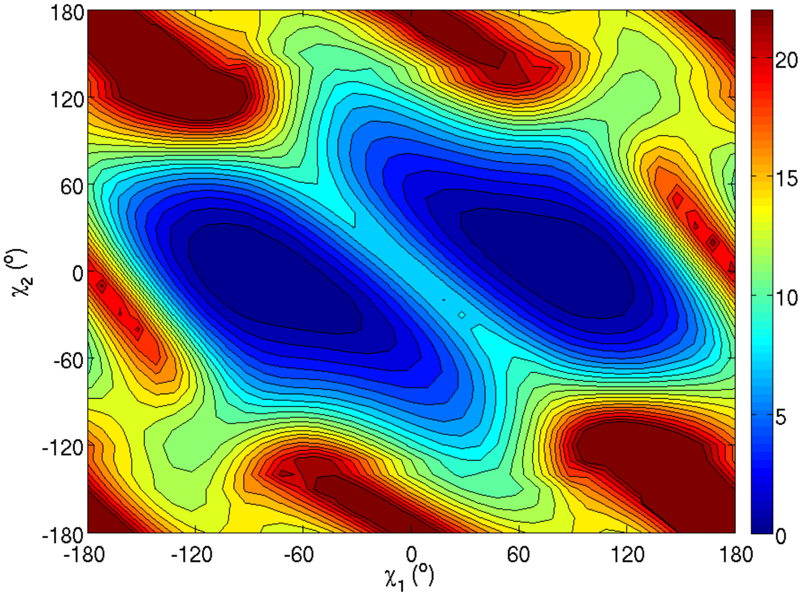

Figure 4.25. Relaxed potential energy 2D surface scans for analogue **1**. Conformations present in structurally characterized polymorphs of analogue **1** are listed in Table 4.3.

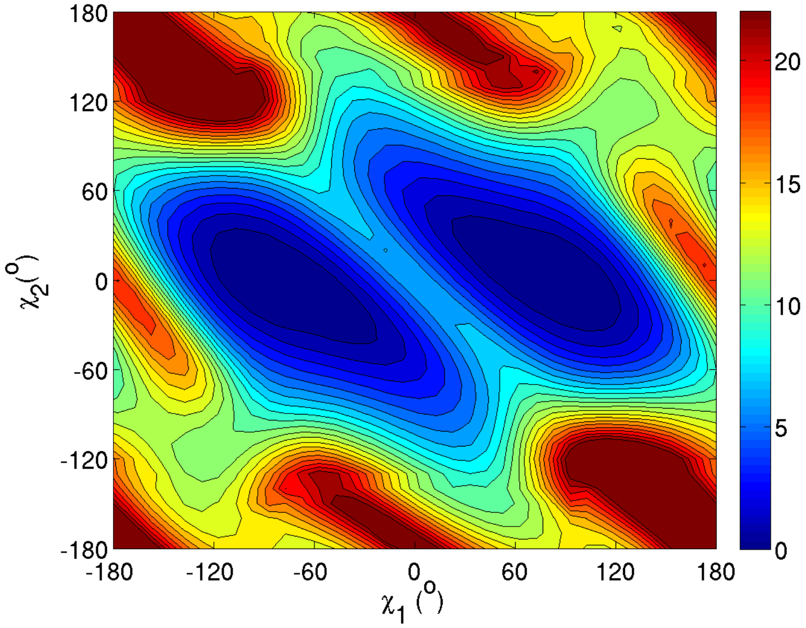

Figure 4.26. Relaxed potential energy 2D surface scans for analogue **3**. Conformations present in structurally characterized polymorphs of analogue **3** are listed in Table 4.7.

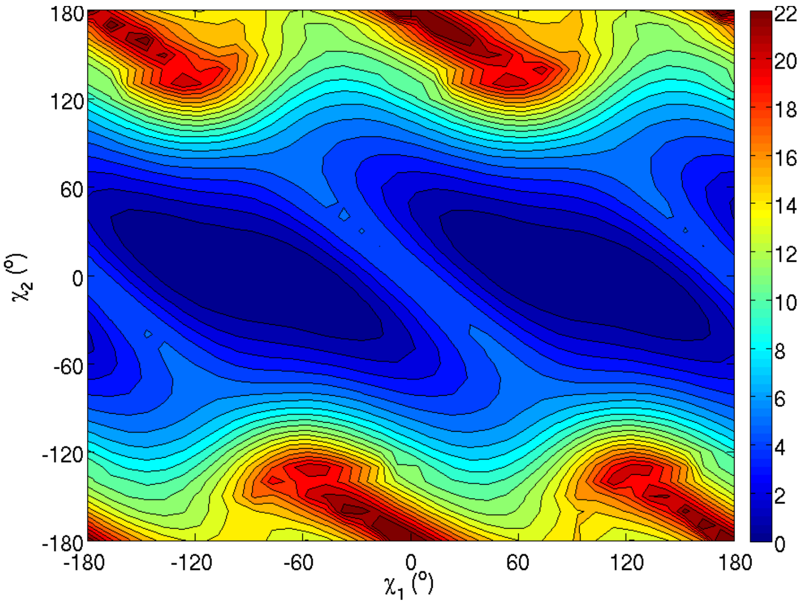

Figure 4.27. Relaxed potential energy 2D surface scans for FA.

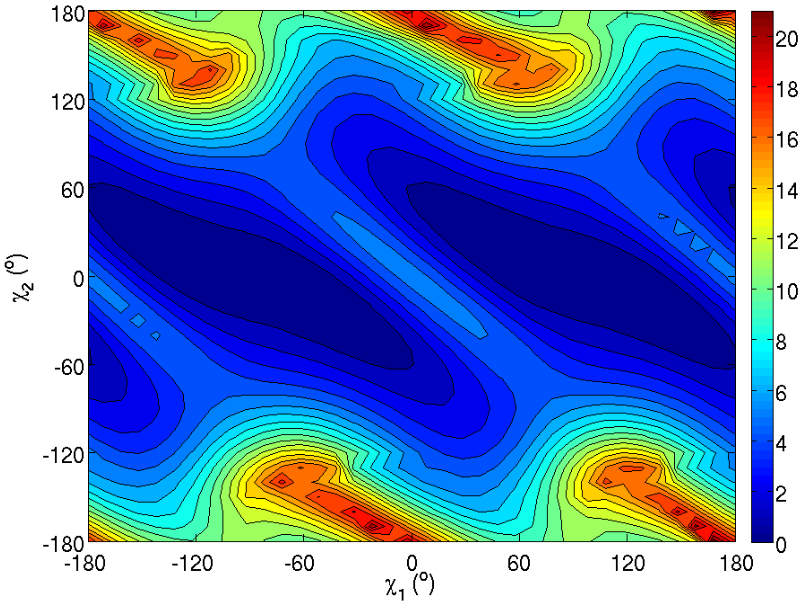

Figure 4.28. Relaxed potential energy 2D surface scans for analogue **2**. Conformations present in structurally characterized polymorphs of analogue **2** are listed in Table 4.5.

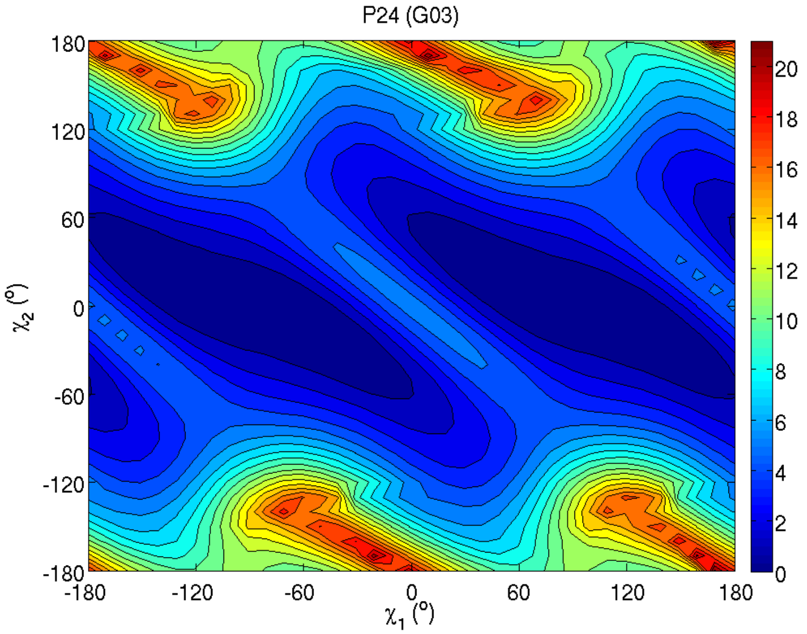

Figure 4.29. Relaxed potential energy 2D surface scans for analogue **4**.

Table 4.9. Difference in the relaxed potential energy (ΔE_{conf}) among the experimentally determined conformations for each analogue and the lowest energy conformation calculated in Gaussian03.

	ΔE_{conf} (kcal/mol)
TA form I	0.2
TA form II	0.8
TA form III *a*	0.5
TA form III *b*	0.4
TA form IV *a*	0.3
TA form IV *b*	0.1
TA form IV *c*	0.2
1-form I	0.2
1-form II	0.9
1-form III *a*	1.9
1-form III *b*	0.6
2-form I	0.5
2-form II	0.3
2-form IV *a*	0.4
2-form IV *b*	0.2
2-form IV *c*	0.2
2-form IV *d*	0.2
2-form IV *e*	0.4
2-form IV *f*	0.4
3-form I	0.3
3-form II	0.6
4-form I	0.2
MA form I	0.2
FA form I *a*	0.1
FA form I *b*	0.1

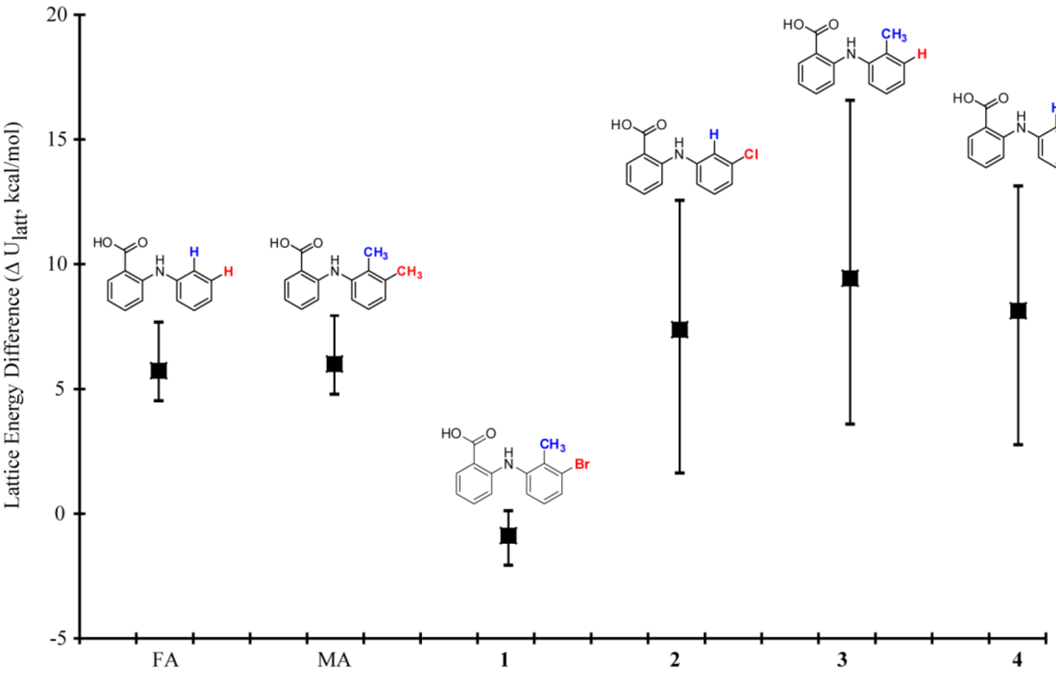

Figure 4.30. Lattice energy (ΔU_{latt}) difference distribution plot from lattice energy substitution calculations for analogues FA, MA, and **1-4** in the four crystal structures observed experimentally for TA. The maximum, average and minimum values for the lattice energy difference among the four 'virtual' structures are shown in the graph.

Table 4.10. Lattice energy difference calculated ($\Delta\ U_{latt}$) from lattice energy substitution for analogues FA, MA, and **1-4** in the four crystal structures observed experimentally for TA in Material Studio using Compass force field.

	TA-form I	TA-form II	TA-form III	TA-form IV
MA-$\Delta U_{lattice}$ (kcal/mol)	7.9	6.2	4.8	5.1
FA-$\Delta U_{lattice}$ (kcal/mol)	7.7	5.9	4.5	4.8
1-$\Delta U_{lattice}$ (kcal/mol)	0.1	0.1	-2.1	-1.6
2-$\Delta U_{lattice}$ (kcal/mol)	12.6	1.6	6.3	9.1
3-$\Delta U_{lattice}$ (kcal/mol)	16.6	3.6	7.4	10.2
4-$\Delta U_{lattice}$ (kcal/mol)	13.1	2.8	7.3	9.4

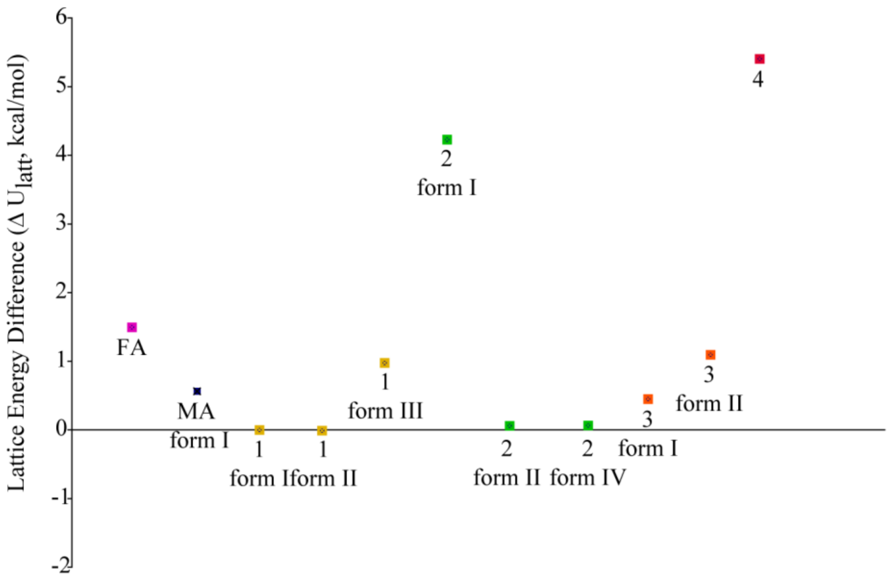

Figure 4.31. Lattice energy difference (ΔU$_{latt}$) from lattice energy substitution calculations of TA in the ordered crystal structures observed experimentally for analogues FA, MA, and **1-4**. The maximum, average and minimum values for the lattice energy difference are shown in the graph.

Table 4.11. Lattice energy difference calculated (Δ U$_{latt}$) from lattice energy substitution of TA in the crystal structures observed experimentally for analogues FA, MA, and **1-4** in Material Studio using Compass force field.

	FA		
ΔU$_{lattice}$ (kcal/mol)	1.4		
	MA form I		
ΔU$_{lattice}$ (kcal/mol)	0.6		
	1-form I	**1-form II**	**1-form III**
ΔU$_{lattice}$ (kcal/mol)	0	0	1.0
	2-form I	**2-form II**	**2-form IV**
ΔU$_{lattice}$ (kcal/mol)	4.2	0.1	0.1
	3-form I	**3-form II**	
ΔU$_{lattice}$ (kcal/mol)	0.5	1.1	
	4		
ΔU$_{lattice}$ (kcal/mol)	5.4		

4.5 References

1. Bernstein, J.; *Polymorphism in Molecular Crystals*; Oxford University Press: Oxford Clarendon Press, New York, **2002**.

2. Byrn, S.; Pfeiffer, R.; Ganey, M.; Hoiberg, C.; Poochikian, G., Pharmaceutical Solids - a Strategic Approach to Regulatory Considerations. *Pharmaceutical Research* **1995,** 12, (7), 945-954.

3. Brittain, H. G.; *Polymorphism in Pharmaceutical Solids*; M. Dekker: New York, **1999**.

4. Motherwell, W. D. S.; Ammon, H. L.; Dunitz, J. D.; Dzyabchenko, A.; Erk, P.; Gavezzotti, A.; Hofmann, D. W. M.; Leusen, F. J. J.; Lommerse, J. P. M.; Mooij, W. T. M.; Price, S. L.; Scheraga, H.; Schweizer, B.; Schmidt, M. U.; van Eijck, B. P.; Verwer, P.; Williams, D. E., Crystal structure prediction of small organic molecules: a second blind test. *Acta Crystallographica Section B-Structural Science* **2002,** 58, 647-661.

5. Gavezzotti, A., Generation of Possible Crystal-Structures from Molecular-Structure for Low-Polarity Organic Compounds. *Journal of the American Chemical Society* **1991,** 113, (12), 4622-4629.

6. Holden, J. R.; Du, Z. Y.; Ammon, H. L., Prediction of Possible Crystal-Structures for C-containing, H-containing, N-Containing, O-containing, and F-containing Organic Compounds. *Journal of Computational Chemistry* **1993,** 14, (4), 422-437.

7. Leusen, F. J. J., Ab initio prediction of polymorphs. *Journal of Crystal Growth* **1996,** 166, (1-4), 900-903.

8. Lommerse, J. P. M.; Motherwell, W. D. S.; Ammon, H. L.; Dunitz, J. D.; Gavezzotti, A.; Hofmann, D. W. M.; Leusen, F. J. J.; Mooij, W. T. M.; Price, S. L.; Schweizer, B.; Schmidt, M. U.; van Eijck, B. P.; Verwer, P.; Williams, D. E., A test of crystal structure prediction of small organic molecules. *Acta Crystallographica Section B-Structural Science* **2000,** 56, 697-714.

9. Williams, D. E.; Starr, T. L., Calculations of Crystal Structures of Hydrocarbons by Molecular Packing Analysis. *Computers & Chemistry* **1977,** 1, (3), 173-177.

10. Roy, S.; Matzger, A. J., Unmasking a Third Polymorph of a Benchmark Crystal-Structure-Prediction Compound. *Angewandte Chemie-International Edition* **2009,** 48, (45), 8505-8508.

11. Bacchi, A.; Mori, G.; Pelizzi, G.; Pelosi, G.; Nebuloni, M.; Panzone, G. B., Polymorphism-Structure Relationships of Rifamexil, An Antibiotic Rifamycin Devirative. *Molecular Pharmacology* **1995,** 47, (3), 611-623.

12. Gelbrich, T.; Hursthouse, M. B., Systematic investigation of the relationships between 25 crystal structures containing the carbamazepine molecule or a close analogue: a case study of the XPac method. *Crystengcomm* **2006,** 8, (6), 448-460.

13. Kitamura, M.; Hara, T., Dependence of polymorphism on molecular structure of BPT esters. *Crystal Growth & Design* **2007,** 7, (9), 1575-1579.

14. López-Mejías, V.; Kampf, J. W.; Matzger, A. J., Polymer-Induced Heteronucleation of Tolfenamic Acid: Structural Investigation of a Pentamorph. *Journal of the American Chemical Society* **2009,** 131, (13), 4554.

15. Lutker, K. M.; Matzger, A. J., Crystal Polymorphism in a Carbamazepine Derivative: Oxcarbazepine. *Journal of Pharmaceutical Sciences* 99, (2), 794-803.

16. Lutker, K. M.; Tolstyka, Z. P.; Matzger, A. J., Investigation of a privileged polymorphic motif: A dimeric ROY derivative. *Crystal Growth & Design* **2008,** 8, (1), 136-139.

17. Mesley, R. J.; Houghton, E. E., Infrared Identification of Pharmaceutically Important Sulphonamides with Particular Reference to Occurrence of Polymorphism. *Journal of Pharmacy and Pharmacology* **1967,** 19, (5), 295.

18. Borchardt, T. B.; Stowell, J. G.; Byrn, S. R., The Crystallization of 5-Methyl-2-[(2-nitrophenyl)amino]-3-thiophenecarbonitrile in the Presence of Structurally Similar Compounds. *Molecular Crystals and Liquid Crystals Science and Technology Section a-Molecular Crystals and Liquid Crystals* **1998,** 313, 271-276.

19. Chen, S. A.; Xi, H. M.; Yu, L., Cross-nucleation between ROY polymorphs. *Journal of the American Chemical Society* **2005,** 127, (49), 17439-17444.

20. He, X. R.; Griesser, U. J.; Stowell, J. G.; Borchardt, T. B.; Byrn, S. R., Conformational color polymorphism and control of crystallization of 5-methyl-2-[(4-methy1-2-nitrophenyl)amino]-3-thiophenecarbonitrile. *Journal of Pharmaceutical Sciences* **2001,** 90, (3), 371-388.

21. Li, H.; Stowell, J. G.; Borchardt, T. B.; Byrn, S. R., Synthesis, conformational polymorphism, and construction of a G-T diagram of 2-[(2-nitrophenyl)amino]-3-thiophenecarbonitrile. *Crystal Growth & Design* **2006,** 6, (11), 2469-2474.

22. Li, H.; Stowell, J. G.; He, X. R.; Morris, K. R.; Byrn, S. R., Investigations on solid-solid phase transformation of 5-methyl-2-[(4-methyl-2-nitrophenyl)aminol-3-thiophenecarbonitrile. *Journal of Pharmaceutical Sciences* **2007,** 96, (5), 1079-1089.

23. Harrison, W. T. A.; Yathirajan, H. S.; Anilkumar, H. G., An orthorhombic polymorph of 10,11-dihydrocarbamazepine. *Acta Crystallographica Section C-Crystal Structure Communications* **2006,** 62, O240-O242.

24. Hempel, A.; Camerman, N.; Camerman, A.; Mastropaolo, D., Oxcarbazepine: structure and anticonvulsant activity. *Acta Crystallographica Section E-Structure Reports Online* **2005,** 61, O1313-O1315.

25. Leech, C. K.; Florence, A. J.; Shankland, K.; Shankland, N.; Johnston, A., 10,11-dihydrocarbamazepine (form III). *Acta Crystallographica Section E-Structure Reports Online* **2007,** 63, O675-O677.

26. Mei, X. F.; August, A. T.; Wolf, C., Regioselective copper-catalyzed amination of chlorobenzoic acids: Synthesis and solid-state structures of N-aryl anthranilic acid derivatives. *Journal of Organic Chemistry* **2006,** 71, (1), 142-149.

27. Wolf, C.; Liu, S. L.; Mei, X. F.; August, A. T.; Casimir, M. D., Regioselective copper-catalyzed amination of bromobenzoic acids using aliphatic and aromatic amines. *Journal of Organic Chemistry* **2006,** 71, (8), 3270-3273.

28. Lang, M. D.; Grzesiak, A. L.; Matzger, A. J., The use of polymer heteronuclei for crystalline polymorph selection. *Journal of the American Chemical Society* **2002,** 124, (50), 14834-14835.

29. Price, C. P.; Grzesiak, A. L.; Matzger, A. J., Crystalline polymorph selection and discovery with polymer heteronuclei. *Journal of the American Chemical Society* **2005,** 127, (15), 5512-5517.

30. Mitchell-Koch, K. R.; Matzger, A. J., Evaluating computational predictions of the relative stabilities of polymorphic pharmaceuticals. *Journal of Pharmaceutical Sciences* **2008,** 97, (6), 2121-2129.

31. Price, S. L.; Stone, A. J.; Lucas, J.; Rowland, R. S.; Thornley, A. E., The Nature of Cl···Cl Intermolecular Interactions. *Journal of the American Chemical Society* **1994,** 116, (11), 4910-4918.

32. Capacci-Daniel, C.; Dehghan, S.; Wurster, V. M.; Basile, J. A.; Hiremath, R.; Sarjeant, A. A.; Swift, J. A., Halogen/methyl exchange in a series of isostructural 1,3-bis(m-dihalophenyl) ureas. *Crystengcomm* **2008,** 10, (12), 1875-1880.

33. Desiraju, G. R.; Sarma, J., The Chloro-methyll Exchange Rule and Its Volations in the Packing of Organic Molecular Solids. *Proceedings of the Indian Academy of Sciences-Chemical Sciences* **1986,** 96, (6), 599-605.

34. Sbit, M.; Dupont, L.; Dideberg, O.; Liegeois, J. F.; Delarge, J., Structure of 2-diphenylamino-carboxylic acid. *Acta Crystallographica Section C-Crystal Structure Communications* **1987,** 43, 926-928.

35. Roy, S.; Banerjee, R.; Nangia, A.; Kruger, G. J., Conformational, concomitant polymorphs of 4,4-diphenyl-2,5-cyclohexadienone: Conformation and lattice energy compensation in the kinetic and thermodynamic forms. *Chemistry-a European Journal* **2006,** 12, (14), 3777-3788.

36. Anderson, K. M.; Goeta, A. E.; Steed, J. W., Supramolecular synthon frustration leads to crystal structures with Z ' > 1. *Crystal Growth & Design* **2008,** 8, (7), 2517-2524.

CHAPTER 5

PEERING AT A BURIED POLYMER-CRYSTAL INTERFACE: PROBING HETEROGENEOUS NUCLEATION BY SUM FREQUENCY GENERATION VIBRATION SPECTROSCOPY

PUBLISHED IN *LANGMUIR* 2011, *27*, 2162-2165.

5.1 Introduction

The formation of a crystal from a supersaturated solution requires the assembly of molecules to form a structured motif that, at a critical size, leads to nucleation; this early stage of self-assembly typically dictates the ultimate solid-state form.[1] Nucleation is generally a heterogeneous process, during which nuclei develop on a surface so that the entropic penalty associated with ordering can be offset by favorable enthalpic interactions at the interface. These assembly processes on a foreign surface can occur with different degrees of specificity ranging from non-specific adsorption to the oriented growth of crystals on the nucleating surface.[2] The appropriate choice of heterogeneous nucleation promoters can exercise control over crystal polymorphism by manipulating the nature of molecular recognition events occurring at the crystal-heteronucleant interface.

Recently, sum frequency generation vibrational spectroscopy (SFG-VS) has emerged as a valuable analytical technique for examining molecular structures and orientation distributions at interfaces with submonolayer sensitivity.[34-17] By exploiting a second-order nonlinear optical process that provides sensitivity to vibrational modes taking place in noncentrosymmetric environments,[3-17] SFG-VS offers the unique opportunity to unravel the interactions governing phase selection at the polymer-crystal interface during the process of polymer-induced heteronucleation (PIHn). PIHn has recently been established as a powerful screening technique for the novel solid-form discovery of single[18-20] and multicomponent[21, 22] composition in addition to demonstrating promise in metal-organic systems.[23]

Acetaminophen (ACM, Figure 5.1), a common analgesic and antipyretic drug that crystallizes in two stable forms,[24, 25] was utilized as the model compound in this study. The less thermodynamically stable orthorhombic form was shown to have better physical properties when compared to the pharmaceutically distributed monoclinic form. Therefore, the selective production of different ACM forms has been the subject of numerous investigations aimed at elucidating the properties of different ACM polymorphs and exploring their commercial viability. ACM heteronucleates from aqueous solution in the less thermodynamically stable crystal form, the orthorhombic form, on poly(methyl methacrylate) (PMMA, Figure 5.1), whereas the monoclinic crystal form is observed on poly(*n*-butyl methacrylate) (PBMA, Figure 5.1).[18] Because the polymers employed are completely insoluble under these crystallization conditions, the differences in the polymorphs observed are a product of the unique and directional interfacial interactions between ACM and each heteronucleant surface. Revealing the differences in the SFG vibrational spectra collected from the interfaces between these two polymers and ACM crystals of different polymorphs should provide a better understanding of the molecular interactions occurring at each interface as well as suggest a pathway for the selective formation of the metastable polymorph.

5.2 Experimental Section

5.2.1 Materials

ACM was obtained from ICN Biomedicals Inc. (Irvine, CA) and was stored at room temperature. Deuterated PMMA was purchased from Polymer Source Inc. (Montreal, Canada) and was stored at room temperature. Deuterated PBMA was synthesized following a previously reported method.[26]

5.2.2 Preparation of Polymer Thin Films

All polymer samples were prepared by spin coating 2 w/w % polymer solutions onto optically clear right-angle CaF2 prisms (Altos Photonics, Bozeman, MT) at 2500 rpm on a Speedline Technologies spin coater. The thicknesses of both PMMA (Aldrich, MW15 000) and PBMA (Scientific Polymer Products Inc.) thin films were approximately 100 nm.

5.2.3 Crystallizations From Aqueous Solution

The ACM crystals examined were grown from aqueous supersaturated solutions (17 mg/mL at 25 °C) by submerging the entire prism with the polymer film in the supersaturated solution overnight. Samples were left to dry in air prior to any measurement. Raman spectroscopy confirmed that the ACM formed orthorhombic crystals on the PMMA surface and monoclinic crystals on the PBMA surfaces when grown from solution (Figure 5.2 and Table 5.1). Raman spectra were collected using a Renishaw inVia Raman microscope equipped with a Leica microscope, RenCam CCD detector, 633 nm He-Ne laser, 1200 lines/nm grating, and 50 μm slit. Spectra were collected in extended scan mode in the range of 3400–100 cm^{-1} and analyzed using Wire 2.0 software package. Calibration was performed using a silicon standard.

5.2.4 Crystallizations From Sublimation

Powdered ACM (~200 mg) was added to a sublimation chamber. Polymer coated films were suspended in contact with a flat aluminum plate in contact with an ice/water bath and sublimation proceed while the chamber was submerged in an oil bath at 150 °C under vacuum. After 15 min, all ACM had sublimed off the bottom of the chamber. Raman spectroscopy confirmed that only monoclinic crystals formed on both PMMA and PBMA surfaces when the ACM crystals were sublimed onto these polymer films.

5.2.5 Optical Microscopy

Images of monoclinic and orthorhombic ACM crystals grown from aqueous supersaturated solution onto PBMA and PMMA (Figure 5.3), respectively, were collected using a Spot Flex Mosaic 15.2 camera couple to a Leica DMLP microscope. Images were processed using Spot Advanced software (v. 4.6).

5.2.6 Sum Frequency Generation Measurements

The SFG-VS setup is a commercial system from Ekspla (Vilnius, Lithuania). The system is driven by a 20 ps 20 Hz Nd:YAG laser. A portion of the laser beam is frequency doubled to 532 nm and used for the visible beam in the SFG experiments. Another portion of the beam is tripled and passed to an Optical Parametric Generation/Optical Parametric Amplification stage. The tunable visible beam that is generated there is then sent to a Difference Frequency Generation stage with a portion of the fundamental 1064 nm beam to produce the tunable infrared beam that is used in the SFG experiment. The 532 nm beam and the tunable IR beam are mixed on the sample to produce SFG, which is then collected and sent through a computer controlled monochromator and detected by a PMT. The resolution of the system is ~5 cm^{-1}. SGF spectra of the polymer-crystal interface at different polarizations combinations were collected for the C=O region when the ACM crystals remained in contact while the polymer coated prism as illustrated in Figure 5.4.

5.2.7 Fourier Transform Infrared spectra of PMMA and PBMA in air

Fourier Transform Infrared (FTIR) spectra were collected from PMMA and PBMA in air using a Nicolet Magna 550 FTIR spectrometer (Figure 5.5). The C=O stretching peaks for PMMA and PBMA have similar peak centers, at 1734 and 1730 cm^{-1}, respectively. Since such signals are dominated by the C=O groups in the bulk, they are contributed from non-hydrogen bonded C=O groups.

5.2.8 Sum Frequency Generation spectra from PMMA and PBMA in air and in water

SFG spectra were collected from PMMA in air and in water using ssp and ppp polarization combinations (Figure 5.6 and Table 5.2). In air, both spectra were dominated by a peak centered at ~1730 cm^{-1}, showing that the surface C=O groups on PMMA in air are free (or non-hydrogen bonded) C=O groups. In water, the observed C=O peaks shifted to ~1715 cm^{-1}, indicating hydrogen bond formation between PMMA surface C=O groups and water molecules.

SFG spectra were collected from PBMA in air and in water using ssp and ppp polarization combinations (Figure 5.7 and Table 5.3). Deionized (DI) water was utilized in the experiment (18.2 $M\Omega^{-cm}$). DI water obtained from a Millipore ultrapure water system (Billerica, MA, USA). In air, both spectra were dominated by a peak centered at ~1730 cm^{-1}, showing that the surface C=O groups on PBMA in air are free (or non-hydrogen bonded) C=O groups. In water, the observed C=O peaks shifted to ~1710 cm^{-1}, indicating hydrogen bond formation between PBMA surface C=O groups and water molecules. The data was fitted to a single Lorentzian peak.

According to the fitted signal strength ratio χ_{ppp}/χ_{ssp}, it was found that the orientations of C=O groups in air and in water on PMMA and PBMA are not very different (Figure 5.8 and Tables 5.4 - 5.5).

5.3 Results and Discussion

Crystal formation in PIHn typically occurs on a polymer surface in contact with a supersaturated solution. Bulk polymer structure provides only limited insight into functionality displayed on the surface of a polymer; therefore, to elucidate the interactions occurring at an interface with a polymer in contact with solution, structure at the solid-liquid interface must be determined. Previous reports[15, 27, 28] on the surface chemical structure of PMMA and PBMA indicate that the PMMA surface is dominated by ester methyl groups oriented toward the surface normal in air. When PMMA is placed in contact with water, these ester methyl groups do not reorient. The PBMA surface in air is dominated by the side-chain terminal methyl groups, tilting toward the surface normal with a broad distribution. In water, these methyl groups still dominate the PBMA surface but reorient toward the surface with a much narrower orientation distribution. SFG-VS studies of PMMA and PBMA in the C=O stretching frequency region imply the presence of C=O groups on both PMMA and PBMA surfaces. By comparing the ratios of peak intensities in different polarization combinations, the orientation of C=O functional groups can be determined.[29] The C=O orientation is similar on both surfaces in both air and water (Figures 5.8 and Tables 5.4–5.5).

SFG spectra of the crystal/polymer interfaces with crystals grown from solution and dried in air are presented in Figure 5.9. In the SFG spectra of the interface between orthorhombic ACM crystals grown on PMMA, two peaks are observed (Figure 5.9, A and B). The peak at ~1730 cm^{-1} originates from the unbound C=O of the PMMA, as established by the FTIR spectra of bulk PMMA and PBMA, which presents a single peak around 1730 cm^{-1} corresponding to the C=O stretch (Figure 5.5). Raman vibrational spectroscopy confirms that ACM does not have a C=O stretch around 1730 cm^{-1} (Figure 5.2 and Table 5.1). The peak at 1705 cm^{-1} is produced by the hydrogen bonded C=O of PMMA with ACM. This clearly shows hydrogen bonding occurs between the ACM crystals and the C=O group in the case of PMMA.

In the SFG spectra obtained for the monoclinic ACM grown on PBMA (Figure 5.9, C and D), two peaks are observed. Similar to the case of ACM crystals growth on PMMA, the weak peak at ~1730 cm^{-1} belongs to the free C=O in PBMA. A very distinct peak at 1650 cm^{-1} is observed which originates from the amide I stretch of the ACM crystals. The absence of a peak at ~1705 cm^{-1} provides evidence that no hydrogen bonding exists between the PBMA C=O groups in the case of the monoclinic crystals. The absence of amide I signal from the orthorhombic ACM crystals grown on PMMA could be due to the orientation of the amide I transition moment in the orthorhombic crystals at the interface generating very little SFG signal, e.g., they may lie down at the interface. The differences in SFG spectra shown in Figure 5.9 imply that the ability of the ACM molecules in solution to hydrogen bond to the polymer C=O groups plays an important role in the polymorph selection process; this strong directional intermolecular interaction promotes the formation of the metastable form only in the case of PMMA.

In contrast to the above polymorph selection method, when the ACM crystals were grown by sublimation, only the monoclinic form was observed on both PMMA and PBMA, indicating that molecular interactions at the polymer-ACM solution interface and the polymer-ACM vapor interface are different. The ACM crystals grown by sublimation display distinctive SFG vibrational spectra (Figure 5.10) when compared to those formed from solution (Figure 5.9). No peak is observed at ~1705 cm^{-1} which confirms the absence of hydrogen bonding between the polymer C=O groups and the ACM crystals for the sublimed samples. The ACM amide I signal around 1650 cm^{-1} is prominent for ACM crystals sublimed on both the PMMA and PBMA. This is a clear indication that the absence of solvent, in this case water, plays an important role in the phase selection process.

The contrasting phase selection behavior for PIHn of ACM in the presence or absence of solvent presents two possibilities for the mechanism leading to the phase selective nucleation of one polymorph versus the other: a reorientation of the polymer surface functionality or a role for solvent during crystallization. Determination of the C=O orientation on the PMMA and PBMA surfaces in air and in water by SFG-VS suggest that these surfaces are not remarkably different, which should not lead to substantial differences in the initial interactions between such surface C=O groups and ACM molecules in solution. In contrast, SFG–VS studies on the C-H stretching frequency region indicate reorientation of terminal methyl groups only in the case of PBMA. Possibly the terminal methyl groups dominating the PBMA surface interact favorably with the hydrophobic groups on ACM, leading to the steric effects which changes the surface C=O orientation to hinder the hydrogen bond formation between PBMA and

ACM. For PMMA, the surface ester methyl groups would not have this steric effect, therefore the surface C=O groups can form hydrogen bonds with ACM, mediated by water, directing the formation of orthorhombic crystals in the case of PMMA.

5.4 Conclusions

This study highlights the ability of SFG to probe the distinct molecular interactions occurring at a solid-solid interface and demonstrates how the phase-selection mechanism of PIHn is most likely determined by the different structures of surface-dominating ester methyl groups on PMMA and ester butyl groups on PBMA, which may affect interfacial interactions. Additionally, this study emphasizes the dependence of the polymorph selection process on both the polymer and the solvent media because it is possible to change the solid form in the presence of different solvents. Understanding the process of PIHn in the context of the observed interfacial molecular interactions will ultimately allow the construction of an interface model with molecular-level detail and therefore will provide a rational basis for improving methods for polymorph discovery and selection based on the heteronucleation on polymers.

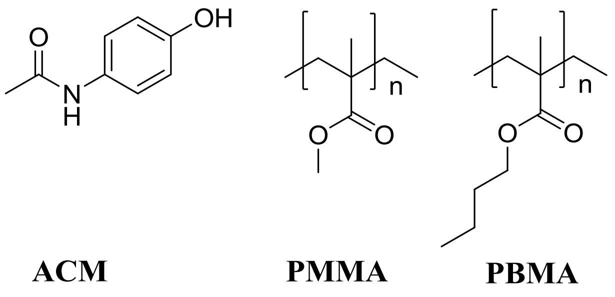

Figure 5.1. Chemical structures of acetaminophen (ACM), poly(methyl methacrylate) (PMMA) and poly(*n*-butyl methacrylate) (PBMA).

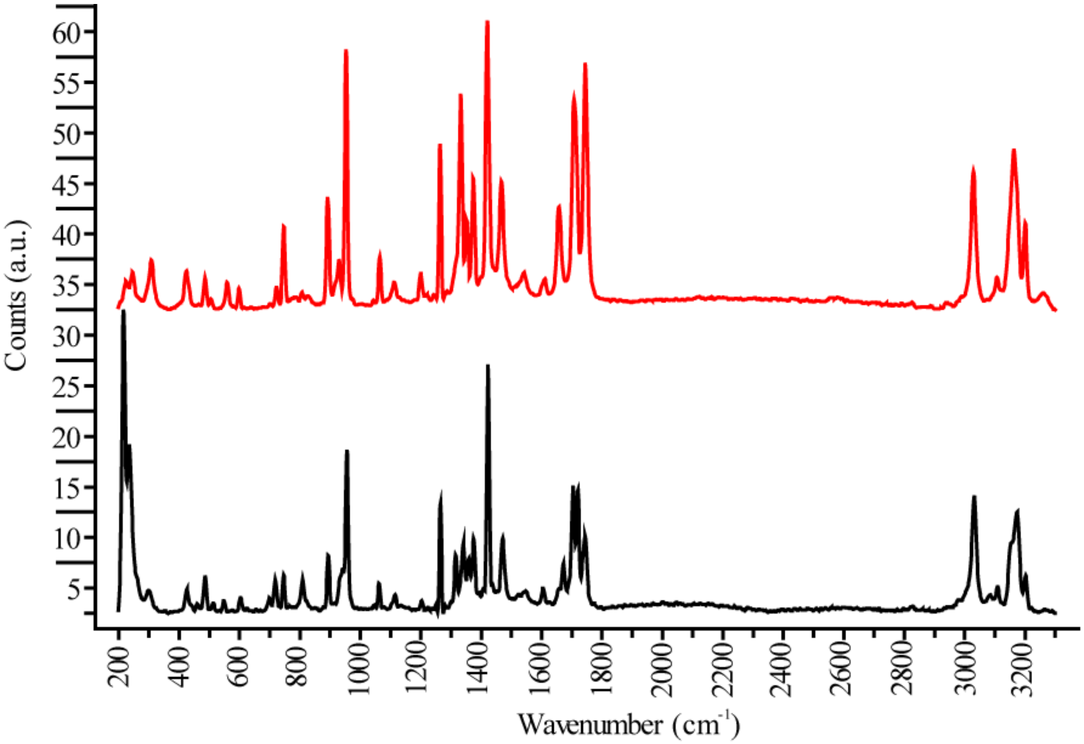

Figure 5.2. Raman spectra of monoclinic (top/red) and orthorhombic (bottom/black) acetaminophen crystals grown on PBMA and PMMA from an aqueous solution, respectively.

Table 5.1. Frequencies of Raman vibrational modes (cm^{-1}) of monoclinic and orthorhombic ACM grown from a supersaturated aqueous solution onto PBMA and PMMA, respectively, as well as PMMA and PBMA polymer that were used as heteronucleant.

monoclinic ACM (cm^{-1})	orthorhombic ACM (cm^{-1})	PMMA (cm^{-1})	PBMA (cm^{-1})
3330	3333	3007	2940
3067	3080	2958	2918
2935	2939	2848	2880
1650	1653	1730	1730
1621	1626	1451	1451
1613	1612	1245	1302
1563	1579	1124	1233
1517	1514	989	1124
1374	1377	812	1063
1325	1329	600	1003
1258	1282	121	968
1238	1247		846
1170	1222		601
1019	1171		121
970	1109		
858	1021		
835	968		
797	862		
651	800		
627	652		
503	626		
465	510		
391	394		
328	332		
203	122		

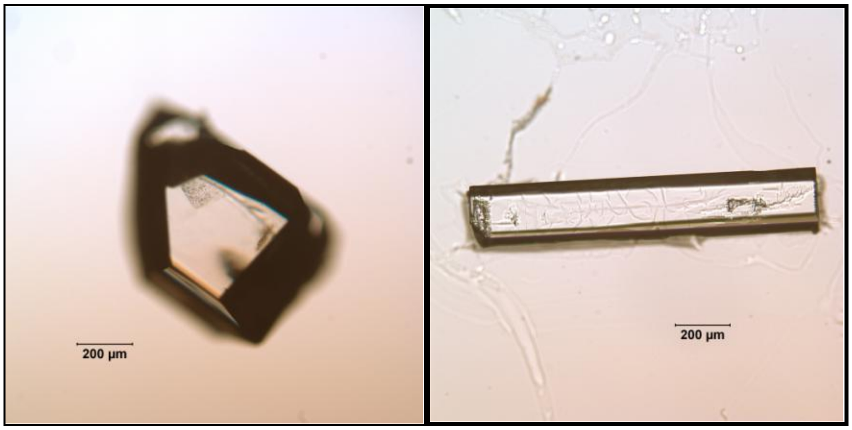

Figure 5.3. Optical microscopy of monoclinic ACM grown on PBMA (right) and orthorhombic ACM (left) grown on PBMA.

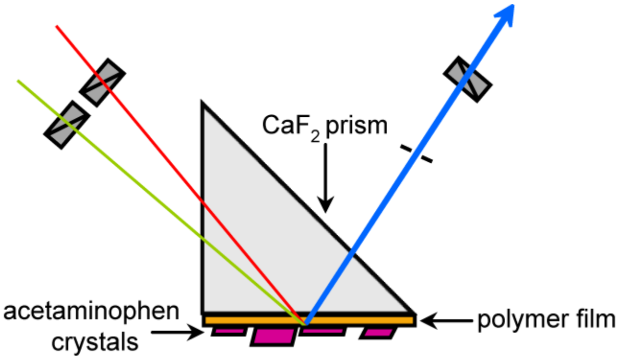

Figure 5.4. Experimental SFG set up for proving the polymer-crystal interface.

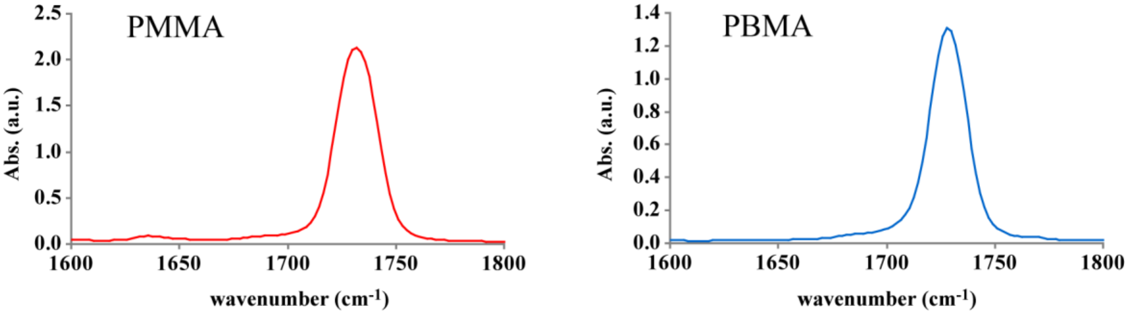

Figure 5.5. FTIR spectra collected from PMMA (left) and PBMA (right) in air.

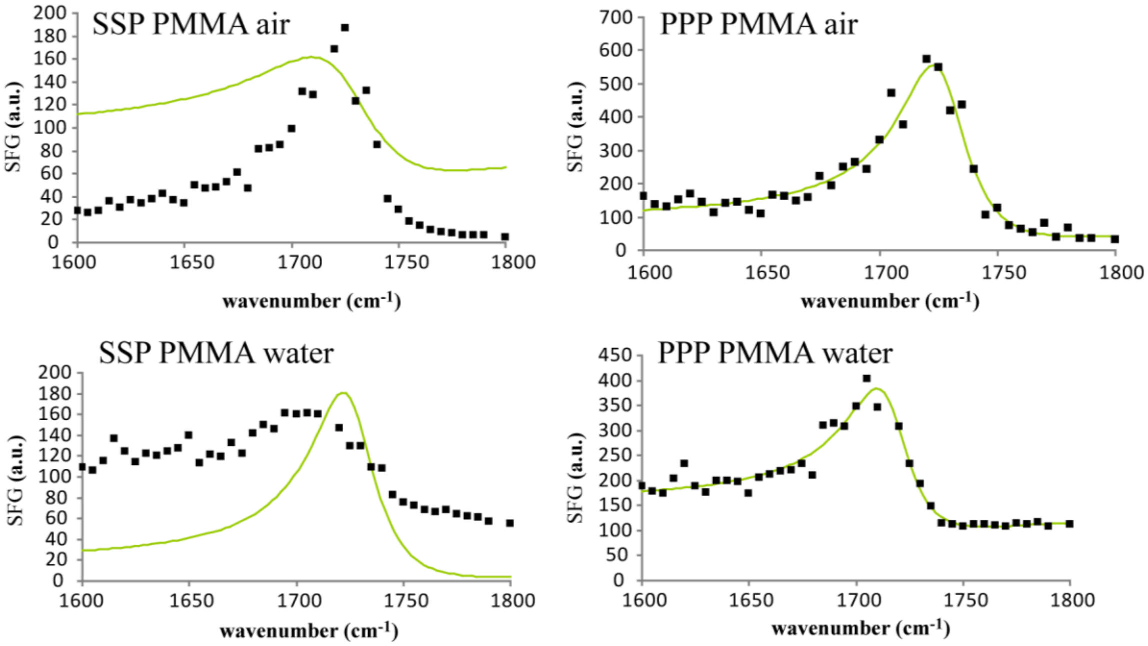

Figure 5.6. SFG spectra collected from PMMA in air (top) and in water (bottom) using ssp (left) and ppp (right) polarization combinations. The dotted line is an aid to the eye to emphasize the peak shift between air and water. The data is fitted to a Lorentzian line shape.

Table 5.2. Fit values to data in Figure 5.6.

	SSP PMMA air	**PPP PMMA air**	**SSP PMMA water**	**PPP PMMA water**
offset	3	37	47	101
NR	-3.3	-6.3	-6.6	-6.7
oscillator strength	230	365	200	248
peak center	1726	1728	1728	1717
peak width	18.4	17.4	29.9	17.6

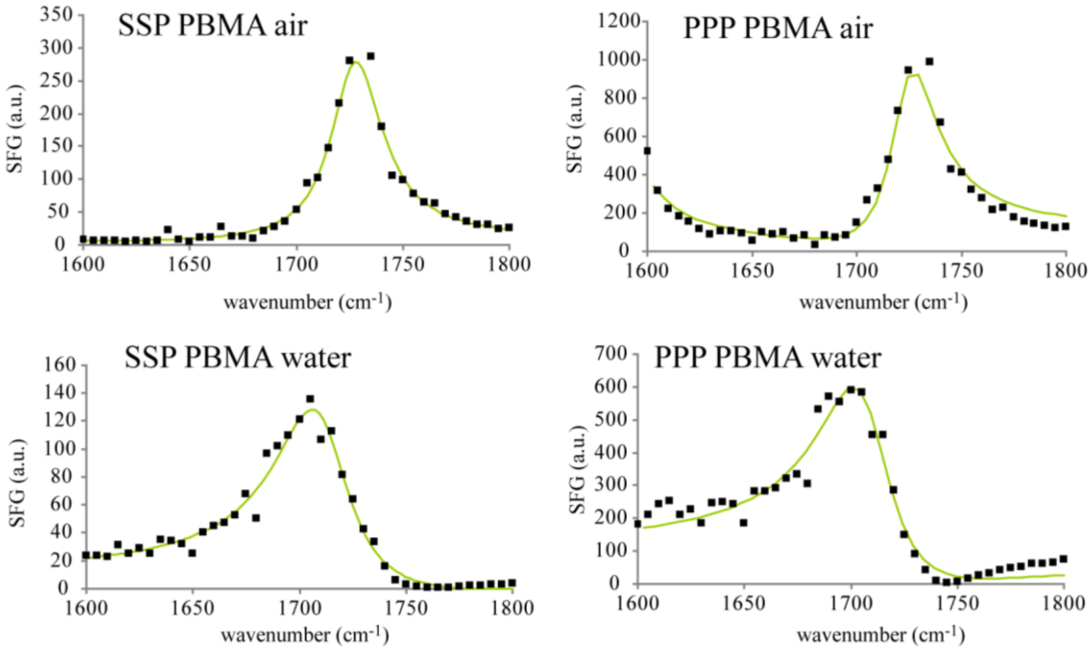

Figure 5.7. SFG spectra collected from PBMA in air (top) and in water (bottom) using ssp (left) and ppp (right) polarization combinations. The dotted line is an aid to the eye to emphasize the peak shift between air and water. The data is fitted to a Lorentzian line shape.

Table 5.3. Fit values to data in Figure 5.7.

	SSP PBMA air	PPP PBMA air	SSP PBMA water	PPP PBMA water
offset	5	57	-1	6
NR	0.98	2.98	-2.8	-8.9
oscillator strength	246	362	229	429
peak center	1727	1724	1711	1709
peak width	14.9	13.2	21.4	20.3

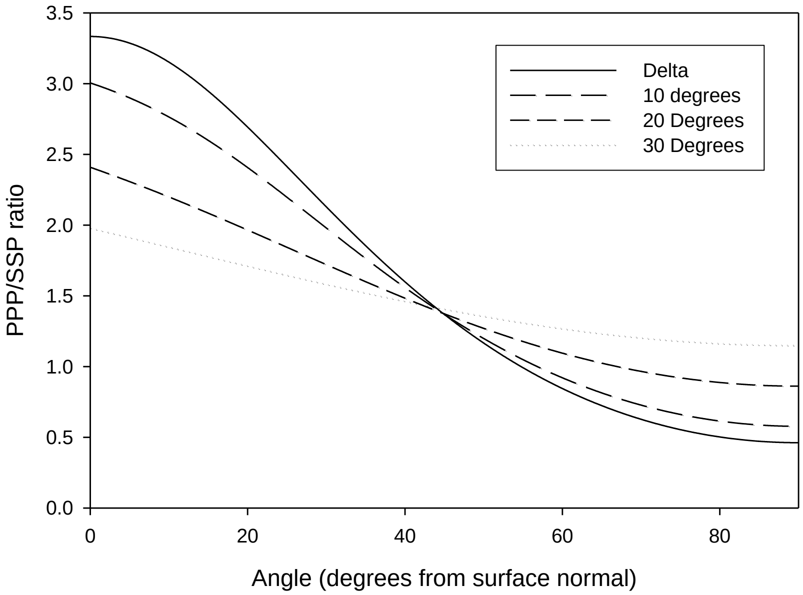

Figure 5.8. C=O orientation plot for various orientational angles and distributions.

Table 5.4. The fitted signal strength ratio χ_{ppp}/χ_{ssp} of C=O stretching from PMMA in air and in water.

	PMMA in air	**PMMA in water**
χ_{ppp}/χ_{ssp}	1.7	2.1

Table 5.5. The fitted signal strength ratio χ_{ppp}/χ_{ssp} of C=O stretching from PBMA in ACM saturated solution.

	PBMA in air	**PBMA in water**
χ_{ppp}/χ_{ssp}	1.7	2.0

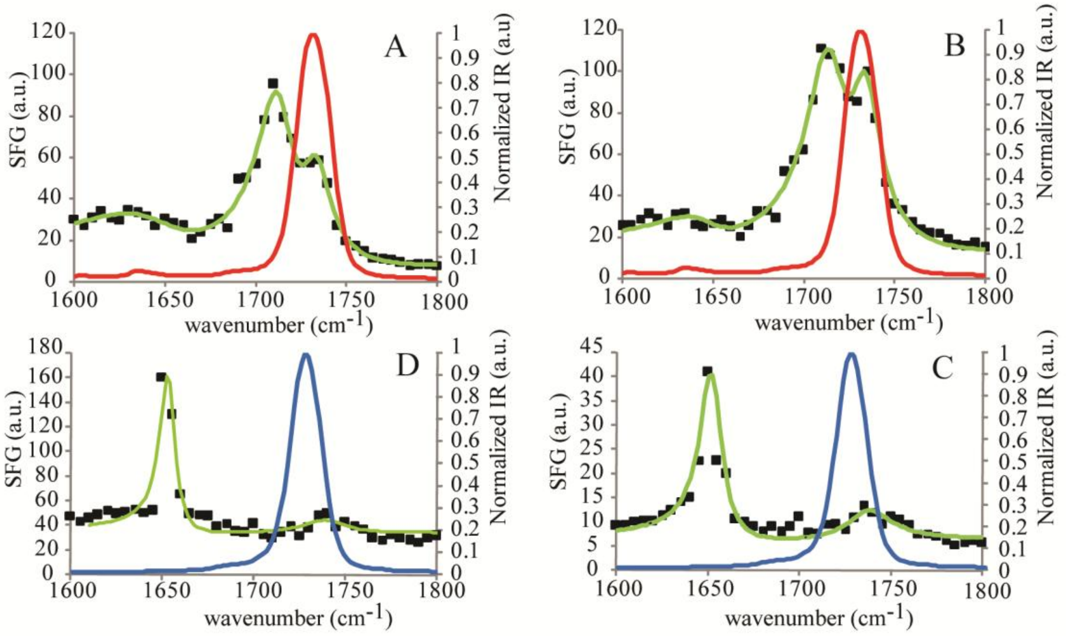

Figure 5.9. SFG spectra of the polymer-ACM crystal interface with crystals grown from a supersaturated solution on (A) PMMA with a PPP polarization combination, (B) PMMA with an SSP polarization combination, (C) PBMA with a PPP polarization combination, and (D) PBMA with an SSP polarization combination. (The polarization combinations are ordered sum frequency, visible, and infrared.) The normalized IR absorbance of the PMMA and PBMA films are overlaid in red and blue, respectively.

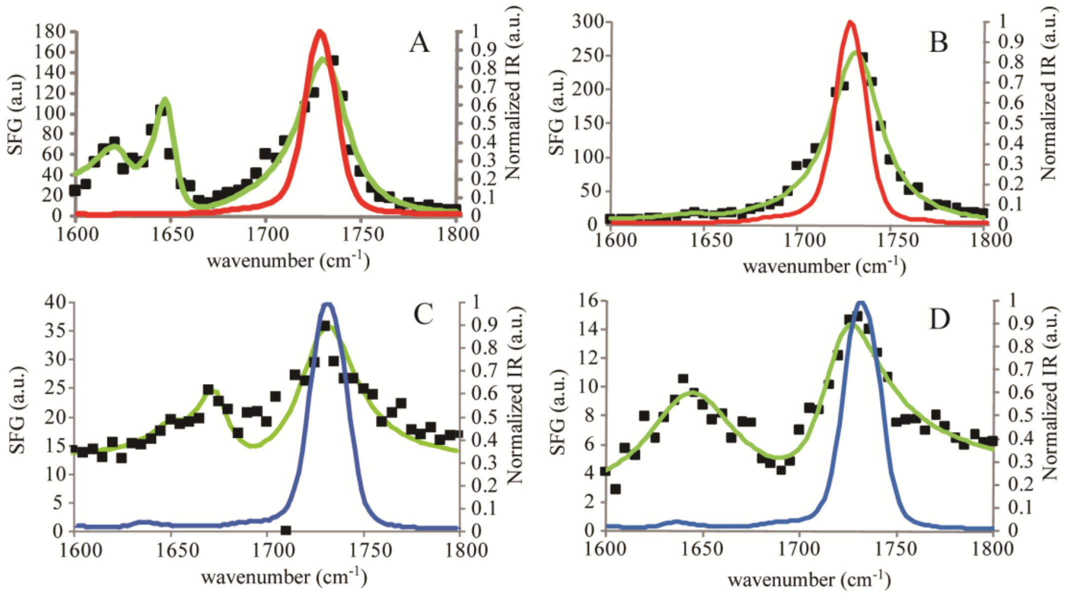

Figure 5.10. SFG spectra of the polymer-ACM crystal interface with crystals grown from sublimation: (A) PMMA with a PPP polarization combination, (B) PMMA with an SSP polarization combination, (C) PBMA with a PPP polarization combination, and (D) PBMA with an SSP polarization combination. The normalized IR absorbance of the PMMA and PBMA films are overlaid in red and blue, respectively.

5.5 References

1. Tao, J.; Yu, L., Kinetics of cross-nucleation between polymorphs. *Journal of Physical Chemistry B* **2006,** 110, (14), 7098-7101.

2. Weissbuch, I.; Addadi, L.; Lahav, M.; Leiserowitz, L., Molecular Recognition at Crystal Interfaces. *Science* **1991,** 253, (5020), 637-645.

3. Shen, R. Y.; The Principles of Nonlinear Optics; Wiley: New York, 1984.

4. Shen, Y. R., Surface-Properties Probed by 2nd-Harmonic and Sum-Frequency Generation. *Nature* **1989,** 337, (6207), 519-525.

5. Chen, Z.; Shen, Y. R.; Somorjai, G. A., Studies of polymer surfaces by sum frequency generation vibrational spectroscopy. *Annual Review of Physical Chemistry* **2002,** 53, 437-465.

6. Eisenthal, K. B., Liquid interfaces probed by second-harmonic and sum-frequency spectroscopy. *Chemical Reviews* **1996,** 96, (4), 1343-1360.

7. Moore, F. G.; Richmond, G. L., Integration or segregation: How do molecules behave at oil/water interfaces? *Accounts of Chemical Research* **2008,** 41, (6), 739-748.

8. Gopalakrishnan, S.; Liu, D. F.; Allen, H. C.; Kuo, M.; Shultz, M. J., Vibrational spectroscopic studies of aqueous interfaces: Salts, acids, bases, and nanodrops. *Chemical Reviews* **2006,** 106, (4), 1155-1175.

9. Kim, J.; Cremer, P. S., IR-Visible SFG investigations of interfacial water structure upon polyelectrolyte adsorption at the solid/liquid interface. *Journal of the American Chemical Society* **2000,** 122, (49), 12371-12372.

10. Gautam, K. S.; Schwab, A. D.; Dhinojwala, A.; Zhang, D.; Dougal, S. M.; Yeganeh, M. S., Molecular structure of polystyrene at air/polymer and solid/polymer interfaces. *Physical Review Letters* **2000,** 85, (18), 3854-3857.

11. Baldelli, S., Surface structure at the ionic liquid-electrified metal interface. *Accounts of Chemical Research* **2008,** 41, (3), 421-431.

12. Ye, H. K.; Gu, Z. Y.; Gracias, D. H., Kinetics of ultraviolet and plasma surface modification of poly(dimethylsiloxane) probed by sum frequency vibrational spectroscopy. *Langmuir* **2006,** 22, (4), 1863-1868.

13. Jayathilake, H. D.; Zhu, M. H.; Rosenblatt, C.; Bordenyuk, A. N.; Weeraman, C.; Benderskii, A. V., Rubbing-induced anisotropy of long alkyl side chains at polyimide surfaces. *Journal of Chemical Physics* **2006,** 125, (6).

14. Geiger, F. M., Second Harmonic Generation, Sum Frequency Generation, and chi((3)): Dissecting Environmental Interfaces with a Nonlinear Optical Swiss Army Knife. *Annual Review of Physical Chemistry* **2009,** 60, 61-83.

15. Wang, J.; Chen, C. Y.; Buck, S. M.; Chen, Z., Molecular chemical structure on poly(methyl methacrylate) (PMMA) surface studied by sum frequency generation (SFG) vibrational spectroscopy. *Journal of Physical Chemistry B* **2001,** 105, (48), 12118-12125.

16. Stiopkin, I. V.; Jayathilake, H. D.; Bordenyuk, A. N.; Benderskii, A. V., Heterodyne-detected vibrational sum frequency generation spectroscopy. *Journal of the American Chemical Society* **2008,** 130, (7), 2271-2275.

17. Wang, J.; Chen, X. Y.; Clarke, M. L.; Chen, Z., Vibrational spectroscopic studies on fibrinogen adsorption at polystyrene/protein solution interfaces: Hydrophobic side chain and secondary structure changes. *Journal of Physical Chemistry B* **2006,** 110, (10), 5017-5024.

18. Price, C. P.; Grzesiak, A. L.; Matzger, A. J., Crystalline polymorph selection and discovery with polymer heteronuclei. *Journal of the American Chemical Society* **2005,** 127, (15), 5512-5517.

19. Grzesiak, A. L.; Matzger, A. J., New form discovery for the analgesics flurbiprofen and sulindac facilitated by polymer-induced heteronucleation. *Journal of Pharmaceutical Sciences* **2007,** 96, 2978-2986.

20. López-Mejías, V.; Kampf, J. W.; Matzger, A. J., Polymer-Induced Heteronucleation of Tolfenamic Acid: Structural Investigation of a Pentamorph. *Journal of the American Chemical Society* **2009,** 131, (13), 4554.

21. Porter, W. W.; Elie, S. C.; Matzger, A. J., Polymorphism in carbamazepine cocrystals. *Crystal Growth & Design* **2008,** 8, (1), 14-16.

22. Grzesiak, A. L.; Matzger, A. J., Selection of protein crystal forms facilitated by polymer-induced heteronucleation. *Crystal Growth & Design* **2008,** 8, (1), 347-350.

23. Grzesiak, A. L.; Uribe, F. J.; Ockwig, N. W.; Yaghi, O. M.; Matzger, A. J., Polymer-induced heteronucleation for the discovery of new extended solids. *Angewandte Chemie-International Edition* **2006,** 45, (16), 2553-2556.

24. Haisa, M.; Kashino, S.; Kawai, R.; Maeda, H., Monoclinic Form of Para-Hydroxyacetanilide. *Acta Crystallographica Section B-Structural Science* **1976,** 32, 1283-1285.

25. Haisa, M.; Kashino, S.; Maeda, H., Orthorhombic Form of Para-Hydroxyacetanilide. *Acta Crystallographica Section B-Structural Science* **1974,** B 30, 2510-2512.
26. Banks, A. R.; Fibiger, R. F.; Jones, T., Convenient Synthesis of Methacrylates. *Journal of Organic Chemistry* **1977,** 42, (24), 3965-3966.
27. Clarke, M. L.; Chen, C. Y.; Wang, J.; Chen, Z., Molecular level structures of poly(n-alkylmethacrylate)s with different side chain lengths at the polymer/air and polymer/water interfaces. *Langmuir* **2006,** 22, (21), 8800-8806.
28. Wang, J.; Chen, C. Y.; Chen, Z., Detection of molecular structure on poly(methyl methacrylate) (PMMA) surface by sum frequency feneration (SFG) vibrational spectroscopy. *Abstracts of Papers of the American Chemical Society* **2001,** 222, 164.
29. Tyrode, E.; Johnson, C. M.; Baldelli, S.; Leygraf, C.; Rutland, M. W., A vibrational sum frequency spectroscopy study of the liquid-gas interface of acetic acid-water mixtures: 2. Orientation analysis. *Journal of Physical Chemistry B* **2005,** 109, (1), 329-341.

CHAPTER 6

ON THE MECHANISM OF POLYMORPH SELECTION BY POLYMER HETERONUCLEI

6.1 Introduction

In the pursuit of new crystalline phases of molecular compounds, altering crystallization variables such as temperature, solvent and degree of supersaturation is common. However, such methods do not explicitly target nucleation which is often the critical step in determining the ultimate solid-state form produced. Polymer-induced heteronucleation (PIHn) has been established as a general approach for controlling solid form selection and discovery in which an array of polymer heteronucleants provides kinetic access to polymorphs.[1] Demonstrations of PIHn for small molecules,[2-5] supramolecular complexes,[6, 7] and proteins[8,9] are established; however, in spite of its success in controlling crystal polymorphism, little is understood about its mechanism.

PIHn utilizes insoluble polymers to affect solid form selection. Unlike soluble additives, heterogeneous additives can only interact with molecules at the solid-solution interface which leads to crystal growth where interactions are confined to one crystal face; this stands in stark contrast to the use of soluble additives where inhibition can occur to varying degrees through blocking the addition of subsequent molecules to all of the growing crystal faces.[10-12] As a result the phase-selection mechanism occurring during PIHn cannot be explained using the same rationale as with soluble additives. An alternative mechanism could be that the polymer inhibits crystal growth by preferential retention of specific nuclei types inside the swollen polymer, which in turn would delay the onset of crystallization and inhibit formation of a given polymorph. Experimentally, acceleration of crystal formation is instead observed ruling out inhibition through competitive retention of nuclei inside a polymer matrix as a mechanism for PIHn and pointing to a promotion of growth at a heterogeneous interface.

Heterogeneous nucleation can occur with different levels of specificity ranging from nonspecific adsorption to the oriented growth of crystals on a surface. During nonspecific adsorption, solute molecules cluster on the surface without specific orientation and the mere presence of an interface promotes nucleation by lowering surface energy of the aggregate. Other modes of promoting nucleation include employing structural matching between the nucleating crystal and the surface, as in the case of epitaxial crystal growth,[13-15] although the oriented arrangement of molecules by means of selective interfacial interactions should also be possible at an amorphous surface. Epitaxy does not present a viable explanation for the success of PIHn because the polymers utilized do not present significant order. As a result two possible mechanisms remain plausible to explain phase-selection using polymers as heteronuclei, one involves nonspecific adsorption of molecules to form crystal nuclei and the other involves the oriented arrangement of nucleating molecules on the polymer surface. These outcomes are differentiated between here by elucidating the preferred modes of crystal growth in PIHn under several conditions and the results are interpreted with the aid of computation.

Acetaminophen (ACM, Figure 6.1) is a common analgesic and antipyretic drug which crystallizes in two stable forms,[16] the less thermodynamically favorable orthorhombic form[17] and the monoclinic form.[18] Selective crystallization of orthorhombic and monoclinic ACM using various insoluble polymers as heteronuclei has previously been reported.[1] ACM heteronucleates from aqueous supersaturated solution in the monoclinic form on poly(*n*-butyl methacrylate) (PBMA, Figure 6.1), whereas the orthorhombic form is observed on structurally similar poly(methyl methacrylate) (PMMA, Figure 6.1).[1] Therefore, ACM serves as a good model compound for understanding how these polymer heteronucleants exercise control over crystallization of these polymorphs.

6.2 Experimental Section

6.2.1 Materials

ACM was obtained from ICN Biomedicals Inc. (Irvine, CA) and was stored at room temperature. PBMA, PMMA, Nylon 6/9, Nylon 6/12 and Nylon 11 were purchased from Scientific Polymer Products Inc. (Ontario, NY).

6.2.2 Preparation of Polymer Thin Films

All polymer samples were prepared by spin coating 3 w/w % polymer solutions (benzene) onto microscope slides (75 × 25 × 1 mm) at 2500 rpm on a Specialty Coatings Systems G3P-8 spin coater. Coated slides were annealed at 85 °C under vacuum for 4 hrs.

6.2.3 Crystallization From Aqueous Solution

ACM crystals were grown from aqueous supersaturated solutions (17 mg/mL, at 25 °C) on submerged microscope slides coated with polymer. The slides were aligned vertically in the vial to minimize the possibility that crystals that nucleated in solution would deposit on the microscope slide. Samples were air dried prior to analysis.

6.2.4 Crystallization from Vapor Phase Deposition

Powdered ACM (~200 mg) was added to a sublimation chamber. Polymer-coated microscope slides were held in contact with a flat aluminum plate cooled by an ice/water bath, and sublimation proceeded while the chamber was evacuated ($\sim 15 \times 10^{-3}$ Torr) and submerged in an oil bath at 150 °C. After ~15 min, all ACM had sublimed from the bottom of the chamber.

6.2.5 Optical Microscopy

Images of monoclinic and orthorhombic ACM crystals grown from aqueous supersaturated solution onto PBMA and PMMA, respectively, were collected using a Spot Flex Mosaic 15.2 camera coupled to a Leica DMLP microscope. Images were processed using Spot Advanced software (version 4.6).

6.2.6 Powder X-ray Diffraction

Powder X-ray Diffraction (PXRD) analysis was performed using a Bruker D8 Advance diffractometer equipped with a LynxEye detector and graphite monochromated Cu-Kα radiation (1.5406 Å, 40 kV, 40 mA). Diffractograms were collected at room temperature from 5° to 50° with a 0.05° step size while the sample was rotated at 60 rpm. All powder patterns were processed in Jade Plus (v. 8.2).

6.2.7 Molecular Modeling

All of the binding energy (Φ_{BE}) calculations, including molecular dynamic simulations, were performed using the CHARMM macromolecular modeling package version c36a4[19, 20] on dual 2.66 GHz Intel Quad Core Xeon CPUs. Molecular structures of the oriented faces were obtained by cleaving the room temperature crystal structures of ACM (CSD reference codes HXACAN and HXACAN01)[17, 18] along each preferred crystallographic plane using Materials Studio v4.3. Based on previously reported Bravais-Friedel-Donnay-Harker (BFDHE) and attachment energy (AE) morphology predictions for ACM,[21] additional faces were chosen as suitable negative controls due to their morphological prevalence. Each crystal face had dimensions of ~60 × 40 Å^2 and contained ~285 molecules. Parameters and partial charges for ACM molecules were taken from the CHARMM Generalized Force Field (CGenFF).[22] PBMA and PMMA were represented as trimers with syndiotactic configuration[23] and capped with hydrogen atoms at the terminal sites. The molecular structure of each trimer was constructed using Material Studio v4.3. Parameters and partial charges for each polymer were assigned from our in-house automated parameterization tool, MATCH.[24]

Vapor phase crystallization of ACM utilizing PMMA and PBMA as heteronucleants was mimicked by cooling each polymer onto seven different faces of the monoclinic ACM crystal lattice ((001), (21-1), (020), (021), (120), (110), and (002) faces) and onto seven different faces of the orthorhombic ACM crystal lattice, ((002), (121), (201), (212), (222), (221), and (220) faces). The polymer was placed ~20 Å apart from the surface of the ACM face and the temperature was cooled to 150 K with an exponential cooling schedule of $T(\mathrm{t}) = T_o\exp^{-k\mathrm{t}}$, where k is the cooling rate constant and t is the iteration number. Different cooling schedules were explored using initial temperatures, T_o, of 900 or 600 K and k = 0.05, 0.01 or 0.005. In each iteration, the polymer model was lowered by 1 Å towards the face of the ACM face, a 50 or 100 ps molecular dynamics simulation was performed with a center of mass restraint on the trimer followed by a minimization of the polymer model without restraints. During the dynamics phase, a non-bonded cutoff of 15 Å was used and van der Waals switching and electrostatic force shifting functions were implemented between 10 Å and 12 Å. All ACM atoms were fixed, hydrogen bonds were restrained using the SHAKE[25] algorithm and the time step was 2 fs. Final energy minimizations were performed with heavy atom restraints on the ACM atoms and no non-bonded cutoffs.

6.2.8 Binding Energy Calculation

Three hundred independent docking simulations were performed for each combination of oligomer and ACM face using different initial seed values and the overall surface binding energies ($\Phi_{BE(h,k,l)}$) were estimated from the energy difference between the most favorable energy complex in vacuum (Φ_{IE}), and the minimized energy of the free components (Φ_{PM}, polymer model and Φ_{CF}, crystal face) in vacuum (Equation 1).[26]

$$\Phi_{BE(h,k,l)} = \Phi_{IE} - (\Phi_{PM} + \Phi_{CF(h,k,l)}) \qquad (1)$$

6.3 Results and Discussion

Phase determination and preferred orientation (PO) analysis was conducted by PXRD on polymer coated glass slides with the as-grown ACM crystals. Comparison of the diffraction patterns with the 2θ values of known crystal structures was used for phase identification.[17, 18] In accord with what was previously reported,[1] ACM heteronucleates from aqueous supersaturated solution in the monoclinic form on PBMA, whereas the orthorhombic form is observed on PMMA (Figure 6.2). In both polymer-polymorph combinations the crystals were found to be strongly oriented along specific crystallographic planes. Because both polymers are insoluble under this crystallization condition and possess no long range order it can be concluded that the differences in PO observed by PXRD results from unique interactions that occur at the polymer–crystal interface when molecules selectively nucleate on the surface. Analysis of the relevant polymer–crystal interfaces provides insights into some of the kinetic aspects of polymer-induced phase selection.

ACM crystals heteronucleated on PBMA present a prismatic morphology (Figure 6.2). PXRD analysis revealed two prominent reflections occurring at 13.8° (001) and 27.8° (002), (Figure 6.3a), these correspond to those of monoclinic ACM with orientation of the crystals along {001}. This could arise through crystal nucleation from the (001) face or the (002) face, which cannot be distinguished by PXRD. Hydroxyl groups appear perpendicular to the (001) face whereas in the case of the (002) face, the amide portion of the ACM molecule is perpendicular to the surface (Figure 6.4). This indicates that PBMA is interacting either with the amide or with the hydroxyl portion of ACM in the case of the (002) face and the (001) face, respectively (Figure 6.4a). Hydrogen-bonding is typically assumed to be among the most directional types of intermolecular interactions, but interfacial hydrogen-bonding to either the amide or the hydroxyl groups on monoclinic ACM is not likely given that the PBMA surface is dominated by terminal methyl groups of the ester side chain when in contact with both air and water.[27] Examination of the crystal structure of monoclinic ACM reveals the presence of grooves when observed along the *ac* plane (Figure 6.4b). Therefore, crystal nucleation mediated by hydrophobic interactions between the ester side chain in PBMA and the grooves at this interface, the (001) face, provides a possible pathway for the nucleation of monoclinic ACM on PBMA in the presence of water as solvent.

ACM crystals heteronucleated on PMMA present a plate-like habit (Figure 6.2). PXRD of ACM crystals grown on PMMA yields a diffractogram with a single major reflection at 24.1°(002) in 2θ (Figure 6.3b). The presence of PO along the (002) face indicates that crystal nucleation occurs from the family of planes along *ac*, {001}, in orthorhombic ACM. A view of the *ac*-plane of orthorhombic ACM with the (002) face indicated is shown in Figure 6.5. Hydrogen-bonded molecular sheets lay planar along {001}. Morphology predictions suggest that fast growth for orthorhombic ACM occurs along {100}, {010}, and {001}.[21] These predictions and the PXRD results suggest that when PMMA is utilized as the heteronucleant in aqueous media, it has the ability to secure the hydrogen-bonded molecular sheets of ACM that form along the fast growing {001}, making it possible to harvest this polymorph versus the thermodynamically more stable monoclinic form.

In a previous study, the polymer–crystal interface of ACM grown from supersaturated aqueous solution on PBMA and PMMA was investigated through Sum Frequency Generation Vibrational Spectroscopy (SFG-VS)[28] in order to determine the molecular-level interactions responsible for phase-selection. The presence of the amide I stretch in the SFG-VS spectra was only observed for monoclinic ACM crystals grown on PBMA. The absence of the amide I stretch signal at the PMMA–orthorhombic ACM interface suggested that the amide was oriented parallel to the interface which is consistent with the molecular structure of {001} in orthorhombic ACM (Figure 6.5), and supports the current experimental data indicating that orthorhombic ACM preferentially nucleates along {001} on PMMA when it crystallizes from water. Additionally, the SFG-VS study of the polymer–crystal interface revealed that hydrogen-bonding to the polymer carbonyl oxygen only occurred in the case of PMMA–orthorhombic ACM, which confirms that phase-selection is dictated by hydrogen-bonding for this particular polymer–crystal combination.

To determine the role of solvent during the PIHn process, ACM crystals were deposited by sublimation onto PBMA and PMMA. Under the vapor phase deposition condition, only the monoclinic form of ACM was observed (Figure 6.6). Although the same form is selectively produced in the absence of solvent, PXRD revealed POs that are unique to each of the polymers utilized for heteronucleation. The experimental PXRD pattern of ACM crystals deposited on PMMA (Figure 6.6b) indicate that the extent of PO along {001} is significantly greater than that of ACM crystals deposited on PBMA (Figure 6.6a) where multiple orientations are observed. These observations are discussed below in the context of the computed interaction energies.

Surface binding energies (Φ_{BE}) between various ACM crystal faces with PBMA and PMMA trimers were estimated using docking simulations to reveal molecular-level factors influencing phase-selection during PIHn in vacuum. These data are summarized in Table 6.1. Among the crystal faces interacting with PBMA, six of them have significantly favorable Φ_{BE}. These six faces with lower Φ_{BE} values belong to those of the monoclinic crystal phase and the calculated Φ_{BE} values are within 4 kcal/mol of the lowest energy complex which suggests a thermodynamically driven competition among these faces. Indeed, in Figure 6.6a the reflections associated with each of these faces are observed in the diffractograms of ACM crystals grown on PBMA through vapor deposition, suggesting that a significant population of each of these crystal faces are aligned along the polymer substrate.

The Φ_{BE} value for the polymer–crystal interface involving PBMA and the (002) face in monoclinic ACM is significantly less favorable than those from the (001) face. This difference arises from the more favorable electrostatic energy contributions for the (001) face compared to the (002) face in the monoclinic crystal phase. In both the (001) and the (002) faces, the trimer is able to maintain extensive nonspecific interactions within the surface grooves which results in dispersion (van der Waals) interactions of comparable magnitude. PXRD is unable to distinguish if crystals are nucleated from the (001) face or the (002) face, therefore the docking simulations provide the best evidence that a larger numbers of crystals nucleate from the (001) face.

Unlike the case of PBMA-induced heteronucleation, the results for PMMA presented in Table 6.1 show a clear preference for the (001) face, where Φ_{BE} for this face is over 6 kcal/mol more favorable than any other face examined. These results are consistent with the PO observed in the diffractogram of ACM crystals grown on PMMA by vapor deposition where mainly two reflections occurring at 13.8°(001) and 27.8°(002) are observed (Figure 6.6b). The large difference in Φ_{BE} between the (001) face and the (002) face modeled in the presence of PMMA seems to arise from a different mechanism from that of PBMA-induced nucleation. In this case, the docked PMMA trimer exhibits more favorable dispersion (van der Waals) interactions with the (001) face than the (002) face of the monoclinic crystal while the electrostatic energy contributions are comparable.

For both polymer models, the most favorable orthorhombic face is more than 4 kcal/mol higher in energy than the most favorable monoclinic face, reaffirming that under vapor phase crystallization conditions the emergence of orthorhombic ACM is unlikely. The calculated Φ_{BE} for the orthorhombic (002) face in contact with both PBMA and PMMA was the least favorable among all the faces studied and more than 10 kcal/mol less favorable than the most favorable monoclinic face. Not surprisingly, it is the weaker electrostatic interactions that result in the relative disfavoring of the orthorhombic (002) face over the other faces. The presence of only the monoclinic form in ACM crystals deposited from sublimation suggests a possible role of solvent in aiding the nucleation process of orthorhombic ACM on the PMMA surface.

In order to establish the role of solvent in facilitating nucleation under the polymer-induced heteronucleation condition, an additional class of polymers was tested. Nylon 6/9, Nylon 6/12 and Nylon 11 (Figure 6.7) were utilized as polymer heteronucleants for ACM crystals in ethanol, acetonitrile, and acetone where, unlike PBMA and PMMA, no dissolution of the polymer will occur. These Nylons were also utilized as heteronucleants under vapor phase deposition. Table 6.2 summarizes these results.

Results are consistent across the three Nylons and indicate that aprotic solvents facilitate nucleation along {001} in monoclinic ACM (Figures 6.8 and 6.9). In the absence of solvent, nucleation along {001} in monoclinic ACM is also favored (Figure 6.10) whereas in the presence of a protic solvent Nylons promote the nucleation along {001} in orthorhombic ACM (Figure 6.11). The results obtained for Nylons support the hypothesis that the presence of a protic solvent, in this case water, working in concert with the polymer is responsible for directing the phase selectivity of orthorhombic ACM grown on PMMA.

6.4 Conclusions

This combined experimental and computational effort provides insights into the mechanism of phase-selection by PIHn through unraveling distinct intermolecular interactions occurring at each preferred nucleation face under different crystallization conditions. Results indicate that the phase-selection mechanism of PIHn depends on the difference in the accessibility of the functional groups on the surface of the polymer heteronucleants which may affect interfacial interactions and ultimately direct nucleation along a given crystal face, the PO plane. Moreover, results emphasize the dependence of the polymorph selection process on both the polymer surface and the solvent media because it was possible to change solid form in the absence of solvent as well as in the presence of different solvents based on their ability to donate a hydrogen-bond. The rationalization of the intermolecular interactions directing phase-selection during the process of PIHn will allow for the further development of better methodology for the control and selection of solid forms based on polymer heteronucleants.

ACM **PBMA** **PMMA**

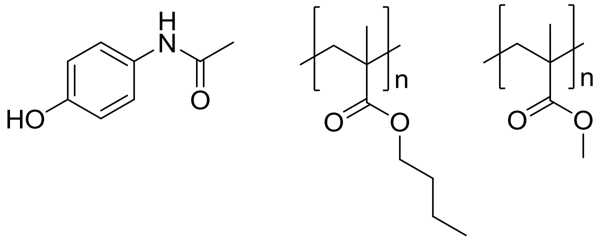

Figure 6.1. Chemical structures of acetaminophen (ACM), poly(*n*-butyl methacrylate) (PBMA), and poly(methyl methacrylate) (PMMA).

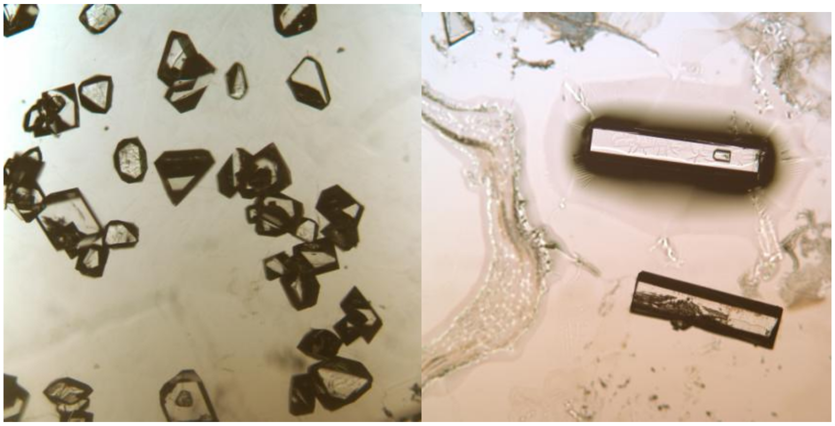

Figure 6.2. Optical microscopy of monoclinic ACM grown on PBMA (left) and orthorhombic ACM (right) grown on PMMA.

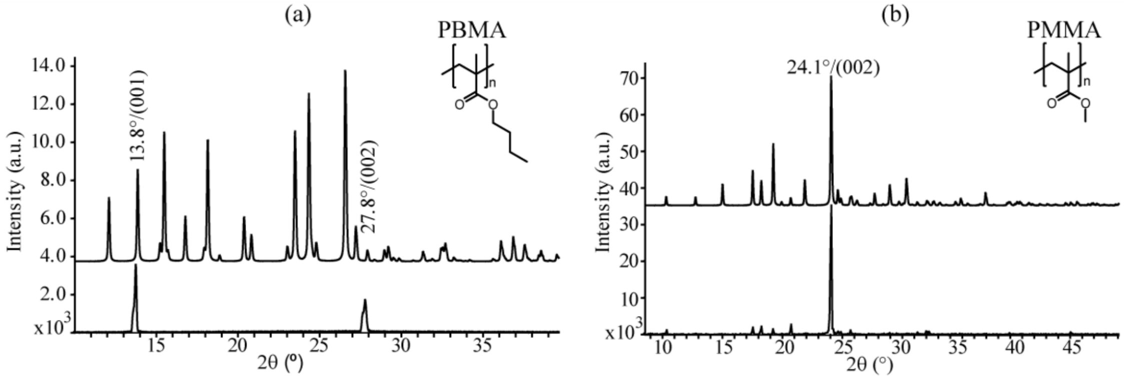

Figure 6.3. PXRD of monoclinic ACM nucleated on PBMA (a) and orthorhombic ACM nucleated on PMMA (b) from a supersaturated aqueous solution (bottom), along with the simulated PXRD pattern of monoclinic[18] and orthorhombic[17] ACM with no PO (top).

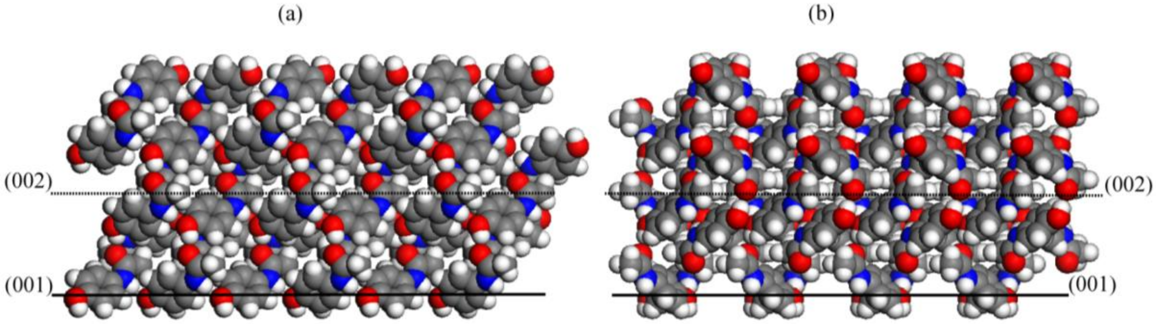

Figure 6.4. View of the *bc* plane (a) and the *ac* plane (b) of monoclinic ACM with the (001) and (002) faces indicated.

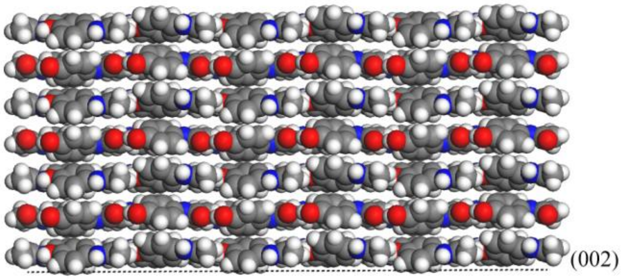

Figure 6.5. View of the *ac*-plane of orthorhombic ACM with the (002) face indicated.

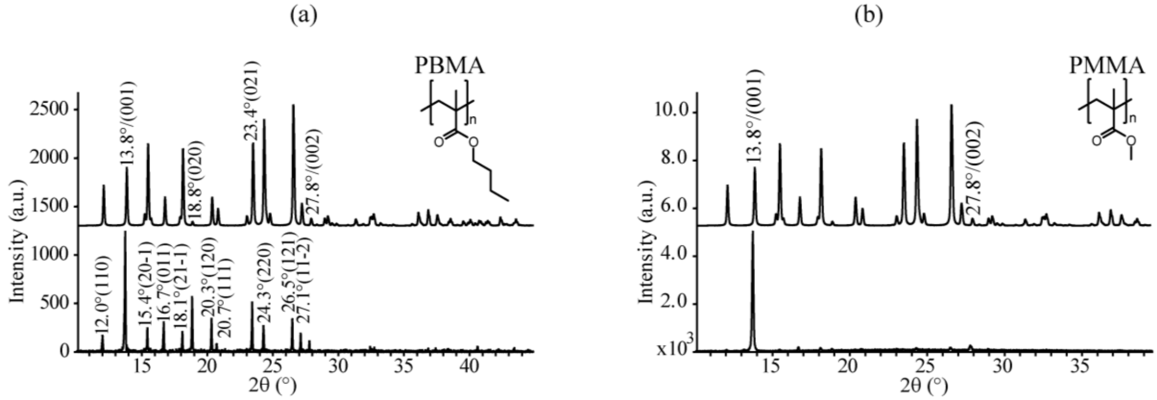

Figure 6.6. PXRD of ACM deposited by sublimation on PBMA (a) and PMMA (b) (bottom) along with their simulated PXRD patterns of monoclinic[18] ACM with no PO (top).

Table 6.1. Relative surface binding energies ($\Phi_{BE(hkl),}$ kcal/mol) of PO faces of ACM crystals deposited on PBMA and PMMA estimated from docking simulations.

$\Delta(\Phi_{BE})$ (kcal/mol)	**PBMA**	**PMMA**
$\Phi_{BE(001)monoclinic}$	0.0	0.0
$\Phi_{BE(21-1)monoclinic}$	-0.9	6.4
$\Phi_{BE(020)monoclinic}$	-1.4	9.2
$\Phi_{BE(021)monoclinic}$	2.3	7.0
$\Phi_{BE(120)monoclinic}$	2.6	9.1
$\Phi_{BE(110)monoclinic}$	2.6	9.5
$\Phi_{BE(002)monoclinic}$	7.3	9.3
$\Phi_{BE(002)orthorhombic}$	9.4	14.7
$\Phi_{BE(121)orthorhombic}$	4.4	8.8
$\Phi_{BE(201)orthorhombic}$	4.0	8.0
$\Phi_{BE(212)orthorhombic}$	3.5	7.1
$\Phi_{BE(222)orthorhombic}$	3.2	7.7
$\Phi_{BE(221)orthorhombic}$	2.7	6.8
$\Phi_{BE(220)orthorhombic}$	6.6	12.5

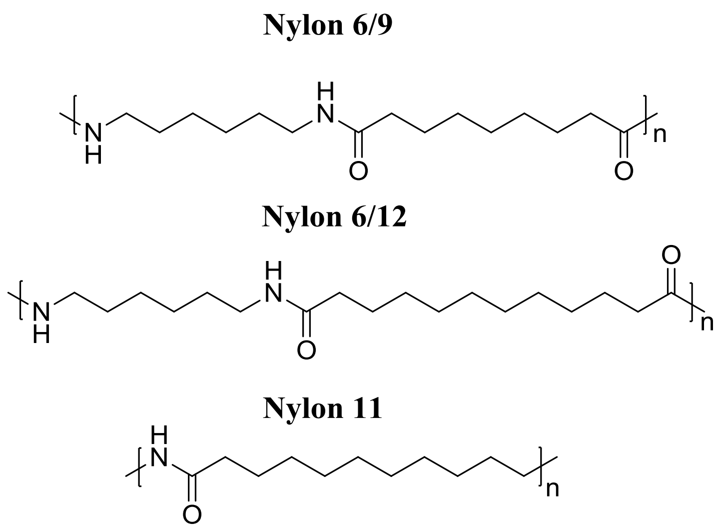

Nylon 6/9

Nylon 6/12

Nylon 11

Figure 6.7. Chemical structures of Nylon 6/9, Nylon 6/12, and Nylon 11.

Table 6.2. Summary of the major orientations observed by PXRD in ACM grown using Nylons as heteronucleants under different crystallization conditions.

Nylon	ethanol	acetonitrile	acetone	vacuum
6/9	$\{001\}_{\text{orthorhombic}}$	$\{001\}_{\text{monoclinic}}$	$\{001\}_{\text{monoclinic}}$	$\{001\}_{\text{monoclinic}}$
6/12	$\{001\}_{\text{orthorhombic}}$	$\{001\}_{\text{monoclinic}}$	$\{001\}_{\text{monoclinic}}$	$\{001\}_{\text{monoclinic}}$
11	$\{001\}_{\text{orthorhombic}}$	$\{001\}_{\text{monoclinic}}$	$\{001\}_{\text{monoclinic}}$	$\{001\}_{\text{monoclinic}}$

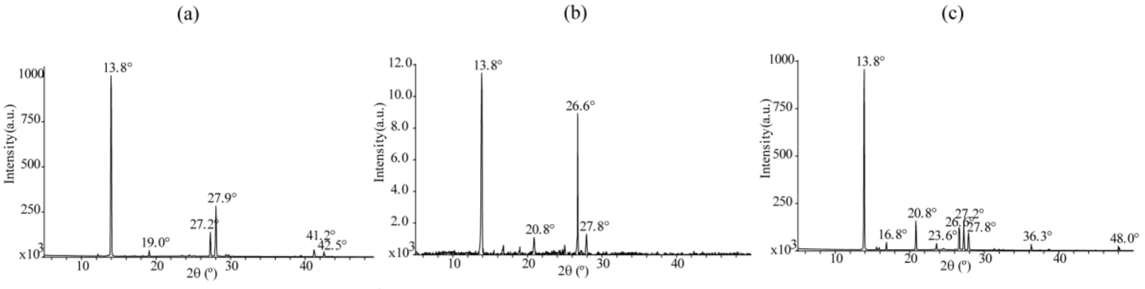

Figure 6.8. PXRD pattern of monoclinic ACM grown on Nylon 6/9 (a), Nylon 6/12 (b), and Nylon 11 (c) from a supersaturated acetonitrile solution.

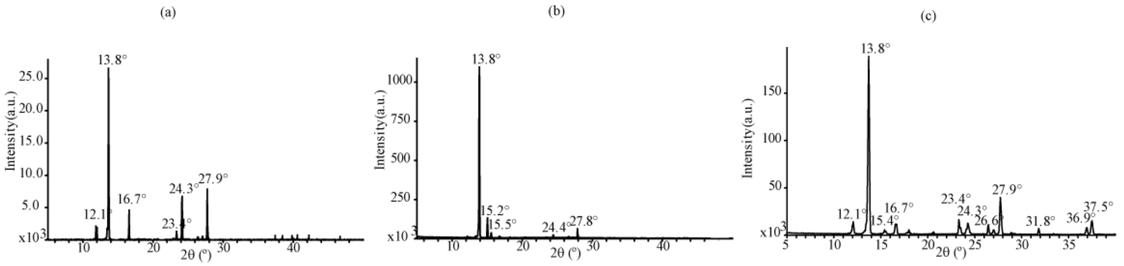

Figure 6.9. PXRD pattern of monoclinic ACM grown on Nylon 6/9 (a), Nylon 6/12 (b), and Nylon 11 (c) from a supersaturated acetone solution.

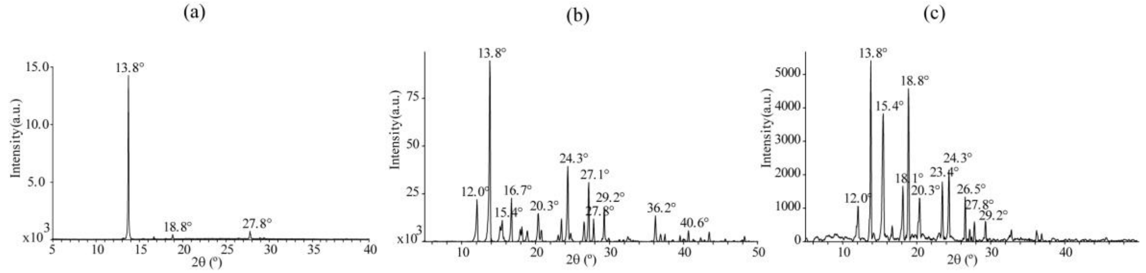

Figure 6.10. PXRD pattern of monoclinic ACM grown on Nylon 6/9 (a), Nylon 6/12 (b), and Nylon 11 (c) by sublimation.

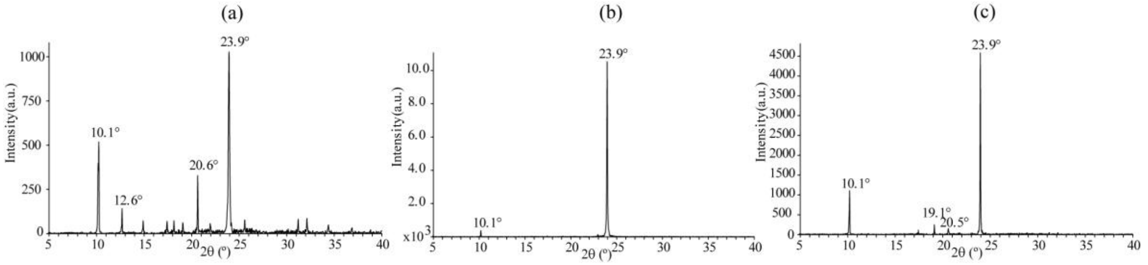

Figure 6.11. PXRD pattern of orthorhombic ACM grown on Nylon 6/9 (a), Nylon 6/12 (b), and Nylon 11 (c) from a supersaturated ethanol solution.

6.5 References

1. Price, C. P.; Grzesiak, A. L.; Matzger, A. J., Crystalline polymorph selection and discovery with polymer heteronuclei. *Journal of the American Chemical Society* **2005,** 127, (15), 5512-5517.
2. Grzesiak, A. L.; Matzger, A. J., New form discovery for the analgesics flurbiprofen and sulindac facilitated by polymer-induced heteronucleation. *Journal of Pharmaceutical Sciences* **2007,** 96, 2978-2986.
3. López-Mejías, V.; Kampf, J. W.; Matzger, A. J., Polymer-Induced Heteronucleation of Tolfenamic Acid: Structural Investigation of a Pentamorph. *Journal of the American Chemical Society* **2009,** 131, (13), 4554.

4. Lutker, K. M.; Tolstyka, Z. P.; Matzger, A. J., Investigation of a privileged polymorphic motif: A dimeric ROY derivative. *Crystal Growth & Design* **2008,** 8, (1), 136-139.

5. Porter, W. W.; Elie, S. C.; Matzger, A. J., Polymorphism in carbamazepine cocrystals. *Crystal Growth & Design* **2008,** 8, (1), 14-16.

6. Grzesiak, A. L.; Matzger, A. J., Selection and discovery of polymorphs of platinum complexes facilitated by polymer-induced heteronucleation. *Inorganic Chemistry* **2007,** 46, (2), 453-457.

7. Grzesiak, A. L.; Uribe, F. J.; Ockwig, N. W.; Yaghi, O. M.; Matzger, A. J., Polymer-induced heteronucleation for the discovery of new extended solids. *Angewandte Chemie-International Edition* **2006,** 45, (16), 2553-2556.

8. Grzesiak, A. L.; Matzger, A. J., Selection of protein crystal forms facilitated by polymer-induced heteronucleation. *Crystal Growth & Design* **2008,** 8, (1), 347-350.

9. Foroughi, M. L.; Kang, Y.; Matzger J. A., Crystal Growth & Design, **2011**, (ASAP).

10. Weissbuch, I.; Shimon, L. J. W.; Landau, E. M.; Popovitzbiro, R.; Berkovitchyellin, Z.; Addadi, L.; Lahav, M.; Leiserowitz, L., Tailormade auxiliaries for nucleation, growth and dissolution of organic-crystals. *Pure and Applied Chemistry* **1986,** 58, (6), 947-954.

11. Weissbuch, I.; Zbaida, D.; Addadi, L.; Leiserowitz, L.; Lahav, M., Design of polymeric inhibitors for the control of crystal polymorphism- induced enenatiomeric resolution of racemic histidine by crystallization at 25°C. *Journal of the American Chemical Society* **1987,** 109, (6), 1869-1871.

12. Weissbuch, I.; Addadi, L.; Lahav, M.; Leiserowitz, L., Molecular Recognition at Crystal Interfaces. *Science* **1991,** 253, (5020), 637-645.

13. Ward, M. D.; Yu, L., Selective nucleation and discovery of organic polymorphs through epitaxy. *Abstracts of Papers of the American Chemical Society* **2002,** 223, 116-IEC.

14. Mitchell, C. A.; Yu, L.; Ward, M. D., Selective nucleation and discovery of organic polymorphs through epitaxy with single crystal substrates. *Journal of the American Chemical Society* **2001,** 123, (44), 10830-10839.

15. Hooks, D. E.; Fritz, T.; Ward, M. D., Epitaxy and molecular organization on solid substrates. *Advanced Materials* **2001,** 13, (4), 227-+.

16. Perrin, M. A.; Neumann, M. A.; Elmaleh, H.; Zaske, L., Crystal structure determination of the elusive paracetamol Form III. *Chemical Communications* **2009**, (22), 3181-3183.

17. Haisa, M.; Kashino, S.; Maeda, H., Orthorhombic Form of Para-Hydroxyacetanilide. *Acta Crystallographica Section B-Structural Science* **1974,** B 30, (OCT15), 2510-2512.

18. Haisa, M.; Kashino, S.; Kawai, R.; Maeda, H., Monoclinic Form of Para-Hydroxyacetanilide. *Acta Crystallographica Section B-Structural Science* **1976,** 32, (APR15), 1283-1285.

19. Brooks, B. R.; Brooks, C. L.; Mackerell, A. D.; Nilsson, L.; Petrella, R. J.; Roux, B.; Won, Y.; Archontis, G.; Bartels, C.; Boresch, S.; Caflisch, A.; Caves, L.; Cui, Q.; Dinner, A. R.; Feig, M.; Fischer, S.; Gao, J.; Hodoscek, M.; Im, W.; Kuczera, K.; Lazaridis, T.; Ma, J.; Ovchinnikov, V.; Paci, E.; Pastor, R. W.; Post, C. B.; Pu, J. Z.;

Schaefer, M.; Tidor, B.; Venable, R. M.; Woodcock, H. L.; Wu, X.; Yang, W.; York, D. M.; Karplus, M., CHARMM: The Biomolecular Simulation Program. *Journal of Computational Chemistry* **2009,** 30, (10), 1545-1614.

20. Brooks, B. R.; Bruccoleri, R. E.; Olafson, B. D.; States, D. J.; Swaminathan, S.; Karplus, M., Charmm - a Program for Macromolecular Energy, Minimization, and Dynamics Calculations. *Journal of Computational Chemistry* **1983,** 4, (2), 187-217.

21. Nichols, G.; Frampton, C. S., Physicochemical characterization of the orthorhombic polymorph of paracetamol crystallized from solution. *Journal of Pharmaceutical Sciences* **1998,** 87, (6), 684-693.

22. Vanommeslaeghe, K.; Hatcher, E.; Acharya, C.; Kundu, S.; Zhong, S.; Shim, J.; Darian, E.; Guvench, O.; Lopes, P.; Vorobyov, I.; MacKerell, A. D., CHARMM General Force Field: A Force Field for Drug-Like Molecules Compatible with the CHARMM All-Atom Additive Biological Force Fields. *Journal of Computational Chemistry* 31, (4), 671-690.

23. Bovey, F. A.; Tiers, G. V. D., Polymer NSR spectroscopy .2. The high resolution spectra of methyl methacrylate polymers prepared with free radical and anionic initiators. *Journal of Polymer Science Part a-Polymer Chemistry* **1996,** 34, (5), 711-720.

24. Yesselman, J.; Price, D.; Knight, J.L.; Brooks, C. L. 3rd, *in preparation.*

25. Vangunsteren, W. F.; Berendsen, H. J. C., Algorithms for Macromolecular Dynamics and Constraint Dynamics. *Molecular Physics* **1977,** 34, (5), 1311-1327.

26. Myerson, A. S.; Jang, S. M., A comparison of binding energy and metastable zone width for adipic acid with various additives. *Journal of Crystal Growth* **1995,** 156, (4), 459-466.

27. Chen, Z.; Shen, Y. R.; Somorjai, G. A., Studies of polymer surfaces by sum frequency generation vibrational spectroscopy. *Annual Review of Physical Chemistry* **2002,** 53, 437-465.

28. McClelland, A.A.; López-Mejías, V.; Matzger A. J.; Chen, Z, *Langmuir*, **2011**, *27*, (6), 2162-2165.